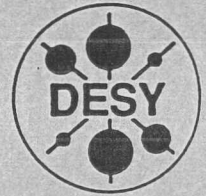




\*X1998-00698\*

DEUTSCHES ELEKTRONEN-SYNCHROTRON



DESY-THESIS-1998-005

April 1998

*frat anzulegen*

*C, D*

Measurement of the Proton Structure Functions  
 $F_2(x, Q^2)$  and  $F_L(x, Q^2)$  with the H1 Detector  
at HERA

by

A. A. Glazov

Eigennummer	DESY	Leihfrist
Eigentum von		
Zugang	29. APR. 1998	
Abgabe		
Leihfrist		
Leihperiode	7	days

ISSN 1435-8085

NOTKESTRASSE 85 - 22603 HAMBURG

DESY behält sich alle Rechte für den Fall der Schutzrechtserteilung und für die wirtschaftliche Verwertung der in diesem Bericht enthaltenen Informationen vor.

DESY reserves all rights for commercial use of information included in this report, especially in case of filing application for or grant of patents.

To be sure that your reports and preprints are promptly included in the HEP literature database send them to (if possible by air mail):

DESY  
Zentralbibliothek  
Notkestraße 85  
22603 Hamburg  
Germany

DESY  
Bibliothek  
Platanenallee 6  
15738 Zeuthen  
Germany

# Measurement of the Proton Structure Functions $F_2(x, Q^2)$ and $F_L(x, Q^2)$ with the H1 Detector at HERA

## DISSERTATION

zur Erlangung des akademischen Grades  
doctor rerum naturalium  
(Dr. rer. nat.)

im Fach Physik

eingereicht an der

Mathematisch-Naturwissenschaftlichen Fakultät I  
der Humboldt-Universität zu Berlin

von

**Alexandre Alimovich Glazov**

geboren am 26. Dezember 1966 in Dubna, Russland

Präsident der Humboldt-Universität zu Berlin  
Prof. Dr. Dr. hc. H. Meyer

Dekanin der Mathematisch-Naturwissenschaftlichen Fakultät I  
Frau Prof. V. Bonacic-Koutecky

Gutachter/innen:

1. Prof. Dr. J. Dainton
2. Prof. Dr. T. Lohse
3. Prof. Dr. P. Söding

Tag der mündlichen Prüfung: 13.02.1998

## Abstract

Measurements of the inclusive cross section for the deep-inelastic scattering of positrons off protons are presented at momentum transfers  $8.5 \leq Q^2 \leq 120 \text{ GeV}^2$  for data collected by the H1 experiment at HERA in the years 1994 and 1996. These measurements lead to the so far most precise extraction of the proton structure function  $F_2(x, Q^2)$  in the Bjorken  $x$  range  $1.3 \cdot 10^{-4} \dots 0.08$ . At large inelasticity  $y > 0.6$  the longitudinal structure function  $F_L(x, Q^2)$  has been determined for the first time at low  $x \lesssim 10^{-3}$  using novel techniques. This thesis focuses on the chain of the data analysis, extending from the luminosity measurement to next-to-leading (NLO) order QCD fits. All results of the presented analyses have been included into H1 publications. A noticeable outcome of the latest cross section measurement performed at  $y = 0.86$  is an indication of a departure from the QCD prediction which could require a larger contribution of the longitudinal structure function to the cross section than expected by NLO QCD.

## Zusammenfassung

Die vorliegende Arbeit beschreibt Messungen des inklusiven Streuquerschnitts von Positronen und Protonen im tiefinelastischen Bereich von Viererimpulsüberträgen  $8.5 \leq Q^2 \leq 120 \text{ GeV}^2$ . Die Messungen beruhen auf Daten, die in den Jahren 1994 und 1996 mit dem H1-Experiment am Beschleuniger HERA aufgezeichnet wurden. Die in der Arbeit vorgestellten Analysemethoden führten zu den bisher präzisesten Messungen der Protonstrukturfunktion  $F_2(x, Q^2)$  im Bereich von Bjorken  $x$  Werten zwischen 0.00013 und 0.08 durch das H1 Experiment. Zum ersten Mal wurde auch die longitudinale Strukturfunktion  $F_L(x, Q^2)$  bestimmt. Dies erforderte eine Ausdehnung des bisher erschlossenen Meßbereichs hin zu großen Inelastizitätswerten von  $y > 0.6$ . Dazu wurden neue Techniken entwickelt und angewandt, u.a. zur Identifikation des gestreuten Positrons, zur Behandlung des Photoproduktionsuntergrundes sowie eine in tiefinelastischen Streuexperimenten erstmalig angewandte Idee, die Funktion  $F_L$  unter der Annahme zu extrahieren, daß die andere Funktion,  $F_2$ , durch Daten soweit festgelegt ist, daß sie vermittels der QCD-Evolutionsgleichungen als bekannt vorausgesetzt werden kann.

Die Doktorarbeit befaßt sich hauptsächlich mit der ausführlichen Darstellung der Analyse der Daten der Jahre 1994 und 1996, die mit verschiedenen Konfigurationen des H1-Detektors aufgenommen wurden. Dabei werden alle Aspekte der Analyse, von der Luminositätsmessung bis hin zu QCD-Fitprozeduren behandelt. Alle Resultate dieser Doktorarbeit wurden in Publikationen der H1-Kollaboration aufgenommen. Ein besonders bemerkenswertes Resultat dieser Arbeit besteht in der Beobachtung eines Verhaltens des tiefinelastischen Streuquerschnitts bei großen  $y < 0.9$ , das von den Erwartungen aus der QCD abweicht. Dies ist wahrscheinlich auf die longitudinale Strukturfunktion  $F_L$  zurückzuführen, welche größer sein könnte, als es sich aus den Daten bei kleineren  $y$  und der QCD in "next-to-leading order" ergibt.

# Contents

<b>1</b>	<b>Introduction</b>	<b>3</b>
<b>2</b>	<b>HERA and the H1 Detector</b>	<b>10</b>
2.1	HERA	10
2.2	H1 Detector	11
2.2.1	Luminosity System	13
2.2.2	Central and Forward Tracking Systems	13
2.2.3	Liquid Argon Calorimeter	15
2.2.4	Backward Detectors in 1994 and 1996	16
2.2.5	Trigger System and Offline Selection of Events	20
<b>3</b>	<b>Basics of the Cross Section Measurement</b>	<b>22</b>
3.1	Determination of the Event Kinematics	22
3.2	Kinematics and Detector Reconstruction	25
3.3	Monte Carlo Models and Analytical Tools	27
3.4	Radiative Corrections	28
3.5	Electron Identification	31
3.6	Backgrounds to Deep Inelastic Scattering	34
3.6.1	Photoproduction ( $\gamma p$ ) Background	34
3.6.2	Non- $ep$ Background	36
3.7	Cross Section Determination	37
3.8	Extraction of Structure Functions	39
<b>4</b>	<b>Data Treatment</b>	<b>41</b>
4.1	Data Samples	41
4.2	Run Selection	42
4.3	Stability Studies	43
4.4	Vertex Analysis	44
4.5	Satellite Bunch Corrections to the Luminosity Measurement	46
4.6	Trigger Definitions and Performance	48

<b>5</b>	<b>Detector Alignment and Calibration</b>	<b>55</b>
5.1	Determination of the Electron Scattering Angle . . . . .	55
5.2	Calibration of Backward Electromagnetic Calorimeters . . . . .	62
5.3	Hadronic Energy Scale . . . . .	70
<b>6</b>	<b>DIS Event Selection</b>	<b>74</b>
6.1	Vertex Reconstruction Efficiency . . . . .	76
6.2	Backward Tracker – Calorimeter Link . . . . .	85
6.3	Estimators of Cluster Properties . . . . .	86
6.4	$E - p_z$ Cut . . . . .	88
6.5	Event Validation using the Central Inner Proportional Chamber . . . . .	89
6.6	Event Validation using the Central Drift Chambers . . . . .	90
<b>7</b>	<b>DIS Cross Section, <math>F_2</math> and <math>F_L</math> Results</b>	<b>94</b>
7.1	Final Monte Carlo Simulation Adjustment and Control Plots . . . . .	94
7.2	Summary of the Systematic Error Sources . . . . .	98
7.3	DIS Cross Section and $F_2(x, Q^2)$ Results . . . . .	100
7.4	Determination of the Gluon Distribution $xg(x, Q^2)$ . . . . .	100
7.5	QCD Fit for the Extraction of the Structure Function $F_L(x, Q^2)$ . . . . .	103
7.5.1	Theoretical Uncertainties of the $F_2^{\text{fit}}$ Extrapolation . . . . .	104
7.5.2	Systematic Errors of the $F_2^{\text{fit}}$ Extrapolation . . . . .	106
7.6	Extraction of the Structure Function $F_L(x, Q^2)$ . . . . .	107
7.7	$F_2(x, Q^2)$ at High $y$ . . . . .	108
<b>8</b>	<b>Conclusions</b>	<b>110</b>
<b>A</b>	<b>Tables of the Experimental Results</b>	<b>113</b>
<b>B</b>	<b>Z-Vertex Reconstruction</b>	<b>118</b>

# Chapter 1

## Introduction

### Cross Section of Deep Inelastic Scattering (DIS)

In the inclusive deep inelastic electron-proton scattering neutral current process,  $ep \rightarrow eX$ , an electron is scattered off a proton and any hadronic final state  $X$  is produced. Due to  $\phi$  symmetry the cross section for this process can be expressed by two variables. They are defined in terms of the four momenta of the incident and the scattered electron,  $k, k'$ , and of the incident proton,  $P$  as

$$Q^2 = -(k - k')^2 \quad x = \frac{Q^2}{2P(k - k')}. \tag{1.1}$$

Here  $Q^2$  corresponds to the four momentum transfer squared in the reaction. The dimensionless variable  $x$  corresponds in the parton model to the fraction of the proton momentum taken by the parton which is hit by the exchanged photon or  $Z$  boson. Another important dimensionless variable is

$$y = \frac{P(k - k')}{Pk} \tag{1.2}$$

which corresponds in the rest frame of the proton to the fraction of the incoming lepton energy carried by the exchanged boson. It is often called the "inelasticity" variable. The  $y$  variable is related to  $Q^2, x$  and the center of mass energy squared  $S$  by the equation<sup>1</sup>  $Q^2 = Sxy$ . Both  $x$  and  $y$  variables are limited to values between 0 and 1.

The cross section of the  $ep \rightarrow pX$  process can be expressed as

$$\sigma \sim L_{\alpha\beta}W^{\alpha\beta}. \tag{1.3}$$

In this formula  $L_{\alpha\beta}$  denotes the leptonic tensor describing the interaction between the electron and the virtual exchange boson. The hadronic tensor  $W^{\alpha\beta}$  corresponds to the boson-proton interaction. In Quantum Electro Dynamics (QED) the lepton-photon vertex is well defined and therefore  $L_{\alpha\beta}$  is completely calculable. Using Lorenz invariance and current conservation the hadronic tensor, however, can only be reduced to two functions related to the structure of the proton. The DIS cross section has the well-known form:

$$\frac{d^2\sigma}{dx dQ^2} = \kappa \left( F_2(x, Q^2) - \frac{y^2}{Y_+} F_L(x, Q^2) \right) \quad Y_+ = 2(1 - y) + y^2 \quad \kappa = \frac{2\pi\alpha^2}{Q^4 x} Y_+ \tag{1.4}$$

for the particular choice of the structure function  $F_2(x, Q^2)$  and the longitudinal structure function  $F_L(x, Q^2)$ .

<sup>1</sup>Here and in all following formulae the proton and electron masses are neglected

One can consider the  $ep$  scattering process as the interaction of a flux of virtual photons<sup>2</sup> with the proton. The double differential DIS cross section can be written as:

$$\frac{d^2\sigma}{dx dQ^2} = \Gamma(y) (\sigma_T + \epsilon(y)\sigma_L), \quad (1.5)$$

where  $\Gamma(y) = Y_+\alpha/(2\pi Q^2 x)$  stands for the flux factor,  $\epsilon(y) = 2(1-y)/Y_+$  defines the photon polarization and  $\sigma_T, \sigma_L$  correspond to the cross sections of the interaction of transverse and longitudinally polarized photons, respectively. These cross sections are related to the structure functions as

$$\begin{aligned} F_2(x, Q^2) &= \frac{Q^2}{4\pi^2\alpha} (\sigma_T(x, Q^2) + \sigma_L(x, Q^2)) \\ F_L(x, Q^2) &= \frac{Q^2}{4\pi^2\alpha} \sigma_L(x, Q^2). \end{aligned} \quad (1.6)$$

The longitudinal structure function  $F_L$  is directly proportional to  $\sigma_L(x, Q^2)$ . A quantity often used as a measure for the amount of photon-proton scattering with different polarization is the ratio

$$R(x, Q^2) = \frac{\sigma_L}{\sigma_T} = \frac{F_L(x, Q^2)}{F_2(x, Q^2) - F_L(x, Q^2)}. \quad (1.7)$$

From the formula 1.6 one can derive the relation  $0 \leq F_L(x, Q^2) \leq F_2(x, Q^2)$  enforced by the positivity of the cross sections  $\sigma_L$  and  $\sigma_T$ . Since the contribution of the longitudinal structure function to the DIS cross section (Eq. 1.4) is proportional to  $y^2$ , the  $F_2(x, Q^2)$  term dominates at  $y < 0.5$  and most of the DIS experimental data have been interpreted as a measurement of the structure function  $F_2$ .

### Quark Parton Model

The modern history of the DIS experiments started in the early sixties when the first results on the scattering of high energy electrons ( $7 < E_e < 17$  GeV) off nuclear targets were obtained at the Stanford Linear Accelerator Center (SLAC). The remarkable outcome of these experiments was that the structure function  $F_2$ , measured at values of the four momentum transfer squared of about 5 GeV<sup>2</sup>, showed very little dependence on  $Q^2$ , but depended only on the variable  $x$ . This kind of behaviour ('scaling') was predicted by Bjorken [2]. The explanation of this phenomenon has been given within the Quark Parton Model (QPM) [3].

The basic idea of this model is to consider the DIS as scattering off pointlike, quasifree constituents within the proton, viewed from the frame in which the proton has infinite momentum. In this frame, given that  $Q^2 \gg M_P^2$  ( $M_P$  - proton mass) and  $x$  is non vanishing, the scattering is incoherent from individual free partons. The latter are associated with either constituent or sea quarks [4, 5].

In the parton model the structure function  $F_2$  can be expressed as a sum of the (anti)quark momentum distributions  $xq_i(x)$  weighted with the square of their electric charge  $e_i$ :

$$F_2(x) = \sum_i e_i^2 x [q_i(x) + \bar{q}_i(x)]. \quad (1.8)$$

The functions  $q_i(x)$  are considered to be the probability momentum density functions of the partons  $i$  inside the proton. The proton consists of two  $u$  and one  $d$  quarks, therefore the counting rules

$$\int_0^1 dx (u(x) - \bar{u}(x)) = 2 \quad \int_0^1 dx (d(x) - \bar{d}(x)) = 1 \quad (1.9)$$

<sup>2</sup>The definition of a virtual photon flux is not strict. The only constraint, is that it should lead to the correct formulae for real photon scattering in the  $Q^2 \rightarrow 0$  limit. We will use the virtual flux definition of Hand [1].



must be satisfied. A number of further sum rules [6, 7, 8, 9] were derived for different combinations of structure functions which have been extensively tested with the experimental data.

The cross sections  $\sigma_T$  and  $\sigma_L$  depend on the spin of the proton constituents. In the approximation  $Q^2 \gg M_p^2$  they are given as:

$$\begin{aligned} \sigma_T &= 0 & \text{for spin } & 0 \\ \sigma_L &= 0 & \text{for spin } & \frac{1}{2} \end{aligned} \quad (1.10)$$

with an intermediate result for higher spins. The first experimental results showed that the ratio  $R = \sigma_L/\sigma_T$  is consistent with zero. This supported the hypothesis that quarks are fermions, i.e. their spin is equal to  $1/2$ . Therefore the quark parton model predicts  $\sigma_L = 0$  which leads to the so-called Callan-Gross relation [10]:

$$F_L(x) = 0. \quad (1.11)$$

## QCD and DIS

Further lepton and neutrino nucleon scattering experiments observed a violation of the scaling hypothesis, i.e. a weak, logarithmic dependence of the structure function  $F_2$  on  $Q^2$  and also a non-zero longitudinal structure function  $F_L$ . These effects were explained in the framework of Quantum Chromodynamics (QCD) – a field theory which describes the strong interaction between quarks as mediated by gluons.

The basic objects of this theory are quarks – fermions with fractional electric charge. They obey the SU(3) internal “colour” symmetry, which, being extended to a local gauge symmetry, gives rise to additional zero mass vector bosons, the gluons. These carry the colour interaction between quarks. Due to the non-Abelian structure of the SU(3) group the self-coupling of gluons is possible, leading, in contrast to the Abelian QED, to an *antiscreening* effect from vacuum polarization. As a result, the coupling constant  $\alpha_S$ , calculated according to the renormalization group equation, is a decreasing function of the characteristic energy scale in the reaction. In the leading order approximation it is given by the equation:

$$\alpha_S(Q^2) = \frac{4\pi}{\beta_0 \ln \frac{Q^2}{\Lambda^2}} \quad \text{with} \quad \beta_0 = 11 - \frac{2}{3}n_f, \quad (1.12)$$

where  $n_f$  is the number of quark *flavours* and  $\Lambda$  characterizes the strength of the coupling. The latter depends on the number of active flavours and (for higher order calculations) on convention, used for the definition of  $\alpha_S(Q^2)$ .

The coupling constant  $\alpha_S$  is an experimentally measurable quantity. A convenient way of its presentation is to derive its value at  $Q^2 = M_Z^2$  where  $M_Z$  is the mass of the  $Z^0$  boson. The world average value is now  $\alpha_S(M_Z^2) = 0.118 \pm 0.003$  [11] corresponding to  $\Lambda$  values of about 200 MeV.

The decrease of the coupling constant with rising energy scale is known as asymptotic freedom. On the other hand, if  $Q^2 \rightarrow \Lambda^2$ , the strong coupling constant, derived from Eq. 1.12, increases to infinity. This is a sign of the breakdown of the perturbative calculation at  $Q^2 \sim \Lambda^2$ .

The applicability of the perturbative QCD (pQCD) calculations to the DIS processes follows from the factorization theorem (see for example [12]). It states, that the structure function can be factorized into “short distance” dependences, which can be calculated in pQCD, and into “long distance” dependences, which should be taken from outside the theory, for example, from experiment. Formally, factorization leads to expressions of the structure functions as a convolution of coefficient functions  $C_a^{V,i}$ , given by pQCD for a particular exchanged boson  $V$ , parton  $i$  and a structure function  $a$ , and parton distributions  $f_{i/h}$ , which are specific to the hadron  $h$  but universal for  $V$  and  $a$ . For the structure function  $F_2$  the theorem leads to the expression:

$$F_2^{V,h}(x, Q^2) = \sum_{i=f,\bar{f},g} \int_x^1 dz C_2^{V,i} \left( \frac{x}{z}, \frac{Q^2}{\mu^2}, \frac{\mu_F^2}{\mu^2} \alpha_S(\mu^2) \right) f_{i/h}(z, \mu_F, \mu^2), \quad (1.13)$$

where the summation is performed over all partons (quarks, antiquarks and gluons).

Two scales are present in Eq. 1.13. The factorization (renormalization) scale  $\mu_F$  ( $\mu$ ) serves to absorb the infrared (ultraviolet) divergent part in the perturbation theory.

Both  $\mu_F$  and  $\mu$  are arbitrary parameters. By convention, two schemes are most often used: the DIS scheme in which the structure function  $F_2$  is given by the parton model formula 1.8 to all orders of perturbation theory, i.e.  $C_2^{Vq} = e_q^2 \delta(1-x)$ ,  $C_2^{V\bar{q}} = e_q^2 \delta(1-x)$ ,  $C_2^{Vg} = 0$ ,  $\mu = \mu_F = Q^2$ ; and the modified minimal subtraction scheme ( $\overline{MS}$ ), where only the divergent part is absorbed into the renormalized quark distribution, and  $\mu = \mu_F$  is chosen such as to define the parton distributions directly in terms of hadronic matrix elements. The latter scheme is more often used for the theoretical calculation while the former is specific to DIS experiments.

For the longitudinal structure function, the leading order coefficient functions are scheme independent [13]:

$$F_L(x, Q^2) = x \sum_{i=f, \bar{f}} e_f^2 \int_x^1 \frac{dz}{z} f_i(z, Q^2) \left\{ \frac{\alpha_S}{2\pi} [2C_F \frac{x}{z}] + \dots \right\} \\ + x \sum_{i=f, \bar{f}} e_f^2 \int_x^1 \frac{dz}{z} g(z, Q^2) \left\{ \frac{\alpha_S}{2\pi} [4T_R (1 - \frac{x}{z})] + \dots \right\}, \quad (1.14)$$

where  $C_F = 4/3$ ,  $T_R = 1/2$  and  $g(z, Q^2)$  denotes the gluon density function. Note that the expression for  $F_L(x, Q^2)$  is proportional to  $\alpha_S$ . Therefore this structure function can be considered as a radiative correction. In this sense the Callan-Gross relation (Eq. 1.11) is valid in the QCD Born approximation.

A remarkable feature of the parton densities in QCD is the possibility to extrapolate them from certain  $Q_0^2$  to any other  $Q^2$  value using the DGLAP evolution equations [14]. These equations can be derived from the factorization formula 1.13 exploring the structure functions independence of the choice of  $\mu = \mu_F$ . In terms of gluon ( $g(x, Q^2)$ ), singlet ( $\Sigma(x, Q^2) = \sum_i q_i(x, Q^2) + \bar{q}_i(x, Q^2)$ ) and nonsinglet ( $q^{NS}(x, Q^2)$ , like,  $q_i(x, Q^2) - \bar{q}_i(x, Q^2)$ ) density functions, the evolution equations can be written as:

$$\frac{d}{d \ln Q^2} \begin{pmatrix} \Sigma(x, Q^2) \\ g(x, Q^2) \end{pmatrix} = \frac{\alpha_S(Q^2)}{2\pi} \int_x^1 \frac{dz}{z} \\ \times \begin{pmatrix} P_{qq}(\frac{x}{z}, \alpha_S(Q^2)) & 2n_f P_{qg}(\frac{x}{z}, \alpha_S(Q^2)) \\ P_{gq}(\frac{x}{z}, \alpha_S(Q^2)) & P_{gg}(\frac{x}{z}, \alpha_S(Q^2)) \end{pmatrix} \begin{pmatrix} \Sigma(z, Q^2) \\ g(z, Q^2) \end{pmatrix} \quad (1.15)$$

for the coupled pair of singlet-gluon equations and as:

$$\frac{d}{d \ln Q^2} q^{NS}(x, Q^2) = \frac{\alpha_S(Q^2)}{2\pi} \int_x^1 \frac{dz}{z} P_{qq}(\frac{x}{z}, \alpha_S(Q^2)) q^{NS}(z, Q^2) \quad (1.16)$$

for each of the nonsinglet distributions. In these equations  $P_{qq}, P_{qg}, P_{gq}, P_{gg}$  denote so-called splitting functions. Each of them is calculable as a power series in  $\alpha_S$ :

$$P_{qq} = P_{qq}^{(0)}(z) + \frac{\alpha_S}{2\pi} P_{qq}^{(1)}(z) + \dots \\ P_{qg} = P_{qg}^{(0)}(z) + \frac{\alpha_S}{2\pi} P_{qg}^{(1)}(z) + \dots \\ P_{gq} = P_{gq}^{(0)}(z) + \frac{\alpha_S}{2\pi} P_{gq}^{(1)}(z) + \dots \\ P_{gg} = P_{gg}^{(0)}(z) + \frac{\alpha_S}{2\pi} P_{gg}^{(1)}(z) + \dots \quad (1.17)$$

The leading order splitting functions  $P_{ab}^{(0)}(x)$  have a physical interpretation as the probabilities of finding a parton of type  $a$  in a parton of type  $b$  with a fraction  $x$  of the longitudinal momentum of the parent parton and a transverse momentum squared much less than  $\mu^2$  [15]. The interpretation as

probabilities implies that the splitting functions are positive definite for  $x < 1$ , and satisfy the sum rules

$$\begin{aligned} \int_0^1 dx P_{qq}^{(0)}(x) &= 0 \\ \int_0^1 dx x \left[ P_{qq}^{(0)}(x) + P_{gq}^{(0)}(x) \right] &= 0 \\ \int_0^1 dx x \left[ 2n_f P_{qg}^{(0)}(x) + P_{gg}^{(0)}(x) \right] &= 0, \end{aligned} \quad (1.18)$$

which correspond to quark number and momentum conservation in the splitting of quarks and gluons, respectively.

Both the leading order and  $O(\alpha_S)$  contributions to the splitting and coefficient functions have been calculated (see [16] for a review).

An important feature of the factorization theorem (Eq. 1.13) and of the evolution equations (Eq. 1.15, 1.16) is that the low limit of the convolution integrals is not zero but equal to  $x$ . This allows to have definite predictions of the theory without knowledge of the parton densities at lower  $x$ . Based on this fact, the QCD fit techniques have been developed and applied to the experimental data: The parton density distributions are parameterized at some fixed  $Q^2$  by smooth analytical functions. They are evolved to other  $Q^2$  values where the structure functions are derived and compared with the data. A minimization procedure allows to determine the parton density functions for  $Q^2 > Q_{min}^2$  and  $x > x_{min}$  where  $Q_{min}^2$  is defined by the validity of pQCD and  $x_{min}$  corresponds to the minimum  $x$  reached by the considered experiments.

### Small $x$ Physics

The DGLAP evolution equation effectively sums up the leading  $\alpha_S \ln Q^2$  terms. When the  $ep$  center of mass energy is large (as in the kinematic region of the HERA experiments), there is a second variable which can become large, namely  $1/x = Sy/Q^2$ . Therefore, in this case one should also consider the leading  $\alpha_S \ln(1/x)$  contributions. Different approaches have been developed in this direction.

The most radical of them is related to the BFKL evolution equation [19] which evolves the parton densities to smaller  $x$ . A famous prediction of this equation is the power-like growth of the gluon density

$$xg(x, Q^2) \sim x^{-\lambda}, \quad (1.19)$$

where  $\lambda$ , for fixed  $\alpha_S$ , and to leading order, can be expressed as  $\lambda = (3\alpha_S/\pi)4 \ln 2 \sim 0.5$ . Recently, the higher order corrections to the BFKL equation have become available [20] which lower the predicted value of  $\lambda$ .

Another way to treat the  $\ln(1/x)$  terms is to include them into the coefficient and splitting functions [21]. A powerful technique to calculate these  $\ln(1/x)$  corrections is based on the so-called  $k_T$  factorization theorem [22].

It turned out that these corrections are rather difficult to include and their effect is relatively small if an observable structure function  $F_2$  is considered (see, for example [23]). This is related to the factorization scheme dependence of the corrections. It is possible to find a scheme which minimizes their effect [24]. Additionally, the contribution of  $\ln(1/x)$  terms can be absorbed into the input distributions.

To diminish the factorization scheme dependence, it was proposed by Catani [26] to rewrite the evolution equation in terms of different hadronic observables  $F_A$  and  $F_B$  (for instance,  $F_2$  and  $F_L$ ):

$$\frac{dF_A(x, Q^2)}{d \ln Q^2} = \int_x^1 \frac{dz}{z} \left[ \Gamma_{AA} \left( \frac{x}{z}, \alpha_S \right) F_A(z, Q^2) + \Gamma_{AB} \left( \frac{x}{z}, \alpha_S \right) F_B(z, Q^2) \right] \quad (1.20)$$

Since this equation relates the scaling violation of physical observables to the actual values of the observables, the kernels  $\Gamma_{AB}$  are physical observables as well. Owing to the formal similarity to the DGLAP equations splitting functions, they are termed as physical splitting functions (PSF). By construction, PSF are factorization scheme independent, and can be unambiguously calculated in perturbation theory. Similarly, Thorne has recently developed evolution equations to leading order in  $\ln(1/x)$  and  $\alpha_S$  [27], directly for the nonsinglet structure function  $F_2^{NS}$  and a coupled system of equations for singlet  $F_2^S$  and  $dF_2/d\ln Q^2$ .

A remarkable feature of the new resummation techniques is that although they give very similar predictions to the structure function  $F_2$ , for the second independent structure function, like  $F_L$ , the results are rather different. For example,  $F_L$  derived from Thorne's equations is about two times lower than the NLO DGLAP estimation if the same  $F_2$  input is used. The same relation is true for the BFKL-inspired colour dipole model [28].

### Experimental status

Since the famous SLAC results till nowadays many data have been collected by various lepton-nucleon DIS experiments (see [29] for review). Presently, the DIS experiments provide the most accurate determination of the different quark densities inside various hadrons. The running coupling constant  $\alpha_S$  has been rather precisely measured from the scaling violation of the structure functions. Many other important results have been obtained, including precision measurements of the electroweak mixing angle, of Cabibbo-Kobayashi-Maskawa matrix elements and of quark masses. In general, the outcome of these studies is a well-established validity of the QCD calculations.

The kinematic domain has been dramatically extended since the first  $ep$  collider facility, HERA, started to operate. The large center of mass energy  $\sqrt{S} \approx 300$  GeV allowed to reach extremely small  $x$  values  $\leq 0.0001$  in the DIS region with millions of events and, with increasing luminosity, also extremely large  $Q^2$  of 30000 GeV<sup>2</sup> at high  $x$ .

Since 1992, the start of the physics operation, HERA increased each year the delivered luminosity. The physics analysis in the first years concentrated on low  $x$ , where many new phenomena had been expected, as was briefly outlined in the previous section. Below we will describe the main experimental results obtained by the H1 experiment, one of the two collaborations working at HERA in the colliding mode.

The first data, based on the initial year of the HERA running (1992), showed a remarkable rise of the structure function  $F_2$  towards low  $x$  [30]. This rise was confirmed with more than ten times the luminosity ( $0.271 \text{ pb}^{-1}$ ) in 1993 [31]. The  $Q^2$  behaviour of the structure function has been successfully described by the DGLAP evolution equations in NLO which lead to a large gluon contribution at low  $x$  [32].

The data collected during the 1994 year of operation had statistical errors of the DIS cross section measurement of 2 – 3% for  $Q^2 < 50$  GeV<sup>2</sup>. A detailed study of the systematic effects allowed to reduce them up to 5% in the central part of the kinematic region. This represents so far the most precise determination of the structure function  $F_2$  performed by the H1 collaboration [33]. The data have been included into many global QCD fits, which describe them well down to  $Q^2 = 1$  GeV<sup>2</sup>.

The further inclusive DIS cross section measurements have been split into different regions. The high  $Q^2$  analysis continued to use increased luminosity. Recently, the preliminary results based on a combination of data from the years 1994 – 1997 have been presented [37]. The “low  $Q^2$ ” ( $Q^2 \leq 120$  GeV<sup>2</sup>) and correspondingly low  $x$  analysis has the ultimate goal to reach 2 – 3% total uncertainty of the cross section measurement, which would allow the precise determination of the gluon density and of  $\alpha_S$  [38]. This requires a tremendous work on the study of different systematic effects. It has not been reached yet.

Other developments are related to an extended coverage of the kinematic range of the measurement. Owing to the upgrade of the H1 detector in winter 1994-1995, data at extremely low  $Q^2$  ( $Q^2 >$

0.35 GeV<sup>2</sup>) were collected [39], which allowed to study the transition between DIS and photoproduction at low  $x$ .

The structure function measurement at HERA remains incomplete until the longitudinal structure function  $F_L$  is measured. This requires to change the center of mass energy in the  $ep$  collision. For precise data a set of several runs with different proton energies is needed [40]. This measurement will be of a great theoretical importance, since it could distinguish between different models describing the low  $x$  QCD evolution as was discussed in the previous section.

A first attempt to obtain some information about the longitudinal structure function was performed by H1 with 1994 data [41]. The idea of this new approach was based on the fact that the DIS cross section is unambiguously defined at low  $y$  by the  $F_2$  structure function while at high  $y$   $F_2$  and  $F_L$  have similar contributions (see Eq. 1.4). A unique feature of the HERA data is the wide range of  $y$  values covered,  $y > 0.01$ . The analysis of the data was extended to the high  $y$  range where the DIS cross section was extracted. The structure function  $F_2$  was estimated using a NLO QCD fit to the H1 data at lower  $y < 0.35$ , where  $F_2$  is determined independently of  $F_L$ . This then was derived by subtracting the  $F_2$  part from the measured cross section.

This analysis showed the great importance of reaching the highest  $y$  values in the cross section measurement. The higher  $y$  values are reached, the smaller errors can be achieved for the  $F_L$  determination. High values of  $y$  require to measure the scattered electron at energies down to a few GeV, i.e. in a region where background processes and DIS in itself complicate the unambiguous identification of the scattered electron. New possibilities in this direction have been opened as the result of the H1 detector upgrade.

Recently, a new preliminary measurement of the inclusive deep inelastic scattering cross section at low  $Q^2$  performed by H1 has been presented [42]. This analysis comprises the 1995 and 1996 data in the  $Q^2$  intervals 2 – 8.5 GeV<sup>2</sup> and 12 – 90 GeV<sup>2</sup> respectively. The combination of all H1 results on the structure function  $F_2$  allowed to perform a new more precise determination of the gluon density. The extension of the cross section measurement to  $y = 0.86$  lead to a further determination of the longitudinal structure function  $F_L$ . While the precision of the  $F_2$  measurement is on the same accuracy level as the 1994 data analysis, the higher sensitivity at larger  $y$  permitted a more accurate determination of  $F_L$ . An interesting outcome of this analysis is that the extracted  $F_L$  values tend to be larger than the NLO QCD prediction.

In this thesis several analyses are described which were part of H1 publications. This concerns the 1994 data studies of the structure functions  $F_2$  [33] and  $F_L$  [41] and the new, still preliminary result of the cross section measurement for the 1996 running period [42]. Parts of the 1994  $F_2$  analysis have been already described in detail in several Ph.D. theses [34, 35, 36]. Thus particular emphasis is given here to the  $F_L$  analyses and to the 1996 data.

This thesis is organized as follows. Firstly, the H1 detector is described (Chapter “HERA and H1 Detector”) before and after the upgrade in winter 1994-1995. Secondly, the main ingredients of the inclusive DIS cross section measurement are presented in the Chapter “Basics of the Deep Inelastic Scattering Cross Section Measurement”. The next three Chapters closely follow the experimental procedure of the cross section determination: Chapter “Data Treatment” presents the general data selection and luminosity calculation; Chapter “Detector Alignment and Calibration” is devoted to the kinematic variable determination in data and Monte Carlo simulation; Chapter “DIS Event Selection” describes the DIS selection criteria and study of their efficiencies. Finally, the Chapter “Results” presents the results of the DIS measurement and determination of the structure functions  $F_2(x, Q^2)$  and  $F_L(x, Q^2)$ . In the Appendix the procedure of the event interaction point  $Z$  coordinate reconstruction is explained.

## Chapter 2

# HERA and the H1 Detector

In this chapter the HERA machine and the H1 detector are introduced. A brief overview of the accelerator chain delivering protons with nominal energy of 820 GeV and electrons with 27.6 GeV energy is given first. The H1 detector is situated in the North interaction region of the HERA ring. In its subsequent description emphasis is given to those subdetectors which are particularly important for the deep inelastic scattering (DIS) cross section measurement.

## 2.1 HERA

The Hadron-Electron-Ring-Anlage HERA consists of two separate, 6.3 km long storage rings designed to accelerate 820 GeV protons and 30 GeV electrons (or positrons), see Tab. 2.1. Two big detectors were built in the late eighties which use HERA in its  $ep$  colliding mode. These are located in the North Hall (H1) and in the South Hall (ZEUS). The layout of the HERA machine together with the injection system is illustrated in Fig. 2.1.

In the years 1994 and 1996 the HERA collider was operating with positrons<sup>1</sup>. The HERA particle beams were delivered in so-called bunches with 96 ns bunch crossing intervals. A typical run contained 170 (1994) or 190 (1996) filled bunches. Since the commissioning in 1992, HERA has each year

<sup>1</sup>This thesis describes only data taken in positron-proton colliding mode at HERA. For  $Q^2 < 133.5 \text{ GeV}^2$  discussed in the thesis, the effect of the  $Z^0$  exchange for the deep inelastic cross section is negligible. Thus we will use the name "electron" as a synonym to "positron". The name "positron" will be used only in those parts of the analysis closely related to the HERA operation or when the charge of the particle needs to be distinguished.

	<i>p</i> -ring	<i>e</i> -ring	units
Nominal energy	820	30	GeV
Magnetic field	4.68	0.165	T
Total number of particles	2.1	0.8	$10^{13}$
Number of bunches	210	210	
$\sigma_X/\sigma_Y$ at I.P.	0.29/0.7	0.26/0.02	mm
$\sigma_Z$	110	8.0	mm
Luminosity	$1.5 \times 10^{31} \text{ cm}^{-2} \text{ s}^{-1}$		
Integrated Luminosity	50 $\text{pb}^{-1}/\text{year}$		

Table 2.1: HERA design parameters (from [44]).  $\sigma_{X,Y,Z}$  stand for the X, Y, and Z spread of the beam at the interaction point (I.P.).

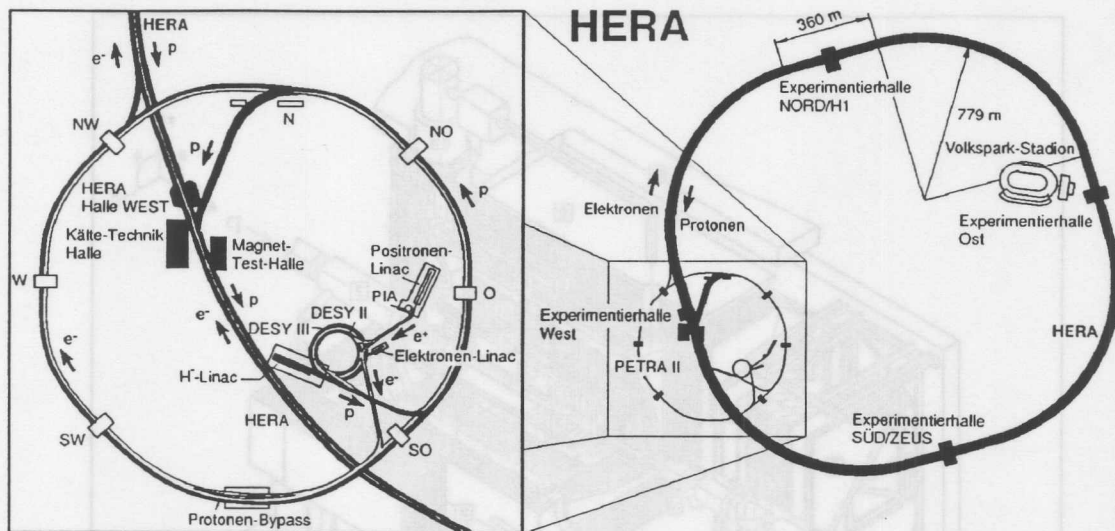


Figure 2.1: Schematic view of the  $ep$  storage ring HERA (right) together with the major experiments. The left figure presents a zoomed view of the HERA preaccelerator chain.

increased the currents of the proton and electron beams. The maximum beam currents achieved in 1994 were 60 mA and 30 mA for the proton and electron beams, respectively. These values were increased to 75 mA and 35 mA in 1996.

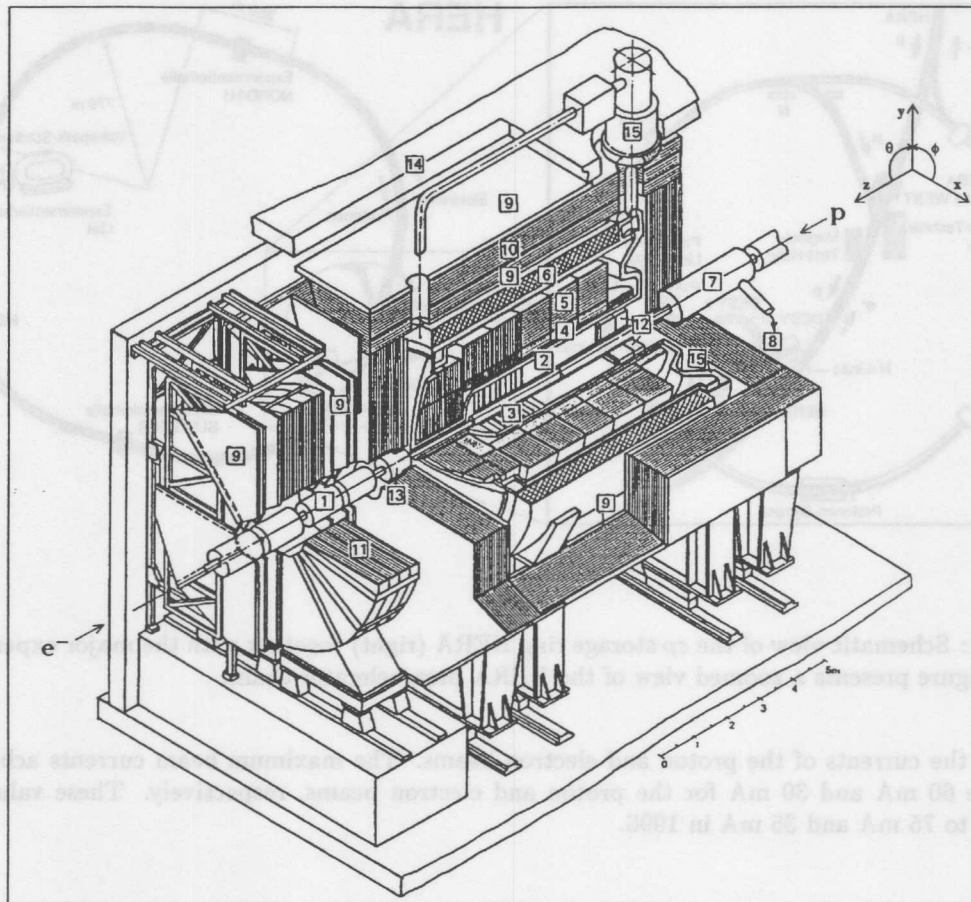
## 2.2 H1 Detector

The H1 experiment [45] was designed as a general purpose detector to study high-energy interactions of electrons and protons at HERA. A schematic 3D view of the detector is presented in Fig. 2.2.

The H1 detector is arranged cylindrically symmetric around the beam axis. The imbalance in the energy of the electron and the proton colliding beams implies that the detector is better instrumented in the outgoing proton direction, which defines, by convention, the positive  $Z$  direction of the H1 coordinate system. The components of the detector situated on the positive side from the interaction point are referred to as “forward”. Similarly the negative side is referred to as “backward”. The region around the interaction point is called the “central” part of the apparatus.

The H1 detector (Fig 2.2) is composed of a central (2) and a forward (3) tracking chamber system surrounded by electromagnetic and hadronic calorimeters (4,5): a Liquid Argon calorimeter in the central and forward directions and a Lead-Scintillator (BEMC) and later a Lead-Fiber calorimeter (Spacal) in the backward part (12). A superconducting coil outside the Liquid Argon calorimeter provides a uniform magnetic field of 1.2 T. The iron return yoke (10) surrounding the whole detector contains several layers of streamer tubes (9). These measure the hadronic shower tails using an analog readout system and the muon tracks using a digital readout system. In the forward direction the measurement of muons is performed by drift chambers (9) placed in a toroidal magnetic field (11).

This thesis describes cross section measurements using data taken in 1994 and in 1996. The instrumentation of the H1 detector in the central and forward directions was similar in these years. The backward part, however, was upgraded during the shutdown of the machine operation in the



1	Beam pipe and beam magnets	9	Muon chambers
2	Central tracking device	10	Instrumented iron yoke
3	Forward tracking device	11	Forward muon toroid
4	Electromagnetic LAr calorimeter	12	Backw. electromagn. calorimeter (BEMC)
5	Hadronic LAr calorimeter	13	PLUG calorimeter
6	Superconducting coil (1.15 T)	14	Concrete shielding
7	Compensating magnet	15	Liquid argon cryostat
8	Helium supply for 7		

Figure 2.2: 3D view of the H1 detector.



central tracking		
angular-radial coverage	$15^\circ < \theta < 165^\circ$	$150 < r < 850$ mm
jet chambers: spatial resolution	$\sigma_{r\phi} \approx 200$ $\mu\text{m}$	$\sigma_z = 22.0$ mm
Z-chambers: spatial resolution	$\sigma_{r\phi} = 25$ and $58$ mm	$\sigma_z \approx 350$ $\mu\text{m}$
momentum- $dE/dx$ resolution	$\sigma_p/p^2 < 0.01$ $\text{GeV}^{-1}$	$\sigma(dE)/dE = 10\%$
forward tracking		
angular-radial coverage	$7^\circ < \theta < 25^\circ$	$120 < r < 800$ mm
spatial resolution	$\sigma_{x,y} = 1$ mm	
trigger proportional chambers		
angular coverage, channels	$7^\circ < \theta < 175^\circ$	3936

Table 2.2: Main parameters of the Central and Forward tracking chambers in the H1 detector (from [45]). The angular coverage of the central tracker is given based on the inner jet chamber CJC1.

winter 1994/1995. In the following discussion the common parts of the 1994 and the 1996 operation periods will be introduced first. The description of the backward part, which is most important for the low  $Q^2$  deep inelastic scattering analysis, will be presented next. A description of the H1 trigger system and of the online and offline analysis chains concludes the chapter.

### 2.2.1 Luminosity System

The H1 luminosity system consists of two calorimeters, one tagging very low  $Q^2$  electrons, the “electron tagger” (ET), and one detecting radiated photons, the “photon detector” (PD). These calorimeters are situated in the HERA tunnel at  $Z$  positions of  $-33.4$  m and  $-103$  m, respectively. The luminosity is measured by counting the rate of the Bethe-Heitler (BH) bremsstrahlung process  $ep \rightarrow ep\gamma$ , either using the photon detector only (for the offline luminosity determination) or using the PD and the ET simultaneously (for the online measurement).

The electromagnetic calorimeter of the electron tagger consists of  $7 \times 7$  cells covering a total area of  $154 \times 154$   $\text{mm}^2$ . Electrons scattered with an energy different from the beam energy are deflected in the magnetic field created by the HERA focusing magnets. The electrons leave the beam pipe and can be detected by the ET if their energy is between 10 GeV and 20 GeV (for low emission angles corresponding to  $Q^2 < 0.01$   $\text{GeV}^2$ ). Apart from the luminosity measurement the electron tagger is used also for the study of “photoproduction” processes at very low  $Q^2$  (Sec. 3.6).

The photon detector consists of  $5 \times 5$  cells covering a total area of  $100 \times 100$   $\text{mm}^2$ . Photons originating from the interaction region leave the proton beam pipe through a window at  $Z = -92.3$  m, where the beam pipe bends upwards, and hit the PD. The angular acceptance of the photon detector is approximately equal to 0.5 mrad. Photons with energies larger than 2 GeV can be measured by the detector. Photons emitted collinearly by the initial state radiation deep inelastic process, see Sec. 3.1, can also be investigated using the PD.

### 2.2.2 Central and Forward Tracking Systems

The H1 tracking system has been designed in order to provide triggering, reconstruction and momentum measurement of charged particle tracks. Particle trajectories are bent in the magnetic field. Due to the asymmetry of the colliding beam energies the hadronic final state particles are boosted in the forward direction which leads to an asymmetric detector design. To achieve good track reconstruction efficiency over a maximum angular range, two mechanically distinct detector modules were constructed, the central tracker (CTD) and the forward tracker (FTD). The main parameters of these devices are summarized in Tab. 2.2.

## Central Tracking Device

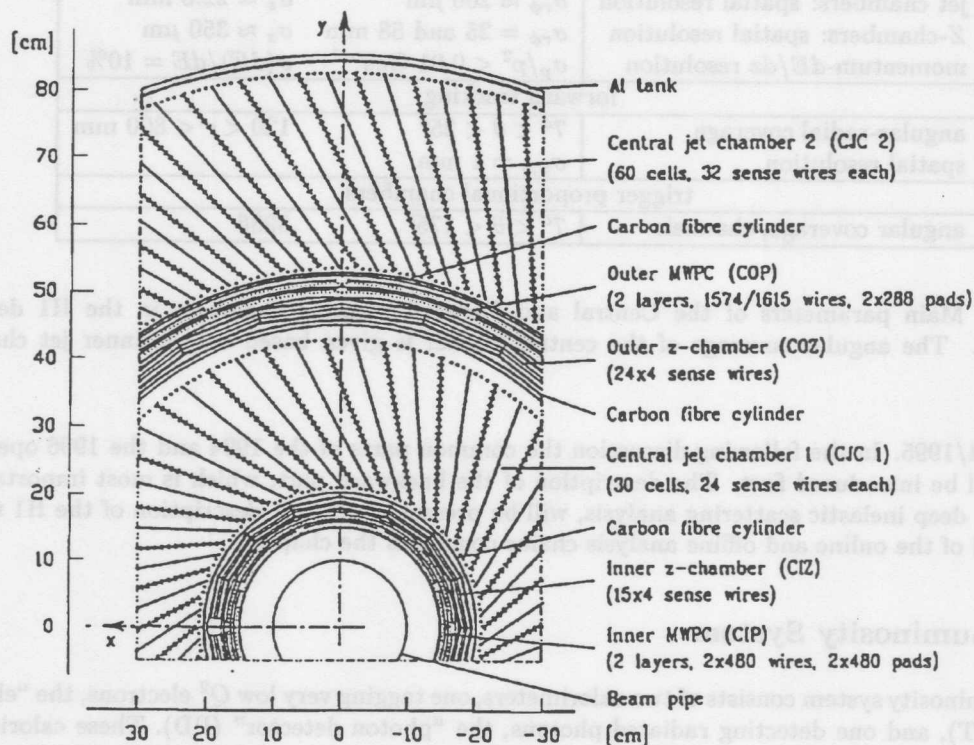


Figure 2.3: Radial view of the H1 central tracker

- Central jet chambers: CJC1 and CJC2.** Track reconstruction in the central region is based on two coaxial cylindrical chambers, CJC1 and CJC2. The active length of these chambers in  $Z$  direction is 2200 mm. The radial coverage of the chambers is between 203 mm and 451 mm for CJC1 and between 530 mm and 844 mm for CJC2. The wires in the chambers are oriented parallel to the beam axis. The drift cells are inclined with respect to the radial direction by about  $30^\circ$ , such that in the presence of the magnetic field the ionisation electrons drift approximately perpendicular to stiff, high momentum tracks which originate at the nominal interaction point. This gives an optimal resolution in the  $r - \phi$  plane, which is found to be about  $170 \mu\text{m}$  at 1 cm drift distance. A resolution at the percent level of the wire length is achieved in the  $Z$  coordinate measurement by comparing the signal amplitudes readout at both wire ends ("charge division" technique).

Track recognition in the CJC is based on the more precise  $r - \phi$  information. The track parameters are constrained imposing a common interaction vertex requirement. Tracks from secondary vertices (restricted to decays of neutral particles into a pair of oppositely charged particles), cosmic muons and background interactions are recognized and treated separately. The  $Z$  information of the tracks is significantly improved during a fit using  $\theta_{track}^i, Z_{vertex}$  as  $N_{track} + 1$  fit parameters. The resulting precision of the  $Z$  vertex determination is about 1 cm.

- Central Z-chambers: CIZ and COZ.** Two thin drift chambers, the central inner chamber (CIZ) and the central outer one (COZ), are mounted at the CJC1 inner cylinder and in between the CJC1 and CJC2 chambers, respectively. In these chambers the drift direction is parallel to the beam axis with the wires strung on polygonal support structures around the axis. The CIZ (COZ) comprises 15 (24) rings of 12 (9) cm length in  $Z$  direction with 4 layers of sense wires in

each ring. The internal  $Z$  resolution of the chambers is about  $250 \mu\text{m}$  at 1 cm drift distance. The  $r - \phi$  coordinate is measured using also the charge division method with a precision of 1-2% of  $2\pi$ .

The vertex fitted tracks recognized in the CJC were supplied with the  $Z$  chamber information using a combined fit-reconstruction procedure based on the neural network deformable template approach (see Appendix A for details). The vertex position determination is thereby greatly improved to 2 mm. Due to the  $Z$  chambers the  $\theta$  measurement accuracy for individual tracks improved from about 10 mrad to 1 mrad.

- **Central proportional chambers: CIP and COP.** The inner multiwire proportional chamber (CIP) is placed closest to the beam pipe at an average radius of 161 mm. The angular coverage of the chamber is  $9^\circ < \theta < 171^\circ$ . The chamber is composed of 60 sectors of 36.5 mm length in  $Z$  direction and of 8 sectors in  $\phi$ .

The central outer proportional chamber (COP) has an angular acceptance of ( $25^\circ < \theta < 155^\circ$ ). The chamber consists of 18 sectors in  $Z$ -direction of 12.1 cm length and of 16 sectors in  $\phi$ .

Both chambers provide a fast timing signal with a time resolution better than the 96 ns separation time between consecutive HERA bunch crossings. A "ray" combination of pads hit in the CIP with pads hit in the COP and in the forward proportional chambers (FWPC) is used to trigger on charged particle trajectories originating from the interaction region.

### Forward Tracker

The forward tracking detector is an integrated system consisting of three identical supermodules. Each supermodule includes: three different orientations of planar wire drift chambers designed to provide accurate  $\theta$  measurements, a multiwire proportional chamber (FWPC) for fast triggering, a passive transition radiator and a radial wire drift chamber which provides accurate  $r - \phi$  information.

### 2.2.3 Liquid Argon Calorimeter

The calorimetric measurement in the central and forward directions is provided by the Liquid Argon calorimeter (LAr). It covers the angular range between  $4^\circ$  and  $153^\circ$ . The LAr calorimeter is situated inside the large H1 coil. It is divided in two parts: an inner electromagnetic calorimeter and an outer hadronic one. A segmentation along the beam axis is done in eight self-supporting "wheels" of about 0.6 m length. The six barrel wheels are segmented in  $\phi$  into eight identical stacks or octants.

The total thickness of the electromagnetic part varies between 20 and 30 radiation lengths for electrons and 1.0 – 1.4 interaction lengths for hadrons. The hadronic part has a thickness of 5 to 9 interaction lengths. Shower tails are reconstructed in the streamer tube system embedded in the flux return iron.

The energy resolution of the electromagnetic calorimeter is about  $\sigma/E = 10\%/\sqrt{E} \oplus 0.01$ . The hadronic calorimeter has an energy resolution of  $\sigma/E \approx 50\%/\sqrt{E} \oplus 0.02$ . The hadronic calorimeter is non compensating. The charge output for hadrons is about 30% smaller than that for electrons. A special software weighting technique, originally proposed in [46], is applied to get the proper hadronic scale for hadrons.

Both the absolute energy scale and the resolution of the LAr calorimeter have been verified using test beams up to a few hundreds of GeV and H1 data. By comparing the measured track momenta of electrons and positrons with the corresponding energy deposits in the LAr calorimeter, the electromagnetic energy scale is presently known up to 3%. By studying the  $P_t$  balance between the scattered electron and the hadronic final state particles the hadronic energy scale is known with an uncertainty of 4%.

## 2.2.4 Backward Detectors in 1994 and 1996

For kinematic reasons the backward detectors are the most important parts of the H1 detector for the measurement of deep inelastic scattering at low  $Q^2 \leq 120 \text{ GeV}^2$ . The scattered electron is identified as a cluster in the backward electromagnetic calorimeter (see Sec 3.5). The angular measurement of the scattered electron relies mainly on the impact point determination in the backward tracking chamber (Sec. 5.1).

In the 1994-1995 winter shutdown the equipment of the backward part of the H1 detector was exchanged. The backward proportional chamber (BPC) was replaced by the backward drift chamber (BDC) and the backward electromagnetic calorimeter (BEMC) by a lead-fiber "spaghetti" calorimeter (Spacal).

Subsequently the 1994 detector setup is discussed. Then the new detectors are presented. The new possibilities owing to the H1 detector upgrade, but also new problems are discussed next.

### The 1994 H1 Backward Detector

#### Backward Proportional Chamber (BPC)

The backward multiwire proportional chamber was attached to the  $+Z$  side of the BEMC. It was made of four planes of wires with vertical, horizontal and  $\pm 45^\circ$  orientation. Sense wires were strung every 2.5 mm and combined into pairs during the readout. The BPC covered the radial region between 135 mm and 650 mm, which corresponded to a  $\theta$  acceptance of  $174.5^\circ < \theta < 155.5^\circ$ .

Three out of four planes were required to reconstruct a track element, and an about 98% average efficiency was estimated from the data. The angular resolution provided by the BPC was of the order of 2 mrad with about 1 mrad coming from the chamber resolution itself and a bigger contribution due to preshowering effects in the material in front of the chamber.

#### Backward Calorimeter (BEMC)

The first H1 backward calorimeter was a conventional electromagnetic lead-scintillator sandwich [47]. The calorimeter comprised 88 stacks aligned parallel to the beam pipe and mounted in an aluminum barrel of 162 cm diameter. The calorimeter front face was located at a distance of  $Z = -144 \text{ cm}$  from the interaction point. A schematic view of the BEMC calorimeter is given in Fig. 2.4.

The BEMC stacks were multilayer lead-scintillator sandwich structures with 50 active sampling layers made of plastic scintillator of 4 mm thickness. The active layers were interleaved with 49 layers of 2.5 mm lead. The entire structure corresponded to an average of 22.5 radiation lengths and one hadronic interaction length. The Molière radius of the BEMC was equal to 3.4 cm. The scintillation light collected by four wavelength shifters, situated at opposite sides of each quadratic stack was detected by photodiodes (see Fig. 2.4b,c).

An electromagnetic shower induced by a scattered electron was normally confined inside one stack since the stack size was much larger than the Molière radius. Still, in case of an electron impact point being situated close to the edge of the stack, the energy was deposited into several stacks. Thus a cluster was defined using the most energetic stack together with the neighbouring stacks, and the total cluster energy was then defined as the sum of energies reconstructed in them.

A study of the BEMC energy scale is discussed in Sec. 5.2. The result of these studies has been that the absolute BEMC energy scale is known up to 1% over the whole detector volume. Using the QED Compton events the linearity of the BEMC response, i.e. the energy scale dependence on the deposited energy, is determined to be better than 1% for  $E > 4 \text{ GeV}$  [47].

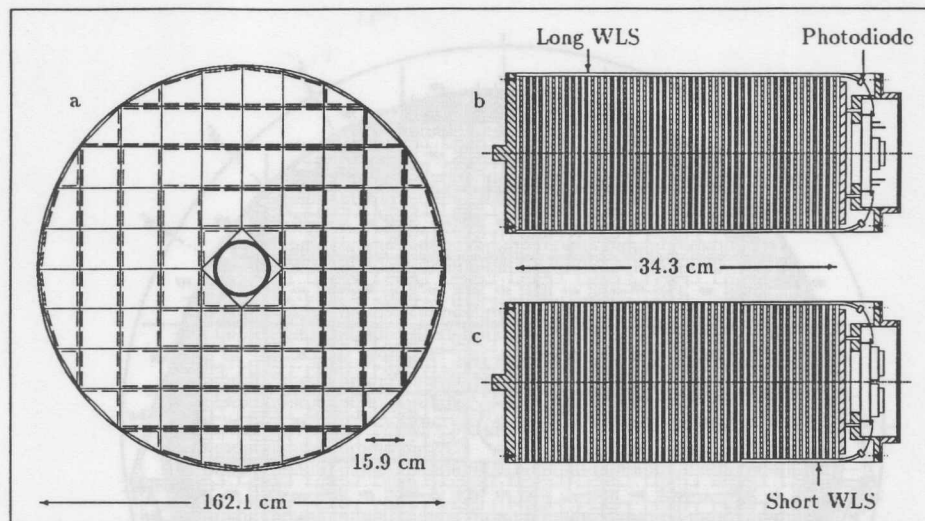


Figure 2.4: a) Transverse view of the backward electromagnetic calorimeter (BEMC). b,c) Longitudinal views of BEMC stacks in two perpendicular planes. The orientation of long wavelength shifters is indicated by horizontal and vertical lines. (from [47])

The BEMC energy resolution was measured at CERN and DESY test beams. It was parameterized like  $\sigma/E = 0.39/E \oplus 0.1/\sqrt{E} \oplus 0.017$  ( $E$  in GeV) [47]. A direct measurement from the 94 data [34], based on the double angle method (see Sec. 5.2) showed a 3.1% resolution at  $E = 27.55$  GeV in good agreement with expectation based on these test beam measurements.

The space point reconstruction in the BEMC stack was based on the relative amount of light collected in its four photodiodes. An energy weighted average of the  $X, Y$  positions determined in all stacks belonging to a cluster defined its center of gravity, see Sec. 5.1. The space point resolution obtained with this method was about 7 mm.

The response of the BEMC to hadronic particles was limited by its low hadronic interaction length. Studies based on CERN SPS test beam data showed that charged pions deposit in the BEMC about 45% of their energy. About 40% of the pions passed the BEMC as minimum ionizing particles (with an energy deposit of  $\sim 1$  GeV independent of the particles' energy).

### The 1996 H1 Backward Detector

#### Backward Drift Chamber (BDC)

The backward drift chamber [48] replaced the proportional chamber BPC as the new backward tracking device. The BDC is subdivided into 8 octants consisting of 4 double layers. The signal wires are strung in polygons around the beam axis in order to optimize the  $\theta$  resolution. The double layers are rotated by  $11.25^\circ$  to obtain some measurement of  $\phi$ . Each signal wire is contained in a separate cathode cell. The wires in different planes of the double layers are shifted by half the cell size in order to resolve a right-left ambiguity of the drift origin. The wire spacing is 1 cm for the inner 16 cells in the octant and 3 cm for the outer part. A transition region between the two zones contains cells with 2 cm width. The angular coverage of the BDC is  $153^\circ < \theta < 177.5^\circ$ .

Five out of eight planes were required to reconstruct a track element in 1996. A uniform efficiency of about 98% was estimated from the data. The spatial resolution for individual hits is 0.3 mm,

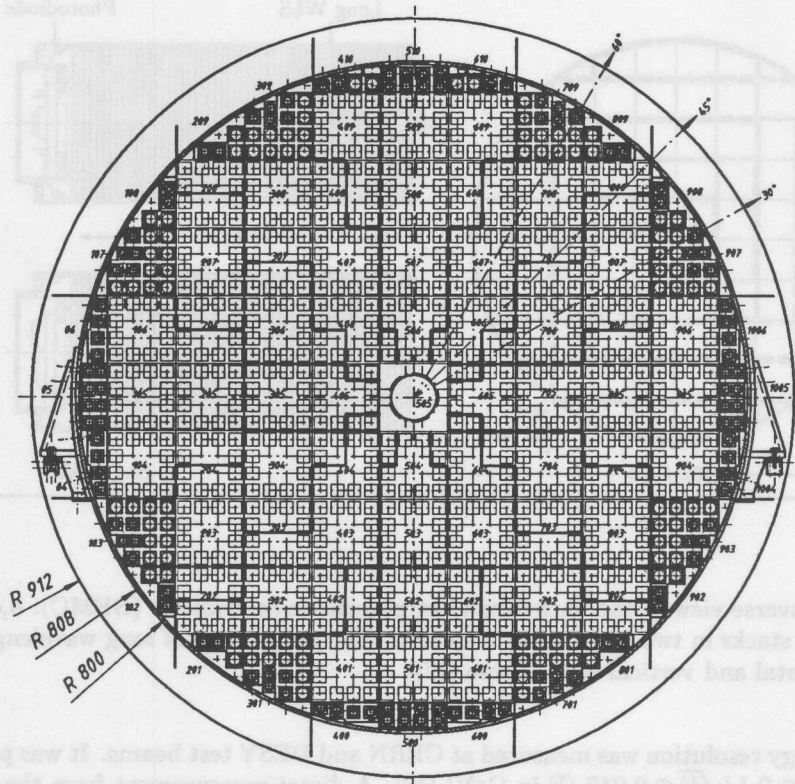


Figure 2.5: Transverse view of the Spacal. Small boxes indicate individual cells. They are combined in  $4 \times 4$  groups into super-modules.

leading to a  $\theta$  resolution better than 0.5 mrad if no showering occurred in the material between the vertex and the BDC.

### Spacal Calorimeter

The Spacal calorimeter [49, 50] comprises the electromagnetic and hadronic sections and the backward plug. The latter was installed in 1996, but it was not used in the present analysis.

The electromagnetic part of the Spacal consists of 1192 cells with an active volume of  $4.05 \times 4.05 \times 25 \text{ cm}^3$  each. A transverse view of the calorimeter is given in Fig. 2.5. The cells are made of grooved lead plates and scintillating fibers with a diameter of 0.5 mm. The scintillation light of each cell is converted into an electric pulse using photomultiplier tubes (PMT). The active length of the electromagnetic Spacal corresponds to 27.47 radiation lengths and 1 hadronic interaction length. The angular coverage of the calorimeter is  $153^\circ < \theta < 177.8^\circ$ .

The use of PMT and an electronic chain with low noise level permits very low trigger thresholds and a reliable reconstruction of small energy deposits. The PMTs provide a time resolution of about 1 ns allowing to reduce the non- $ep$  background on the trigger level.

The electromagnetic energy resolution was measured in test beam experiments [51, 52] and parameterized as  $7.5\%/\sqrt{E} \oplus 2\%$ . The spatial resolution of the calorimeter in the transverse plane was measured to be 3.4 mm.

Backward tracking		
	BPC	BDC
Radial coverage	13.5 – 65.0 cm	6.5 – 70.5 cm
Spatial resolution	1 mm	0.3 mm
Average reconstructed track multiplicity in 5 cm distance around the calorimeter cluster	2.7	11.5

Table 2.3: Comparison of the 1994 and 1996 backward tracking chambers.

Backward calorimetry			
	BEMC	Spacal EM	Spacal HAD
Radial coverage	14 – 79 cm	5.7 – 80 cm	
Sensitive length	$22.5X_0, 0.97\lambda$	$27.5X_0, 1\lambda$	$29.4X_0, 1\lambda$
Molière-radius	3.4 cm	2.55 cm	2.45 cm
Energy resolution at 27.5 GeV	3.1%	3.0%	
Energy resolution at 2 GeV	21.0%	5.6%	
Cell size	$16 \times 16 \text{ cm}^2$	$4.05 \times 4.05 \text{ cm}^2$	$12 \times 12 \text{ cm}^2$
Spatial resolution	7 mm	3.4 mm	

Table 2.4: Comparison of the 1994 and 1996 backward calorimeters

The hadronic part of the Spacal comprises 136 cells of  $12 \times 12 \times 25 \text{ cm}^3$  providing one nuclear interaction length. The fibers are of the same type as in the electromagnetic section but have a larger diameter of 1 mm. The hadronic resolution of the calorimeter is about  $30\%/\sqrt{E}$ .

#### Advantages and Drawbacks of the H1 Backward Detector Upgrade

The main parameters of the H1 backward setups before and after the upgrade are listed in Tables 2.3, 2.4. The consequences of the apparatus change are:

- **Increased angular acceptance.** Both the Spacal and the BDC have a larger radial coverage than their equivalents in 1994. In principle, this allows to measure the DIS cross section down to  $Q^2$  values of  $1 \text{ GeV}^2$ . Unfortunately, this possibility could not be explored in the present analysis due to trigger problems for electrons scattered at large polar angles. The calorimeter cell 14, situated left to the beam pipe, caused a too large beam related trigger rate. Therefore a rather large block of Spacal cells had to be excluded from the inclusive trigger used in the analysis, see Sec. 4.6 for details. Moreover, the remaining inner regions had different trigger problems. Thus the 1996 cross section measurement was restricted to  $Q^2 > 10 \text{ GeV}^2$ . More important for this analysis was the increase of the  $\theta$  acceptance at larger radii which lead to an extended acceptance of high  $y$  events (Sec 3.2).
- **Better spatial resolution.** The Spacal and the BDC have spatial resolutions about two times better than the BEMC and the BPC, respectively. This improved the calorimeter-tracker matching (Sec. 5.1). The Spacal spatial resolution allows for a bias free measurement of the two-photon invariant mass for clusters with separation of 10 cm (Sec 5.2). This permits an energy calibration based on the  $\pi^0 \rightarrow 2\gamma$  decay. Unfortunately, the resolution improvement is marginal in the case of events where the scattered electron preshowers. Moreover, the problem of resolving  $\phi$  and left-right ambiguities in the BDC lead to a much larger track multiplicity.

- **Better calorimeter granularity.** The smaller Spacal cell has been important to measure light meson decays, to avoid overlaps of the cluster of the scattered electron with clusters produced by hadronic final state particles and to better resolve electromagnetic and hadronic showers. It also leads to a very good  $\phi$  resolution in the outer Spacal region, used as a cross check of the CJC charge resolution (Sec. 6.6). The disadvantage of a fine-granularity is that a large luminosity is necessary to get sufficient statistics for a DIS-based calibration of the outer Spacal region. Moreover, local energy scale variations occur, which were found to be up to 1.5% percent from the center to the boundary of a cell.
- **Better calorimeter resolution at low energies.** This allows to measure light mesons decays, and, together with the ability to have triggers with low energy thresholds, to extend the  $y$  range of the measurement (Sec. 3.2). For the present analysis this feature was of greatest importance.
- **Better hadronic coverage and resolution** allow to improve the  $y_h$  resolution at high  $y$  (Sec 3.1). Together with a better energy resolution for low energetic particles, it allowed to reliably include the  $E - p_z$  requirement into the set of standard cuts (Sec 6.4), reducing the influence of radiative corrections and the  $\gamma p$  background.

A conclusion of this comparison could be that for  $Q^2 \geq 10 \text{ GeV}^2$  and scattered electron energies bigger than 10 GeV both experimental setups have comparable potentials. This situation will hold until a large luminosity ( $> 50 \text{ pb}^{-1}$ ) will be collected allowing a precise determination of the Spacal energy scale also for the outer detector volume. The new setup has definite advantages for the measurements of DIS events with low energy of the scattered electron. The possibilities of the new detector in the low  $Q^2$  region where explored in a short run period in October 1997 with a specially tuned trigger setup. In this region the Backward Silicon Tracker [53] is being used which completed the upgrade of the backward region.

### 2.2.5 Trigger System and Offline Selection of Events

The H1 trigger system comprises three levels of event filtering, L1, L2, L4. An additional selection (on level L5) occurs during the offline event processing. The L2 level was not present in 1994; it was commissioned in 1996.

The L1 trigger level provides a trigger decision after  $2.5 \mu\text{s}$ . During this time the full event information is stored in pipelines. The trigger conditions, *subtriggers*, are composed as logical combinations of *trigger elements* which represent trigger signals coming from the different detector components. Any L1 subtrigger can be *prescaled* with a *prescale gap*  $i$ , i.e. only one out of  $i + 1$  events with the subtrigger conditions fulfilled is selected. If the subtrigger conditions are fulfilled the “raw” bit is set. If the event is actually selected by this subtrigger, the “actual” bit is set. L1 accepts events if at least one subtrigger has an actual bit set.

L2 validates the L1 decision using more complicated algorithms within  $20 \mu\text{s}$ . Two kinds of second level trigger techniques are used in H1: neural network and topological triggers. In the present analysis a topological trigger, selecting clusters in the outer region of Spacal, was used for the high  $y$  cross section analysis (Sec. 4.6).

After a positive L2 signal occurred, the readout of the event is started. The complete event information is then transferred to the trigger level L4. The latter is a software filter residing on a processor farm consisting of 30 parallel processors. Additional background suppression, using reconstructed event information, is performed here.

The offline reconstruction is then performed on the L5 level. The L5 event processing can be performed several times and also in external laboratories. The events are classified according to their physics properties. Unclassified events are rejected. Selected events are written to so-called Data Summary Tapes (DST), which are normally used as a basis for the further physics analysis.



The analysis described in this thesis used PAW-format [54] ntuples created from the DST. About 16 Gbyte of condensed information has been collected and transferred over the network to the DESY-IfH Zeuthen computer center. The physics analysis was performed using the PAW package extended, by means of the shared library mechanism, to handle the H1 offline library programs and H1 database calls. An average DIS cross section analysis job was running on five parallel SGI Challenge processors during three hours.

Chapter 3

Basics of the Cross Section Measurement

This chapter is devoted to the description of the basic ingredients of the DIS cross section measurement. It starts with the introduction of the methods used to determine the event kinematics. The "classic" method based on the scattered electron only is presented. Hydroic methods are discussed, which are specific to the ep collider experiment. A brief comparison of the methods in terms of resolution and reconstruction follows.

The DIS kinematics is strongly affected by the QED radiative corrections. The usage of variables based on the hydroic final state particles requires an understanding of the basic properties of hydroic energy flow. Monte Carlo models and analytical calculation programs used for this purpose are discussed.

The determination of the event kinematics is impossible without correct recognition of the scattered electron. For some kinematic ranges, in particular for high  $y$  events, this determination can become ambiguous. Different methods of the electron identification are introduced in this chapter. Background processes which could mimic a DIS event are discussed next.

The chapter is ended with the presentation of the method used for the determination of the double differential cross section. The method of extraction of the proton structure functions is discussed.

8.1 Determination of the Event Kinematics

A schematic representation of the deep inelastic scattering process is given in Fig. 8.1. The inclusive cross section for this type of reaction is described by two variables  $Q^2$ , the negative four-momentum transfer squared, and  $x$ , the Bjorken variable, which in the parton model represents the momentum fraction of the struck quark. The  $Q^2$ ,  $x$  variables are related to  $z$ , the relative energy transfer from the incoming electron to the quark, and  $Y = 4E_e E_p x$ , the  $cas$  energy, by the equation  $Q^2 = 2zY$ . Here  $E_e(E_p)$  denotes the electron (proton) beam energy.

In terms of the scattered electron energy  $E_e'$  and the polar angle  $\theta$ , the quantities  $Q^2$  and  $y$  can be written as:

$$Q^2 = 4E_e E_e' \sin^2(\theta/2) \quad (8.1)$$

The subscript 'e' is used to emphasize that  $y$  and  $Q^2$  are determined by the scattered electron only. This defines the so-called "electron method" of reconstructing the event kinematics.

## Chapter 3

# Basics of the Cross Section Measurement

This chapter is devoted to the description of the basic ingredients of the DIS cross section measurement. It starts with the introduction of the methods used to determine the event kinematics. The "classic" method based on the scattered electron only is presented. Hadronic methods are discussed, which are specific to the  $ep$  collider experiment. A brief comparison of the methods in terms of resolution and reconstruction follows.

The DIS kinematics is strongly affected by the QED radiative corrections. The usage of variables based on the hadronic final state particles requires an understanding of the basic properties of hadronic energy flow. Monte Carlo models and analytical calculation programs used for this purpose are discussed.

The determination of the event kinematics is impossible without correct recognition of the scattered electron. For some kinematic ranges, in particular for high  $y$  events, this determination can become ambiguous. Different methods of the electron identifications are introduced in this chapter. Background processes which could mimic a DIS event are discussed next.

The chapter is ended with the presentation of the method used for the determination of the double differential cross section. The method of extraction of the proton structure functions is discussed.

### 3.1 Determination of the Event Kinematics

A schematic representation of the deep inelastic scattering process is given in Fig. 3.1. The inclusive cross section for this type of reactions is described by two variables  $Q^2$ , the negative four-momentum transfer squared, and  $x$ , the Bjorken variable, which in the parton model represents the momentum fraction of the struck quark. The  $Q^2, x$  variables are related to  $y$ , the relative energy transfer from the incoming electron to the quark, and  $S = 4E_p E_e$ , the c.m.s energy, by the equation  $Q^2 = Sxy$ . Here  $E_e(E_p)$  denotes the electron (proton) beam energy.

In terms of the scattered electron energy  $E'_e$  and the polar angle  $\theta_e$  the quantities  $Q^2$  and  $y$  can be written as:

$$y_e = 1 - \frac{E'_e(1 - \cos\theta_e)}{2E_e} \quad Q_e^2 = 2E'_e E_e(1 + \cos\theta_e) = \frac{E_e'^2 \sin^2\theta_e}{1 - y_e} \quad (3.1)$$

The subscript 'e' is used to emphasize that  $y$  and  $Q^2$  are determined by the scattered electron only. This defines the so-called "Electron method" of reconstructing the event kinematics.

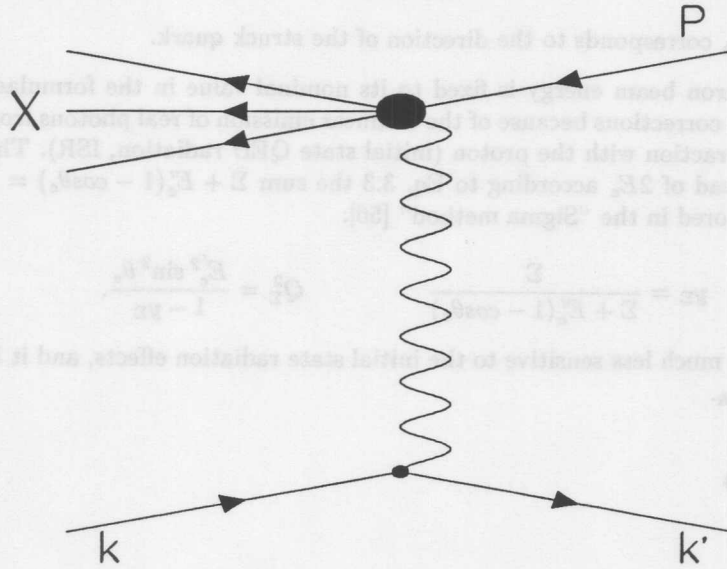


Figure 3.1: Schematic view of the DIS of a lepton of momentum  $k$  off a nucleon of momentum  $P$  producing a final state  $X$  and secondary lepton with momentum  $k'$ .

From the formulae above it follows that for those events with the electron scattered into the backward calorimeter ( $\theta_e > 150^\circ$ ),  $y$  depends mostly on the scattered electron energy  $E'_e$ , i.e. the lower is  $E'_e$ , the higher  $y$  values are reached in the event. On the other hand, for low  $y < 0.1$ , the  $Q^2$  variable is almost solely defined by the scattered electron angle. This is illustrated in the kinematic plane plot, see Fig. 3.3. Iso- $E'_e$  lines in the  $Q^2, x$  plane are almost parallel to  $y$  and iso- $\theta_e$  lines at low  $y$  are about parallel to  $Q^2$ .

A unique possibility of a collider DIS experiment is to reconstruct the kinematics also using the hadronic final state particles. Still, since it is impossible to build a detector with complete  $4\pi$  angular coverage, some leakage of particles along the beam axis is unavoidable. For the HERA experiments with a large imbalance of incoming proton and electron beam energies, the leakage along the incoming proton beam direction is more important. Thus, one has to use variables which are most insensitive to these losses. These can be derived from the transverse momentum balance in the event:

$$0 = P_t^{in} = P_t^{out} = E'_e \sin \theta_e + P_{t,h}, \quad P_{t,h} = \sum_a E_a \sin \theta_a \quad (3.2)$$

and utilizing the conservation of the difference of energy and longitudinal momentum:

$$(E_p^{in} - P_{z,p}^{in}) + (E_e - P_{z,e}) = 2E_e = E'_e(1 - \cos \theta_e) + \Sigma, \quad \Sigma = \sum_a E_a(1 - \cos \theta_a). \quad (3.3)$$

In both equations the summation  $\sum_a$  is performed over all hadronic final state particles, and the masses are neglected.

Using the  $\Sigma$  variable it is possible to express  $y$  in another manner:

$$y = \frac{2E_e - E'_e(1 - \cos \theta_e)}{2E_e} = \frac{\Sigma}{2E_e} = y_h. \quad (3.4)$$

Here the subscript  $h$  denotes the ‘‘Hadron method’’ for the determination of  $y$  which was introduced by Jaquet and Blondel [55].

Another important quantity of the event is a hadron angle defined as

$$\cos \theta_h = \frac{P_{t,h}^2 - \Sigma^2}{P_{t,h}^2 + \Sigma^2}. \quad (3.5)$$

In the parton model  $\theta_h$  corresponds to the direction of the struck quark.

The incoming electron beam energy is fixed to its nominal value in the formulae 3.1, 3.4. This leads to large radiative corrections because of the collinear emission of real photons from the incoming electron before its interaction with the proton (initial state QED radiation, ISR). This effect can be largely reduced if instead of  $2E_e$  according to Eq. 3.3 the sum  $\Sigma + E'_e(1 - \cos\theta_e) = E - p_z$  is used. This possibility is explored in the ‘‘Sigma method’’ [56]:

$$y_\Sigma = \frac{\Sigma}{\Sigma + E'_e(1 - \cos\theta_e)} \quad Q_\Sigma^2 = \frac{E_e'^2 \sin^2 \theta_e}{1 - y_\Sigma}. \quad (3.6)$$

By construction,  $y_\Sigma$  is much less sensitive to the initial state radiation effects, and it has a resolution similar to the one of  $y_h$ .

### Resolution Analysis

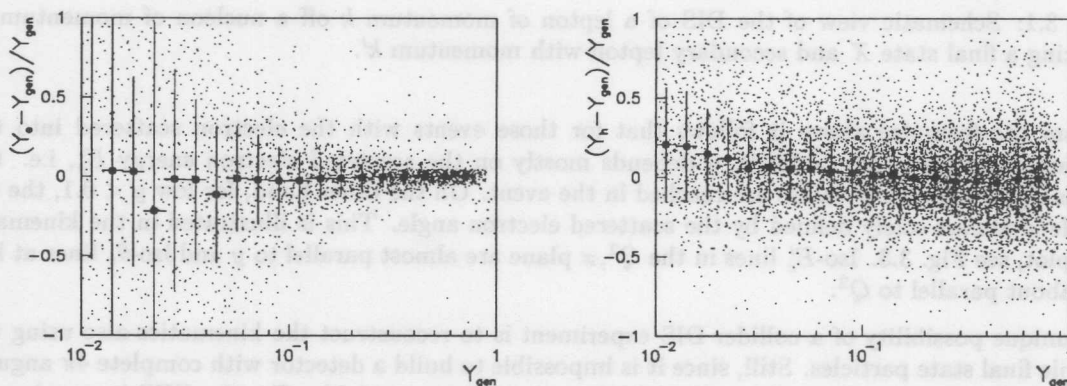


Figure 3.2: Resolutions of  $y_e$  (left) and  $y_h$  (right). The error bars represent the mean values and the spread obtained from Gaussian fits performed to the quantity  $(y_{rec} - y_{gen})/y_{gen}$  in slices of  $y_{gen}$ . The plot is based on the 1996 detector setup. The  $y_e$  resolution is seen to degrade to unacceptably large values at  $y < 0.05$ . The systematic bias of  $y_h$  at  $y < 0.03$  is due to noise affecting the  $\Sigma$  measurement.

The main advantages of having more than just the electron method for the kinematics determination are the possibility to extend the measurement towards low  $y$  values, to cross check the cross section measurement results with different methods for the intermediate  $y$  region and to calibrate the electron and hadronic energy measurements. The resolutions of the electron and hadronic methods are very different at low  $y < 0.05$  and high  $y > 0.3$  as can be seen in Fig. 3.2. For detailed analyses of the different resolution effects we refer to numerous studies published in [59]. Here a brief summary is presented.

The  $Q^2$  resolution for  $Q^2 \geq 7.5 \text{ GeV}^2$  is particularly high ( $\sim 5\%$ ) for the electron method. It is two times worse but still acceptable for the sigma method.

A Monte Carlo study (based on the 1996 detector setup) of the  $y$  resolution for the electron and hadron methods is presented in Fig. 3.2. The resolutions of  $y_e$  and  $y_h$  are dominated by the electromagnetic and hadronic energy resolutions, respectively. They are given by the formulae:

$$\frac{\delta y_e}{y_e} = \frac{1}{y_e} \cdot \frac{1 - \cos\theta_e}{2E_e} \cdot \frac{\delta E'_e}{E'_e} \quad \frac{\delta y_h}{y_h} = \frac{\delta \Sigma}{\Sigma}. \quad (3.7)$$

The  $y_e$  resolution is superior at high  $y$  ( $> 0.3$ ) since it is defined by the electromagnetic energy resolution ( $\delta E'_e/E'_e < 4\%$ ). At lower  $y$ , however, it diverges due to the  $1/y$  term. On the contrary,  $y_h$  contains no  $1/y$  contributions, it is determined by the  $\Sigma$  resolution itself.

The  $\Sigma$  resolution can be expressed as a sum of energy dependent and constant components. The main contribution to the latter comes from the noise of the calorimeter cells and from particle rescattering on the detector material. The noise level is about  $\Sigma_{noise} = 0.2$  GeV. Thus the measurement below  $y = 0.01$  is spoiled unless a special topological noise suppression is applied. The effect of the noise component to the  $y_h$  resolution is seen in Fig. 3.2 as a systematic bias of  $y_h$  at lowest  $y$  values. For very large  $y$  the hadron angle is pointing backwards (see Fig. 3.3), and the  $\Sigma$  measurement gets more affected by the worse hadronic energy resolution of the backward calorimeters. Therefore the  $\Sigma$  method was restricted to the  $y$  interval of 0.01 – 0.6.

## 3.2 Kinematics and Detector Reconstruction

The  $(Q^2, x)$  plane of the DIS cross section measurement at low  $Q^2$  at HERA is presented in Fig. 3.3. The iso- $\theta$  lines displayed in the figure correspond to different detector limits:  $\theta_h > 5^\circ$  is the Liquid Argon calorimeter acceptance limit,  $15^\circ < \theta < 165^\circ$  is the range covered by the central drift chambers,  $153^\circ < \theta < 174^\circ$  corresponds to the limits of the backward calorimeter and up to  $170^\circ$  extends the acceptance of the central inner proportional chamber (see chapter 2).

The LAr forward acceptance limit,  $\theta_h = 5^\circ$ , corresponds for the whole kinematic range of the measurement to  $y < 0.01$ .

For the precise determination of the electron scattering angle and for the suppression of background events coming from non- $ep$  interactions (see 3.6.2), it is important to have a well reconstructed event vertex. It follows from the kinematic plot that:

- For all  $y$  values and  $Q^2 > 50$  GeV<sup>2</sup> the scattered electron angle is less than  $165^\circ$ , thus the event vertex can be reconstructed from the electron itself.
- For  $Q^2 < 15$  GeV<sup>2</sup> and  $0.5 > y > 0.01$  the hadron angle is bigger than  $15^\circ$ , the hadronic final state vertex can be used.
- For  $Q^2$  between 15 GeV<sup>2</sup> and 50 GeV<sup>2</sup> and the low  $y$  region ( $y < 0.05$ ) two different techniques could be used. The standard one is to use apart from the central drift chamber also the vertices reconstructed using the forward drift chambers. This approach was applied to the 1994 data. Another possibility is to perform a vertex reconstruction based on the scattered electron using the central inner proportional chamber. This covers the complete  $y$  range starting from  $Q^2 > 15$  GeV<sup>2</sup>. That method was used for the 1996 data analysis (see 6.1).
- For low  $Q^2 < 50$  GeV<sup>2</sup> and high  $y > 0.5$  the hadron angle points backwards and it leaves the central tracker acceptance  $\theta_h > 165^\circ$ . For the “normal” DIS events there is always a colour string between the struck quark jet and the proton remnant which for most of the events fills the central region in the H1 laboratory frame with soft particles suitable for the vertex reconstruction. This is not valid for so called rapidity gap events. Still, normally these have relatively big diffractive mass, and thus they also produce tracks reconstructed in the central tracker. Again, the last statement does not hold for vector meson production. A special study of these effects can be found in Sec. 6.1.

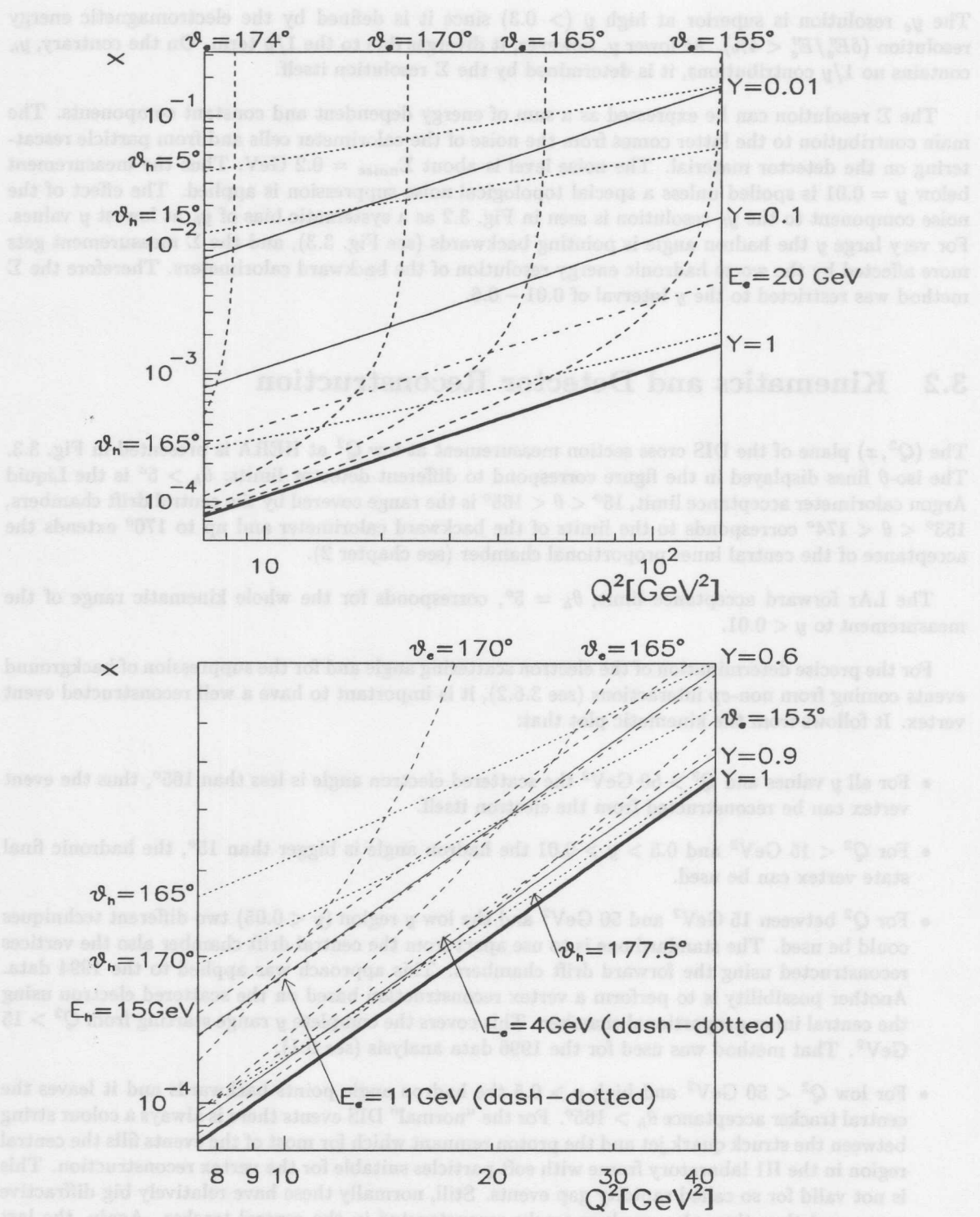


Figure 3.3: Top: complete kinematic region of the DIS cross section measurement as discussed in this thesis. Bottom: zoom into the high  $y$  region.

The kinematic plane in Fig. 3.3 corresponds to the Born level kinematics. In the presence of radiation, especially of the initial state radiation and when the electron method is used for the  $Q^2, x$  reconstruction, the situation changes dramatically. For example, radiative high  $y_e$  events have often very low invariant mass of the hadronic final state with  $\theta_h$  below the forward tracker acceptance. Detailed understanding of these effects requires Monte Carlo simulation studies. Different Monte Carlo simulation programs used in the analysis are presented in the next section. Details of the vertex determination in the case of QED radiation are presented in Sec. 6.1.

### 3.3 Monte Carlo Models and Analytical Tools

Before we start the description of the Monte Carlo programs used in the analysis, it is important to stress that the inclusive DIS cross section measurement is almost independent of the specific Monte Carlo model used for the simulation. This is related to the model independent definition of the kinematic variables and redundancy of the kinematics measurement. Efficiencies of all selection criteria, detector calibration, resolution figures and partially even radiative corrections were directly derived from the data.

Nevertheless a direct measurement from data of the acceptance and smearing of the kinematic variables is complicated, since several effects have a correlated influence on them. These are, for example, detector resolution and radiative corrections. In general, a sophisticated unfolding technique is necessary in this case. To simplify this procedure the Monte Carlo simulation is a very useful tool. If the detector resolution and radiative smearing effects are fully and correctly implemented into the simulation, then the multidimensional unfolding procedure for the DIS cross section measurement can be replaced by a simple bin-by-bin iterative approach which is explained in Sec. 3.7. The primary task of the analysis in this case is to prove that the Monte Carlo model describes the reconstruction and smearing of the main kinematic variables ( $E'_e, \theta_e, \Sigma$ ) appropriately.

We now turn to the discussion of the different components of the Monte Carlo simulation ordered according to their importance for the inclusive cross section measurement.

- The largest importance for the DIS kinematics reconstruction has the correct simulation of the detector response. It was performed using the GEANT simulation program [58]. The simulation of the individual subdetectors was first intensively studied using results of test beam experiments. Next they were put into the common H1SIM package describing the H1 detector. The simulation was then improved according to the detector performance at HERA.
- The QED radiative corrections lead to large changes in the event kinematics if the electron method is used. The simulation of radiative events was performed using the HERACLES [61] program included into the DJANGO [60] package. HERACLES contains first order radiative corrections, the simulation of real Bremsstrahlung photons and of the  $F_L(x, Q^2)$  structure function. These calculations were cross checked using an analytical package HECTOR [62]. Two different branches are included into the latter, a complete leading order calculation (TERAD) and one using the leading log approximation (HELIOS). The effects of the next-to-leading order radiative corrections were also included into the HECTOR program. The elastic contribution to the QED Compton events was calculated using the COMPTON [63] program.
- The details of the hadronic final state description influence the analysis through the vertex reconstruction efficiency (see the previous section),  $E - p_Z$  determination (see Sec. 5.3 for details) and electron identification at large values of  $y$  (Sec 3.5). Different models have been used in the analysis. The main simulation was performed with the DJANGO program which included the ARIADNE [65] and JETSET [66] models. Several cross checks were performed using the LEPTO [64], RAPGAP [68] and HERWIG [67] packages.

LEPTO, RAPGAP and HERWIG contain different DGLAP evolution based parameterizations of parton showers and of matching them to leading order exact matrix elements. ARIADNE is

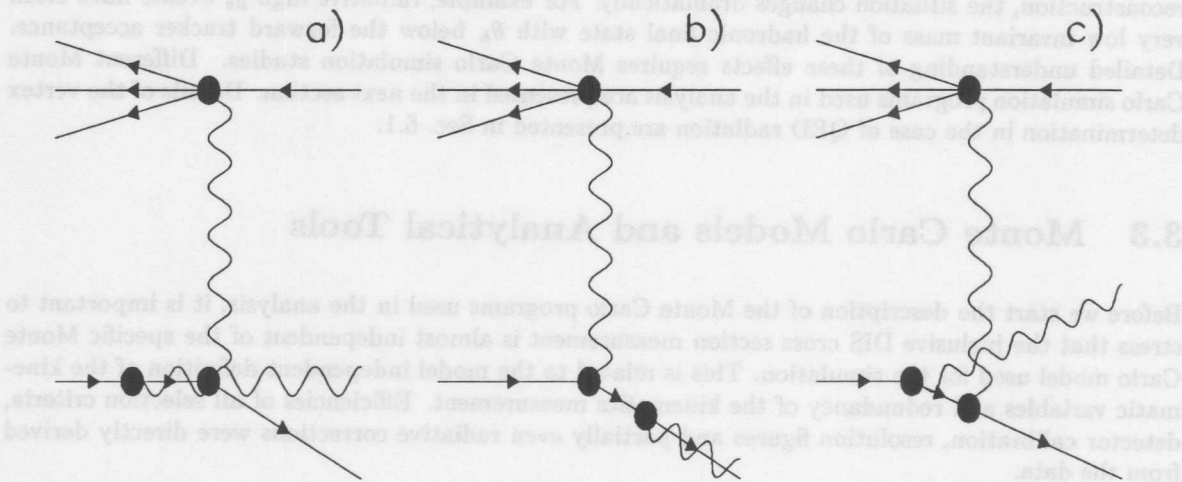


Figure 3.4: A schematic representation of the ISR (a), FSR (b) and QED Compton (c) processes.

based on the colour dipole model, where gluon emission originates from a colour dipole stretched between the struck quark and the proton remnant. The partonic final state of ARIADNE is rather closely related to the one expected from BFKL evolution [69]. Recent experimental data collected at HERA are favorably described by this model (see [70] for a review).

For the hadronisation of the perturbative partons to the observable hadrons, the LEPTO, RAPGAP and ARIADNE programs use the LUND string model [71], as implemented in the JETSET code, while HERWIG uses a built-in cluster [72] model.

The RAPGAP program was used in the analysis to study the effect of the colourless diffractive exchange and of the diffractive production of vector mesons.

- The DIS cross section measurement at high  $y$  is deteriorated by the  $\gamma p$  background, as it is discussed in Sec. 3.6.1. The PHOJET [73] event generator was used to study this effect. This program includes so called soft and hard mechanisms of the  $\gamma p$  interactions as well as the major final state formations: non-diffractive, single and double diffractive and vector meson production.

More than 1 million and about 2 millions of simulated events were used in the 1994 and 1996 data analyses, respectively. Complete simulation of one DIS event requires about 40 sec on a SGI Challenge processor [74], i.e. about 30000 hours of computer time was needed to simulate the whole Monte Carlo sample; most of it was performed at DESY-IfH Zeuthen.

### 3.4 Radiative Corrections

QED radiative corrections arise in the deep inelastic scattering process due to the exchange of additional virtual or the emission of real photons. These processes are suppressed by factors  $\alpha_{QED} = 1/137$  for each photon line, still in some regions of phase space the QED radiative corrections may become large.



In the “leading log” approximation (LLA), three major sources of radiative corrections can be distinguished. All of them are related to the emission of a real photon from the electron. The first one is the initial state radiation (ISR), when the photon is emitted almost collinearly from the electron before its interaction with the proton. The second one is the final state radiation (FSR). In this case the photon is emitted at small angles from the scattered electron. The third one is the QED Compton process. It can be considered as a subclass of ISR and FSR processes with the photon emitted at large angles and a small variation of the electron direction before and after exchange of the virtual photon. A signature of the QED Compton events is a back-to-back  $\phi$  distribution of the radiative photon and the scattered electron (see Fig. 3.4).

Different methods of the kinematics’ reconstruction are differently affected by the radiative corrections. For example, the sigma method makes use of the  $E - p_z$  conservation in the event. Therefore it absorbs ISR effects into its definition and the radiative corrections get reduced. On the contrary, the electron method is most influenced by the radiation effects since it uses the information for the scattered electron only. In this chapter we will concentrate on it.

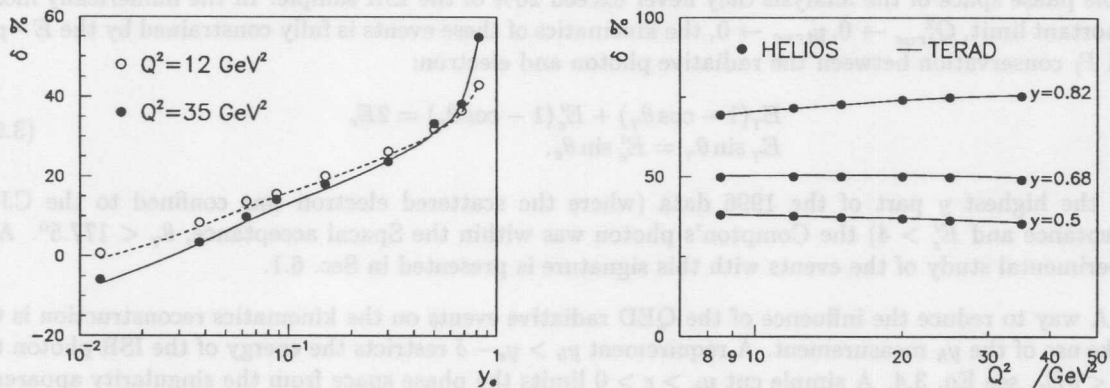


Figure 3.5: Comparison of the radiative correction calculations in the electron method between HERACLES (circles) and HELIOS (lines), left, and between HELIOS and TERAD, right. The left plot is based on the  $F_2$  parameterization as given by GRV LO 94 [17] and  $F_L$  is set to zero. The calculations presented in the right figure use  $F_2$  and  $F_L$  parameterizations as obtained from a QCD fit to H1 data (Sec 7.5).

All initial, final state and QED Compton photon emissions lead to lowering the energy of the scattered electron. Therefore, the reconstructed  $y_e$  value is bigger than the “true” one, which corresponds to photon exchange calculated at the hadronic vertex. For the ISR and QED Compton events the “true” energy of the incident electron is smaller than the beam energy, therefore the reconstructed  $Q_e^2$  is larger than the “true” one. Finally, for the QED Compton events the “true” angle of the electron scattering is much smaller than  $\theta_e$  reconstructed between the electron beam and the scattered direction, which also leads to low “true”  $Q^2$  values. Since the DIS cross section is large at low  $y$  and low  $Q^2$ , this induces big radiative effects despite the smallness of  $\alpha_{QED}$ .

Obviously, the radiative corrections depend on the DIS cross section at the “true”  $Q^2, y$  values. It is easy to estimate the minimal  $Q^2$  values involved in the case of ISR process. In the collinear approximation one has:  $Q_{true}^2 = 2(E_e - E_\gamma)E_e'(1 + \cos\theta_e)$ . Due to the kinematic condition  $y > 0$  the difference between the beam and the radiative  $\gamma$  energies is limited to  $(E_e - E_\gamma) > 0.5(1 - \cos\theta_e)E_e'$ . Therefore, the ratio of the reconstructed  $Q_e^2$ , using the electron method, and the “true”  $Q^2$  can be

estimated as:

$$\frac{Q_e^2}{Q_{true}^2} \leq \frac{E_e}{E'_e} \frac{2}{1 - \cos \theta_e}. \quad (3.8)$$

For the highest  $y$  (i.e. lowest  $E'_e$ ) and lowest  $Q^2$  reached in the analysis,  $E'_e = 4$  GeV and  $Q^2 = 12$  GeV<sup>2</sup>, the minimum  $Q_{true}^2$  value achieved with initial state radiation is  $Q_{min}^2 = 1.5$  GeV<sup>2</sup> – a region well covered by the DIS cross section measurements performed at HERA [33, 39, 77, 78] and fixed target experiments [80, 81].

A part of ISR events could be studied experimentally using the Photon Detector calorimeter of the luminosity system (Sec. 2.2.1). These data were used for the structure function  $F_2$  measurement performed at low  $Q^2$  [33].

The final state radiation photon is normally located in the same cluster as the scattered electron, leaving, therefore, the Born kinematics unchanged. A study performed in [76] showed that only about 1.5% of FSR events were resolved in two electromagnetic clusters in the Spacal. This effect was well described by the DIS Monte Carlo simulation. In the case of BEMC, having much worse granularity, the fraction of resolved final state radiation was negligible.

The Compton events have relatively small contributions to the radiative corrections. For the whole phase space of the analysis they never exceed 20% of the ISR sample. In the numerically most important limit,  $Q_{true}^2 \rightarrow 0$ ,  $y_{true} \rightarrow 0$ , the kinematics of these events is fully constrained by the  $E - p_z$  and  $P_t$  conservation between the radiative photon and electron:

$$\begin{aligned} E_\gamma(1 - \cos \theta_\gamma) + E'_e(1 - \cos \theta_e) &= 2E_e \\ E_\gamma \sin \theta_\gamma &= E'_e \sin \theta_e. \end{aligned} \quad (3.9)$$

For the highest  $y$  part of the 1996 data (where the scattered electron was confined to the CJC acceptance and  $E'_e > 4$ ) the Compton's photon was within the Spacal acceptance,  $\theta_\gamma < 177.5^\circ$ . An experimental study of the events with this signature is presented in Sec. 6.1.

A way to reduce the influence of the QED radiative events on the kinematics reconstruction is to make use of the  $y_h$  measurement. A requirement  $y_h > y_e - \delta$  restricts the energy of the ISR photon to  $E_\gamma < \delta E_e$ , see Eq. 3.4. A simple cut  $y_h > \epsilon > 0$  limits the phase space from the singularity apparent in the DIS cross section at the  $y \rightarrow 0$  limit. The requirement of the hadronic vertex existence is found to be equivalent to a cut  $W_h = \sqrt{S(1-x)y} > 15$  GeV. Therefore this provides effectively a selection of events with  $y_h > 0.0025$ .

The radiative effects were included into Monte Carlo simulation, based on the HERACLES program. A comparison of the radiative corrections estimated with the Monte Carlo program and the HELIOS branch of the HECTOR package is shown in Fig. 3.5, left. The radiative corrections were calculated using the GRV LO 1994 parameterization of the structure function  $F_2(x, Q^2)$  [17].  $F_L(x, Q^2)$  was taken to be equal to 0. A cut  $W_h > 4$  GeV was applied in both programs, related to limitations in the LEPTO program. One can see, that the corrections are similar for different  $Q^2$  values and they agree well for both estimations. The radiative corrections are largest at large  $y$ . Therefore we will concentrate on this domain in the following comparisons.

Fig. 3.5-right presents a check of the LLA estimation with the complete  $O(\alpha_{QED})$  order calculation performed by the TERAD branch of the HECTOR program. A perfect agreement is seen. For these calculations the used  $F_2(x, Q^2)$  and  $F_L(x, Q^2)$  parameterizations were those obtained in a QCD fit which is described in Sec. 7.4.

The radiative corrections depend on the structure functions used for their calculation. Therefore an iterative procedure described in Sec. 3.7 was performed with the measured cross section used to estimate the radiative correction. This procedure has an ambiguity at high  $y$  where both structure functions  $F_L$  and  $F_2$  contribute. Thus they can not be unfolded independently.

An estimation of this effect is presented in Fig. 3.6-left. The lines in this figure correspond to the HELIOS based radiative correction calculation with  $F_2^{QCD}(x, Q^2)$  and  $F_L^{QCD}(x, Q^2)$  obtained from

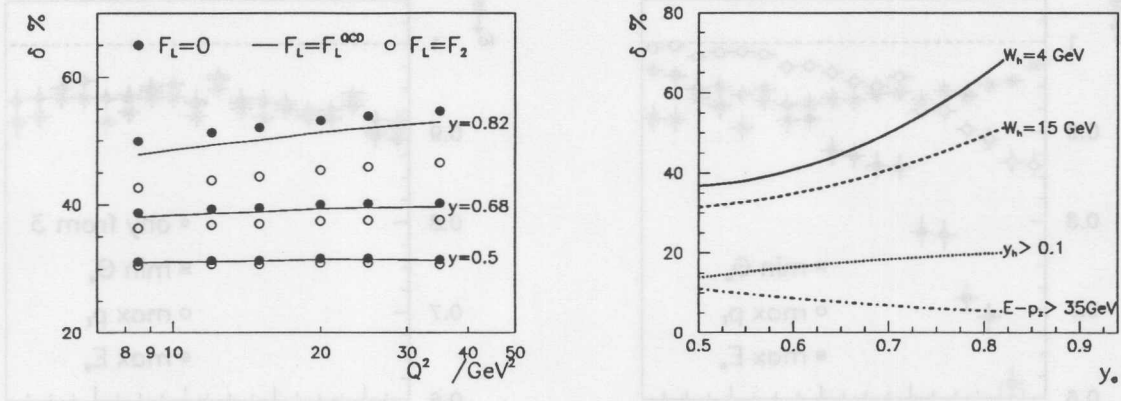


Figure 3.6: Left: Dependence of the radiative corrections on different assumptions made for the structure function  $F_L$ , see text. The curves are calculated for  $W_h > 15$  GeV. Right: Dependence of the radiative corrections at  $Q^2 = 20$  GeV<sup>2</sup> on different cuts using hadronic variables.

the QCD fit. A cut  $W_h > 15$  GeV was applied corresponding to the hadronic vertex requirement which was used in the highest  $y$  analysis. The solid and open circles show the radiative corrections for two extreme assumptions:  $F_L = 0$  and  $F_L = F_2$ , respectively. The corresponding structure functions  $F_2$  were recalculated keeping the Born double differential cross section constant.  $F_2$  for the assumption  $F_L = 0$  is equal to  $F_2'(x, Q^2) = \kappa\sigma = F_2^{QCD}(x, Q^2) - y^2/Y_+ F_L(x, Q^2)$  and  $F_2$  for  $F_L = F_2$  is equal to  $F_2'(x, Q^2) = \kappa\sigma/(1 - y^2/Y_+)$ . One can see in Fig. 3.6-left that the variations of the radiative corrections for the highest  $y$  value reach 10% leading to an up to a 7% uncertainty in the double differential cross section measurement. The uncertainty becomes much smaller at lower  $y$  values.

Fig. 3.6-right shows the dependence of the radiative corrections on different cuts based on hadronic variables. The HELIOS program and the  $F_2, F_L$  parameterizations obtained in the QCD fit were used for the calculations. The  $W_h > 15$  GeV cut, which is equivalent to the hadronic vertex requirement, reduces the corrections at  $y = 0.82$  by  $\sim 15\%$  to about 50%. The  $y_h > 0.1$  selection, used in the high  $y$  1994 analysis<sup>1</sup>, lowers the corrections by additional 20 – 30%. Finally, the  $E - p_z$  cut applied for the 1996 data, diminished the corrections down to  $\sim 5\%$ . Thus the dependence of the radiative corrections on the longitudinal structure function  $F_L$  became negligible.

### 3.5 Electron Identification

The reconstruction of the DIS event kinematics is impossible without correct identification of the scattered electron. The electron identification procedure in the present analysis started from the energy cluster in the backward electromagnetic calorimeter. From the kinematic plane, Fig. 3.3, it follows that at  $y < 0.5$  the energy of the scattered electron is bigger than that of the energy of the hadronic jet, and the angle of the hadronic jet is smaller than that of the electron. Thus an electron was identified with the electromagnetic cluster of maximum energy in the backward calorimeter ( $E^{max}$  ordering).

The situation becomes different for high  $y > 0.5$ . A zoomed view into this region is given in Fig. 3.3-bottom. Only the part corresponding to the special high  $y$  analysis  $7.5 \text{ GeV}^2 < Q^2 < 43 \text{ GeV}^2$  is presented here. Using this plot the following observations can be done:

<sup>1</sup>The  $E - p_z$  cut was not available in the 1994 analysis due to poor BEMC hadronic coverage. The  $y = 0.1$  value corresponds to central emission of the hadronic jet, therefore it was reconstructed in LAr calorimeter.

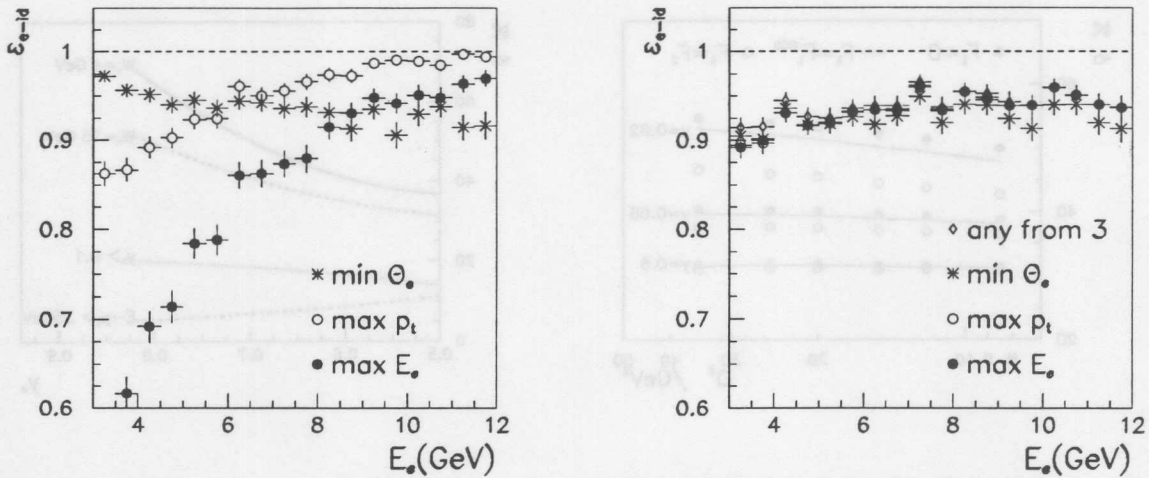


Figure 3.7: Electron identification probability as a function of the generated scattered electron energy. The left plot corresponds to the selection among the three most energetic Spacal clusters without applying selection criteria on the clusters' properties. The right plot shows the identification probability in the case of restricting the electron candidate search to clusters linked to a CJC track and satisfying  $RCL_{log} < 5$  cm condition (see Sec. 6). Solid circles correspond to selecting the cluster with maximum energy, open with maximum  $P_t$  and crosses with minimum  $\theta$ . Diamonds correspond to the probability, that the electron cluster is present among any of the validated clusters. The probability that the electron corresponds to one of the three hottest Spacal clusters was found to be  $> 99.5\%$  for  $E_e' > 3$  GeV. (from [75])

- The energy of the scattered electron becomes small (the line  $y = 0.6$  is practically parallel to the line  $E = 11$  GeV). It is even less than the total energy of the hadronic jet being always bigger than 15 GeV.
- The scattered electron angle (with respect to the incoming electron) is large, it lies in the central proportional chamber acceptance and for  $y > 0.75$ ,  $Q^2 > 12$  GeV<sup>2</sup> in the acceptance of the inner jet chamber CJC1.
- The scattered electron angle is smaller than the hadron angle. This can be also seen in the following formula:

$$\tan \frac{\theta_h}{2} = \frac{y}{1-y} \tan \frac{\theta_e}{2}. \quad (3.10)$$

It becomes clear that the maximum energy definition is not optimal for the electron identification at low energies. Still, it can give the correct answer since the backward hadronic jets are normally broad and deposit energy in several clusters corresponding to different particles. Unfortunately, this introduces a large dependence on the knowledge of the formation of the hadronic final state particles in the Monte Carlo simulation.

A first possibility to improve the electron identification algorithm is to restrict the search for the electron candidate to those clusters in the backward calorimeter, that are satisfying properties of electromagnetic clusters produced by a charged particle. The discussion of these additional selection criteria can be found in Sec. 6. The drawback of this approach are difficulties in the efficiency determination of the cuts, already performed during the electron identification.

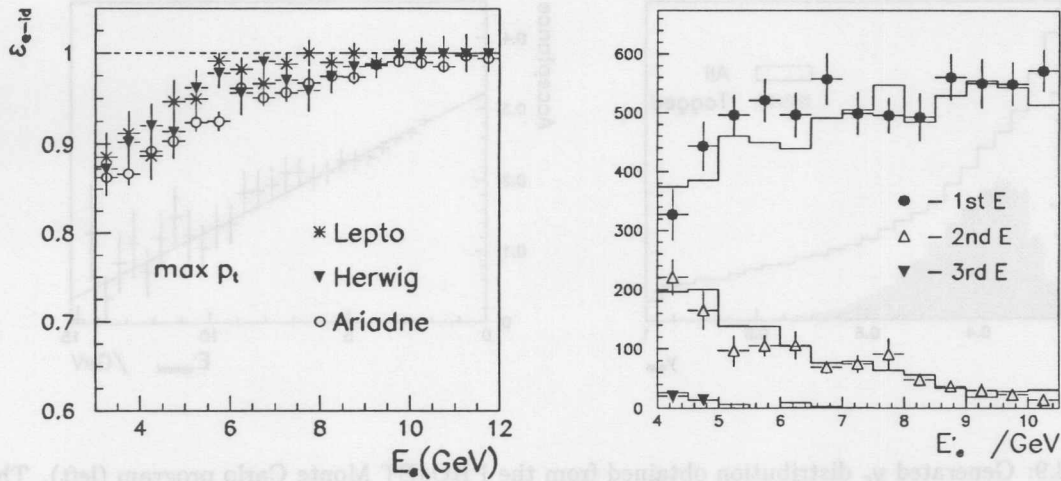


Figure 3.8: Left: comparison of the electron identification probability based on  $P_t$  ordering for different Monte Carlo models (from [75]). Right: experimental and Monte Carlo distributions of the scattered electron energy detected in the highest (solid circles), next-to-highest (open triangles) and next-to-next-to-highest (solid triangles) energy cluster in the Spacal. The plot corresponds to the  $F_L$  1996 analysis (see Sec. 4). Electron identification is based on  $P_t$  ordering using the CJC track validation. The  $\gamma p$  background is subtracted using clusters linked to negative tracks (see next section).

As an alternative different kinematic criteria can be tried. First, as discussed above, one can use the cluster with minimal polar angle, restricting the search to clusters with  $E > E_{min} = 3$  GeV ( $\theta^{min}$  ordering). By construction, this approach can be applied for  $y > 0.5$  only.

The second approach is based on the  $P_t$  balance in the event (Eq. 3.2) which imposes that the transverse momentum of the electron is compensated by the sum of  $P_t$  of the hadronic final state particles. Therefore, in most of the cases the electron is the particle, which has the largest  $P_t$  ( $P_t^{max}$  ordering). This method is applicable to the whole  $y$  range of the measurement.

A comparison of the different electron identification methods was done based on the Monte Carlo simulation. Events with the generated electrons in the backward calorimeter acceptance were selected. An electron was assumed to be recognized correctly if the cluster energy and angle were determined with 20% and 10 mrad precision with respect to the generated values. It was found, that the genuine electron was among the three (two) highest energy clusters in the backward calorimeter with  $> 99.5\%$  probability if its energy was bigger than 3(6.5) GeV. Therefore only the three highest energy clusters were considered in the analysis (two for 1994 analysis).

In Fig. 3.7-left the electron identification probability of the pure kinematic selection is presented. Fig 3.7-right corresponds to the case when the electron candidate search is restricted to the clusters passing the electron identification cuts (cluster-track link [Sec. 6.6] and  $RCL_{log} < 5$  cm [Sec 6.3]). Fig. 3.8-left shows the comparison of the pure kinematic  $P_t^{max}$  ordering between different Monte Carlo models. Finally, Fig. 3.8-right presents the experimental and simulated distributions based on the 1996 analysis with maximum  $P_t$  electron identification, when the electron was detected in the highest or the next two energy clusters in the Spacal.

In these plots one can see that the largest electron identification probability at high  $y$  has the  $\theta^{min}$  ordering, the  $P_t^{max}$  requirement is between the energy and  $\theta$  ordering, it is never worse than the energy ordering. The cluster validation brings all the methods close together; they are approaching

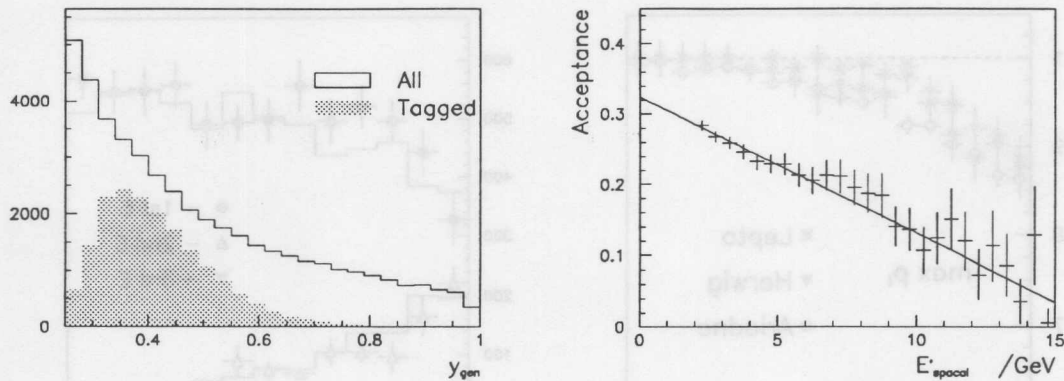


Figure 3.9: Generated  $y_e$  distribution obtained from the PHOJET Monte Carlo program (left). The shaded histogram corresponds to the electrons scattered in the tagger acceptance. The tagger acceptance as a function of the SPACAL cluster energy (right).

the limit, caused by the track link and cluster radius cut inefficiencies. Comparison of the different hadronisation models shows some differences, for example ARIADNE is systematically lower than HERWIG and LEPTO-MEPS, but this difference is on the level of 3%. The comparison of the data and Monte Carlo simulation shows that the latter describes the dynamics of the energy behaviour of the relation between the electron and hadronic final state particles energy rather well.

The electron identification methods chosen for the DIS cross section measurement were  $E^{max}$  with cluster validation for the 1994 data and  $P_t^{max}$  for the 1996 data. The other methods were used in order to estimate systematic effects.

### 3.6 Backgrounds to Deep Inelastic Scattering

As discussed in the previous section at high  $y$  or equivalently low  $E'_e$  the energy of the hadronic jet becomes bigger than the energy  $E'_e$ . In case of very low momentum transfer squared,  $Q^2 \sim 0$ , the scattered electron escapes the backward calorimeter acceptance. If the event occurred at high  $y$ , however, the hadronic jet particles can produce a cluster in the backward electromagnetic calorimeter, which could be misidentified as an electron (*faked electron*). This effect is known as the *photoproduction* or  $\gamma p$  background.

Another source of false DIS signatures could come from non- $ep$  interactions, caused by particles leaving the beam and scattering off the beam-line elements (*beam-wall* interactions) or due to beam interactions with the residual gas (*beam-gas* interactions). Similar to the photoproduction background, the non- $ep$  background is more significant at low  $E'_e$ , but contrary to the former it is strongly suppressed by the event timing and interaction vertex constraints.

We will discuss both background sources in the next sections.

#### 3.6.1 Photoproduction ( $\gamma p$ ) Background

The photoproduction background comes from  $ep$  interactions at very low  $Q^2 \sim 0$  and high  $y > 0.2$ . The importance of this background is caused by the  $1/Q^4$  rise of the cross section, Eq. 1.4. Without

a special  $\gamma p$  reduction the  $\gamma p$  background could be 5 – 2 times bigger than the DIS signal for the kinematic interval  $2 < E'_e < 10$  GeV.

Part of the photoproduction events is detected directly by the electron tagger (see Sec. 2.2.1). In Fig. 3.9-left, the  $y$  acceptance of the electron tagger is illustrated. It was calculated by averaging over different beam positions on a run dependent basis. One can see that the electron tagger acceptance (ET) is maximal for  $y \sim 0.35$ . For this interval the hadronic jet energy is less than  $\sim 15$  GeV. The electron tagger acceptance as a function of the faked electron candidate's energy, reconstructed in SPACAL is given in Fig. 3.9-right. Since the total hadronic jet energy is limited to  $\sim 15$  GeV, the acceptance becomes low for  $E' > 10$  GeV, but it rises nearly linearly up to 25% for  $E' \approx 3$  GeV. Thus contrary to the standard  $F_2$  data analysis performed for  $y \leq 0.6$ , the high  $y$  cross section analysis can profit from an appreciably increased part of  $\gamma p$  events tagged by the electron tagger. The acceptance variations as a function of the polar angle of the faked electron candidate were found to be small in the angular range considered here.

A background to the  $\gamma p$  events detected in the ET arises from overlap of Bethe-Heitler and normal deep inelastic scattering events. It was suppressed by the requirement of no energy deposit in the photon detector and  $E - p_z^{tot} < 70$  GeV with the photon detector and electron tagger contributions added:

$$E - p_z^{tot} = \Sigma + E'_e(1 - \cos \theta_e) + 2E'_{e \text{ tagger}} + 2E'_{\gamma \text{ tagger}}, \quad (3.11)$$

compare Eq. 3.3.

Two kinds of hadronic final state particles build the most prominent sources for the production of the faked electron clusters. Firstly these are  $\pi^0$  particles, which decay into  $2\gamma$ . Depending on the opening angle between the photons (which is defined by the  $\pi^0$  energy), they form one or two clusters of electromagnetic energy in the backward calorimeter. In most cases the  $\gamma$  quanta convert into  $e^-e^+$  pairs in the detector material behind the central tracker, producing track elements in the backward tracker. On the contrary, inside the central tracker the showering effects are small. Therefore the CIP validation, Sec. 6.5, is very effective in rejecting this sort of events, and the "CIP rejected event sample" could be used to check the Monte Carlo description of this background component.

The second source of faked electron clusters is related to charged hadronic particles. Due to the largely non compensating energy response of both BEMC and Spacal (Sec. 2.2.4) the reconstructed energy was normally much smaller than the true particle energy. The hadronic energy clusters are also broader than the electromagnetic ones both in transverse and longitudinal directions. Hence they were suppressed by the cluster radius and hadronic energy fraction selection criteria which are described in Sec. 6.3. An important rôle for this background rejection played the backward tracker-calorimeter link requirement (see Sec. 6.2) because of the bigger spread in the reconstructed hadronic cluster center position and the deeper longitudinal penetration of hadrons as compared to electromagnetic energy deposits. A control of the Monte Carlo description of this background component was based on the events rejected because of a too large cluster radius.

An estimation of the remaining photoproduction background in the DIS selected sample was done in the analysis using two methods. In the first case it was based on the number of PHOJET events which passed all analysis selection criteria. The subsample of events tagged by the electron tagger allowed to cross check the Monte Carlo estimation. A modification of this approach was based on the direct usage of experimental events with the scattered electron detected in the electron tagger corrected event by event for the tagger acceptance (Fig 3.9-right). Further tests were based on the samples rejected by the CIP validation and cluster radius requirement There represent were enriched  $\gamma p$  event samples to be described by the simulation.

A further method of evaluating the background contamination was developed during the analysis of 1996 data. Positrons scattered at very high  $y > 0.75$  traverse the CJC (Fig. 3.3-bottom). The requirement to link the CJC track to a selected Spacal cluster additionally reduced the remaining background from both  $\pi^0$  and charged hadrons. In the CJC the particle charge is determined. A

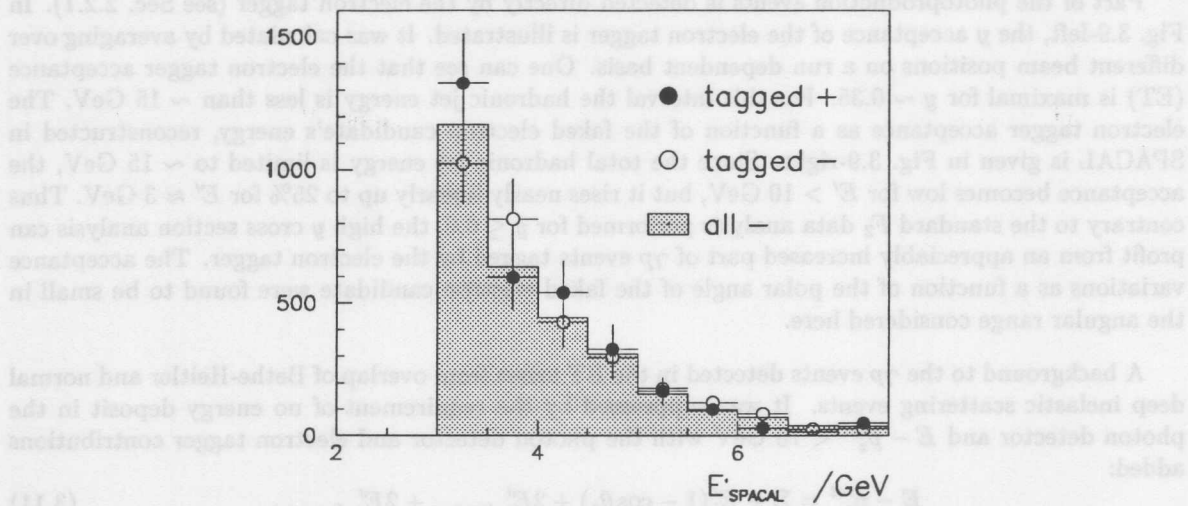


Figure 3.10: Spacal cluster energy distributions. Solid (open) circles: the tagged  $\gamma p$  events, corrected for the tagger acceptance, with Spacal clusters linked to CJC tracks with positive (negative) charge; shaded histogram: distribution of all events with negative charge. All selection cuts (Sec. 6), apart from the  $E - p_z$  requirement, were applied.

positive charge requirement removed all negative hadrons. Assuming a charge symmetry of the background, the remaining background in the positively charged sample could be estimated by the amount of rejected events with negative tracks.

A detailed study of the background charge symmetry was performed based on the PHOJET Monte Carlo simulation [75]. The result of this study was that for  $E' > 3$  GeV the background charge asymmetry is consistent with zero with a 1% statistical error. A direct experimental check comes from the tagged photoproduction sample, see Fig. 3.10. Here the SPACAL energy distributions of the tagged positive and negative track events, corrected for the tagger acceptance, are presented together with the distribution of all negative track events. The plot is done after all selection cuts (Sec. 6), apart from the  $E - p_z$  condition because the tagger acceptance is lower if the latter requirement is applied. Within the limited statistics, corresponding to at most 3% charge asymmetry, the positive and negative background energy distributions are equal. Also a good agreement is observed between the background estimate based on tagged events and the distribution obtained by selecting clusters with linked tracks of negative charge.

### 3.6.2 Non- $ep$ Background

The non- $ep$  background has a rate much higher than that of  $ep$  collisions before any selection, but it is effectively suppressed already at the trigger level by different timing and minimal energy deposit requirements. Further selections, described in Sec. 6, reduce it to the permille level. It has non-negligible effect only for special studies, like the vertex reconstruction efficiency for low  $E'_e$ .

The remaining non- $ep$  background was estimated by means of special unpaired non-colliding particle bunches, the so-called *pilot bunches*. Having no matching bunch to collide with, they can interact with residual beam gas or beam line elements only. Using the proton (electron) pilot bunch events it



is possible to study the effects of the proton (electron) beam-gas and beam-wall interactions. Empty bunch events permit to determine the random background, e.g. caused by cosmic or beam halo muons. Normalizing the amount of pilot bunches to the number of colliding bunches, one can estimate the non- $ep$  background as:

$$N_{bg} = N_{p-pilot} \frac{n_{collide}}{n_{p-pilot}} + N_{e-pilot} \frac{n_{collide}}{n_{e-pilot}} + N_{empty} \frac{n_{collide}}{n_{empty}}, \quad (3.12)$$

where  $N_{p-pilot}$ ,  $N_{e-pilot}$ ,  $N_{empty}$  are the event numbers for proton-pilot, electron-pilot and empty bunches found in the final DIS sample;  $n_{collide}$ ,  $n_{p-pilot}$ ,  $n_{e-pilot}$ ,  $n_{empty}$  are the numbers of colliding, proton-pilot, electron-pilot and empty bunches, respectively.

Alternatively, the normalization factors in formula 3.12 were obtained by a direct fit to the total measured cross section as described in Sec. 6.1. The resulting factors were found to be consistent with the estimation based on Eq. 3.12.

### 3.7 Cross Section Determination

The cross section determination in the presented analysis was performed in  $Q^2, x$  and  $Q^2, y$  bins. The  $Q^2, x$  binning was chosen for the  $F_2$  part of the measurement at  $y < 0.6$ . The main reason for such a binning was the fact that  $Q^2, x$  are the basic variables describing the  $F_2$  evolution. For higher  $y$  the influence of the longitudinal structure function  $F_L$  becomes large (see 1). The analysis, performed in this region, had the goal to extract this structure function. The variable, which prescribes the relative contribution of  $F_L$  to the DIS cross section, is  $y$ . Therefore the  $Q^2, y$  binning was selected.

The bin size and bin boundaries were chosen according to the following considerations: 1) the kinematic resolution in  $\delta x/x$  is approximately constant for more than three decades in  $x$ . Therefore a logarithmically equidistant  $x$  binning was used, the resolution being below the bin size; 2) for the  $y$  binning at  $y > 0.6$  and the  $Q^2$  binning, where the resolution is perfect, the bin size was defined by the collected statistics; 3) the same  $Q^2$  binning was chosen for the whole range of  $x, y$  considered

The following bin boundaries were selected:

$Q^2$ /GeV <sup>2</sup> :								7.499	10.00
	13.34	17.78	23.71	31.62	42.17	56.23	74.99	100.0	
	133.4								
$x$ :		0.000158	0.000251	0.000398	0.000631				
	0.001	0.00158	0.00251	0.00398	0.00631				
	0.01	0.0158	0.0251	0.0398	0.0631				
	0.1	0.158	0.251						

For the high  $y$  binning, just one bin from 0.6 to 0.8 was chosen for the 1994 data analysis and two bins 0.6 – 0.75, 0.75 – 0.9 for the 1996 data analysis.

The double differential cross section is quoted for the following fixed “central” points in the bins:

$Q_c^2$ /GeV <sup>2</sup> :							8.5	12
	15	20	25	35	45	60	90	120

$x_c$ :	0.0002	0.00032	0.0005	0.0008
0.0013	0.002	0.0032	0.005	0.008
0.013	0.02	0.032	0.05	0.08
0.13	0.2			

The central values for the  $y$  bins were selected to be 0.7 for the 1994 data and 0.68, 0.82 for the 1996 data. The  $x$  values corresponding to these  $y$  bins were calculated using beam energies of 820 GeV and 27.6 GeV for the proton and electron beams, respectively.

The main formula for the calculation of the double differential cross section used in the analysis is given below:

$$\frac{d^2\sigma(x, Q^2)}{dx dQ^2} = \frac{N_{data} - N_{\gamma p} - N_{bg}}{A \cdot \mathcal{L}} \frac{1}{\epsilon} \frac{1}{1 + \delta} BC, \quad (3.13)$$

with

$N_{data}$  Total amount of selected events per bin;

$N_{\gamma p}$  Total amount of  $\gamma p$  background estimated from the Monte Carlo simulation or from tagged events;

$N_{bg}$  Total amount of non- $ep$  background events estimated using the pilot bunches;

$A$  Detector acceptance calculated using the full Monte Carlo simulation. It is defined as the ratio of the number of reconstructed to the number of generated events  $A = N_{rec}/N_{gen}$ ;

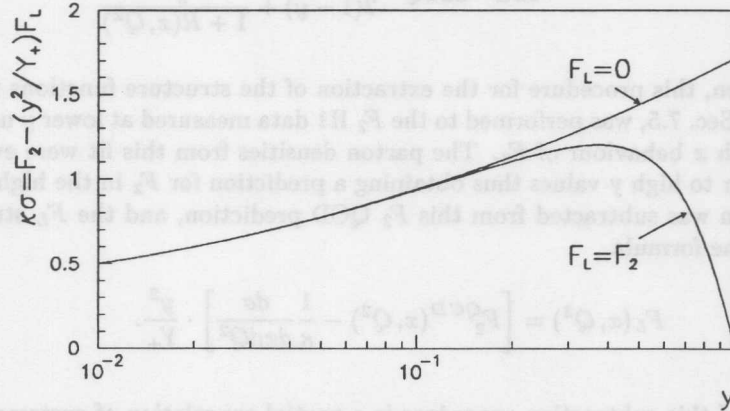
$\mathcal{L}$  Total integrated luminosity using the luminosity detector measurement corrected for the satellite bunch contribution;

$\epsilon$  Extra efficiency corrections, not included or not properly described in the Monte Carlo simulation;

$\delta$  Radiative corrections estimated from the Monte Carlo simulation or from analytic programs,  $\delta = \sigma_{rad}/\sigma_{Born} - 1$ . Here  $\sigma_{rad}, \sigma_{Born}$  denote the bin integrated full and Born cross sections;

$BC$  Bin center corrections calculated as  $BC = d^2\sigma/dx dQ^2 / \sigma_{Born}$ .

The radiative correction, the bin center correction and acceptance are calculated using some model of the double differential cross section behaviour. If the prediction of the model gives a result too different from the measurement, obtained with the formula 3.13, an iteration is needed with a DIS cross section model fitted to the measurement. In this analysis a QCD fit to the  $F_2$  data was performed (Sec. 7.4). The parameterizations of the  $F_2$  and  $F_L$  structure functions, obtained from this fit, were used to specify the DIS cross section model. The difference between the double differential cross section measurement, extracted with an initially "uncorrected" cross section based on the GRV-94 LO structure functions with  $F_L = 0$ , and the one, based on  $F_2$  and  $F_L$  obtained from the QCD fit, was less than 1% for all bins. Thus no additional iteration was necessary.

Figure 3.11:  $F_L$  influence on the DIS cross section

In the case when the radiative corrections are completely included into the Monte Carlo simulation, formula 3.13 can be simplified using the following identity:

$$N_{gen} = \mathcal{L}^{MC} \sigma_{rad}. \quad (3.14)$$

Then one obtains the definition of the so-called ‘‘Monte Carlo method’’:

$$\frac{d^2\sigma(x, Q^2)}{dx dQ^2} = \frac{N_{data} - N_{\gamma p} - N_{bg}}{N_{rec}^{MC}} \frac{1}{\epsilon} \frac{\mathcal{L}^{MC}}{\mathcal{L}} \frac{d^2\sigma^{MC}(x, Q^2)}{dx dQ^2} \quad (3.15)$$

The formula has to be modified if the background is estimated using clusters with linked tracks of negative charge:

$$\frac{d^2\sigma(x, Q^2)}{dx dQ^2} = \frac{N_{data}^+ - N_{data}^-}{N_{rec}^{MC+} - N_{rec}^{MC-}} \frac{1}{\epsilon} \frac{\mathcal{L}^{MC}}{\mathcal{L}} \frac{d^2\sigma^{MC}(x, Q^2)}{dx dQ^2} \quad (3.16)$$

### 3.8 Extraction of Structure Functions

The deep inelastic double differential cross section in the one-photon exchange approximation is defined by the two structure functions,  $F_2(x, Q^2)$  and  $F_L(x, Q^2)$ , as was discussed in Sec. 1. The  $F_L$  structure function is limited to the interval  $0 - F_2$  due to the positivity of the cross sections  $\sigma_T$  and  $\sigma_L$  (Eq. 1.6). The rôle of the two structure functions is different for different  $y$  domains. At low  $y < 0.1$  the influence of the  $F_L$  structure function is negligible. In the intermediate range ( $y \approx 0.3$ ) the  $F_L$  contribution is of the order of the present systematic errors of the measurement, and at high  $y > 0.6$  it becomes comparable to the size of the  $F_2$  part (see Fig. 3.11).

Thus for low  $y$  the DIS measurement can be directly interpreted as a determination of  $F_2$ . In the intermediate  $y$  range a model is needed for  $F_L$  or  $R$  in order to obtain  $F_2$ . A standard approach is to assume  $R$  to be given by NLO QCD, using some input parton densities. By convention, GRV

parameterizations were used in the past H1 analysis. The  $F_2$  structure function is given then by the formula:

$$F_2(x, Q^2) = \frac{Q^4 x}{2\pi\alpha^2} \frac{d\sigma}{dx dQ^2} \frac{1}{2(1-y) + \frac{y^2}{1+R(x, Q^2)}} \quad (3.17)$$

In the high  $y$  region, this procedure for the extraction of the structure functions was inverted. A QCD fit, described in Sec. 7.5, was performed to the  $F_2$  H1 data measured at lower  $y$  using fixed target data to define the high  $x$  behaviour of  $F_2$ . The parton densities from this fit were evolved in  $Q^2$  for fixed  $x$ , i.e. from lower to high  $y$  values thus obtaining a prediction for  $F_2$  in the high  $y$  domain. The measured cross section was subtracted from this  $F_2$  QCD prediction, and the  $F_L$  structure function was extracted using the formula

$$F_L(x, Q^2) = \left[ F_2^{QCD}(x, Q^2) - \frac{1}{\kappa} \frac{d\sigma}{dx dQ^2} \right] \cdot \frac{y^2}{Y_+}. \quad (3.18)$$

A salient feature of this subtraction procedure is a partial cancelation of systematic errors, since the cross sections at low and high  $y$  are measured using a common set of data. The longitudinal structure function obtained in this procedure is based on the assumption that  $F_2$  at highest  $y$  is in accordance with NLO QCD. This assumption can be verified experimentally if HERA is run at higher beam energies as is envisaged for the year 1998.

The discussion in the next chapters will focus on the determination of the different components of the basic Eq. 3.13. First, general data quality studies will be presented, which ensure the correct calculation of the luminosity  $\mathcal{L}$ , of the event selection efficiency and acceptance calculation. Next, the calibration of the detector will be discussed, which provides a correct reconstruction of the event kinematics and, thus,  $N_{data}, N_{MC}$  is obtained in a given bin. Detailed studies of the detector efficiencies follow which define the extra correction term  $\epsilon$ . The radiative corrections and background contributions have been already mentioned in the present chapter, some additional control plots will be presented together with general data and Monte Carlo simulation comparisons. These studies will be concluded with a list of systematic errors and the final DIS cross section result.

## Chapter 4

# Data Treatment

The chapter introduces the data samples used in the present analysis. Different criteria for the run selection and a complete list of runs rejected in the 1996 analysis are given. The stability of the DIS cross section measurement is presented next. Then the corrections are discussed for satellite bunch effects on the luminosity measurement. Finally different triggers and their efficiencies are discussed.

### 4.1 Data Samples

Several data samples taken by the H1 detector in 1994 and in 1996 are used in this thesis. They are characterized in Tab. 4.1. All of them are based on the electron identification in the backward electromagnetic calorimeters with  $Q^2$  values limited to  $7.5 - 133.5 \text{ GeV}^2$ . Apart from the obvious difference in the year of data taking and thus in the backward experimental setup of the H1 detector, the datasets differ in the trigger definition. The main data collected in 1994 and in 1996 were based on the so-called S0 trigger. It triggered solely on the backward calorimeter information, i.e. if the energy deposit was bigger than a certain threshold the event was accepted. This “minimum bias” feature of the trigger made it perfectly suitable for the inclusive cross section measurement. The corresponding analyses will be referred to in this thesis as “ $F_2$  1994” and “ $F_2$  1996” since the bulk of the obtained data points was interpreted as a determination of the structure function  $F_2$  although the highest  $y$  part of the “ $F_2$  1996” analysis was used for the  $F_L$  extraction.

In the lower energy range the background rate due to beam-gas and beam-wall interactions rises very fast. In order to suppress it an additional trigger requirement is necessary. The demand of a “ray” track pointing to the interaction region reconstructed in the multiwire proportional chambers was used for this purpose. This requirement is similar to the vertex condition which is always included

Name	Luminosity $\text{nb}^{-1}$	Trigger used	$E'_e$ range GeV	$Q^2$ range $\text{GeV}^2$	date
‘ $F_2$ Close triangles’	1739.5	S0	$> 11$	12 – 120	16.08-18.10 1994
‘ $F_2$ Open triangles’	266.06	S0	$> 11$	8.5	18.10-24.10,27.10-01.11 1994
‘ $F_L$ 94’	1250.0	S6	6.5 – 11	8.5 – 35	16.08-18.10 1994
‘ $F_2$ 96’	4763.6	S0,S1,S3,S9	$> 6.9$	12 – 90	5.09-25.11 1996
‘ $F_L$ 96’	2621.7/4520.8	S9,S2	4 – 6.9	12 – 25	5.09-25.11 1996

Table 4.1: Data samples used in the analysis. The luminosity values are corrected for the satellite bunch contribution. The trigger definitions depend on the year, see Sec. 4.6. Data samples based on S0 trigger are ‘inclusive’, i.e. they cover the whole phase space without any tracker requirement. The triggers S6 (in 1994) and S9 (in 1996) contained a MWPC ray condition.

in the DIS cross section analysis. For the low energy, high  $y$  range the vertex reconstruction efficiency is normally high (see also Sec. 3.2), but still for special classes of events, like low mass diffractive production, it can be low. This requires more detailed studies of the trigger efficiency at low energy, see Sec. 4.6 for details. The data analyses performed with the additional ray trigger condition will be referred to as " $F_L$  1994" and " $F_L$  1996", since they were used for the determination of the structure function  $F_L$ .

Although the MWPC ray requirement greatly reduced the proton beam induced background, still the triggers using this ray condition S6 in 1994 and S9 in 1996 had to be prescaled in order to reduce their rate. Together with a strict data selection, this led to lower luminosity available for the high  $y$  analyses as compared to the  $F_2$  analysis based on the S0 triggers.

The energy limits, listed in Tab. 4.1, correspond to the final presentation of the results of the DIS cross section measurement. They were expanded during the analysis in order to have overlaps of different datasets, allowing comparisons between them.

## 4.2 Run Selection

The data taking by the H1 detector is split into *luminosity runs*. A run is a number of events collected by the experiment under similar conditions. Each run has an integrated luminosity value. Other important database information is also considered to be run dependent. The run size can vary from about 1000 to 1000000 events.

Another important time unit for the data taking is the *luminosity fill* or HERA run. It is defined from the moment HERA announces luminosity until the positron or both beams are dumped. During a fill many runs are taken. Beam parameters like the average  $Z$  vertex position or the size of the satellite bunches are usually stable within one fill.

Before starting the DIS cross section analysis a preselection of the data sample is necessary. This insures stable detector and background conditions for the analysis and rejects obvious hardware problems. This preselection was done on a run by run basis applying the following criteria:

1. *Trigger phase 3,4 (94 data) or 2,3,4 (96 data)*. There are four trigger phases with different subtrigger prescaling factors corresponding to different periods in the data taking for one luminosity fill. Phase 1 corresponds to the beginning of a HERA run, high positron beam current and usually large proton background. Phase 4 near the end of the luminosity fill has the most comfortable machine background conditions but the positron beam current decreased to one half till one third of its initial value. In Phase 1 the backward calorimeter triggers were disabled or highly prescaled, while the tracker high voltages are ramping up. Phase 2 was rare in 1994. All phases 2-4 were used in the 1996 data analysis.
2. *Run quality: good or medium*. Each run is classified first by the H1 shift crew and after by different offline analysis criteria as *good*, *medium* or *poor*. This classification relies mainly on the operation status of the main detector components. A run can be classified as poor if some obvious hard- or software problems are found.
3. *Hardware - high voltage status*. Each run was checked for the hardware branches actually included into the readout. It was rejected if one of the important branches was absent. The fraction of time when all relevant detector components were at nominal high voltage was calculated. If this fraction was lower than 80% (1994) or 70% (1996) the run was not accepted. A low fraction of time with nominal HV value could mean many trips, detector instability, usually due to high background rate. This leads also to large luminosity corrections, increasing the error on its calculation. Finally runs were checked to have the backward calorimeter triggers enabled. The following important branches were used in the 'branch in readout' check: central trigger,

calorimeter trigger, calorimeter ADC, central drift chamber, proportional chambers, backward chamber, luminosity system. The following subdetectors were required to have nominal HV status: BEMC, BPC, CIP, COP, CIZ, CJC, LAr, ToF in 1994 and SPACAL, BDC, CIP, COP, CIZ, CJC, LAr in 1996.

4. *Large trigger prescale.* For the 1994 data only a few runs were prescaled for the subtrigger S0. They were rejected. In the  $F_L$  1994 analysis the maximum accepted prescale factor for the subtrigger S6 was 5. For the 96 data analysis the prescale factor of the subtrigger S3 was required to be smaller than 30, see Sec. 4.6 for details of the trigger treatment.
5. Only data collected during the  $e^+p$  mode of HERA operation were used for the 1994 data. The first accepted run number was 84601 (runs before had classifications problems, for details see [34]). In 1996 only data with the “new trigger setup”, were used starting from run 157877.

On top of these preselection criteria several runs or run ranges were rejected due to specific problems found during the run stability analysis. This is described in the next section.

### 4.3 Stability Studies

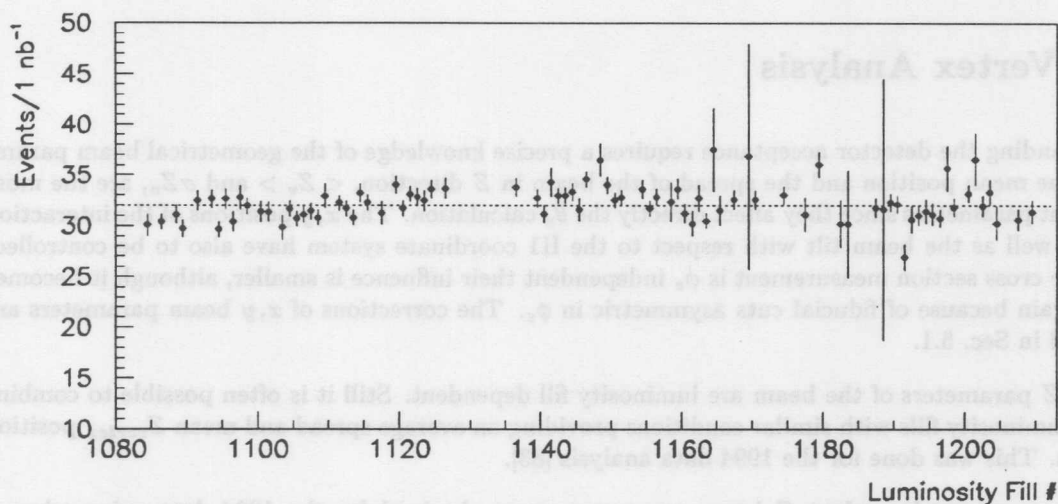


Figure 4.1: Yield in 1996 as a function of the luminosity fill number (from [75]).

An important check of the data quality used for the cross section measurement is the stability of the measurement as a function of time. A minimal ‘time slice’ for the H1 experiment is one run for which an integrated measured luminosity is available. The relative event yield (number of selected DIS events per  $\text{nb}^{-1}$  of integrated luminosity) as a function of the luminosity run number is thus considered to be the basic quantity for the stability study.

It is essential to introduce a fiducial cut for the DIS event selection in the stability study in order to eliminate the acceptance dependence on variations of the colliding beam position, see the next section. A cut of  $\theta_e < 171^\circ$  was used for this purpose in the 1996 data analysis. The cut  $\theta_e < 173^\circ$  cut was the basic fiducial cut for the 1994 data selection.

In order to increase the statistical significance of the yield measurement, for the 1996 data this was studied as a function of the luminosity fill number. Still, if a luminosity fill showed some problems the studies for that fill were made at the run level in order to isolate a potential problem.

One of the features of the 1996 data has been the presence of large contributions to the luminosity due to colliding satellite bunches. The satellite bunch fraction was varying from one luminosity fill to another. A reliable luminosity measurement required a fill depended correction of the luminosity for the satellite bunch effect. The discussion of this correction is given in Sec. 4.5.

In Fig. 4.1 the yield distribution as a function of the luminosity fill number is presented after applying all selection cuts. The list of rejected runs during the analysis of the stability distributions is given in Tab. 4.2.

162081-162111,162081-162111	Level 2 trigger problems
157927-157928,157937-157938,169186-169222	Spacal triggers rejected on Level 4
159591-159594	Non standard Spacal prescale factors, loss of luminosity
166072	Spacal trigger problems
168471-168488	Spacal HV problems
170550-171573	CIP readout problems

Table 4.2: Additional run selection for the 1996 data (together with [75]).

## 4.4 Vertex Analysis

Understanding the detector acceptance requires a precise knowledge of the geometrical beam parameters. The mean position and the spread of the beam in  $Z$  direction,  $\langle Z_v \rangle$  and  $\sigma Z_v$ , are the most important parameters since they affect directly the  $\theta_e$  calculation. The  $x, y$  positions of the interaction point as well as the beam tilt with respect to the H1 coordinate system have also to be controlled. Since the cross section measurement is  $\phi_e$  independent their influence is smaller, although it becomes larger again because of fiducial cuts asymmetric in  $\phi_e$ . The corrections of  $x, y$  beam parameters are discussed in Sec. 5.1.

The  $Z$  parameters of the beam are luminosity fill dependent. Still it is often possible to combine several luminosity fills with similar conditions providing an average spread and mean  $Z_{vertex}$  position for them. This was done for the 1994 data analysis [83].

The run range dependent  $Z$  beam parameters were obtained for the 1994 data using triggers based on the electron tagger (see Sec. 2.2.1). Since the acceptance of the electron tagger does not depend on the  $Z$  vertex position, this selection is ideal for an unbiased determination using the vertex reconstructed from hadronic final state particles.

The method was cross checked with the DIS event selection based on the backward calorimeter triggers. Potentially, this selection can produce a bias to the vertex distribution, since for events with positive  $Z$  vertex position lower  $Q^2$  values can be detected than for events with a negative one. The following selection was performed in order to diminish this bias:

1. a cut  $160^\circ < \theta_e < 172^\circ$  to ensure 100% backward calorimeter acceptance and one  $Q^2$  range independently of the  $Z$  vertex position in the zone from  $-40$  cm to  $+40$  cm;
2. a cut  $15 < E'_e < 25$  GeV, which selects events in the intermediate  $y$  domain where the background contribution is small and the  $Z$  vertex reconstruction efficiency is largest (see Sec. 3.2);



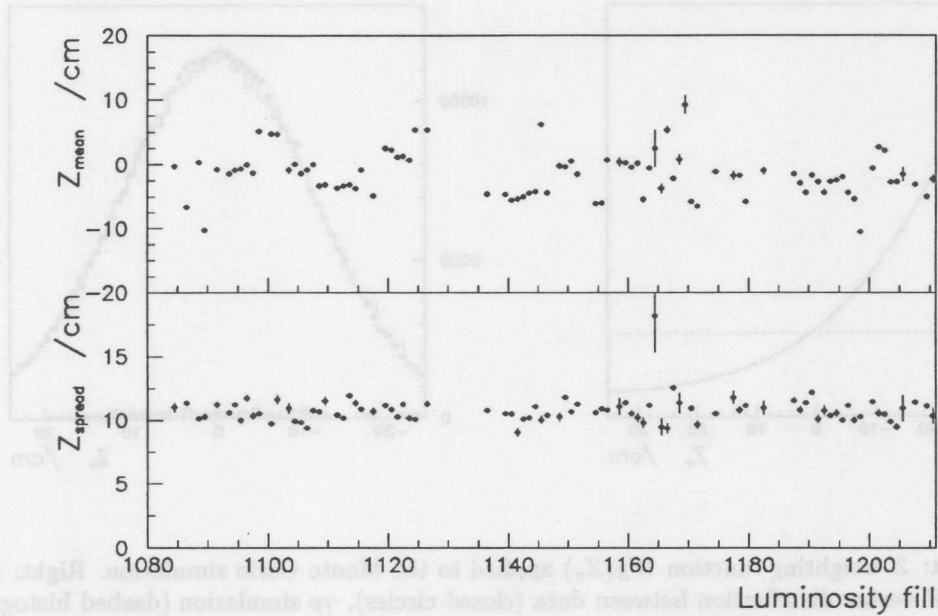


Figure 4.2: Mean  $Z$  vertex position (top) and its spread (bottom) as a function of the luminosity fill number for fills selected in the 1996 data analysis.

3. a cut  $N_{track} > 1$  to use only events with a reconstructed hadronic vertex and thus to avoid acceptance differences for events with the scattered electron inside or outside the active volume of the CJC.

It was found, that the estimations of  $\langle Z_v \rangle$  based on tagged  $\gamma p$  and DIS events agree within 2 mm. This leads to a 0.3 mrad uncertainty of the  $\theta_e$  acceptance which was included into the systematic error of the  $\theta_e$  determination.

In 1996 the inclusive e-tagger trigger was strongly prescaled. Thus the second method was used as the default one. The mean  $Z_{vertex}$  position and its spread as a function of the fill number obtained by this procedure are presented in Fig. 4.2.

For the DIS acceptance calculation, it would be ideal to have a Monte Carlo simulation performed with the  $Z$  vertex distribution obtained from the data. In practice this is difficult to achieve. For example, the final run selection is usually fixed only after many Monte Carlo files have already been produced. Therefore Monte Carlo files were simulated at different fixed mean  $Z$  and  $Z$  spread values and then *reweighted* to the data distribution.

For each Monte Carlo simulation file  $i$  (normally consisting of 100000 events), the luminosity ( $\mathcal{L}_i^{MC}$ ) and the  $Z$  vertex mean and spread ( $\overline{Z}_i^{MC}$ ,  $\sigma_{Z,i}^{MC}$ ) are given. Then the combined  $Z$  vertex distribution, normalized to one, is given by the following relation:

$$N^{MC}(Z) dZ = \sum_{i=1}^{N_{MC}} \frac{1}{\sqrt{2\pi}\sigma_{Z,i}^{MC}} \exp\left(-\frac{(Z - \overline{Z}_i^{MC})^2}{2\sigma_{Z,i}^{MC^2}}\right) \frac{\mathcal{L}_i^{MC}}{\sum_{j=1}^{N_{MC}} \mathcal{L}_j^{MC}} dZ. \quad (4.1)$$

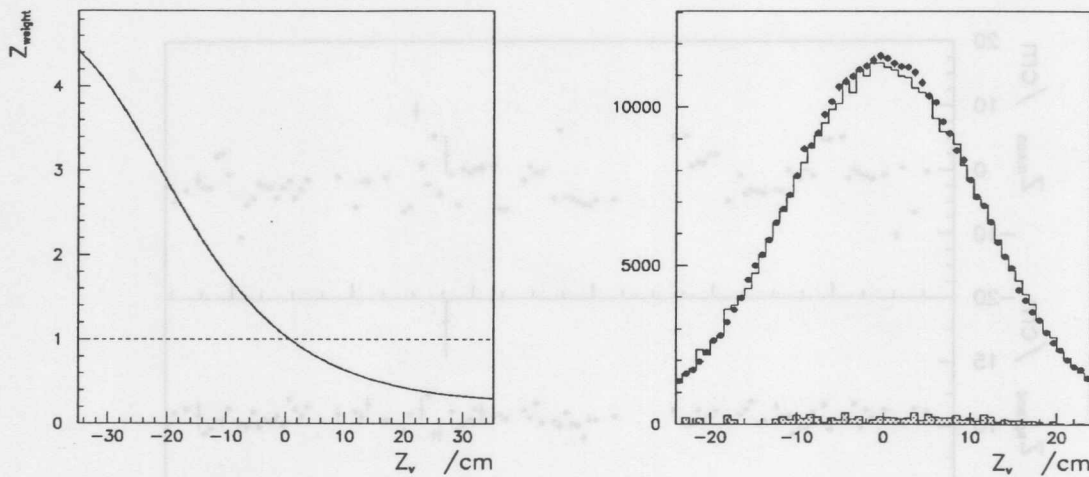


Figure 4.3: Left:  $Z$  weighting function  $W_Z(Z_v)$  applied to the Monte Carlo simulation. Right: comparison of the  $Z$  vertex distribution between data (closed circles),  $\gamma p$  simulation (dashed histogram) and the sum of  $\gamma p$  and DIS Monte Carlo simulations (open histogram). Experimental and Monte Carlo distributions are normalized absolutely. Both plots are based on 1996 data analysis.

The same formula is valid for data. Therefore, each Monte Carlo event was weighted with an additional weight:

$$W_Z(Z_v) = \frac{N^{data}(Z_v)}{N^{MC}(Z_v)}. \quad (4.2)$$

By construction,  $\int_{-\infty}^{+\infty} W_Z(Z) N^{MC}(Z) dZ = 1$ , thus this weighting conserves the Monte Carlo luminosity. It is equivalent to a simulation using  $dN^{data}(z)$  for the  $Z$  vertex distribution.

It is still important to have simulated mean  $Z$  vertex positions not far from the data since large shifts lead to large event weights and therefore to big statistical errors. For 1996 data the first Monte Carlo files were produced with the default position in 1994,  $\bar{Z} = 5.6$  cm. In order to reduce the weights, the last files were simulated with a mean position of  $Z = -5$  cm. Fig. 4.3-left displays the resulting weighting function. A comparison of the data and reweighted Monte Carlo distributions is given in the right plot.

## 4.5 Satellite Bunch Corrections to the Luminosity Measurement

The HERA proton beam has a complicated longitudinal structure [82], leading to the presence, apart from the main interaction region (*main bunch*), of several neighbouring ones, *satellite bunches* [34]. They manifest themselves in the presence of additional peaks in the  $Z$  vertex distribution. Most pronounced is the *forward* (or *late*) satellite, corresponding to an average  $Z$  distance of +70 cm with respect to the main bunch (see Fig. 4.4).

The H1 luminosity measurement system (Sec. 2.2.1) can not determine the position of the interaction point of the Bethe-Heitler photon. Therefore it measures the sum of the luminosities of the main

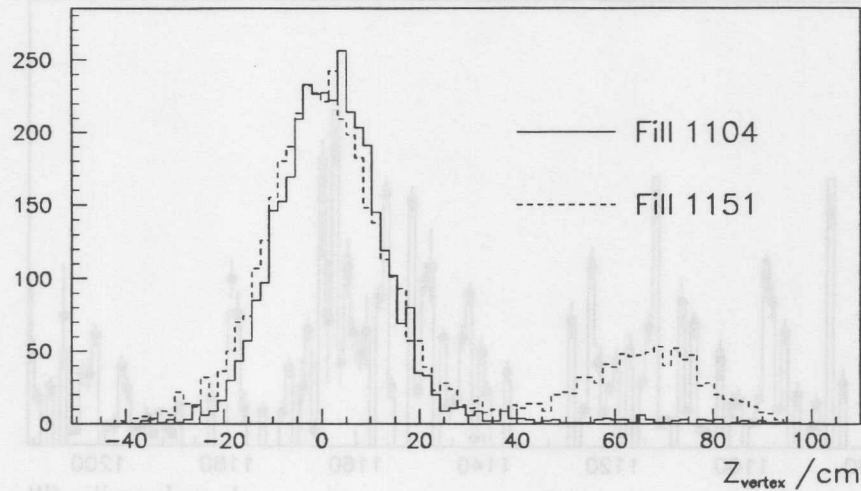


Figure 4.4:  $Z$  vertex distribution for two different fills in the 1996 running period. The main interaction region is seen to peak at  $Z \approx 0$ . The second peak around  $+70$  cm in the luminosity fill 1151 corresponds to the forward satellite bunch which was almost absent in fill 1104.

and satellite bunches. A procedure to unfold the main bunch luminosity from this sum was developed for the 1994 data [83].

One of the main components of this method was a special run performed in 1994, when the nominal position of the interaction region was shifted by  $\Delta Z = +70$  cm in order to increase the angular acceptance of the measurement towards large  $\theta_e$ . This has been called “shifted vertex” data taking, in contrast to the standard unshifted “nominal vertex” running. A similar run was performed in 1995 with the upgraded backward part of the H1 detector.

The method consists of several steps. Firstly, events from the “shifted vertex” period and from the “nominal vertex” period were selected with identical sets of selection criteria. A  $Z$  vertex cut was made around the nominal positions for the shifted vertex data and the position of the forward satellite bunch in the nominal vertex data. Then the luminosity fraction carried by the forward satellite ( $\mathcal{L}_{fwd\ sat\ frac}$ ) was calculated as:

$$\mathcal{L}_{fwd\ sat\ frac} = \frac{N_{fwd\ sat}}{N_{svz}} \frac{\mathcal{L}_{svz}}{\mathcal{L}_{nominal\ total}}. \quad (4.3)$$

Here  $N_{fwd\ sat}$  ( $N_{svz}$ ) denotes the number of events selected in the forward satellite (shifted vertex) sample and  $\mathcal{L}_{svz}$  ( $\mathcal{L}_{nominal\ total}$ ) corresponds to the luminosity of the shifted vertex (nominal vertex) data. The total fraction of the luminosity carried by all satellite bunches was obtained using the FToF (see Sec. 2.2.1) system, normalizing the luminosity of the other satellites to the forward one (see [83] for details).

A similar analysis was performed for the 1996 data. The forward satellite luminosity fraction was determined as a function of the luminosity fill number, see Fig. 4.4 for a typical  $Z$  vertex distribution for two different luminosity fills with large and small fractions of the satellite bunches. Since for some fills the statistics collected in the satellite bunch region was not big enough to determine its mean position using a Gaussian fit, this was taken as the nominal position of the main bunch plus  $67 \pm 3$  cm. The spread of the satellite bunch was assumed to be equal to the spread of the main bunch. The

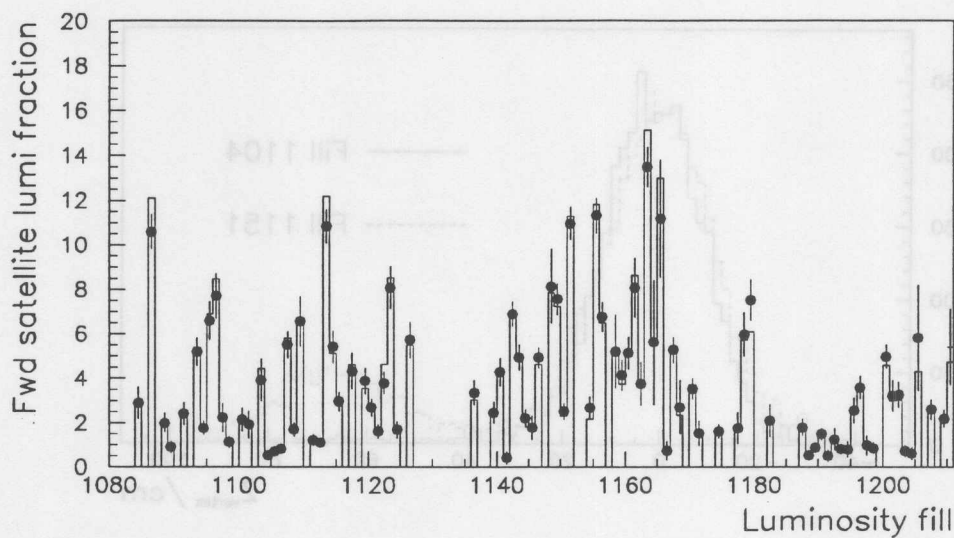


Figure 4.5: Fraction of luminosity (in %) carried by the forward satellite bunch as a function of the luminosity fill number, 1996 data analysis. The histogram presents the result obtained by normalizing to the main bunch. The dots correspond to the normalization using the 1995 shifted vertex data.

standard (see Sec. 6) selection criteria were applied to the 1995 shifted vertex and satellite bunch event samples. Additionally a more strict 3 cm cut on the error of the reconstructed  $Z$  vertex position was used.

Another approach to obtain the luminosity fraction carried by the forward satellite is to normalize it not to the shifted vertex data sample but to the main bunch of the same nominal vertex data. The advantage of this method is that systematic effects are avoided which could arise due to different data properties in the 1995 and 1996 running periods. The problem of this approach is the different detector coverage for the  $Z \approx 0$  cm and  $Z \approx 70$  cm interaction positions. Therefore, a cut  $163^\circ < \theta_e < 171^\circ$  and further additional selection criteria, listed in the previous section, were applied to unify the acceptance.

A comparison of the luminosity fractions carried by the forward satellite obtained with these two different methods is given in Fig. 4.5. In general one can see good agreement. The strict cuts used for the main bunch normalization made the statistical error in this approach bigger, thus the shifted vertex normalization was used as default.

## 4.6 Trigger Definitions and Performance

In this section the performance of the triggers used in H1 to collect DIS data for different kinematic intervals is discussed. Since these triggers were primarily based on the information from the backward calorimeter, the calorimeter triggers will be discussed first. For the high  $y$  region,  $y > 0.6$  in 1994 and  $y > 0.7$  in 1996, an additional trigger condition was applied in order to further suppress the non- $ep$  background. This required a  $ray$ , reconstructed in the central proportional chambers, pointing to the nominal vertex position. Although this ray conditions were almost identical for the 1994 and the 1996

1994	
S0	BEMC CL2, minimum bias trigger
S6	BEMC CL1 && Z vertex t0, CIP-COP ray
1996	
S0	SPACAL IET2, minimum bias
S1	SPACAL IET2 && Ray t0, CIP-COP-FPC ray
S3	SPACAL IET2 && SPACAL sum > 12GeV
S9	SPACAL IET1 && Ray t0

Table 4.3: Subtriggers based on the backward calorimeter which were used in the analysis, see text.

data, different techniques were used to estimate the efficiency of this requirement, as will be presented below.

In the 1996 data analysis a complicated trigger mixture with different trigger prescale factors was used. A description of their treatment concludes the section.

#### Calorimeter Trigger Elements

	CL1 (IET0)	CL2 (IET1)	CL3 (IET2)
1994, BEMC	4.5 GeV	7.8 GeV	15 GeV
1996, SPACAL	0.5 GeV	2 GeV	6.5 GeV

Table 4.4: Trigger thresholds available for the backward calorimeters.

The hardware basis of the H1 trigger system was presented in Chapter 2. The essential feature here is that for both the 1994 and the 1996 data taking periods a set of trigger elements was available with different energy thresholds in the backward calorimeters, see Tab. 4.4. A calorimeter trigger element for a given threshold was ‘on’ if an energy collected in a group of cells, corresponding to a cluster in the offline analysis, was bigger than the threshold value. Figure 4.6 shows the trigger efficiency of the BEMC and the Spacal trigger elements as a function of the calorimeter cluster energy.

In 1994 different parts of the BEMC were available for triggering. For the so-called “closed triangles” run period the inner triangular stacks of the calorimeter were excluded from the trigger, for the “open triangle” period they were put back thereby increasing the angular acceptance of the measurement. For the CL1 trigger element it was found that it had reduced efficiency in the left, middle part of the calorimeter for  $E'_e < 8$  GeV. Therefore this region ( $-48 < x_{BEMC} < -32$  cm,  $-48 < y_{BEMC} < 48$  cm) was excluded from the measurement.

For SPACAL a more complicated fiducial volume suitable for the analysis had to be selected, see Fig. 4.7. The innermost box ( $-17.33 < x < 9.13$  cm,  $-9.13 < y < 17.33$  cm) was hardware excluded from the triggering to reduce the trigger rate caused by one of the cells (14) which had a large counting rate of unknown origin (“hot spot”). The inner right region ( $9.13 < x < 24.39$  cm,  $-9.13 < y < 9.13$  cm) corresponds (in 1996) to a supermodule with broken HV steering leading to instability in the trigger efficiency and also in the reconstructed energy. Some other cells in the inner and outer regions were excluded due to different local problems.

It is important to stress, that all fiducial cuts were applied based on the angles  $\theta_e$  and  $\phi_e$  measured by the backward tracker, including the beam tilt corrections (Sec. 5.1). Therefore, the same acceptance regions were selected in the data and the Monte Carlo simulation.

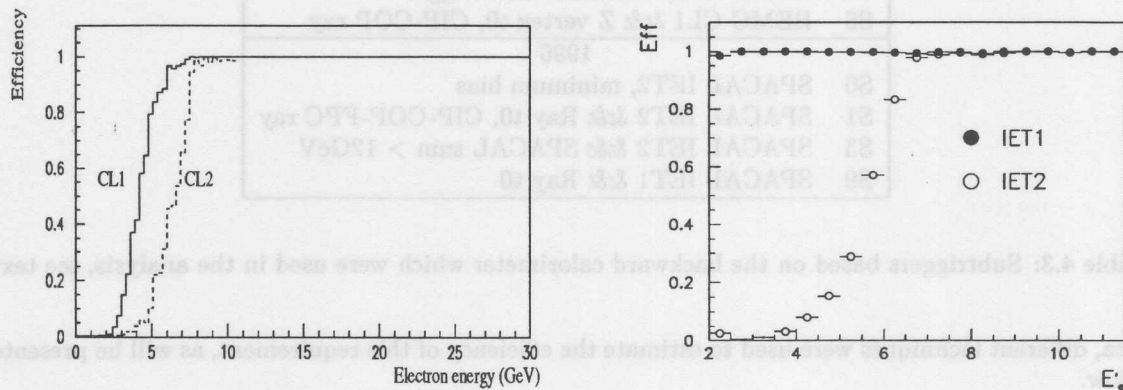


Figure 4.6: Trigger efficiency of the backward calorimeter trigger elements. The left figure displays the 1994 data BEMC trigger efficiencies (from [47]). The right figure corresponds to the 1996 data showing Spacal trigger efficiencies as determined in this thesis. Fiducial cuts are applied as described in the text.

#### Proportional Chambers Trigger Elements

A *ray* is a set of proportional chamber pads triggering due to a charged particle track originating from the interaction point. In the subtrigger S6, used for collecting the high  $y$  data in 1994, a so-called *Z vertex t0* trigger element was used with the ray reconstructed in the chambers CIP and COP only. The subtrigger S9 used in the 1996 data taking could be fired also by the *forward ray* condition which used the forward proportional chambers. The conjunction of the *Z vertex t0* and forward ray conditions was called *ray t0*. However, for the high  $y$  kinematics, the difference of the trigger efficiency between the *Z vertex* and *ray t0* conditions was small, since the hadronic final state particles are spread in the central and backward direction. Thus the *Z vertex t0* condition was most essential in both cases.

Although the central proportional chambers had high single pad efficiency, one could expect that the trigger efficiency should depend on the track multiplicity. Another natural parameter is the hadron angle. An efficiency drop can be expected when this points to outside the COP geometrical acceptance.

In Fig. 4.8-left the *Z vertex t0* trigger element efficiency is studied for events with one track reconstructed in the CJC as a function of  $R_{COP}$ , the radius at which the scattered electron track crosses the COP backward acceptance plane situated at  $Z_{COP} = -110.7$  cm. The radius  $R_{COP}$  is defined in terms of the *Z vertex* position and the angle of the scattered electron as  $R_{COP} = \tan \theta_e (Z_{COP} - Z_{vertex})$ . If  $R_{COP}$  is bigger than the chamber radius, 55 cm, then both CIP and COP are crossed by the scattered electron and the ray condition becomes fulfilled. This is seen in the figure as an efficiency rise.

The end of the COP,  $Z_{COP}$ , is approximately equal to the backward acceptance limit of the CJC,  $Z_{CJC} = -112.5$  cm. The inner chamber CJC1 starts to reconstruct positrons with a high efficiency if  $R_{CJC} = \tan \theta_e (Z_{CJC} - Z_{vertex}) > 30$  cm (see Sec. 6.6). Therefore, in the interval  $R_{COP} > 30$  cm the *one track* condition is equivalent to selecting events with only the electron track reconstructed in the CJC. For  $R_{COP} < 51$  cm the electron is scattered below the COP acceptance and can not satisfy the ray condition. Hence the *Z vertex t0* trigger element efficiency becomes small. For  $R_{COP} < 25.5$  cm the scattered electron goes below the CJC1 acceptance. Thus in this case the “one track” must be

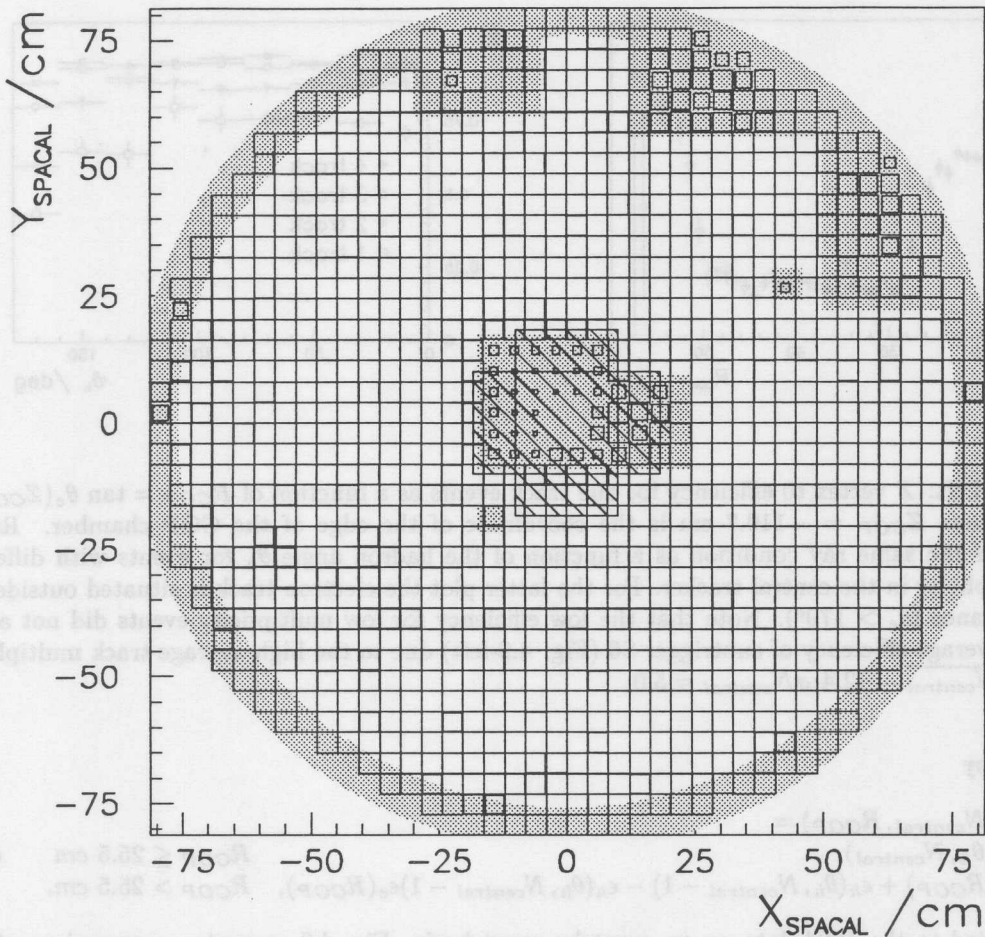


Figure 4.7: SPACAL IET1 trigger efficiency as a function of the electron impact point. The shaded area indicates the regions rejected by the fiducial cut. The radius cut  $R > 76$  cm is due to the BDC acceptance. The fiducial cut for the L2 selection is left hatched.

a track from the hadronic final state which often traverses also the COP. Therefore the efficiency averaged over the possible hadron angles is again higher, it approaches 70%.

In order to reduce the influence of the low trigger efficiency for one track events a requirement of more than one track reconstructed in the central tracking chambers,  $N_{central} > 1$ , was included in the analysis. This requirement in the  $F_L$  analysis is essentially equivalent to the selection of events with a vertex reconstructed with hadrons.

Based on efficiency calculations ( Fig. 4.8) the probability that the ray t0 condition is satisfied by the electron track was parameterized as a function of  $R_{COP}$ ,  $\epsilon_e = \epsilon_e(R_{COP})$ .

The  $Z$  vertex t0 trigger element efficiency as a function of the hadron angle  $\theta_h$  for events with different track multiplicity in the CJC is shown in Fig. 4.8-right. Events with the electron track outside the CJC acceptance were selected (i.e.  $R_{COP} < 25.5$  cm). The obtained efficiency was parameterized as  $\epsilon_h = \epsilon_h(\theta_h, N_{central})$ . The combined  $Z$  vertex t0 efficiency for the electron and hadron tracks is

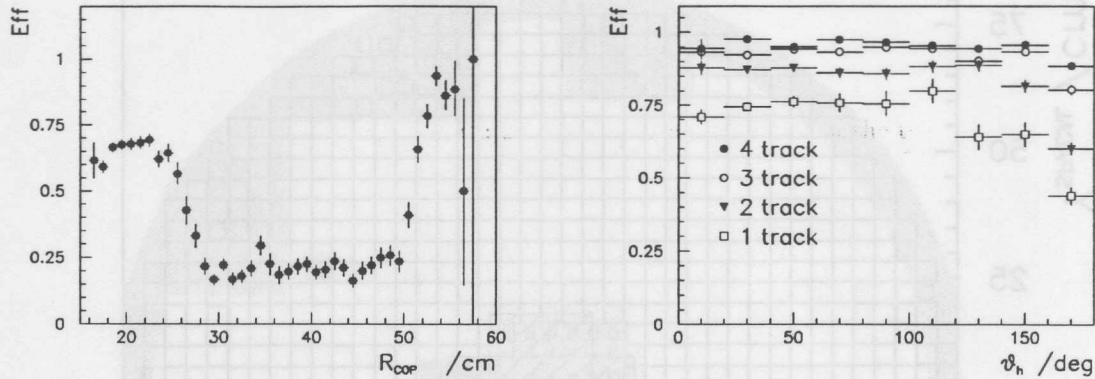


Figure 4.8: Left:  $Z$  vertex  $t_0$  efficiency for one track events as a function of  $R_{COP} = \tan \theta_e (Z_{COP} - Z_{vertex})$ , where  $Z_{COP} = -110.7$  cm is the coordinate of the edge of the COP chamber. Right: Efficiency of the same ray condition as a function of the hadron angle  $\theta_h$  for events with different track multiplicity in the central tracker. For the latter plot the electron track is situated outside the CJC acceptance ( $\theta_e > 170^\circ$ ). Note that the low efficiency for low multiplicity events did not affect much the average efficiency of subtrigger S6 (Fig. 4.9-left) due to the high average track multiplicity at high  $y$ ,  $N_{central} = 12.4$ ,  $\sigma N_{central} = 5.0$ ,

then given by

$$\epsilon_{Zvt_0}(\theta_h, N_{central}, R_{COP}) = \begin{cases} \epsilon_h(\theta_h, N_{central}), & R_{COP} \leq 25.5 \text{ cm} \\ \epsilon_e(R_{COP}) + \epsilon_h(\theta_h, N_{central} - 1) - \epsilon_h(\theta_h, N_{central} - 1)\epsilon_e(R_{COP}), & R_{COP} > 25.5 \text{ cm}. \end{cases} \quad (4.4)$$

It was applied to the 1994 data on an event by event basis. Fig. 4.9 presents a comparison of the model efficiency with a Monte Carlo simulation of the  $Z$  vertex  $t_0$  trigger element efficiency and with its direct measurement based on the S0 trigger which due to the CL2 threshold (see Tab. 4.4) was available only down to 8 GeV. One can see that the efficiency is high and that different estimations of this efficiency give result which are consistent within 1%.

The efficiency of the ray  $t_0$  condition used in the 1996 data was estimated with the help of an additional IET1 SPACAL subtrigger, S5 for  $E'_e > 2$  GeV, and the subtrigger S0 for  $E'_e > 6.5$  GeV. Instead of the MWPC ray, the subtrigger S5 required an energy deposit in the forward part of LAR calorimeter. For scattered electron energies bigger than the IET2 threshold,  $E'_e > 6.5$  GeV, the efficiency estimations based on subtriggers S5 and S0 agree. Therefore, the about 3% inefficiency observed with the subtrigger S5 for  $4 < E'_e < 6.5$  GeV was corrected in the data.

### Calculation of Trigger Weights

A rather complicated mixture of the triggers was used for the  $F_2$  1996 data analysis. Based on the inclusive subtrigger, S0, the analysis used as well subtrigger S1, with the same IET2 energy threshold but the additional ray  $t_0$  condition, subtrigger S3, with a total energy sum requirement corresponding to an energy threshold of 11 – 12 GeV and subtrigger S9, with the lower energy threshold IET1. The subtriggers S1 and S3 were in general less prescaled than S0. They usually had prescale factors 1, while S0 had prescale factors 5,2,1 in phases 2,3,4, respectively. Subtrigger S9 based on IET1 was used as a support of the trigger element IET2 for the lowest energy measurement.



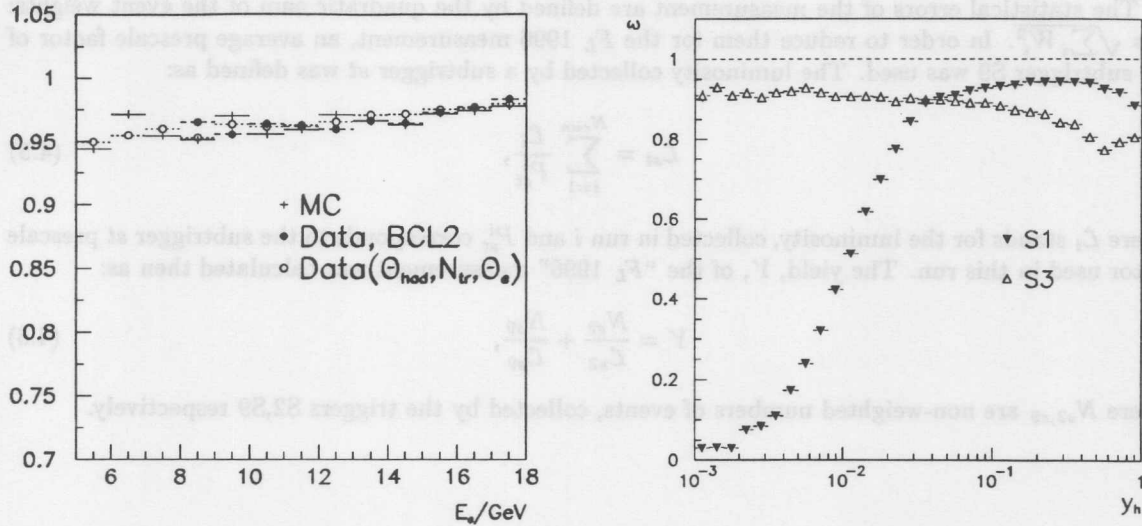


Figure 4.9: Left:  $Z$  vertex t0 condition efficiency for the 1994 data as a function of the scattered electron energy estimated from Monte Carlo simulation (crosses), using the subtrigger S0 (closed points, available for  $E_e' > 8$  GeV only) and a specially developed model (open points, see text). Right: Efficiency of the subtriggers S1 and S3 a function of  $y_h$  based on subtrigger S0 (1996 data).

The trigger efficiency of the subtriggers S1 and S3 as a function of  $y_h$  is presented in Fig. 4.9. One can see, that while the ray t0 condition leads to a low efficiency of the subtrigger S1 in the domain of small  $y$ , subtrigger S3, containing no tracker requirement, is fully efficient in this  $y$  zone. Vice versa, for high  $y$  the efficiency of the S1 subtrigger is high, while it drops for S3, due to the total energy condition.

The prescale factors for the subtriggers S0,S1,S3,S9 varied for different phases of the luminosity fills. Special prescale factors were applied in case of high background rates. In order to correctly calculate the weight for the event, the following procedure was used:

- Subtriggers S0,S1,S3,S9 were sorted according to the prescale factors applied in the run. Starting from the subtrigger with the minimal prescale, the first subtrigger with the *actual* bit (see Sec. 2.2.5) set was selected. If none of the subtriggers had this bit set, the event was rejected.
- Subtriggers with the prescale factors smaller than the selected one were checked. If any of them had a *raw* bit set, the event was rejected. Otherwise, the event was accepted with the weight equal to the prescale factor of the selected subtrigger.

The meaning of this procedure is to divide the total phase space of the DIS cross section measurement into non-overlapping regions with a unique trigger assigned to each of them. Priority is given to triggers with smaller prescale factors. In each of these regions, only the corresponding subtrigger is taken into account, others are ignored, and event weights are defined by the subtrigger prescale factor.

A different strategy was chosen for the  $F_L$  1996 analysis. The analysis was based on subtriggers S9 and S2. S2 had different tracking conditions, leading to an efficiency of about 60% only. Yet for the whole period of data taking this subtrigger was practically not prescaled. Therefore, the procedure explained above was simplified: first, runs with no prescale of S2 were selected; second, the S2 subtrigger was tested on the presence of the *actual* bit, and an event was taken if it was set; third, if it was not set the subtrigger S9 was tested. If the *actual* bit of S9 was set, the event was taken otherwise it was rejected.

The statistical errors of the measurement are defined by the quadratic sum of the event weights:  $\sigma = \sqrt{\sum_i W_i^2}$ . In order to reduce them for the  $F_L$  1996 measurement, an average prescale factor of the subtrigger S9 was used. The luminosity collected by a subtrigger  $st$  was defined as:

$$\mathcal{L}_{st} = \sum_{i=1}^{N_{run}} \frac{\mathcal{L}_i}{P_{st}^i}, \tag{4.5}$$

where  $\mathcal{L}_i$  stands for the luminosity, collected in run  $i$  and  $P_{st}^i$  corresponds to the subtrigger  $st$  prescale factor used in this run. The yield,  $Y$ , of the " $F_L$  1996" measurement was calculated then as:

$$Y = \frac{N_{s2}}{\mathcal{L}_{s2}} + \frac{N_{s9}}{\mathcal{L}_{s9}}, \tag{4.6}$$

where  $N_{s2,s9}$  are non-weighted numbers of events, collected by the triggers S2,S9 respectively.

Figure 4.9: Left: Trigger efficiency for the 1994 data as a function of the scattered electron energy estimated from Monte Carlo simulation (crosses), using the subtrigger S2 (closed points) and a specially developed model (open points, see text). Right: Efficiency of the subtriggers S1 and S3 as a function of  $p_T$  based on subtrigger S0 (1996 data).

The trigger efficiency of the subtriggers S1 and S3 as a function of  $p_T$  is presented in Fig. 4.9. One can see that while the ray to condition leads to a low efficiency of the subtrigger S1 in the domain of small  $p_T$ , subtrigger S3, containing no trigger requirement, is fully efficient in this  $p_T$  zone. Vice versa, for high  $p_T$  the efficiency of the S1 subtrigger is high, while it drops for S3, due to the total energy condition.

The prescale factors for the subtriggers S0,S1,S2,S3 varied for different phases of the luminosity fill. Special prescale factors were applied in case of high background rates. In order to correctly calculate the weight for the event, the following procedure was used:

- Subtriggers S0,S1,S2,S3 were sorted according to the prescale factors applied in the run. Starting from the subtrigger with the minimal prescale, the first subtrigger with the actual hit (see Sec. 2.2.5) set was selected. If none of the subtriggers had the hit set, the event was rejected.
- Subtriggers with the prescale factor smaller than the selected one were checked. If any of them had a run bit set, the event was rejected. Otherwise, the event was accepted with the weight equal to the prescale factor of the selected subtrigger.

The meaning of this procedure is to divide the total phase space of the DIS cross section measurement into non-overlapping regions with a unique trigger assigned to each of them. Priority is given to triggers with smaller prescale factors. In each of these regions, only the corresponding subtrigger is taken into account, others are ignored, and event weights are defined by the subtrigger prescale factor.

A different strategy was chosen for the  $F_L$  1996 analysis. The analysis was based on subtriggers S0 and S2. S2 had different tracking conditions, leading to an efficiency of about 60% only. Yet for the whole period of data taking this subtrigger was practically not prescaled. Therefore, the procedure explained above was simplified: first, runs with no prescale of S2 were selected; second, the S2 subtrigger was tested on the presence of the actual hit, and an event was taken if it was set; third, if it was not set the subtrigger S0 was tested. If the actual hit of S0 was set, the event was taken otherwise it was rejected.

## Chapter 5

# Detector Alignment and Calibration

Measurements of the deep inelastic cross section require to determine precisely the DIS event kinematics which depends on the electron scattering angle, its energy and the energy and direction of the hadronic final state particles. These topics are discussed in the present chapter.

The first subject is the measurement of the polar angle  $\theta_e$ . This is affected by the detector alignment, preshowering effects and the beam tilt with respect to the H1 coordinate system.

We proceed with the energy calibration of the backward electromagnetic calorimeters. A common concept, the double angle calibration, is introduced and differences between the BEMC and Spacal calorimeters are discussed. The results of the crack corrections for the BEMC and the cell-by-cell calibration of the Spacal are presented. A novel feature of the Spacal calorimeter compared to the BEMC is a calibration possibility using the invariant mass of two photons from the  $\pi^0 \rightarrow \gamma\gamma$  decay. The linearity of the calorimeters is discussed as well.

The chapter is concluded with a discussion of the calibration of the hadronic energy flow measurement.

### 5.1 Determination of the Electron Scattering Angle

The H1 detector coordinate system is defined by the central drift chambers. As discussed in Sec. 2.2.2, these are the central jet chambers, CJC1 and CJC2, used for the  $r-\phi$  measurement, and two chambers for the  $Z$ -coordinate determination, CIZ and COZ.

The central drift chambers are the main detectors for the event vertex reconstruction. We will use the term "central vertex" for the vertices measured in these chambers. Additionally, the position of the event vertex can be obtained with the forward tracking device and also with the central inner proportional chamber (CIP) when combined with the backward tracking chamber information [34]. We will denote these methods of the vertex reconstruction as "forward vertex" and "CIP vertex", respectively.

For the  $Q^2$  range considered in this thesis the scattered electron is detected in the backward calorimeter. Its entry point was determined with the backward tracking chambers, the BPC in 1994 and the BDC in 1996. Fig. 5.1 illustrates a DIS event reconstructed in the H1 detector.

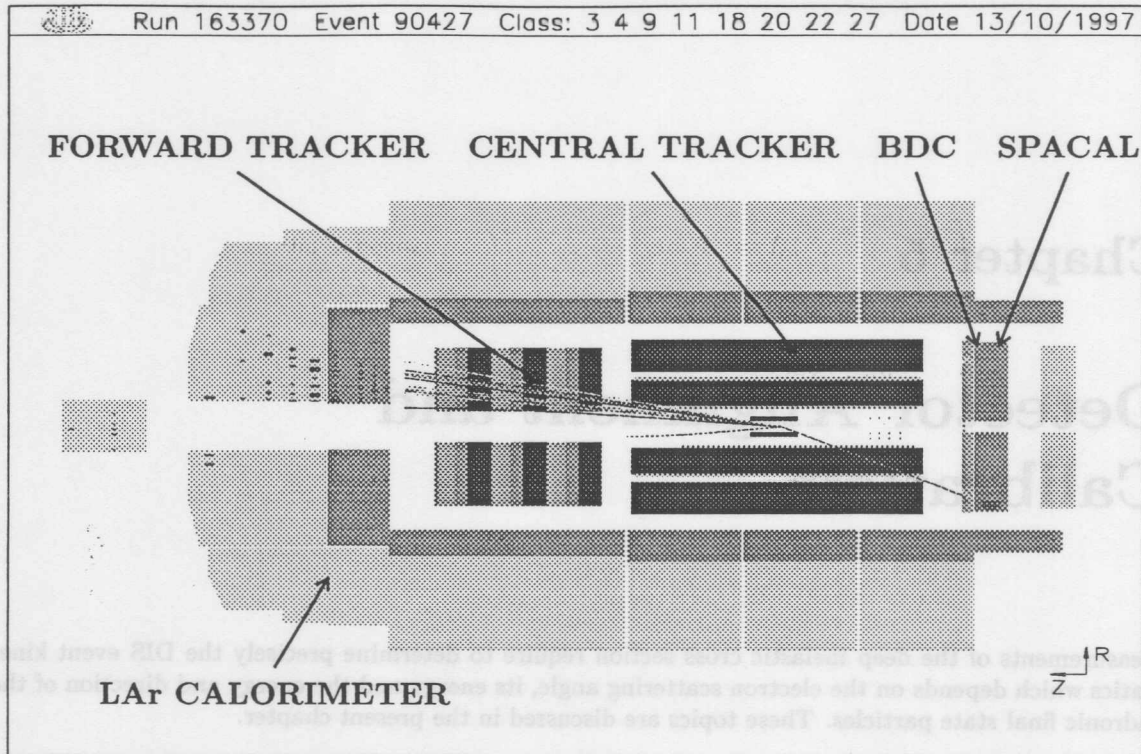


Figure 5.1: An example of a DIS event measured by the H1 detector (R-Z view). The tracks of the hadronic final state particles are detected in the forward tracker. Their energy is measured in the LAr calorimeter. The scattered electron is reconstructed as a track in the CIP, CIZ, CJC1, COZ, COP, BDC and as an energy cluster in the electromagnetic section of the Spacal calorimeter.

The trajectory of the scattered electron for  $E'_e > 4$  GeV can be approximated by a straight line<sup>1</sup>. The polar angle of the scattered electron with respect to the H1 coordinate system is then

$$\theta_e^{H1} = \arctan \frac{\sqrt{(X_{imp} - X_{vertex})^2 + (Y_{imp} - Y_{vertex})^2}}{Z_{imp} - Z_{vertex}}. \quad (5.1)$$

Here  $X_{imp}, Y_{imp}, Z_{imp}$  denote the coordinates of the impact point of the electron determined with the backward tracking chamber and  $X_{vertex}, Y_{vertex}, Z_{vertex}$  are the coordinates of the interaction point.

From the formula above it is clear that the following requirements have to be fulfilled in order to provide a correct  $\theta_e$  measurement:

1. The central tracking chambers have to be aligned internally and also with respect to the other devices used for the impact point position measurement. This should ensure independence of the vertex reconstruction of the event kinematics and from the subdetector used for its determination.
2. The backward tracking chamber must be aligned with respect to the H1 coordinate system.
3. The backward tracking chamber must provide a correct track element for the cluster reconstructed in the backward calorimeter. This is a difficult problem in case of preshowering, when the electron track is surrounded by other charged tracks from  $\gamma$  conversions. An appropriate simulation of the dead material inside the detector is essential to take these effects into account.

<sup>1</sup>this approximation is sufficient for the polar angle measurement.

4. Finally, the beam inclination has to be determined with respect to the H1 coordinate system and the  $\theta_e$  measurement should be corrected accordingly.

Subsequently these points will be elucidated step by step.

#### Central Tracker Alignment, $Z_{vertex}$ Determination

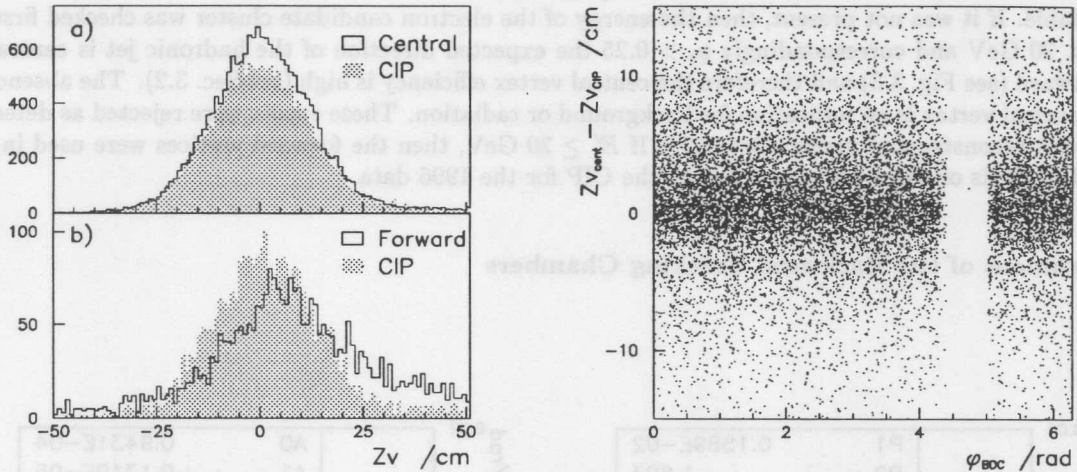


Figure 5.2: Left:  $Z_v$  distribution as reconstructed with central drift, forward drift and CIP chambers. The figures a) and b) correspond to an event selection with the electron candidate situated in the CIP geometrical acceptance. Plot a) and b) show the comparison of the central and forward vertex, respectively, with the CIP vertex. A bias of the forward vertices is visible while the quality of the CIP reconstruction is similar in both cases. Right: CIP – Central tracking chamber alignment. The difference of the Central and CIP  $Z$  vertex coordinates is plotted as a function of  $\phi_{BDC}$ . The gap at  $\phi \approx 4.7$  rad corresponds to the dead CIP sector. The plots are based on the 1996 data.

The alignment of the central drift chambers was performed independently in the  $r - \phi$  plane and in the  $Z$  direction. The  $r - \phi$  measurement was adjusted first between the chambers CJC1 and CJC2. Then the whole tracker was aligned with respect to the LAr calorimeter. The alignment procedure was based on tracks of cosmic muons and on high momentum tracks in  $ep$  interactions.

The masters of the  $Z$  coordinate measurement in the H1 detector are the  $Z$  drift chambers. They were aligned with each other using tracks of cosmic muons [84]. This procedure was cross checked with a measurement from the muon system. The  $Z$  measurement of the CJC was calibrated using the  $Z$  chamber prediction.

Different methods for the reconstruction of the event vertex are presented in Fig. 5.2. For these plots events were selected with the scattered electron traversing the inner proportional chamber CIP. In order to suppress background interactions, a cut on the electron energy  $E'_e > 20$  GeV was applied. In Fig. 5.2-a one can see a comparison of the  $Z$  distributions of the central and CIP vertices for a sample of events with the vertex reconstructed in the central detector. A good agreement is observed between both methods in the mean position of a Gaussian distribution and also in its width. An about 12% inefficiency of the CIP is found which is consistent with one non-operational  $\phi$  sector (see plot on the right and discussion below). In Fig. 5.2-b a similar comparison is given for events with the vertex reconstructed in the forward detector. The mean position as well as the width of the  $Z$  vertex

distribution obtained with the forward tracking chambers are different from those reconstructed in the central tracker, while the CIP vertices are consistent with the latter.

In the right picture the difference is plotted between the  $Z$  vertex position using central and CIP vertices as a function of  $\phi_e$  measured by the BDC. The fact that data points are concentrated along the line  $\Delta Z = 0$  proves a correct relative alignment of these detectors. A gap in the  $\phi$  distribution around  $\approx 4.7$  rad corresponds to one non-operational  $\phi$  sector in the inner CIP cylinder. Note that for the CIP validation (see Sec. 6.5), which used a CIP signal from any of the two CIP cylinders, this inefficiency was unimportant, since the corresponding  $\phi$  sector in the outer CIP cylinder was fully operational with an efficiency  $> 99\%$ .

Due to its superior reconstruction accuracy, the central vertex was selected in the analysis whenever available. If it was not present, then the energy of the electron candidate cluster was checked first. If  $E'_e < 20$  GeV and correspondingly  $y_e > 0.25$  the expected direction of the hadronic jet is central or backward (see Fig. 3.3) and therefore the central vertex efficiency is high (see Sec. 3.2). The absence of the central vertex is an indication for background or radiation. These events were rejected as detected without reconstructed vertex (Sec. 6.1). If  $E'_e \geq 20$  GeV, then the forward vertices were used in the 1994 analysis or those reconstructed by the CIP for the 1996 data.

### Alignment of the Backward Tracking Chambers

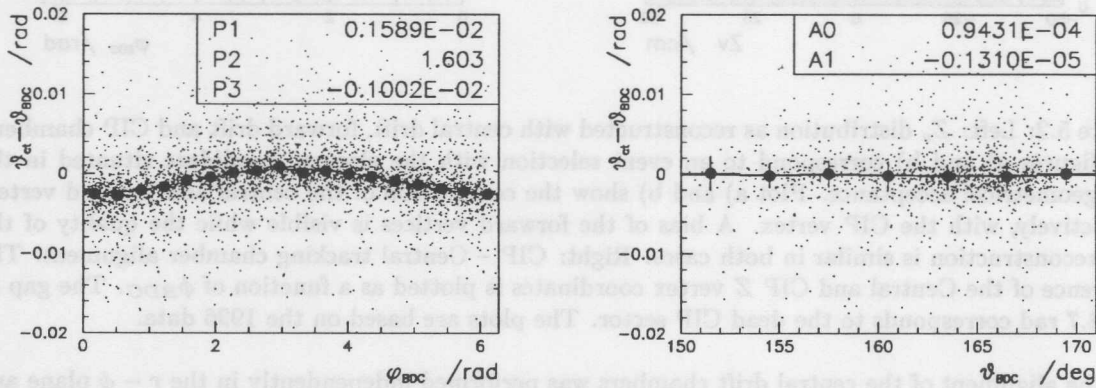


Figure 5.3: Left (right): Difference of the scattered electron polar angle measured with the central tracking chambers and with the BDC as a function of  $\phi_e$  ( $\theta_e$ ) reconstructed with the BDC. The left figure is made before alignment, the right one after, see text. Solid circles with error bars represent the mean values and their statistical error (left plot) or the spread (right plot) of Gaussian fits performed to the quantity  $\theta_{ct} - \theta_{BDC}$  in slices of  $\phi_{BDC}$  (left plot) or  $\theta_{BDC}$  (right plot). The line in the left plot corresponds to a sinusoidal fit the parameters of which are listed as P1 (amplitude), P2 (phase) and P3 (base line shift) (see Eq. 5.2). In the right plot the parameters A0 and A1 represent the offset and slope of a straight line fit.

The alignment of the backward chambers was performed using electron tracks with  $\theta_e$  measured by both the central tracker and the backward tracking chamber. The same procedure was used for the 1994 and the 1996 data, the alignment of the 1996 setup is adduced as an example.

Several selection cuts were applied in order to obtain an event sample best suitable for the alignment procedure. Suppression of the background interactions was done with a cut  $E'_e > 20$  GeV. Events with small estimated errors of  $Z_{vertex}$ ,  $\Delta Z_{vertex} < 1$  cm, and of the track angle  $\theta_e$ ,  $\Delta\theta_e^{track} < 2$  mrad,

	1994, BPC	1996, BDC
X shift	+0.14 cm	+0.23 cm
Y shift	+0.24 cm	+0.025 cm
Z shift	0.0 cm	+0.4 cm

Table 5.1: Backward chamber alignment parameters with respect to the nominal positions given in the databases of 1994 and 1996.

were selected. The latter requirement is equivalent to the demand that the CJC track was linked to at least one of the Z-chambers. Showering effects (see the next section) were reduced by requiring less than 5 tracks to be reconstructed with the BDC inside a 5 cm radius around the center of the Spacal cluster projected to the BDC plane<sup>2</sup>. For the 1994 data those events were used which had one reconstructed BPC hit with estimated uncertainties  $\Delta X, \Delta Y < 0.3$  cm, inside the 5 cm radius around the center of the BEMC cluster projected to the chamber plane.

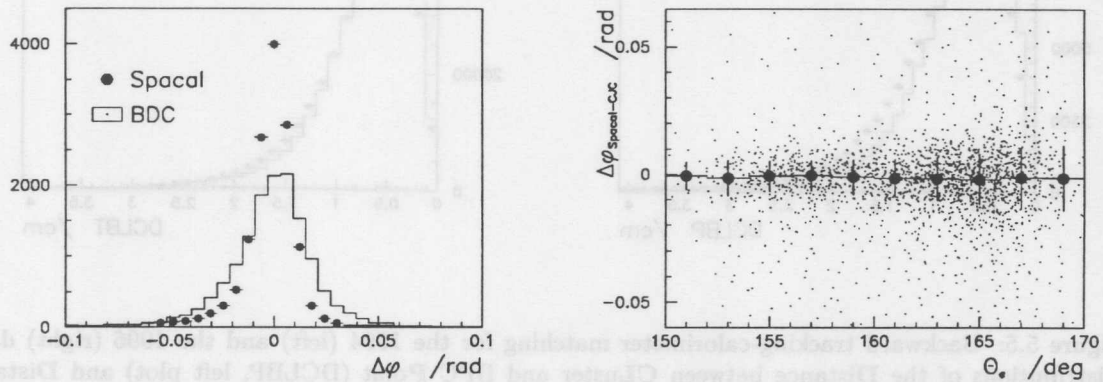


Figure 5.4: Left: Difference between the  $\phi_e$  measurements performed with CJC and Spacal (closed circles) and with the BDC (histogram). Right: Difference  $\Delta\phi = \phi_{CJC} - \phi_{Spacal}$  as a function of the polar angle of the scattered electron. Solid circles with the error bars represent mean values and spreads obtained from Gaussian fits to the  $\Delta\phi$  distributions in  $\theta_e$  slices. The better resolution of the Spacal  $\phi$  measurement relatively to that of the BDC is due to its fine  $\phi$  granularity and to the BDC sense wire geometry.

Fig. 5.3-left shows the difference between the polar angles measured with the central drift chambers and the BDC,  $\Delta\theta = \theta_{ct} - \theta_{BDC}$ , as a function of  $\phi_e$  measured with the BDC. A sinusoidal shape indicates a shift of the detector in the  $x - y$  plane. To get the parameters of this shift a fit of the following functional form was performed:

$$\Delta\theta = P1 \cdot \sin(\phi_e - P2) + P3. \quad (5.2)$$

Here P1 corresponds to an absolute value of the shift in the  $x - y$  plane, P2 to its direction, and P3 measures the  $z$  displacement of the backward tracking chamber. The resulting geometrical corrections for the 1994 and the 1996 detector setups are given in Tab. 5.1.

The difference between the  $\theta_{ct}$  and the corrected  $\theta_{BDC}$  measurements is shown as a function of  $\theta_{BDC}$  in Fig. 5.3-right. A straight line fit to the measurement shows no indication of a misalignment up

<sup>2</sup>The large BDC track multiplicity even in the non-showering case is related to  $\phi$  and up-down ambiguities in the reconstruction [48].

to 0.1 mrad precision. Two different sorts of central tracks are contained in this plot. For  $\theta_e > 158^\circ$  they are linked to the CIZ only, due to the geometrical acceptance of the COZ. Below  $158^\circ$ , both Z-chambers are normally linked. No indication of a “step” between these regions is visible in the distribution. This fact verifies the internal alignment of the Z-chambers.

Fig. 5.4 displays a distribution of the difference between the  $\phi_e$  measurements performed with the CJC and one of the backward detectors: the Spacal or the BDC. One can see, that the Spacal is more precise than the BDC in the CJC acceptance region. This is related to the fine  $\phi$  granularity of the calorimeter which improves with increasing radius.

### Backward Detector Alignment, Preshowering

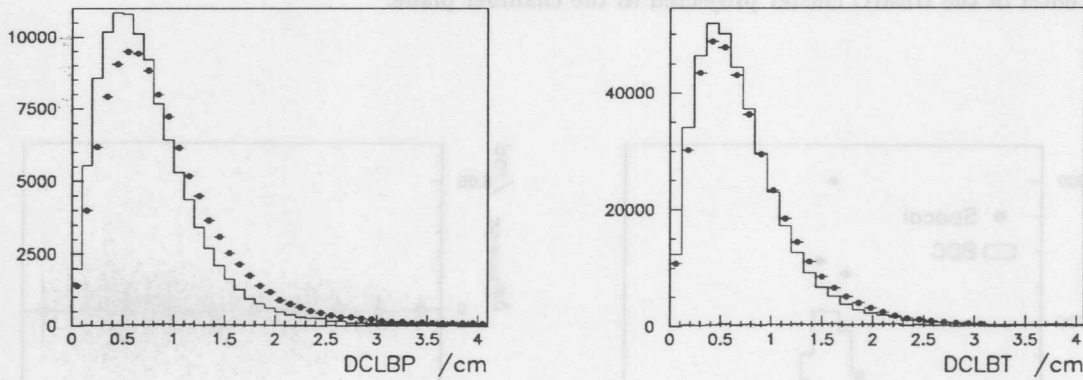


Figure 5.5: Backward tracking-calorimeter matching for the 1994 (left) and the 1996 (right) data. Distributions of the Distance between CLuster and BPC Point (DCLBP, left plot) and Distance between CLuster and BDC Track element (DCLBT, right plot) for data and Monte Carlo simulation (open histograms). Cuts of 3.5 cm and 3 cm were applied on the calorimeter-backward tracker matching for the 1994 and 1996 data, respectively.

The determination of the scattered electron’s impact point in the backward detectors started with a calculation of the calorimeter cluster center position in the  $x - y$  plane. It was defined as a weighted average over the positions of the calorimeter cells belonging to the cluster:

$$X_{cluster} = \sum_{i=1}^N x_i w_i, \quad Y_{cluster} = \sum_{i=1}^N y_i w_i. \quad (5.3)$$

Here the cell positions  $x_i, y_i$  were calculated using information from four photodiodes (“stack centroid”) in case of the BEMC while the geometrical centers were taken for Spacal. The  $w_i$  defines the weight of cell  $i$ . Three different formulae were used for its calculation, based on *linear*, *square root* and *logarithmic* energy weighting:

$$w_i^{lin} = \frac{E_i}{\sum_{j=1}^N E_j}, \quad w_i^{sqrt} = \frac{\sqrt{E_i}}{\sum_{j=1}^N \sqrt{E_j}}, \quad w_i^{log} = \frac{\max(0, w_{cut} + \ln(E_i/E_{cluster}))}{\sum_{j=1}^N \max(0, w_{cut} + \ln(E_j/E_{cluster}))}. \quad (5.4)$$

Here  $E_i$  corresponds to the energy reconstructed in a cell  $i$  and  $w_{cut}$  defines the so-called logarithmic cut-off parameter for the Spacal taken to be 4.85. The cluster center determination relied on the linear method in the BEMC data analysis and on the square root method for the Spacal data. The Spacal “cluster radius” calculation (see Sec. 6.3) used the logarithmic definition of the weights.



In case of the BEMC, the cluster center was predominantly defined by the centroid of the hottest stack. For the Spacal the square root weighting enhanced the contribution of the neighbouring cells which improved the impact point determination.

Special corrections were applied additionally to the linear formula 5.3 to adjust the cluster position determination for the BEMC according to [34]. The non-quadratic innermost Spacal cells were treated as in [87].

The calorimeter based determination of the electron impact point was completed with the  $E'_e$  dependent parameterization of the  $Z$  cluster position. The latter was obtained using Monte Carlo simulation and was checked with the  $\theta_e$  measurement provided by the central and backward tracking chambers.

After the cluster center position was determined, it was associated with the backward tracker measurement. In the analysis a similar method was used for the 1994 and the 1996 data. Firstly, using the reconstructed event vertex the cluster position was projected on the backward chamber plane. Secondly, the closest BPC point (for the 1994 data) or a BDC track element with the closest center (for the 1996 data) to this projection was selected. Distributions of the distance between the projected center of the cluster and the nearest tracker point are displayed in Fig. 5.5. The progress, visible for the 1996 data, results from the better spatial resolution of the Spacal calorimeter.

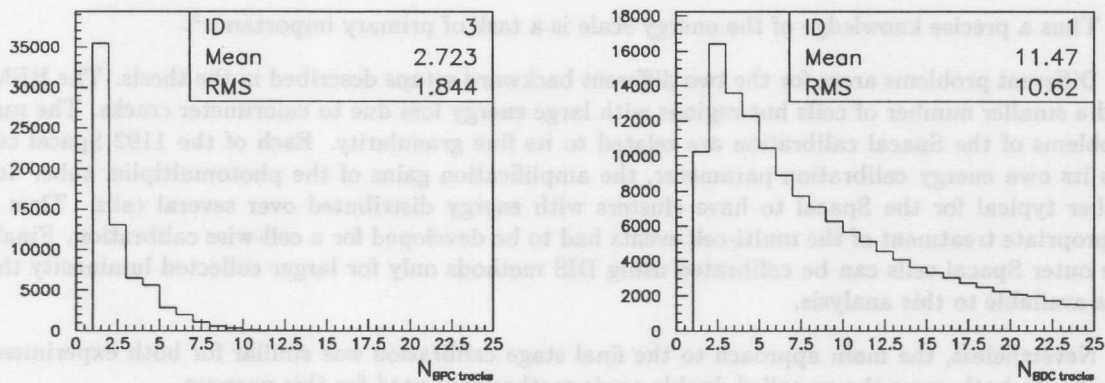


Figure 5.6: Left (right): number of BPC (BDC) track elements inside 5 cm radius around the projection of the BEMC (Spacal) cluster position to the chamber plane.

For events with only the electron track producing hits in the backward tracking chamber, the BPC (BDC) point is better defined. The situation is different in case of events with preshowering in the dead material behind the central tracking chambers. Fig. 5.6 shows a distribution of the number of points (track elements) in the BPC (BDC) situated inside 5 cm radius around the cluster center projected on the tracker plane. The worsening of the situation for the 1996 data is related to the BDC geometry; the showering problems were enhanced with up-down and  $\phi$  ambiguities in the reconstruction [48].

It is clear that a correct description of the dead material in the Monte Carlo simulation is important for the  $\theta_e$  measurement. This was studied with the 1994 data [34] and a similar analysis was performed for the 1995 data [76]. A problem was detected at 20 – 25 cm radius on the tracker plane, where a strong variation of the radius distribution in the data was observed which is still not understood and thus not reproduced in the Monte Carlo simulation. A bad description of the showering effects in this region was found. In this thesis corrections were applied as proposed in both analyses quoted.

### Beam Direction Determination

The previous sections described the procedure of the  $\theta_e^{H1}$  determination with respect to the H1 coordinate system, with the  $Z$  direction defined as the axis of the CJC. For the final calculation of  $\theta_e$ , however, a possible inclination of the beam axis with respect to the H1 coordinate system must be taken into account.

Straight line fits to the dependences  $X_v = f_x(Z_v)$  and  $Y_v = f_y(Z_v)$  were used to determine the beam shift and tilt with respect to the H1 coordinate system. Here  $X_v, Y_v$  and  $Z_v$  are event dependent  $X, Y$  and  $Z$  vertex positions. The fits were performed for each run in the standard procedure of the track reconstruction in the CJC [45]. Typical values of the  $x, y$  beam shift were about 2 – 4 mm and the beam tilt was about 1 – 2 mrad. The beam tilt was corrected on a run by run basis for the 1994 data and on average for the 1996 data since for some short run ranges big variations of the  $z - y$  tilt were observed (up to 2 mrad), which were not confirmed with the photon detector of the luminosity system.

## 5.2 Calibration of Backward Electromagnetic Calorimeters

The main systematic error of the DIS cross section measurement at low and intermediate  $y < 0.3$  comes from the electromagnetic energy scale uncertainty. The reason is the resolution degradation due to the  $1/y$  term in the electron method, see Sec. 3.1.

Thus a precise knowledge of the energy scale is a task of primary importance<sup>3</sup>.

Different problems arose for the two different backward setups described in the thesis. The BEMC had a smaller number of cells but regions with large energy loss due to calorimeter cracks. The main problems of the Spacal calibration are related to its fine granularity. Each of the 1192 Spacal cells has its own energy calibration parameter, the amplification gains of the photomultiplier tube. It is rather typical for the Spacal to have clusters with energy distributed over several cells. Thus an appropriate treatment of the multi-cell events had to be developed for a cell-wise calibration. Finally, the outer Spacal cells can be calibrated using DIS methods only for larger collected luminosity than was available to this analysis.

Nevertheless, the main approach to the final stage calibration was similar for both experimental setups. In both cases the so-called double angle method was used for this purpose.

A new feature of the Spacal calorimeter is a good electromagnetic resolution down to energies of about 0.5 GeV. Together with a better position reconstruction, owing to its finer granularity, it allows to use for calibration the invariant mass of two calorimeter clusters originating from the  $\pi^0 \rightarrow 2\gamma$  decay. An advantage of this method is a much higher cross section of the  $\pi^0$  production compared to the DIS in the outer calorimeter region. Another way to check the energy calibration is to use tracks reconstructed in the central tracker, which resolution improves at low energies. Application of all calibration methods permits an investigation of the Spacal linearity.

### Double Angle Method

The kinematics reconstruction at the  $ep$  collider experiments is over constrained. Besides the angle and energy of the scattered electron one can use those reconstructed from the particles of the hadronic

<sup>3</sup>Since the Monte Carlo simulation is used to determine the acceptance of the DIS measurement, most important is not the absolute value of the energy scale but rather the description of the scale variations by the Monte Carlo simulation.

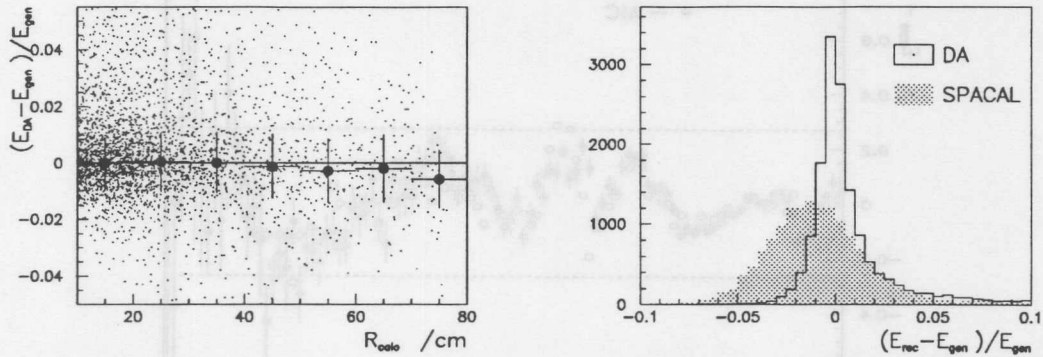


Figure 5.7: Left: Reconstruction of the generated energy  $E_{gen}$  using the double angle method as a function of the radius of the electron impact point. The solid points represent the mean values and the error bars show the spreads of Gaussian fits of the quantity  $(E_{DA} - E_{gen})/E_{gen}$  in slices of  $R_{calo} = \sqrt{X_{Spacal}^2 + Y_{Spacal}^2}$ . Right: Comparison of the DA and the electromagnetic energy reconstructions for the “DA selection” (see text). One can see a 1% bias of the reconstructed Spacal energy which is present in the Monte Carlo simulation before applying of the DA calibration. Both plots belong to the 1996 detector setup.

final state (see Sec. 3.1). A possible combination of the kinematic variables is  $\theta_e$  and  $\theta_h$  leading to the “double angle” (DA) method [57]:

$$y_{DA} = \frac{\tan \frac{\theta_h}{2}}{\tan \frac{\theta_h}{2} + \tan \frac{\theta_e}{2}} \quad E_{DA} = \frac{E_e(1 - y_{DA})}{\sin^2 \frac{\theta_e}{2}}. \quad (5.5)$$

The advantage of the DA method is its independence (to first order) of the energy scale. Essentially, the  $y_{DA}$  resolution at  $y < 0.1$  is similar to the one of  $y_h$ .

For the energy calibrations using the double angle method the following selection was performed (we denote it as “DA selection”) Firstly, a cut  $\theta_h < 80^\circ$  was applied which selected events from the low  $y < 0.15$ , kinematic peak region (see Eq. 5.5). Secondly, a cut on the difference of  $|y_h - y_{DA}|/(y_h + y_{DA}) < 0.2$  was used which rejected events with wrongly reconstructed  $y$ , in most cases due to noise in the LAr calorimeter.

Studies of the DA method reconstruction using the 1996 Monte Carlo simulation are shown in Fig. 5.7. One can see, that the generated electron energy is uniformly reconstructed with this method over the whole backward calorimeter with an about 1% resolution. A small bias of the energy scale for the outer region never exceeds 0.5%. A comparison of the energy measurement with the Spacal and using the DA method shows an approximately three times better resolution of the latter.

### BEMC Calibration

The calibration of the BEMC energy scale was done in two steps. Firstly, corrections of the energy loss in the cracks between the calorimeter cells were performed using an estimation from the Monte Carlo simulation [47]. The corrections distinguished the final reconstructed energy (BCFR) from the uncorrected one (BCLR).

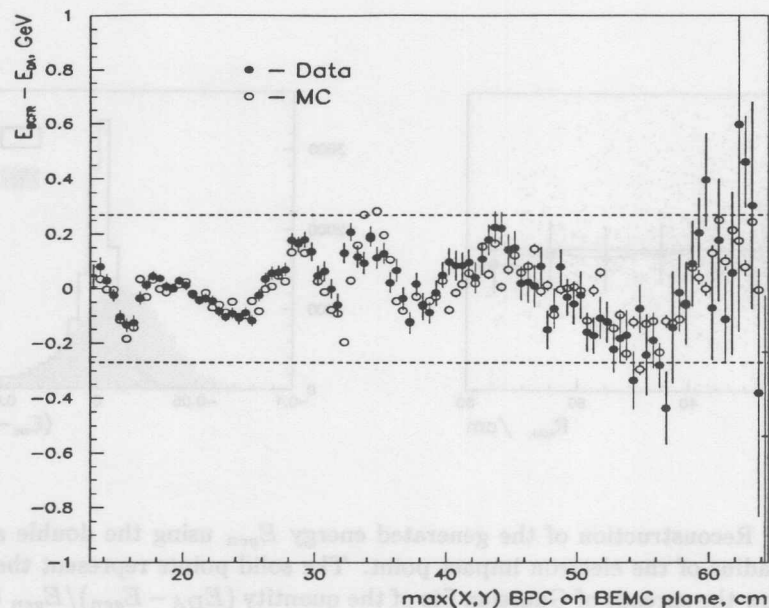


Figure 5.8: Comparison of the BEMC energy calibration for data and Monte Carlo simulation using the double angle method. The difference  $E_{BEMC} - E_{DA}$  is shown as a function of the maximum of the  $|X|$  and  $|Y|$  coordinates of the electron impact point. The dashed lines indicate deviations of  $\pm 1\%$ .

As the second step the DA method was used to calibrate the energy scale depending on the impact point of the scattered electron. In order to study the influence of the cracks the energy scale was expressed as a function of the so-called “quadratic radius” of the BEMC:  $R_{box} = \max(|X|, |Y|)$ . The  $X, Y$  coordinates of the electron impact point were determined using the BPC and then projected to the calorimeter plane.

The results of this double angle calibration showed that:

- The BCFR energy corrections were in general well consistent for data and Monte Carlo simulation.
- For the inner triangles (see Sec. 2.2.4) and for the crack between inner triangles and the first “ring” of quadratic stacks the BCFR energy scale was poorly reproduced. For this region the double angle energy corrections were applied directly to the BCLR value.
- The BCFR energy scale of the first BEMC “ring” ( $16 < R_{box} < 32$  cm) was found to be the same in the data and the simulation, the second “ring” ( $32 < R_{box} < 48$  cm) showed  $-0.7\%$ , and the last one ( $48 < R_{box} < 64$  cm)  $-2.0\%$  difference between the data and the simulation. Half of this difference was applied “ring” dependent to the energy reconstruction in the data and half to the energy reconstruction in the simulation.

Fig. 5.8 shows the difference of the resulting BEMC and the double angle energies as a function of  $R_{box}$ . The fluctuations, including the crack regions at  $R_{box} \approx 16, 32$  cm, are well described by the Monte Carlo simulation. The difference between the BEMC and the double angle energy scales practically never exceeds 1%, the agreement of the data and Monte Carlo scales being even better.

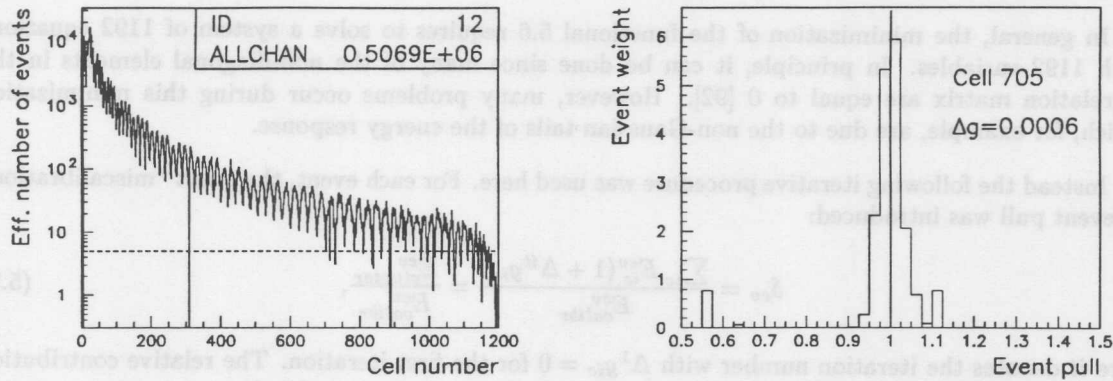


Figure 5.9: Left: Effective number of events per Spacal cell for the “DA selection”. In the Spacal cell numbering scheme “0” corresponds to the innermost and “1192” to the outermost region. The oscillating structure results from the spiral numbering scheme of the Spacal cells. The dashed line indicates the five event limit of the cell dependent calibration (see text). Right: Typical pull distribution for a cell in the outer Spacal region,  $R_{cell} = 69.5$  cm, obtained after 3 iterations of the method described in the text. The line in the middle of the plot indicates the mean pull value obtained using a robust estimator [93].

### Cell Dependent Spacal Calibration

The Spacal calorimeter has a much smaller cell size than BEMC. The energy measurement in each cell of the calorimeter is performed using photomultiplier tubes individually for each cell. Therefore, altogether 1192 amplification gains have to be known to define the Spacal energy scale.

The situation becomes more complicated as the amplification gains of the photomultiplier tubes can vary with time, changes at the percent level were detected during a few hours of operation. A special LED calibration system [88] was developed in order to detect these variations. The LED information is written to the database and used for the Spacal energy reconstruction on level 5 of the H1 data reconstruction chain. The offline analysis showed that the resulting Spacal energy scale is stable in time up to about 1% precision.

Several methods were proposed for the Spacal energy scale determination. These used cosmic muon events [89], beam halo muon events [90] and the kinematic peak shape [91, 92] calibrations. This section introduces the double angle method as used for the Spacal calibration, subsequently the techniques are described suitable for calibrating the lower energy measurement.

The offline Spacal cell-dependent calibration for the 1996 data was performed using the kinematic peak for  $R_{Spacal} < 50$  cm and cosmic muons for the outer region. Time-dependent factors were applied. We will denote the resulting reconstructed Spacal energy as “default energy”. The double angle method was applied additionally to this calibration.

The Spacal calibration task can be expressed as a minimization of the functional of the following type:

$$S(\Delta g_{ic}) = \sum_{ev} \left( E_{calibr}^{ev} - \sum_{ic} E_{ic}^{ev} (1 + \Delta g_{ic}) \right)^2 \rightarrow \min. \quad (5.6)$$

Here the first summation is performed over all selected events while the second one extends over all cells included in the electron’s cluster.  $E_{calibr}^{ev}$  defines the energy scale of the event to which the

calibration is performed, in our case it is equal to  $E_{DA}^{ev}$ .  $E_{ic}^{ev}$  corresponds to the energy measured by the cell  $ic$  for the event  $ev$ . This energy includes all corrections done before the final calibration.  $\Delta g_{ic}$  is the correction to the amplification gain factor of the cell  $ic$  to be determined.

In general, the minimization of the functional 5.6 requires to solve a system of 1192 equations with 1192 variables. In principle, it can be done since many of the non-diagonal elements in the correlation matrix are equal to 0 [92]. However, many problems occur during this minimization which, for example, are due to the non-Gaussian tails of the energy response.

Instead the following iterative procedure was used here. For each event, the event "miscalibration" or event pull was introduced:

$$\delta_{ev} = \frac{\sum_{ic} E_{ic}^{ev} (1 + \Delta^{it} g_{ic})}{E_{calibr}^{ev}} = \frac{E_{cluster}^{ev}}{E_{calibr}^{ev}}, \quad (5.7)$$

here  $it$  denotes the iteration number with  $\Delta^1 g_{ic} = 0$  for the first iteration. The relative contribution of the cell  $j$  to the event pull is given by the fraction of energy deposited in it:

$$w_j^{ev} = \frac{E_j^{ev} (1 + \Delta^{it} g_j)}{E_{cluster}^{ev}}. \quad (5.8)$$

By construction the sum of the weights  $w_j^{ev}$  for any event is equal to 1. Finally, the weighted pull average over all events with removing of outliers [93] was calculated and the correction of all cell amplification gain factors was obtained:

$$\Delta^{it+1} g_j = \Delta^{it} g_j - (\overline{\delta_{ev} w_j^{ev}} - 1). \quad (5.9)$$

The iterative procedure was continued until  $\max_j (\overline{\delta_{ev} w_j^{ev}}) < 0.002$ . Normally, 3 – 4 iterations were needed.

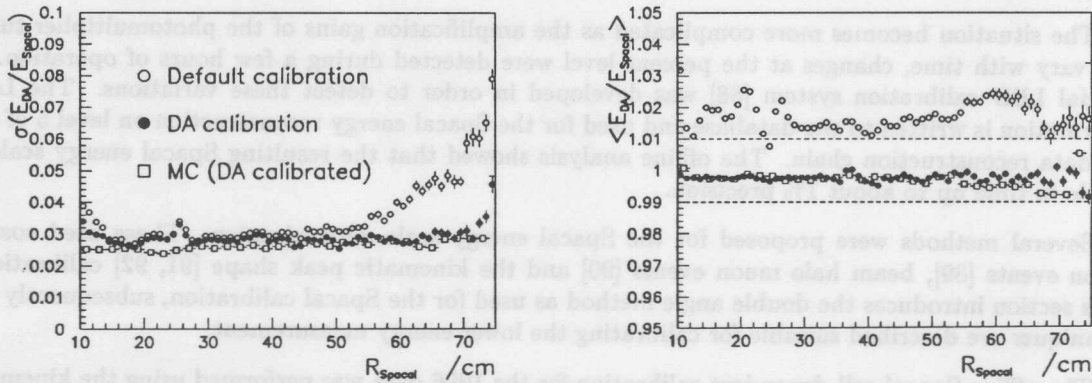


Figure 5.10: Results of the DA Spacal calibration (filled circles) compared to the default calibration (open circles) and calibrated Monte Carlo simulation (open squares). The left plot shows the sigma and the right the mean value of Gaussian fits performed to  $E_{DA}/E_{Spacal}$  distributions in slices of

$$R_{Spacal} = \sqrt{X_{Spacal}^2 + Y_{Spacal}^2}.$$

The sum  $N_{ic}^{eff} = \sum_{ev} w_{ic}^{ev}$  represents the effective number of calibration events available for the cell  $ic$ . The distributions of  $N_{ic}^{eff}$  for all Spacal cells is given in Fig. 5.9-left for the whole 1996 data

sample which corresponds to a luminosity of  $7 \text{ pb}^{-1}$ . One can see that for the outer Spacal region the statistics is low. To increase the statistical significance of the calibration, cells with less than five effective events were combined and calibrated together with a common amplification gain correction. A typical distribution of the pulls weighted with  $w_{ic}^{ev}$  is shown in Fig. 5.9-right for a cell in the outer Spacal region.

Apart from the cell dependent calibration several additional corrections were applied to the Spacal energy measurement. Firstly, the energy dependence on the impact point position inside the hottest cell of the cluster was cured. Up to 1% difference between the energy measurement for the impact point position in the center and at the corner of a cluster were found in the data. Secondly, the cracks between the supermodules (see Fig. 2.5) were corrected for as a function of  $R_{box} = \max(|X_{spacal}|, |Y_{spacal}|)$ . Up to 2% variations of the energy scale were observed, which were only partially described by the Monte Carlo simulation. Thirdly, a one percent change of the energy scale was detected for a ring of  $R_{circle} = \sqrt{X_{spacal}^2 + Y_{spacal}^2} \approx 25 \text{ cm}$ . This effect was absent in the Monte Carlo simulation, it may be related to dead material in front of the backward detectors, see also Sec 5.1.

In the Monte Carlo simulation only corrections for the impact point position inside the hottest cell and  $R_{box}$  dependent crack corrections were applied.

Fig. 5.10 shows the results of the Spacal double angle calibration compared to the default one and the calibrated Monte Carlo simulation. One can see an improvement of the Spacal resolution in the outer region, where the default calibration was done using cosmic tracks. The Spacal energy scale is corrected over the whole calorimeter surface. For the default calibration the fluctuation of the energy scale around  $R_{circle} = 25 \text{ cm}$  is clearly visible.

#### $\pi^0$ Calibration. Tracker Calibration. Spacal Linearity.

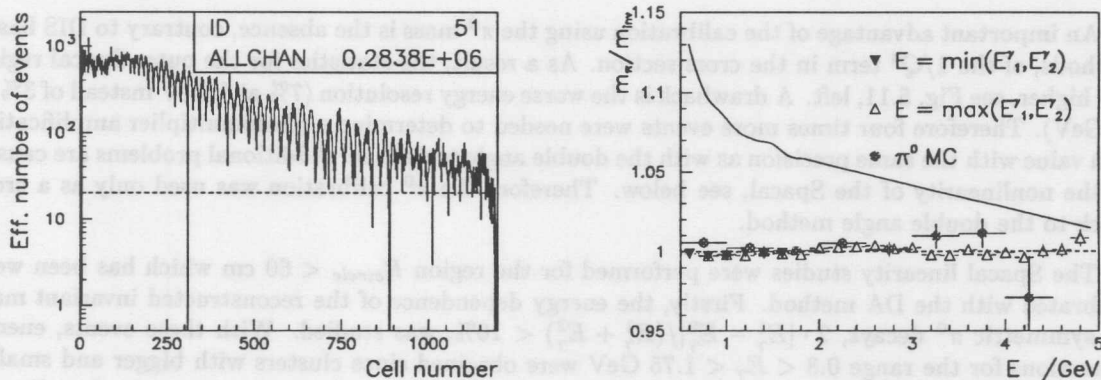


Figure 5.11: Left: Effective number of events as a function of the Spacal cell number for the  $\pi^0$  calibration selection. Right: Energy dependence of the ratio of the  $\pi^0$  mass  $m_{\pi^0}$  and the invariant mass of two clusters  $m_{inv}$ . Open (Closed) triangles present the experimental result as a function of maximal (minimal) energy of two clusters. Circles display the obtained dependence for a dedicated Monte Carlo simulation for both clusters. The line corresponds to the corrections  $f_E$ , applied to the default energy,  $E' = E f_E$ . Centers (error bars) of the symbols correspond to mean values (errors of the mean values) obtained from a Gaussian fit to the peak of the  $m_{\pi^0}/m_{inv}$  distribution.

Salient features of the Spacal calorimeter are a good resolution down to very low energies and a fine granularity (see Tab. 2.4). These allowed to resolve the  $\pi^0 \rightarrow 2\gamma$  decay. The invariant mass of the two  $\gamma$  quanta system could be used for a cell-by-cell calibration, with a method similar to the one described in the previous section. The main functional in this case has a form:

$$S = \sum_{ev} (m_{\pi^0} - m_{inv})^2 \rightarrow \min \quad m_{inv} = \sqrt{2E_1^{ev} E_2^{ev} (1 - \cos \theta_{\gamma\gamma})}. \quad (5.10)$$

Here  $m_{\pi^0} = 0.135$  GeV denotes the  $\pi^0$  mass,  $E_{1(2)}^{ev}$  the energy deposit in the first (second) cluster and  $\theta_{\gamma\gamma}$  the opening angle defined by the vertex and the two Spacal clusters. The difference between typical energies of the DA selection ( $E_e' \approx E_e = 27.55$  GeV) and the photons from the  $\pi^0$  decay ( $E_\gamma \in 0.5 - 5$  GeV) allows to check the Spacal linearity.

In order to obtain an unbiased invariant mass reconstruction and to suppress the background from random coincidences, the following selection criteria were applied:

- to ensure a precise  $\theta_{\gamma\gamma}$  determination only those events were selected which had a central vertex reconstructed inside 30 cm around the nominal position with an estimated error of less than 2 cm;
- to remove background from charged hadrons a cut  $RCL_{log} < 4$  cm and also an *anti* CIP validation, i.e. the requirement to have no triggered CIP pad along the trajectory between the vertex and the Spacal cluster, were used;
- to avoid a possible bias from a partial overlap of the clusters, a cut  $\theta_{inv} = \arccos(1 - m_{\pi^0}^2 / (2E_\gamma^1 E_\gamma^2)) > 70$  mrad was applied which ensured at least 11 cm separation between the clusters;
- the Spacal resolution degrades and the combinatorial background rises at  $E' < 1$  GeV. Still a lot of statistics was collected in this range. As a compromise, cuts  $E_\gamma > 0.5$  GeV and  $\theta_{inv} < 170$  mrad were applied, the latter forced at least one cluster to have an energy bigger than 0.8 GeV;
- no BDC based selection was made, the impact points of the photons were measured with the Spacal.

An important advantage of the calibration using the  $\pi^0$  mass is the absence, contrary to DIS based methods, of the  $1/Q^4$  term in the cross section. As a result, the statistics for the outer Spacal region was higher, see Fig. 5.11, left. A drawback is the worse energy resolution (7% at 1 GeV instead of 3% at 30 GeV). Therefore four times more events were needed to determine a photomultiplier amplification gain value with the same precision as with the double angle technique. Additional problems are caused by the nonlinearity of the Spacal, see below. Therefore the  $\pi^0$  calibration was used only as a cross check to the double angle method.

The Spacal linearity studies were performed for the region  $R_{circle} < 60$  cm which has been well-calibrated with the DA method. Firstly, the energy dependence of the reconstructed invariant mass for symmetric  $\pi^0$  decays,  $2 \cdot |E_\gamma^1 - E_\gamma^2| / (E_\gamma^1 + E_\gamma^2) < 10\%$ , was studied. With these events, energy corrections for the range  $0.8 < E_\gamma < 1.75$  GeV were obtained since clusters with bigger and smaller energies were rejected by the condition  $70 < \theta_{inv} < 170$  mrad. The energy dependence in the adjacent intervals  $0.5 - 0.8$  and  $1.75 - 5$  GeV was measured using asymmetric decays, which had bigger opening angle, with the energy of one of the clusters residing inside the calibrated range.

A special Monte Carlo simulation was performed to study the  $\pi^0$  reconstruction. Single  $\pi^0$  events with uniform energy and  $\theta$  spectra were simulated and reconstructed in the H1 detector. Identical selection cuts were used for data and Monte Carlo events (apart from the  $z_{vertex}$  criteria); the same correction function was used to recalculate the energies of the Spacal clusters.

Fig. 5.11-right shows the obtained energy correction function  $f_E = E'/E$ . For  $E > 1.7$  GeV it was approximated by a straight line. Fig. 5.11 displays also the energy dependence of the ratio  $m_{\pi^0}/m_{inv}$



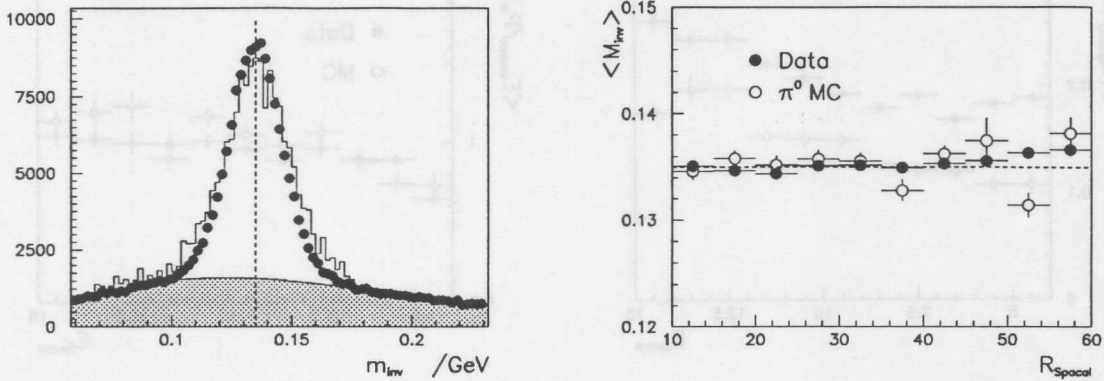


Figure 5.12: Left: distribution of the invariant mass of a pair of Spacal clusters passing the  $\pi^0$  candidate selection. Closed circles correspond to the data distribution. The combinatorial background was estimated using a polynomial fit of the third power, the result is shown as a shaded histogram. The open histogram represents the sum of this background and a special  $\pi^0$  Monte Carlo simulation. Right: the invariant mass as a function of the radius  $R_{spacal} = \sqrt{x_{min}^2 + y_{min}^2}$  of the cluster with minimal energy. Closed (open) circles represent the mean values of the Gaussian fits to the data (Monte Carlo simulation) distributions performed in slices of  $R_{spacal}$ .

derived after applying the corrections. The experimental result is given as a function of the maximal and also the minimal energy of the two clusters while the simulated result represents the combined distribution. A good agreement between data and Monte Carlo simulation is seen.

Fig. 5.12-left compares the experimental and the simulated invariant mass distributions. A clear peak around the  $\pi^0$  mass is seen. The combinatorial background was estimated using a polynomial fit to the data distribution; it was added to the Monte Carlo distribution. The result of the Gaussian fit to the peak region gave  $m_{inv} = 0.1350 \pm 0.0001$  for data and  $m_{inv} = 0.1356 \pm 0.0003$  for Monte Carlo simulation (uncertainties represent statistical errors only).

The comparison between data and Monte Carlo simulation of the  $m_{inv}$  peak position as a function of the entry radius of the photon with lower energy is shown in Fig. 5.12-right. Good agreement between experimental and simulated results is observed. The resulting  $m_{inv}$  is almost independent of the radius which proves the uniformity of the double angle calibration.

The electrons detected in the outer Spacal region ( $R_{circle} > 40$  cm) can be also measured in the inner jet chamber CJC1, see Sec. 2.2.2. Therefore, the energy scale in this range can be checked using the momentum measurement of linked tracks. Fig. 5.13 shows a comparison between data and Monte Carlo simulation of the ratio  $E_{spacal}/P_{track}$  as a function of  $E_{Spacal}$  for those electron candidate clusters, which are linked to a track with positive charge.

Since the electromagnetic resolution of the Spacal for  $E > 1$  GeV is better than 7%, the spread of the distribution  $E_{spacal}/P_{track}$  (Fig. 5.13-left) is defined by the CJC1 momentum measurement. The experimental distribution is wider than the simulated one. The resolution improves towards low energies, but this trend is stopped in the data at  $E \sim 6$  GeV because of the admixture of background from hadronic particles, which spoils the Spacal energy measurement. The energy dependence of the mean value of the ratio  $E_{spacal}/P_{track}$  (right plot) is very similar for data and Monte Carlo simulation. The value of the ratio is close to one proving the correctness of the energy scale determined with the DA calibration. A drop of the ratio at 4–5 GeV is consistent with the energy correction function  $f_E$  obtained from the  $\pi^0$  calibration (see Fig. 5.11-right).

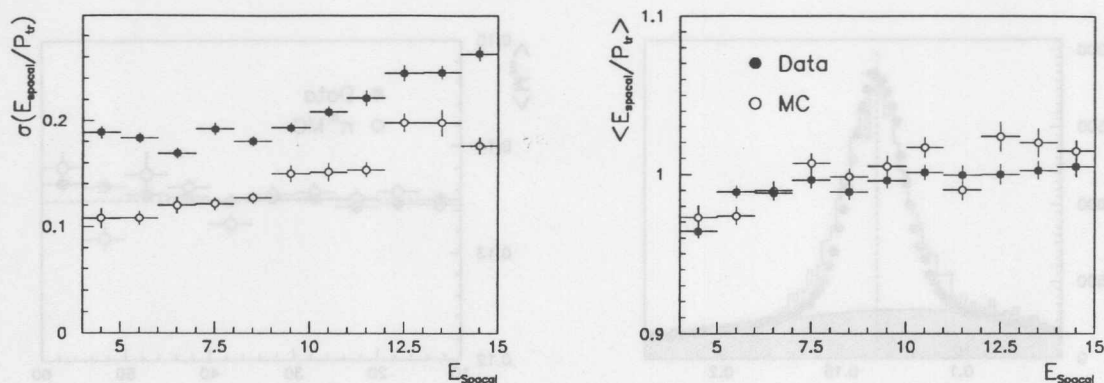


Figure 5.13: Left (Right): spread (mean position) of Gaussian fits performed to the  $E_{\text{Spacal}}/P_{\text{track}}$  distributions in  $E_{\text{Spacal}}$  slices. Closed circles correspond to data and open circles to the Monte Carlo simulation. Standard selection criteria of the  $F_L$  1996 analysis (see Tab. 6.1) have been applied.

### Results of the Spacal Calibration

The Spacal calibration can be summarized as follows:

- The Spacal energy response was calibrated using the double angle method. The cell and impact point position dependent corrections were applied to the energy reconstruction in the data and in the Monte Carlo simulation. As the result the Spacal energy scale was equalized over the calorimeter surface. Data and Monte Carlo simulation agreed to better than 1%. However, the outermost Spacal cells ( $R > 70$  cm) were calibrated only on average due to statistical problems.
- The energy dependent energy correction function  $f_E$  was obtained for  $0.5 < E < 5$  GeV using experimentally measured  $\pi^0$  decays. After applying these corrections identically to the data and to the simulation the nominal  $\pi^0$  mass was reconstructed. The experimental result was equal within 0.5% to the simulated one proving the *consistency of the energy scales* between the data and the Monte Carlo simulation. The invariant mass of the two-photon system was found with about 1% precision to be independent of the energy and of the position of the photons confirming, therefore, the *similarity of the correction function  $f_E$*  between the data and the simulation and the *uniformity of the energy calibration* in both the data and the simulation.
- The energy measurement in the outer Spacal was compared with the momentum reconstruction in the CJC. For  $E'_e > 7$  GeV the energy scales were found to be similar between these two detectors and between the data and the simulation. For  $E'_e < 7$  GeV a decrease of the ratio  $E_{\text{Spacal}}/P_{\text{track}}$  was observed which was consistent with the function  $f_E$ .

## 5.3 Hadronic Energy Scale

The  $y_h$  variable is measured in H1 as a sum of three components:

$$y_h = \frac{\Sigma}{2E_e} = \frac{1}{2E_e} (\Sigma_{LAr} + \Sigma_{\text{Backward}} + \Sigma_{\text{track}}), \quad (5.11)$$

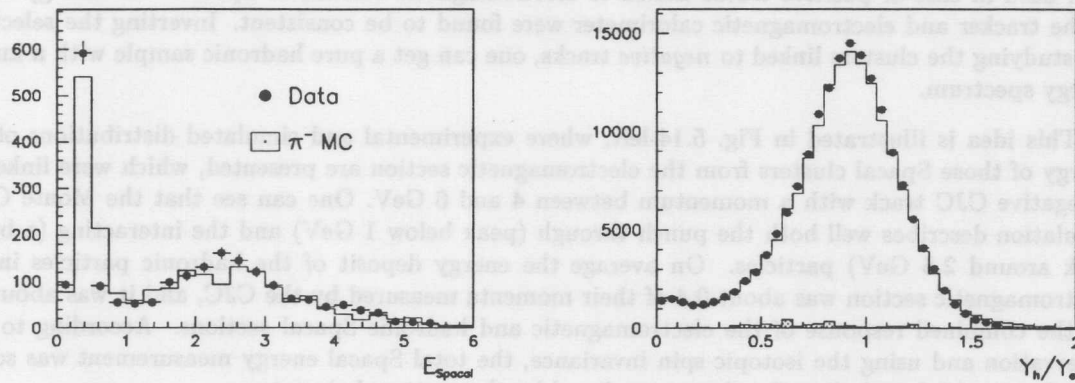


Figure 5.14: Left: Energy distribution of the Spacal clusters reconstructed in the electromagnetic part linked to the CJC track with negative charge and the track momentum between 4 and 6 GeV. Filled circles present data while the open histogram corresponds to the Monte Carlo simulation of the Spacal response to  $\pi^-$  particles. Right: distribution of the  $y_h/y_e$  ratio for DIS events with  $y_e$  in the interval 0.3–0.7. Filled circles correspond to data, dashed histogram to  $\gamma p$  Monte Carlo simulation and the open histogram to the sum of the  $\gamma p$  and DIS distributions.

where  $\Sigma_{LAr}$  corresponds to the part measured by the LAr calorimeter,  $\Sigma_{Backward}$  by the BEMC or the Spacal calorimeter and  $\Sigma_{track}$  by tracks in the central tracker.

A special procedure was developed in order to divide the calculation between the LAr calorimeter and the tracker [94, 95]. Selection criteria were applied to select “good” tracks, suitable for the energy measurement. These tracks were linked to calorimeter clusters with certain separation criteria. For each combined cluster-track object it was decided according to resolution from which of the detectors the energy information should be taken. Finally,  $\Sigma_{LAr}$  ( $\Sigma_{track}$ ) was composed from non-linked calorimeter cells (tracks) and from the combined objects, where the corresponding detector was chosen.

Advantages of this procedure with respect to a pure calorimetric measurement are a better coverage for low momentum charged particles and a better defined energy scale for hadrons.

The last point is significant since all H1 calorimeters are non compensating, i.e. energy scales of hadronic and electromagnetic showers are different. Normally the energy response to hadronic particles is lower than that to electrons and photons. A special technique was used to recognize and correct hadronic energy deposits for the LAr calorimeter, see Sec. 2.2.3. Global average corrections were used for BEMC and Spacal.

Hadronic final state particles produce both electromagnetic and hadronic clusters, the former coming predominantly from  $\pi^0 \rightarrow 2\gamma$  decays, the latter mostly from charged pions. To a good first approximation, according to isotopic spin invariance, one can expect 1/3 of the total energy to be carried by  $\pi^0$ . Still for a precise  $\Sigma$  determination a well tuned Monte Carlo simulation of the hadronic final state is important.

Therefore, two cross checks of the simulation with data are essential. Firstly, a description of the energy response to individual hadronic particles should be studied. Apart from the  $y_h$  measurement, this is also important for the photoproduction background simulation. Secondly, a comparison of the global energy flow must be performed.

A check of the energy description for single particles was done in H1 using test beam experiments and by comparison with the momentum measurement of charged particles using the tracking chambers. In the previous section we saw that the simulated CJC momentum measurement is in good agreement with data in case of positive tracks linked to electromagnetic clusters in Spacal. The energy scales of the tracker and electromagnetic calorimeter were found to be consistent. Inverting the selection, i.e. studying the clusters linked to *negative* tracks, one can get a pure hadronic sample with a known energy spectrum.

This idea is illustrated in Fig. 5.14-left, where experimental and simulated distributions of the energy of those Spacal clusters from the electromagnetic section are presented, which were linked to a negative CJC track with a momentum between 4 and 6 GeV. One can see that the Monte Carlo simulation describes well both the punch through (peak below 1 GeV) and the interacting (a broad peak around 2.5 GeV) particles. On average the energy deposit of the hadronic particles in the electromagnetic section was about 0.4 of their momenta measured by the CJC, and it was about 0.5 for the combined response of the electromagnetic and hadronic Spacal sections. According to this observation and using the isotopic spin invariance, the total Spacal energy measurement was scaled by a factor of 1.5 excluding the cluster produced by the scattered electron.

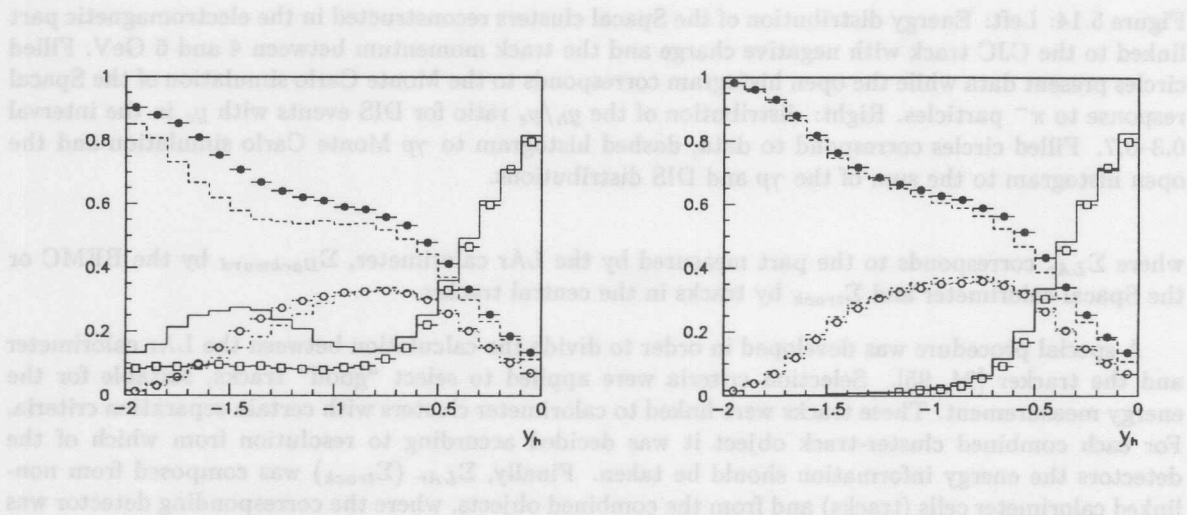


Figure 5.15: Experimental distributions of the fraction of  $y_h$  contributed by tracks (open circles), LAr calorimeter (filled circles) and Spacal (open boxes). The open histograms display the Monte Carlo simulation. The left plot is based on the default Spacal energy treatment, the right plot corresponds to the corrected Spacal response (Eq. 5.12).

The energy flow description was checked by comparing the hadron and electron based reconstruction of the kinematic variables. For the hadronic scale determination in the LAr calorimeter a  $p_t$  balance between the electron and hadronic particles was used. This method is best applicable for high  $Q^2$  events with the scattered electron in the LAr calorimeter acceptance. In the case of the backward calorimeter calibration, a more suitable variable is  $y$  measured with both the electron and hadron methods in the  $y$  range 0.3 – 0.7, where the resolution of  $y_e$  is much better than of  $y_h$ . Fig. 5.14-right, presents the distribution of  $y_h/y_e$  for  $y_e$  measured in this interval. One can see a good agreement between data and Monte Carlo simulation. The tail of the distribution, extending down to 0, corresponds to the ISR events and is also well described.

Apart from the energy scale a large influence on the  $y_h$  resolution has the calorimeter noise, which is of crucial importance for the measurement of  $y_h < 0.05$ , see Sec 3.1. A way to study this contribution is to compare the  $y_h$  composition from different detectors. This is shown in Fig. 5.15, where the fractions of  $y_h$  contributed by tracks, by the LAr calorimeter and by the Spacal are displayed. One can see, that for the default  $\Sigma_{spacal}$  calculation (left plot), its contribution to low  $y_h$  events is high,

although according to the DIS kinematics (see Fig. 3.3) the hadronic jet has a forward direction. One reason for this effect is the rescattering of the scattered electron off the detector material behind the central tracker with secondary particles getting wrongly identified as hadronic final state particles from the primary interaction. In order to suppress the influence of this effect, the hadronic energy measurement in the Spacal,  $E_{had}^{Spacal}$ , was recalculated as:

$$E_{had}^{Spacal'} = \max(0, E_{had}^{Spacal} - 0.03 E_e'), \quad (5.12)$$

which essentially suppresses the Spacal contribution below  $y_h \sim 0.1$ . The resulting  $y_h$  composition distribution is shown in Fig. 5.15-right. One can see, that a good agreement between data and Monte Carlo simulation is achieved here, especially at low  $y$  where the sigma method has been used for the kinematics reconstruction.

Selection criteria	Selection criteria	Selection criteria	Selection criteria	Selection criteria
$N_{vertex} > 1$	Central-GIP	$N_{vertex} > 1$	central-forward	Vertex position
$ z_v  < 34 \text{ cm}$	$ z_v  < 34 \text{ cm}$	$ z_v - z_{jet}  < 30 \text{ cm}$	$ z_v - z_{jet}  < 30 \text{ cm}$	Vertex error
$\langle R_{DCTR} \rangle < 1 \text{ cm}$	$\langle R_{DCTR} \rangle < 1 \text{ cm}$	$\langle R_{DCTR} \rangle < 1 \text{ cm}$	$\langle R_{DCTR} \rangle < 1 \text{ cm}$	Vertex type
$R_{DCTR} < 1 \text{ cm}$	$R_{DCTR} < 1 \text{ cm}$	$R_{DCTR} < 1 \text{ cm}$	$R_{DCTR} < 1 \text{ cm}$	Calorimeter
$R_{DCTR} < 1 \text{ cm}$	$R_{DCTR} < 1 \text{ cm}$	$R_{DCTR} < 1 \text{ cm}$	$R_{DCTR} < 1 \text{ cm}$	backward tracker
$R_{DCTR} < 1 \text{ cm}$	$R_{DCTR} < 1 \text{ cm}$	$R_{DCTR} < 1 \text{ cm}$	$R_{DCTR} < 1 \text{ cm}$	jet
$R_{DCTR} < 1 \text{ cm}$	$R_{DCTR} < 1 \text{ cm}$	$R_{DCTR} < 1 \text{ cm}$	$R_{DCTR} < 1 \text{ cm}$	Cluster radius
$R_{DCTR} < 1 \text{ cm}$	$R_{DCTR} < 1 \text{ cm}$	$R_{DCTR} < 1 \text{ cm}$	$R_{DCTR} < 1 \text{ cm}$	Hadronic fraction
$R_{DCTR} < 1 \text{ cm}$	$R_{DCTR} < 1 \text{ cm}$	$R_{DCTR} < 1 \text{ cm}$	$R_{DCTR} < 1 \text{ cm}$	$E - p_T$
$R_{DCTR} < 1 \text{ cm}$	$R_{DCTR} < 1 \text{ cm}$	$R_{DCTR} < 1 \text{ cm}$	$R_{DCTR} < 1 \text{ cm}$	CP violation
$R_{DCTR} < 1 \text{ cm}$	$R_{DCTR} < 1 \text{ cm}$	$R_{DCTR} < 1 \text{ cm}$	$R_{DCTR} < 1 \text{ cm}$	Back link
$R_{DCTR} < 1 \text{ cm}$	$R_{DCTR} < 1 \text{ cm}$	$R_{DCTR} < 1 \text{ cm}$	$R_{DCTR} < 1 \text{ cm}$	Track charge
$R_{DCTR} < 1 \text{ cm}$	$R_{DCTR} < 1 \text{ cm}$	$R_{DCTR} < 1 \text{ cm}$	$R_{DCTR} < 1 \text{ cm}$	Hadronic cut

Table 5.1: Selection criteria as they were applied to the different data sets presented in this thesis.  $N_{vertex}$  denotes the number of tracks reconstructed in the GIP which were fitted to the primary vertex.  $R_{DCTR}$  denotes the radius of the DCTR. In the case of the "Data Treatment", in the case of the "1984 analysis" data set the angular cut was extended up to  $\theta < 174^\circ$ .

Different data samples are presented in this thesis with different kinematic coverage, background conditions and methods of reconstructing the event kinematics. Consequently, a specific set of selection criteria was applied to each data set. In general, an attempt was made to use a minimal amount of selection criteria in order to minimize the loss of DIS events and to reduce the influence of the description of the efficiency in the Monte Carlo simulation. Still, several supplementary conditions were required for the high  $y$  analysis in order to clean the DIS sample from the  $q\bar{q}$  background.

Both the loss of the DIS events and the background suppression were studied for data and Monte Carlo simulation. For genuine DIS events, some selection criteria, like the electron validation by various tracking chambers, are kinematics independent and can be studied in the background free high  $E_e'$  region. At low  $E_e'$ , the DIS signal is mixed with the  $q\bar{q}$  background. A drop of the efficiency of a cut is defined as

$$\epsilon_{cut} = \frac{N_{cut}}{N_{total}} \quad (5.1)$$

corresponds to a certain amount of background reduction. Here  $N_{cut}$  ( $N_{total}$ ) denotes a total number of events passing all selection criteria (including) cut a.

## Chapter 6

# DIS Event Selection

	$F_2$ -94	$F_L$ -94	$F_2$ -96	$F_L$ -96
Z vertex position	$ Z_v - 5.6  < 30$ cm	$ Z_v - 5.6  < 30$ cm	$ Z_v  < 24$ cm	$ Z_v  < 24$ cm
Z vertex error	$< 6$ cm	$< 6$ cm	$< 8$ cm	$< 8$ cm
Vertex type	central-forward	$N_{central} > 1$	central-CIP	$N_{central} > 1$
Calorimeter -backward tracker link	DCLBP $< 5$ cm	DCLBP $< 3.5$ cm	DCLBT $< 3$ cm	DCLBT $< 3$ cm
Cluster radius	$RCL_{lin} < 5$ cm	$RCL_{lin} < 4$ cm	$RCL_{log} < 4$ cm	$RCL_{log} < 4$ cm
Hadronic fraction	-	-	$< 15\%$ for $E'_e < 20$ GeV	$< 15\%$
$E - p_z$	-	-	$> 35$ GeV	$> 35$ GeV
CIP validation	-	ON	for $E'_e < 20$ GeV	-
Track link	-	-	-	$< 6$ cm
Track charge	-	-	-	$> 0$
Fiducial cut	$\theta_e < 173^\circ$	$\theta_e < 173^\circ$ trigger box cut	trigger ineff. cuts	$R_{CJC} > 30$ cm trigger ineff. cuts

Table 6.1: Selection criteria as they were applied to the different data sets presented in the thesis.  $N_{central}$  denotes the number of tracks reconstructed in the CJC which were fitted to the primary vertex. Fiducial cuts are explained in more detail in chapter 4 on the “Data Treatment”. In the case of the  $F_2$  1994 analysis based on the “open triangles” data set the angular cut was extended up to  $\theta_e < 174^\circ$ .

Different data samples are presented in this thesis with different kinematic coverage, background conditions and methods of reconstructing the event kinematics. Consequently, a specific set of selection criteria was applied to each data set. In general, an attempt was made to use a minimal amount of selection criteria in order to minimize the loss of DIS events and to reduce the influence of the description of the efficiencies in the Monte Carlo simulation. Still, several supplementary conditions were required for the high  $y$  analyses in order to clean the DIS sample from the  $\gamma p$  background.

Both the loss of the DIS events and the background suppression were studied for data and Monte Carlo simulation. For genuine DIS events, some selection criteria, like the electron validation by various tracking chambers, are kinematics independent and can be studied in the background free high  $E'_e$  region. At low  $E'_e$  the DIS signal is mixed with the  $\gamma p$  background. A drop of the efficiency of a cut  $a$  defined as

$$\epsilon_{cut}^a = \frac{N_{cut}^a}{N_{All}}, \quad (6.1)$$

corresponds to a certain amount of background reduction. Here  $N_{all}$  ( $N_{cut}$ ) defines a total number of events passing all selection criteria excluding (including) cut  $a$ .

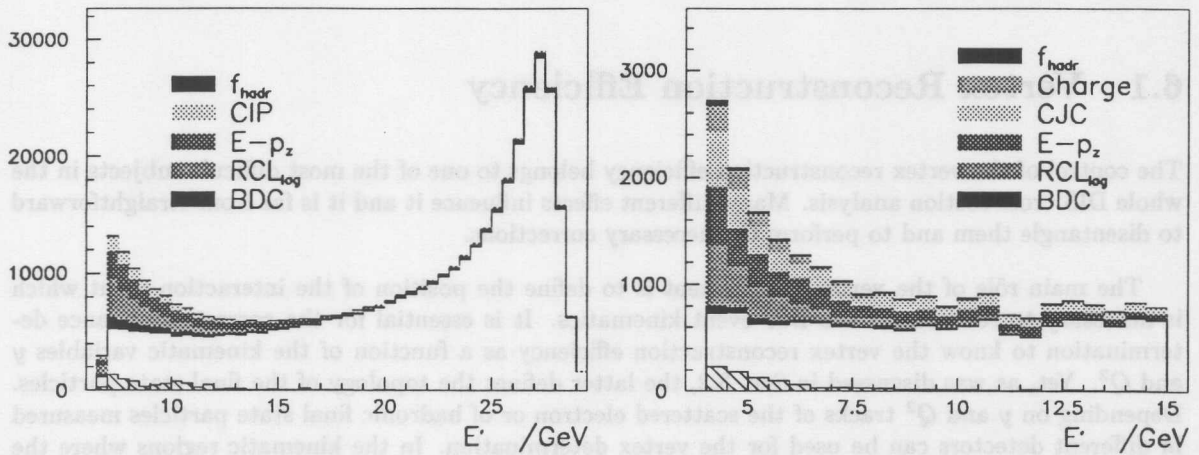


Figure 6.1: Effect of the background reduction cuts on the 1996 data for the  $F_2$  (left) and the  $F_L$  (right) analyses. The open histograms correspond to events having passed all selection criteria. The shaded bands display events rejected by a particular cut with all other selection criteria applied. The dashed histogram is an estimate of the remaining background performed with the PHOJET Monte Carlo simulation for “ $F_2$  1996” and with clusters linked to a negative track for “ $F_L$  1996”. The abbreviations in the figures denote the following cuts: BDC:  $DCLBT < 3$  cm;  $RCL_{log}$ :  $RCL_{log} < 4$  cm;  $E-p_z$ :  $E - p_z > 35$  GeV; CIP: CIP validation;  $f_{hadr}$ : hadronic fraction  $< 15\%$ ; CJC:  $\Delta_{CJC-BDC} < 6$  cm; Charge: positive track charge. All cuts are discussed in detail in Chapter 6.

The list of cuts used in the analyses is given in Tab. 6.1. The list starts with the selection criteria necessary to reconstruct the event kinematics: the  $Z$  vertex cut and the procedure to link backward tracks to calorimeter clusters. The cuts on the properties of the electromagnetic cluster associated with the scattered electron are listed next. These rely on two estimators related to the transverse cluster radius and to the fraction of energy deposited in the hadronic calorimeter behind the cluster (hadronic fraction).

A cut on  $E - p_z = \Sigma + E'_e(1 - \cos\theta_e)$  was used only for the 1996 data due to the poorer hadronic measurement in the backward region in 1994. It helps greatly to reduce  $\gamma p$  background and radiative corrections.

The next selection criteria were used especially for the high  $y$  analyses to suppress the  $\gamma p$  background. The requirement of the CIP validation, i.e. of a CIP pad signal triggered by the electron candidate, reduced photon conversion background, e.g. from the decay  $\pi^0 \rightarrow 2\gamma$ . This background was even stronger suppressed, at the cost of somewhat reduced efficiency and smaller acceptance, by demanding a link between the BDC track element associated with the electron and a track reconstructed in the central drift chambers (track link). The requirement applied to this track to have a positive charge removed the background caused by negative hadronic particles. Events rejected by this cut were useful for the estimation of the remaining background employing its charge symmetry (see Sec. 3.6).

Fig. 6.1 illustrates the effect of the low energy background reduction achieved with different cuts in the 1996 data analysis. The open histogram corresponds to the final data selection. The shaded bands illustrate the rejection power of a particular cut, keeping all other but the considered selection criterion applied. The estimation of the total remaining background is shown as a dashed histogram. Both the  $F_2$  (left plot) and the  $F_L$  (right plot) analyses are presented here. One can see in Fig. 6.1, that for the  $F_2$  analysis the cluster radius cut and the  $E - p_z$  cut are most effective, while for the  $F_L$  analysis the CJC-track link is an even more powerful background filter than the  $E - p_z$  and cluster radius cuts are.

The list of cuts in Tab. 6.1 is concluded with the *fiducial* cut used for each analysis. The subsequent chapter presents a detailed discussion of all selection criteria in the order they occur in Tab. 6.1.

## 6.1 Vertex Reconstruction Efficiency

The control of the vertex reconstruction efficiency belongs to one of the most difficult subjects in the whole DIS cross section analysis. Many different effects influence it and it is far from straightforward to disentangle them and to perform the necessary corrections.

The main rôle of the vertex requirement is to define the position of the interaction point which is necessary to reconstruct the DIS event kinematics. It is essential for the correct acceptance determination to know the vertex reconstruction efficiency as a function of the kinematic variables  $y$  and  $Q^2$ . Yet, as was discussed in Sec. 3.2, the latter defines the topology of the final state particles. Depending on  $y$  and  $Q^2$  tracks of the scattered electron or of hadronic final state particles measured in different detectors can be used for the vertex determination. In the kinematic regions where the vertex reconstruction efficiency becomes low it is difficult to distinguish between the genuine “hardware” inefficiency of the detector and a possible bias of the kinematics determination relying on the hadronic final state particles.

If  $y$  and  $Q^2$  are reconstructed using the electron method additional problems arise from the radiative corrections. The requirement of a hadronic vertex is equivalent to a cut on the hadronic final state invariant mass,  $W$ , which for radiative events passing the  $y$  selection can be set very low. A correct description of the low  $W$  cross section in the Monte Carlo simulation becomes important.

The second goal of the vertex requirement is to equalize the Monte Carlo simulation with the data. A first example of an effect present in the data but not in the Monte Carlo simulation is the satellite bunch interaction (see Sec. 4.5). The vertex cut diminishes its influence, although the satellite bunch effect has still to be taken into account for the correct efficiency estimation. The presence of non- $ep$  background is the second example for a process affecting the estimation of the vertex reconstruction efficiency for the data.

In the following sections all these and some additional phenomena are discussed.

### Measurement of the Vertex Reconstruction Efficiency

The vertex reconstruction efficiency is defined as

$$\epsilon_{\text{vertex}} = \frac{N_{\text{events with vertex}}}{N_{\text{total}}}. \quad (6.2)$$

Here  $N_{\text{events with vertex}}$  is the number of  $ep$  interaction events with a vertex reconstructed by one of the considered detectors<sup>1</sup> (*vertex type requirement*) with acceptable estimated precision ( $\sigma_{Z_{\text{vertex}}}$  cut) lying within a certain range  $\Delta Z$  around the nominal  $Z$  vertex position.  $N_{\text{total}}$  is the total number of  $ep$  interaction events from the same  $Z$  vertex and kinematic interval<sup>2</sup>. Both  $N_{\text{events with vertex}}$  and  $N_{\text{total}}$  are functions of  $Q^2$  and  $y$ .

The quantity  $N_{\text{total}}$  is well-defined for the Monte Carlo simulation. On the other hand, it is difficult to be estimated for the data, since in order to get the genuine contribution one has to subtract non- $ep$  background and events originating from the satellite bunch.

<sup>1</sup>Central and forward (Central and CIP) vertices were used in the 1994 (1996) analyses.

<sup>2</sup>The vertex position enters the  $\theta_e$  calculation and thus defines the event kinematics. To treat events with and without vertex on the same footing the nominal position of the  $Z$  vertex was used in both cases. For the CIP validation method (Eq. 6.4) the vertex reconstructed by the CIP was used.



One can modify Eq. 6.2, loosing a bit of its generality, like:

$$\epsilon_{\text{vertex}} = \frac{N_{\text{events with vertex}}}{N_{\text{total with no vtx outside } Z_0 \pm \Delta Z}}, \quad (6.3)$$

restricting  $N_{\text{total}}$  to those events which are situated inside the studied  $Z$  vertex interval or have no reconstructed vertex at all. This definition assumes no losses (or losses described by the Monte Carlo simulation) due to the vertex position determination. That has been studied independently, see Sec. 5.1.

The new definition (6.3) of the vertex reconstruction efficiency has the advantage that the satellite bunch contribution is reduced to events without reconstructed vertex. Also the non- $ep$  background is suppressed since these events have an almost flat  $Z$  vertex distribution.

Another way to redefine formula 6.2 is possible, if the vertex can be reconstructed also by an other, independent device, in our case by the CIP. Then

$$\epsilon_{\text{vertex}} = \frac{N_{\text{events with vertex \&\& CIP vertex}}}{N_{\text{total \&\& CIP vertex}}}, \quad (6.4)$$

thus the samples are reduced to those events with the vertex determined by the CIP. This approach removes the satellite bunch and non- $ep$  background completely. The CIP vertex is also reconstructed solely from the electron track reducing the dependence of the vertex reconstruction on the hadronic final state. Unfortunately, the CIP validation method can be applied only for events with the scattered electron in the CIP acceptance, thus for large  $Q^2 \gtrsim 20 \text{ GeV}^2$  or high  $y \gtrsim 0.5$  (Fig. 3.3).

In the 1994 data analysis the vertex reconstruction efficiency was studied with the most general definition as given in Eq. 6.2. The definition of Eq. 6.3 was chosen for the 1996 analysis. The CIP validation method (Eq. 6.4) was used in both analyses as a cross check.

The quantity  $N_{\text{total}}$  from Eq. 6.2 can be calculated as  $N_{\text{total}} = (N_{\text{all}} - N_{\text{bg}} - N_{\text{satellite}})$ . Here  $N_{\text{all}}$  is the total number of events satisfying all DIS selection criteria without applying the vertex cut,  $N_{\text{bg}}$  is the number of non- $ep$  background events estimated from the pilot bunches and  $N_{\text{satellite}}$  is the number of events coming from the satellite bunch. The determinations of  $N_{\text{satellite}}$  and  $N_{\text{bg}}$  are described in the next two sections.

### Correction for Satellite Bunch Effects

Let us consider a DIS event with an energy deposited by the scattered electron in the electromagnetic calorimeter at some radius  $R_e$ . If the vertex is not reconstructed it could be still situated in the main or in the forward satellite bunch<sup>3</sup>. Therefore, in a small fiducial volume  $dR_e, dE'_e$  around the point  $R_e, E'_e$ , the number of the DIS events can be calculated as a sum of two contributions:

$$dN(R_e, E'_e) = dR_e dE'_e \left( \mathcal{L}_{\text{nominal}} \frac{d^2 \sigma_{\text{nominal}}}{dR_e dE'_e}(R_e, E'_e) + \mathcal{L}_{\text{fwd satellite}} \frac{d^2 \sigma_{\text{fwd satellite}}}{dR_e dE'_e}(R_e, E'_e) \right). \quad (6.5)$$

Using this formula we define a *probability* that the event originated in the main bunch as:

$$p_{\text{main}}(R_e, E'_e) = \frac{\mathcal{L}_{\text{nominal}} \frac{d^2 \sigma_{\text{nominal}}}{dR_e dE'_e}(R_e, E'_e)}{\mathcal{L}_{\text{nominal}} \frac{d^2 \sigma_{\text{nominal}}}{dR_e dE'_e}(R_e, E'_e) + \mathcal{L}_{\text{fwd satellite}} \frac{d^2 \sigma_{\text{fwd satellite}}}{dR_e dE'_e}(R_e, E'_e)}. \quad (6.6)$$

One can apply this probability as an event *weight* in all event summations. This way the satellite bunch correction will be automatically applied.

<sup>3</sup>The event vertex could be situated also in the backward ( $-70 \text{ cm}$ ) satellite bunch but the fraction of events coming from the backward satellite region is negligible due to its smaller size and kinematic suppression.

The double differential cross section  $d^2\sigma/dR_e dE'_e$  can be calculated as  $d^2\sigma/dxdQ^2 \cdot J$ , where  $J$  denotes the Jacobian of the variables transformation. Due to different  $\theta_e$ , the cross section  $d^2\sigma/dxdQ^2$  is approximately 8 times bigger for the satellite than for the main bunch. On the other hand the Jacobian is approximately equal to 1/4, thus the double differential cross section ratio in the variables  $R_e, E'_e$  is about 2.

The fraction of the luminosity carried by the forward satellite bunch was on average equal to 3.4% in 1994 and to 4.3% in 1996 leading to about 7% and 9% corrections, respectively.

### Non- $ep$ Background Estimation

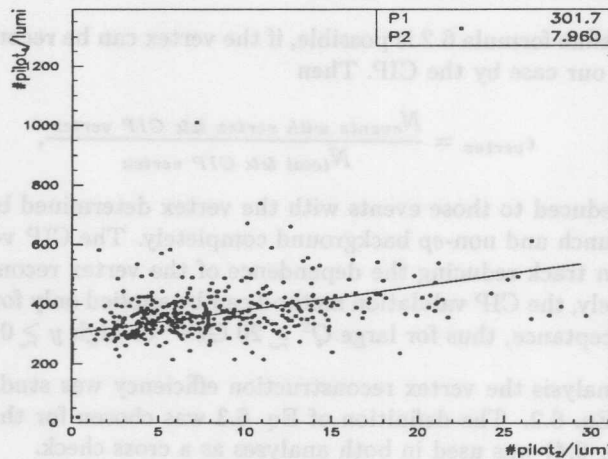


Figure 6.2: Correlation of the yields collected in the colliding bunch ( $\text{pilot}_4$ ) with the proton pilot bunch ( $\text{pilot}_2$ ) for different runs.

The amount of non- $ep$  background events was estimated using the pilot bunches (see Sec. 3.6.2). A standard way to determine the normalization factor for events detected in a pilot bunch  $i$  is to take the ratio of the number of colliding to the number of corresponding pilot bunches (see Eq. 3.12), where  $i = 1$  denotes the electron,  $i = 2$  the proton and  $i = 3$  the empty pilot bunch. As an alternative, the weight factors could be obtained as the ratio of the total currents in the colliding and the pilot bunch, see Tab. 6.2 for the resulting coefficients. Therefore, it has been important to develop a procedure to cross check these coefficients directly from the data.

For the basic event selection, before suppression of the non- $ep$  background<sup>4</sup>, the total cross section  $\sigma_{tot}$  comprises two components, one corresponding to  $ep$  interactions,  $\sigma_{ep}$ , and another one corresponding to the non- $ep$  background,  $\sigma_{bg}$ . The  $ep$  cross section is known to be stable as a function of the run number, after applying appropriate fiducial cuts, see Sec. 4.3. On the contrary  $\sigma_{bg}$  depends strongly on the background conditions for a given run. Comparing the collision yield  $\sigma_{tot}^{run} = N_{colliding}^{run} / \mathcal{L}^{run}$  with the yield of selected events in a pilot bunch for runs with different background conditions, one can obtain the normalization factors.

This procedure is illustrated in Fig. 6.2, where the correlation between the yields in the colliding and in the proton pilot bunches for different luminosity runs is presented. A dependence is seen, but the slope of the straight line fit can not directly be used as an estimation of the pilot bunch normalization factor due to possible correlations between different background conditions.

<sup>4</sup>The following cuts were applied for this study:  $\theta < 173^\circ$ ,  $E' > 7.5$  GeV,  $Z_{vertex} > -100$  cm.

	empty bunch	proton pilot	electron pilot
Ratio of # bunches	4.4	9.1	10.5
Ratio of currents	0.0	11.2	11.3
Fit	$0.0 \pm 1.2$	$8.2 \pm 1.6$	$7.6 \pm 1.8$

Table 6.2: Pilot bunch subtraction coefficients as defined in Eq. 3.12 obtained by different methods for 1994 data. Only statistical errors are given for the fit result.

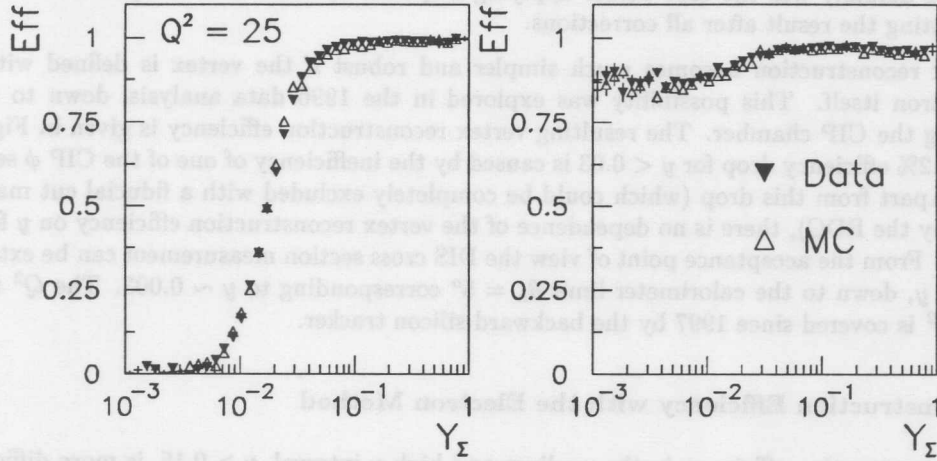


Figure 6.3: Vertex reconstruction efficiency as a function of  $y_{\Sigma}$  for  $Q^2 = 25 \text{ GeV}^2$ . For the left plot only central tracker vertices are used, the right plot is based on both CIP or the central tracker vertices.

In order to get the normalization factors for all sources of the non- $ep$  background associated with different pilot bunches, a minimization of the functional

$$S(\sigma_{ep}, \alpha_{j \text{ pilot}}) = \sum_{irun=1}^{NRUN} \left( \frac{N_{irun}^{colliding} - \sum_{j \text{ pilot}=1}^3 N_{j \text{ pilot}}^{irun} \alpha_{j \text{ pilot}}}{\mathcal{L}_{irun}} - \sigma_{ep} \right)^2 \rightarrow \min \quad (6.7)$$

was performed, where  $\alpha_{j \text{ pilot}}$  denote the desired normalization coefficients. The results are given in Tab. 6.2. From this table one can see, that all three determinations of the pilot bunch coefficients are consistent, although the fit results are somewhat lower. For the most important background source, the proton beam non- $ep$  interactions, the three pilot bunch coefficient determinations are in better agreement. The differences of the coefficients were taken into account for the systematic error estimation.

### Vertex Reconstruction Efficiency with the Sigma Method

We start the discussion of the vertex reconstruction efficiency results with the relatively straightforward case when the kinematics at low  $y$  is determined with the sigma method. Low  $y$  corresponds to high

$E'_e$ , thus the background from non- $ep$  interactions is negligible and also the sigma method is rather insensitive to ISR. That means that apart from the satellite bunch correction the experimental vertex reconstruction efficiency can be easily determined.

Still the problem is far from being trivial. As one can see from the kinematic plot, Fig 3.3, the region  $y < 0.05$  approaches the limit of the CJC acceptance to the hadronic final state. The hadron angle for this kinematic region is proportional to  $y$ , namely  $\theta_h \approx 2y \tan(\theta_e/2)$  (see formula 3.10). It is thus clear, that if the hadronic vertex is used, the vertex reconstruction efficiency has to vary strongly with  $y$ . This is seen in Fig. 6.3-left which presents a calculation of the vertex reconstruction efficiency using only the central tracker. For the 1994 data the drop of the efficiency at the low  $y$  edge of the DIS cross section measurement was not so rapid because in this analysis vertices reconstructed with the forward tracker were also accepted, compare Fig. 6.3-left with Fig. 6.7-b.

A small deviation in the  $y$  resolution, in particular due to the calorimeter noise, lead to migrations from the region  $y < 0.01$  to higher  $y$  values, and caused large changes in the vertex reconstruction efficiency. This actually was the case before applying a special Spacal treatment (see Sec. 5.3), the plot 6.3 presenting the result after all corrections.

The vertex reconstruction becomes much simpler and robust if the vertex is defined with the scattered electron itself. This possibility was explored in the 1996 data analysis, down to  $Q^2 = 20 \text{ GeV}^2$ , using the CIP chamber. The resulting vertex reconstruction efficiency is given in Fig. 6.3-right. About 12% efficiency drop for  $y < 0.03$  is caused by the inefficiency of one of the CIP  $\phi$  sectors, see Sec. 5.1. Apart from this drop (which could be completely excluded with a fiducial cut made on  $\phi_e$  measured by the BDC), there is no dependence of the vertex reconstruction efficiency on  $y$  for the whole  $y$  range. From the acceptance point of view the DIS cross section measurement can be extended towards lower  $y$ , down to the calorimeter limit  $\theta_h = 5^\circ$  corresponding to  $y \sim 0.003$ . The  $Q^2$  region below  $20 \text{ GeV}^2$  is covered since 1997 by the backward silicon tracker.

### Vertex Reconstruction Efficiency with the Electron Method

The vertex reconstruction efficiency in the medium and high  $y$  interval,  $y > 0.15$ , is more difficult to obtain reliably because all problems (background, radiation, diffractive events) affect its determination.

### Effect of Radiative Corrections

A distribution of the hadronic final state invariant mass  $W$  based on the DJANGO Monte Carlo simulation is given in Fig. 6.4. The left plot presents the complete range of the analysis. One can see, that the vertex requirement reduces dramatically the number of events with  $W < 15 \text{ GeV}$  if the vertex is reconstructed from the hadronic final state particles. The right plot displays the  $W$  distribution for events with  $y_e$  situated in the interval  $0.6 - 0.9$ . The range  $W > 235 \text{ GeV}$  corresponds to the Born part of the cross section. A long tail extending to low  $W$  values is caused by initial state radiation.

In the high  $y$  region, for  $Q^2 > 12 \text{ GeV}^2$ , a central vertex requirement can be satisfied also by the electron track. The condition  $N_{central} > 1$ , however, which is important for the trigger efficiency (see Sec. 4.6), is equivalent to requiring the reconstruction of the hadronic vertex.

Studying Fig. 6.4 it becomes clear, that the estimation of the vertex reconstruction efficiency for the electron method depends on the knowledge of the radiative corrections:

- The radiative corrections have to be simulated accurately down to the proton mass  $W = m_p$ . The LEPTO Monte Carlo program, however, had an internal cut of  $W > 4 \text{ GeV}$ . A special study using the HECTOR program (TERAD branch) was performed to estimate the effect of this cut. For  $y = 0.7$  an about 2% influence on the total cross section was obtained. The kinematic interval  $W < 4 \text{ GeV}$  corresponds to the vertex inefficiency region, thus the number of events without reconstructed hadronic vertex was corrected in the Monte Carlo simulation using the TERAD estimation.

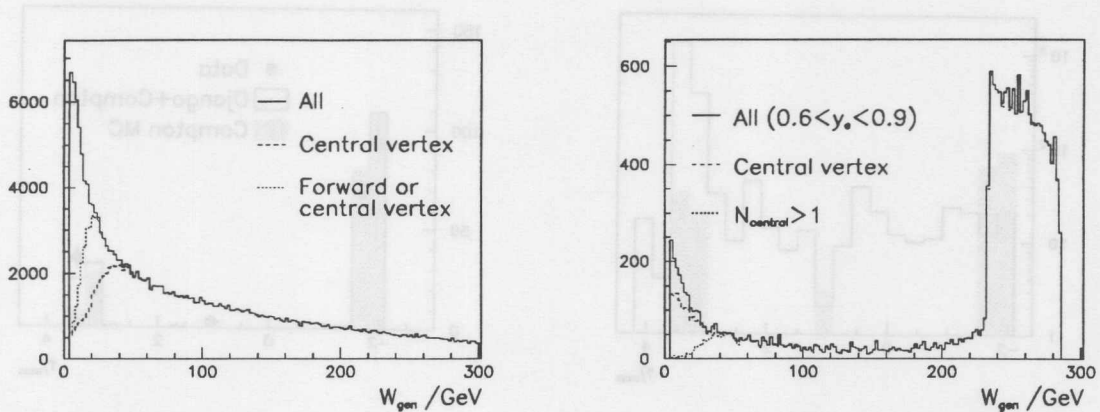


Figure 6.4: Left:  $W$  distributions for the complete range of the DIS analysis for all events (solid line), for events with forward or central vertex (dotted line) and for events with central vertex (dashed line). Right:  $W$  distributions for the high  $y$  range,  $0.6 < y_e < 0.9$ , for all events (solid line), events linked to the central vertex (dashed line) and events with more than one track contributing to the central vertex reconstruction (dotted line). The plots are based on the DJANGO Monte Carlo simulation.

- Radiative corrections depend on the structure functions used for their calculation (Sec. 3.4). Thus an iterative procedure (Sec. 3.7) with a DIS double differential cross section model fitted to the experimental data was needed for their determination and consequently for estimating the vertex reconstruction efficiency.

As an alternative, the radiative corrections for the electron method can be largely reduced by a cut on  $y_h$  or  $E - p_z$ . A drawback of this approach for the vertex reconstruction efficiency determination consists of the correlation between the vertex and  $y_h$  cuts. In the present analysis this approach was used as a cross check of the more general determination in which no cut on hadronic final state variables was performed.

#### Effect of Diffractive Events

For the high  $y$  kinematics the hadron angle points backwards (Sec. 3.2). In a “normal” deep inelastic scattering event, the struck quark is connected with the proton remnant with a colour string, which fills the central region in the H1 laboratory frame with soft particles suitable for the vertex reconstruction. This is seen in Fig. 6.4-right where for the Born region of the cross section ( $W > 235$  GeV) the distribution of events with the additional condition  $N_{central} > 1$  practically coincides with the total one.

The situation can be different for the diffractive events, where the scattered proton is separated from the current jet by a gap in the particles rapidity distribution. A study based on the Monte Carlo program RAPGAP was performed in order to estimate the influence of these events on the vertex reconstruction efficiency. For the simulation containing no vector meson production channels, the resulting  $N_{central} > 1$  cut efficiency for QED Born events in the range  $0.6 < y < 0.9$  was found to be  $> 99\%$  as for the DJANGO estimation. This is related to a relatively large average invariant mass of the diffractive system  $M_{inv} \sim 5$  GeV.

The case of the elastic electroproduction of the vector mesons ( $\rho, \omega, \phi$ ) is different. A relatively large backward boost, which occurs at high  $y$ , and low masses of these particles do not permit them

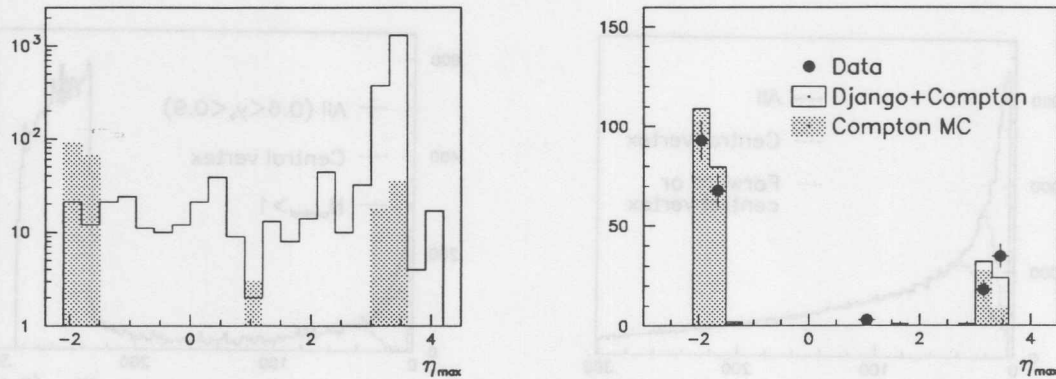


Figure 6.5: Left: distribution of the maximum pseudo rapidity  $\eta_{max}$  measured for events with  $y_e$  reconstructed in the range  $0.7 < y < 0.9$  and the electron track detected in the CJC. The open histogram corresponds to events satisfying the selection  $N_{central} > 1$ . The shaded histogram corresponds to events with  $N_{central} = 1$ . Right: the same  $\eta_{max}$  distribution for events rejected by the cut  $N_{central} > 1$  for data (closed points) and Monte Carlo simulation (open histogram). The distributions are normalized absolutely. The  $\gamma p$  background is subtracted using clusters linked to negatively charged tracks.

to decay at larger opening angles. The energy of the vector meson for the “ $F_L$  1996” analysis, where  $E'_e > 4$  GeV, is around 23 GeV leading to a minimum opening angle of the  $\rho \rightarrow \pi\pi$  decay of  $\theta_{\pi\pi} < 2.5^\circ$ .

The direction of the vector meson coincides with the hadron angle. In the case of the “ $F_L$  1996” analysis it was limited to  $\theta_\rho < 177.5^\circ$ . The Spacal acceptance extends up to  $178^\circ$ , therefore in most cases both the scattered electron and the hadronic particles are detected in the calorimeter leading to reconstructed values of  $E - p_z$  close to the nominal one. These events were triggered by a special trigger S40, introduced in the 1996 data taking period, which comprised the requirement of the Spacal trigger element IET1 (Sec. 4.6), of a special low charged track multiplicity condition in the central tracker and of an additional back-to-back signature of the reconstructed Spacal clusters.

QED Compton events have a similar signature as the light vector mesons (see Sec. 3.4). The HERACLES program did not simulate their elastic contribution, hence a special COMPTON Monte Carlo simulation program was used for this purpose. The Monte Carlo prediction was obtained from combining both simulations with orthogonal sets of cuts in order to avoid double counting of events. Events with  $E'_e, E'_\gamma > 2$  GeV,  $\theta_e, \theta_\gamma < 178.6^\circ$  and  $E'_e, E'_\gamma > 20$  GeV were simulated by the COMPTON program, and the complementary selection was used in DJANGO.

The requirement of the electron track reconstructed in the central tracker and linked to the Spacal cluster diminished the non- $ep$  background to the permille level. The  $E - p_z$  cut reduced the effect of initial state radiation, thus the influence of the low diffractive mass and of the Compton events on the hadronic vertex reconstruction efficiency could be estimated from the data directly.

Fig. 6.5-left shows the distribution of the maximum pseudorapidity defined as

$$\eta_{max} = \max_i [-\log \tan(\theta_i/2)] \quad (6.8)$$

where  $\theta_i$  is the polar angle of an energy cluster  $i$  measured using the LAr or Spacal calorimeters. For non-diffractive events, where the particles populate all angles between the current jet and the proton remnant,  $\eta_{max}$  is equal to the LAr forward acceptance limit  $\eta_{max} \approx 3$ . For diffractive events,

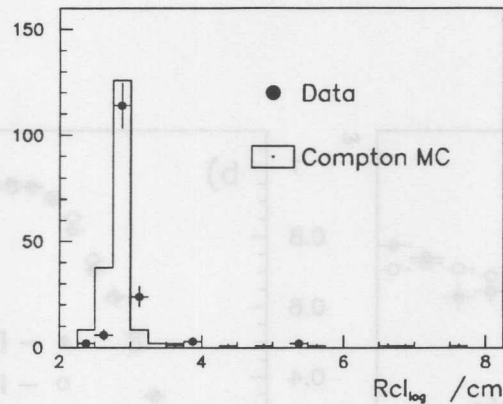


Figure 6.6:  $RCL_{log}$  distribution for the second Spacal cluster in the high  $y$  events with  $N_{center} = 1$  and  $\eta_{max} < 0$ . Dots show the data and the open histogram displays the COMPTON Monte Carlo simulation.

however, it can be lower and in the case of elastic vector meson production it reaches the Spacal region  $\eta_{max} < -1.5$ . Fig 6.5-left presents the distributions for events accepted and rejected by the condition  $N_{center} > 1$ . From the shaded distribution of events with  $N_{center} = 1$  one can see two inefficiency regions at high and at low  $\eta_{max}$ . A comparison of the  $\eta_{max}$  distributions for the rejected events in data and DJANGO Monte Carlo simulation is displayed on the Fig 6.5-right. One can see, that the Monte Carlo simulation is in good agreement with the data. The negative  $\eta_{max}$  region corresponds to elastic scattering, while the positive interval represents the inelastic Compton and ISR events. Fig. 6.6 shows cluster radius distributions (see Sec. 6.3) of the second Spacal cluster for the data and the Monte Carlo simulation for the events with  $\eta_{max} < 0$ . A sharp peak at  $RCL_{log} \leq 3$  cm is seen as expected for electromagnetic energy deposits.

Since the observed hadronic vertex reconstruction inefficiency can be attributed to Compton events, we can conclude that the contribution of the vector mesons to the vertex reconstruction efficiency in the kinematic range of the present analysis is negligible. A final check was performed using the Monte Carlo simulation. A maximum of 0.3% of the vector meson events in the total DIS sample are expected from the RAPGAP calculation.

## Results

In Fig. 6.7 the results of the vertex reconstruction efficiency estimation obtained for the 1994 data are summarized. In Fig. 6.7-a the vertex efficiency as a function of  $y_e$  is displayed calculated using Eq. 6.2. Fig. 6.7-b shows a similar determination for the sigma method. Data and Monte Carlo simulations are in good agreement for these two plots. A cross check of the general method is presented in Fig. 6.7-c using the method based on CIP vertices (Eq. 6.2). All these comparisons were performed for all  $Q^2$  bins used in the analysis, the bin  $Q^2 = 25 \text{ GeV}^2$  is chosen here as an example. The ratio of the experimental vertex reconstruction efficiency to the simulated one as a function of  $y_e$  was fitted by a constant for each  $Q^2$  bin. The result as a function of the  $Q^2$  bin number is given in Fig. 6.7-d. Bins 5-7 ( $Q^2=5 - 7.5 \text{ GeV}^2$ ) were taken from the "open triangles" data sample; for bins 8 - 14 ( $Q^2=12 - 65 \text{ GeV}^2$ ) the "closed triangles" data sample was used. One can see, that for all  $Q^2$  bins used in the analysis the experimental and simulated vertex reconstruction efficiencies agree within 2%.

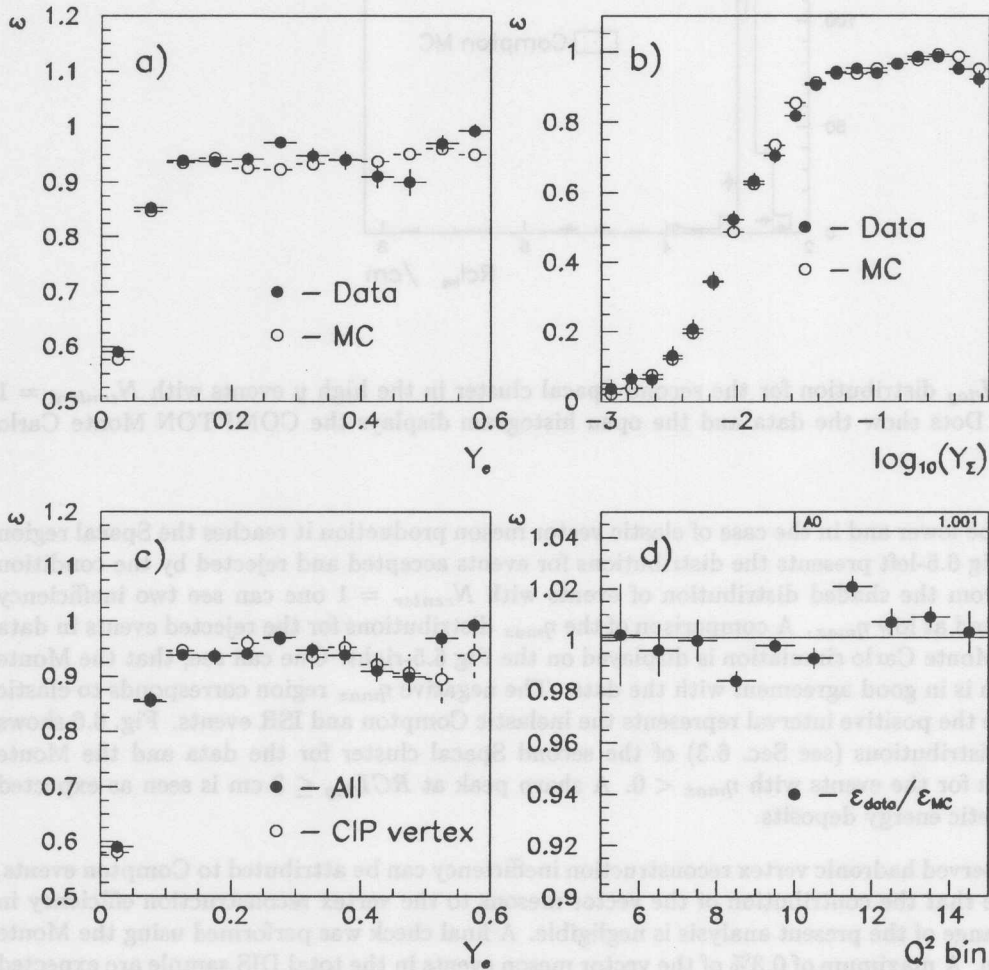


Figure 6.7: Vertex reconstruction efficiency comparison between 1994 data and Monte Carlo simulation. Figures a)-c) are made for the bin  $Q^2 = 25 \text{ GeV}^2$ . a) is the vertex reconstruction efficiency as a function of  $y_e$ , and b) of  $y_\Sigma$ . c) is a comparison of the efficiency obtained by requiring the CIP vertex validation and by using the satellite bunch correction. In Fig. d) the ratio of data to the simulated efficiencies is plotted as a function of the  $Q^2$  bin number (See Sec. 3.7 for the definition of the binning. Bin "7" corresponds to  $Q^2 = 8.5 \text{ GeV}^2$ , bin 15 to  $Q^2 = 60 \text{ GeV}^2$ ). Points for bins 5 to 7 are taken from the open triangles run period, 8 to 14 from one when the inner triangles were closed. The errors are statistical errors.



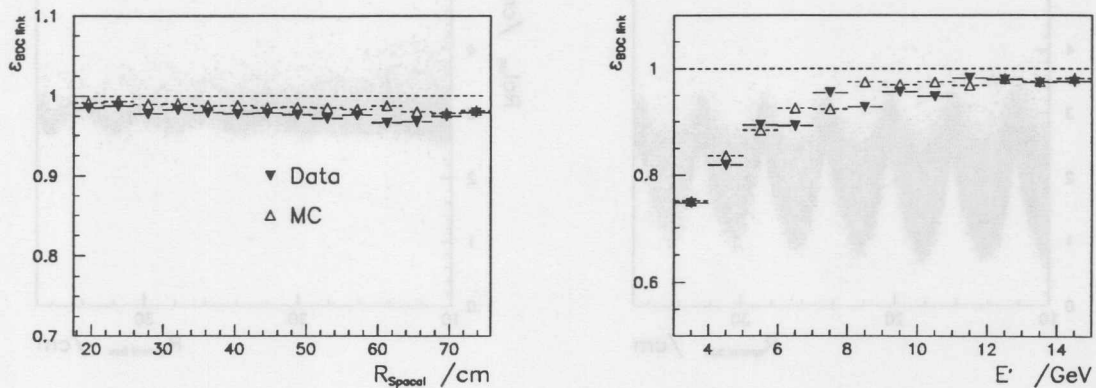


Figure 6.8: BDC-Spacial link efficiency. The left plot presents the link efficiency for DIS events ( $E'_e > 20.$ ) as a function of  $R_{spacial}$ . The right plot displays the background suppression efficiency as a function of  $E'_e$ . Data efficiencies (solid triangles) are compared with the result based on the sum of DIS Monte Carlo and  $\gamma p$  background contribution. The latter were estimated from Spacial clusters linked to a negatively charged track.

## 6.2 Backward Tracker – Calorimeter Link

The backward tracker-calorimeter link is important for the unbiased definition of the event kinematics (Sec. 5.1) and for reducing background to DIS events. There are two important reasons for this reduction: firstly, the requirement of a track permits to reject non-showering neutral particles, which populate especially the region of larger angles,  $\theta_e > 174^\circ$ , below the dead material of the central tracker readout electronics. Secondly, as it will be discussed in the next section, energy clusters produced by hadrons are in general broader, both in transverse and longitudinal directions than electromagnetic ones. The difference in the longitudinal penetration length between the electron and hadrons is larger for low electron energies. The effect on the cluster-backward tracker link gets stronger for particles scattered at small polar angles.

The determination of the backward link efficiency can be thus divided into two steps: firstly, the “hardware” efficiency of the backward tracker must be found, i.e. its ability to detect the scattered electron for the whole fiducial volume used in the analysis. This can be done with events with  $E'_e > 20$  GeV, which are free from background and for which the electron identification is unambiguous. Secondly, a description of the background reduction by the cut should be understood.

For the 1994 data it was found that the BPC efficiency to reconstruct the scattered electron was well reproduced by the Monte Carlo simulation for small radii, but the efficiency for the data was systematically higher than for the Monte Carlo simulation in the outer BPC region (see [34]). Up to 4% corrections were applied to the Monte Carlo simulation for the outermost BPC part.

An estimation of the BDC link efficiencies for the 1996 data and the DIS Monte Carlo simulation is presented in Fig. 6.8-left as a function of the scattered electron impact point on the Spacial plane  $R_{spacial} = \sqrt{x_{cluster}^2 + y_{cluster}^2}$  using data over the whole analysis run period selecting DIS events with  $E'_e > 20$  GeV. One can see that the efficiency was high, uniform over the BDC plane and, apart from a global 1% shift, well reproduced by the simulation. This 1% correction was applied to the Monte Carlo simulation.

The BDC-Spacial link efficiency as a function of the Spacial cluster energy  $E'$  is given in Fig. 6.8-right. The plot is based on the  $F_L$  1996 analysis. The background is estimated from clusters linked to a

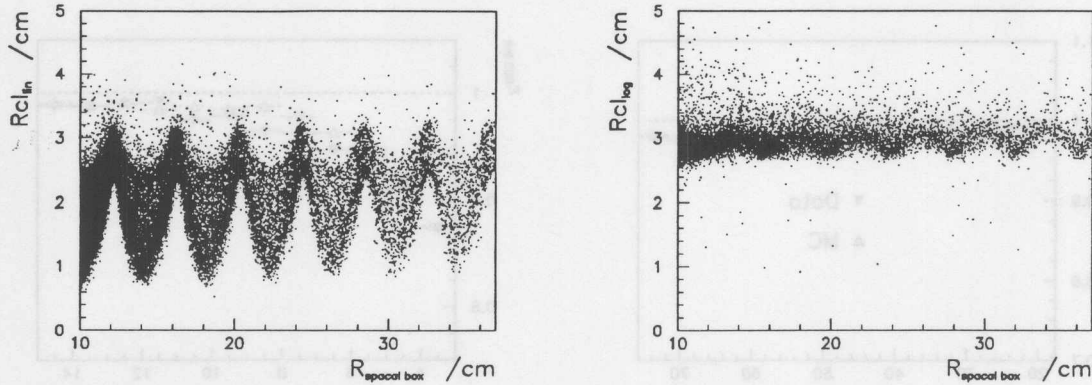


Figure 6.9: Linear (left), Eq. 6.9 and logarithmic (right), Eq. 6.11, second moment estimators for the electromagnetic cluster radius as a function of  $R_{box} = \max(|X_{spacal}|, |Y_{spacal}|)$ .  $R_{box}$  values of  $\sim 10, 14, 18, \dots$  cm correspond to centers of the cells, while  $\sim 12, 16, 20, \dots$  cm to their edges.

track with negative charge. The BDC-Spacal link requirement reduces the background contamination by up to 20%. A good agreement between data and Monte Carlo is seen.

### 6.3 Estimators of Cluster Properties

Estimators of the transverse cluster size, in the 1994 data, and both transverse and longitudinal cluster parameters, in the 1996 data, were used in the analyses in order to suppress hadronic background. This background rejection is based on the fact that the clusters of hadronic particles are broader than those produced by electrons in electromagnetic calorimeters. Moreover, for energies bigger than about 6 GeV, the opening angle between two photons in the decay  $\pi^0 \rightarrow 2\gamma$  is on average smaller than the minimal cluster separation in the calorimeters, thus both photons are detected in one single broad calorimeter cluster.

For the 1994 data an estimator of the transverse dimension of a cluster, the *cluster radius*, was developed based on the weighted sum of distances  $R_i$  between the center of gravity of the cluster as defined in Sec. 5.1 and the centroids of all  $N \geq 1$  stacks belonging to that cluster:

$$RCL_{lin} = \sum_{i=1}^N R_i w_i \quad w_i = \frac{E_i}{E_{cluster}} \quad (6.9)$$

where  $E_i$  denotes the energy reconstructed in stack  $i$  and  $E_{cluster}$  stays for the total energy of the cluster.

It was found that formula 6.9 for the Spacal data leads to an estimator which depends strongly on the scattered electron impact point, see Fig 6.9 left. In case of the Spacal,  $R_i$  is equal to the distance between the center of the cluster and the geometrical center of cell  $i$ . Eq. 6.9 leads to the following inequality:

$$\sum_{i=1}^N R_i w_i \geq \sum_{i=1}^N R_{min} w_i = R_{min}, \quad (6.10)$$

where  $R_{min}$  is the minimum distance among all  $R_i$ . In most cases  $R_{min}$  corresponds to the distance between the center of the cluster and of the hottest cell which varies between 0 and about 3 cm. Thus

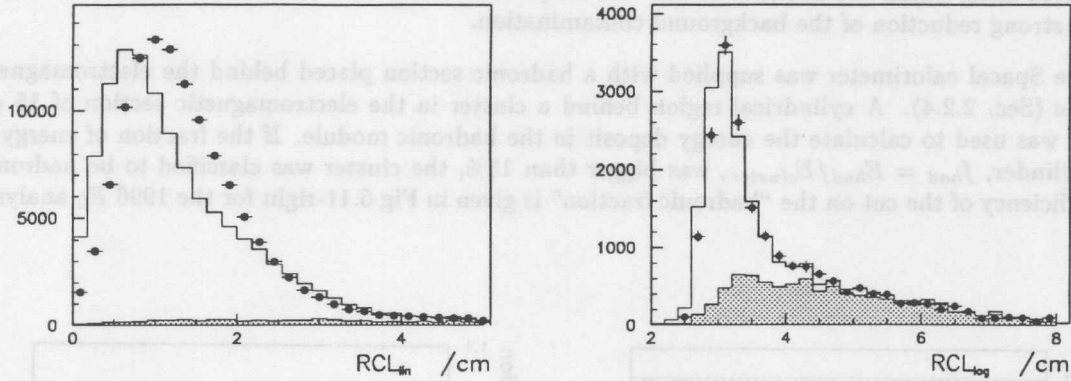


Figure 6.10: Cluster radius distributions for the BEMC (left) and the Spacal (right) calorimeters. The plots are based on the  $F_2$  (left) and  $F_L$  (right) analysis samples with energy selection  $E'_e > 11$  GeV (left) and  $3 < E'_e < 15$  GeV (right). Data are presented as solid points, the shaded histograms correspond to the  $\gamma p$  background, see text, and the open histograms are a sum of a DIS Monte Carlo simulation and the  $\gamma p$  estimation. For both analyses a cut  $RCL < 4$  cm was applied. One can see, that this cut rejects mostly  $\gamma p$  events, while the cut efficiency for DIS events is above 95%.

the estimator of Eq. 6.9 measures mainly the impact point position of the scattered electron with respect to the hottest cluster center, see Fig 6.9-left. This effect was not present in the BEMC since the hottest cell position which was determined with a centroid method using wave length shifters readout ( Sec. 2.2.4) was not fixed at the cell center but followed the true impact point.

To overcome this problem a method was used which was originally proposed in [85] and then implemented for the Spacal calorimeter [50]. The main idea of this approach has been the introduction of an effective cluster radius which is larger than the calorimeter granularity. This could be achieved with a modified weighting in the cluster radius definition using weights depending logarithmically and not linearly on the cell energies and also defining a suitable *cutoff weight* ( $w_{cut}$ ):

$$w_i^{log} = \frac{W_i^{log}}{\sum_{j=1}^N W_j^{log}}, \quad W_i^{log} = \max\left(0, w_{cut} + \ln \frac{E_i}{E_{cluster}}\right). \quad (6.11)$$

Additionally, the linear summation in Eq. 6.9 was replaced by a quadratic one:

$$RCL_{log} = \sqrt{\sum_i (R_i w_i^{log})^2} \quad (6.12)$$

Larger values  $w_{cut}$  lead to smaller cell energies used for the calculation, thus to a large effective cluster radius. For Spacal data  $w_{cut}^{data} = 4.85$  was chosen. The resulting impact point dependence is illustrated in Fig 6.9-right. Comparing Fig. 6.9-right, the logarithmic weights, with the linear weights, Fig. 6.9-left, it becomes apparent that the striking geometry dependence of the latter has been removed. This considerably improves the power for the background rejection of the cluster radius cut. The best adjustment of the Monte Carlo simulation to the data was obtained with  $w_{cut}^{mc} = 5.05$

In Fig. 6.10 cluster radius distributions for the BEMC (left) and Spacal (right) based analyses are presented. The BEMC plot is based on the  $F_2$  analysis,  $E'_e > 11$  GeV, while the plot for the Spacal corresponds to the  $F_L$  selection,  $3 < E'_e < 15$  GeV. For the BEMC plot the  $\gamma p$  background was

estimated using the PHOJET Monte Carlo simulation while for the Spacal plot clusters were used linked to a negatively charged track. A study of the  $RCL < 4$  cm cut efficiency as a function of the Spacal cluster energy is displayed in Fig 6.11-left for the 1996  $F_L$  analysis. The  $\gamma p$  background is estimated using negatively charged tracks. The drop of the efficiency towards low energy corresponds to the strong reduction of the background contamination.

The Spacal calorimeter was supplied with a hadronic section placed behind the electromagnetic module (Sec. 2.2.4). A cylindrical region behind a cluster in the electromagnetic section of 15 cm radius was used to calculate the energy deposit in the hadronic module. If the fraction of energy in this cylinder,  $f_{had} = E_{had}/E_{cluster}$ , was bigger than 15%, the cluster was classified to be hadronic. The efficiency of the cut on the “hadronic fraction” is given in Fig 6.11-right for the 1996  $F_L$  analysis.

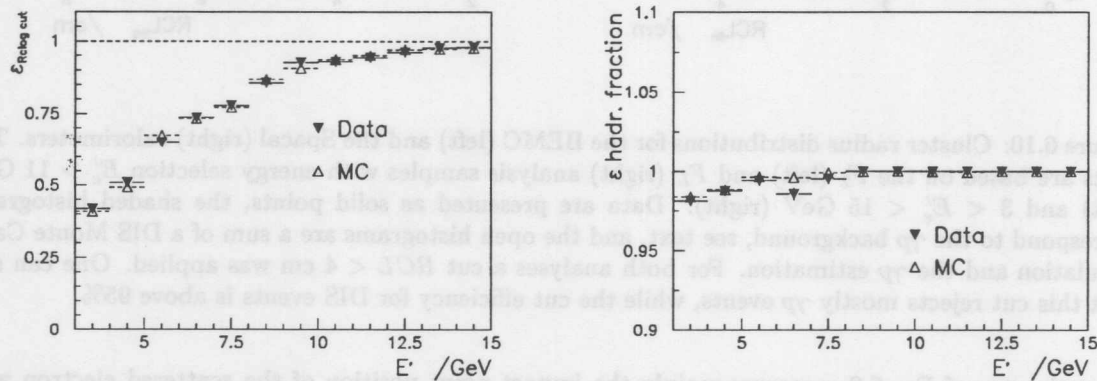


Figure 6.11: Left: efficiency of the cluster radius cut as a function of the cluster energy. Right: efficiency of the cut on the hadronic fraction. Both plots are based on the 1996 data  $F_L$  analysis. Reduction of the efficiencies towards low  $E'_e$  means enlarged rejection of background.

## 6.4 $E - p_z$ Cut

The quantity  $E - p_z = \Sigma + E'_e(1 - \cos\theta_e)$  for a “normal” DIS event should be equal to twice the electron beam energy due to energy and longitudinal momentum conservation (see Sec. 3.1). If  $E - p_z$  for a given event is smaller than  $2E_e$ , outside the measurement resolution, than the following effects could be the reason: i) particles not detected in the calorimeter ( $\mu, \nu$ ); ii) initial state radiation, with a photon of energy  $E_\gamma = E_e - 0.5(E - p_z)$  escaping along the beam pipe; iii) photoproduction event with the electron scattered below the backward calorimeter acceptance.

If the characteristics of the hadronic final state are well described by the Monte Carlo simulation and if the hadronic final state particles emitted backwards are well measured in the detector, then the cut on  $E - p_z$  can be used as a powerful filter against background and radiative corrections. This was rather problematic with the BEMC calorimeter due to its large uncertainty of the hadronic scale and a poor hadronic containment. The  $E - p_z$  cut was used for 1996 data only.

In Fig. 6.12-left the  $E - p_z$  distribution is presented for the  $F_L$  1996 analysis for energies  $3 < E' < 15$  GeV. The distribution has a pronounced peak around the nominal value  $E - p_z = 2E_e \approx 55.0$  GeV. A long tail of the  $E - p_z$  values down to 10 GeV corresponds mainly to ISR events. The background estimated using events with Spacal energy clusters linked to a track with negative charge has an almost flat distribution.

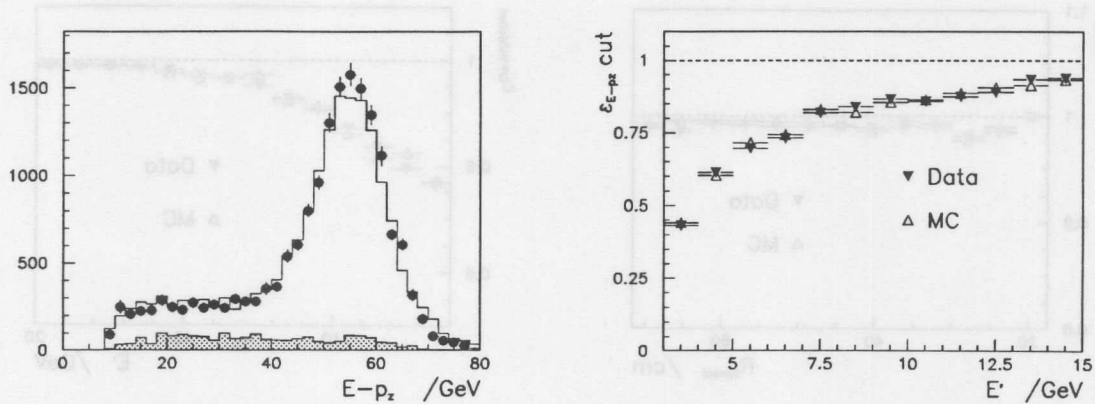


Figure 6.12: Left:  $E - p_z$  distribution for the “ $F_L$  1996” analysis for energies  $3 < E' < 15$  GeV. Solid points present data. The shaded histogram illustrates background estimated from clusters linked to a negative track. The open histogram corresponds to the sum of this background and the DIS Monte Carlo simulation. The analysis cut was set to 35 GeV. Right: Efficiency of the cut  $E - p_z > 35$  GeV as a function of the Spacal cluster energy. The right plot is obtained with the same selection as the left one.

The efficiency of the  $E - p_z > 35$  GeV selection for data and Monte Carlo simulation as a function of the Spacal cluster energy is presented in Fig. 6.12-right. Good agreement between data and Monte Carlo simulation is seen. The reduction of the cut efficiency towards low  $E'_e$  means that the initial state radiation and  $\gamma p$  background events are largely suppressed.

## 6.5 Event Validation using the Central Inner Proportional Chamber

A cluster in the backward calorimeter was defined as *CIP validated* if there was an active pad inside 5 cm distance from the trajectory connecting the backward tracker point with the reconstructed event vertex. The CIP validation was used only for clusters with electron trajectories inside the chamber acceptance region. The latter extends up to about  $171^\circ$ . Thus practically all high  $y > 0.6$  data were subject to the CIP cut.

The main goal of the CIP validation has been to reject background to the DIS events coming from neutral particles, predominantly from  $\pi^0 \rightarrow 2\gamma$  decays. Being situated before the dead material of the central tracker readout electronics, the CIP has a much higher probability to reject photons before conversion than the backward tracking chamber. The CIP validation was preferred to the link to a CJC track in the interval  $0.6 < y \lesssim 0.75$  since it has a larger acceptance region, higher and simpler controllable efficiency.

As was discussed in Sec. 6.2 the estimation of the tracker efficiency can be divided into two parts: the determination of the “hardware” availability of the detector to detect the scattered electron, which can be done in the background free region of  $E'_e > 20$  GeV, and the description of the background suppression. Both are presented in Fig 6.13, as a comparison between data and Monte Carlo simulation. The experimental and simulated distributions agree well.

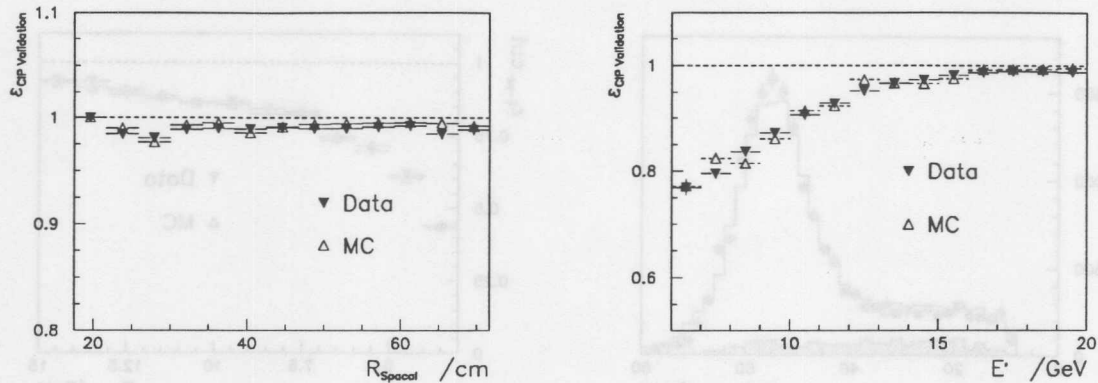


Figure 6.13: CIP validation efficiency for the “ $F_2$  1996” analysis. The left plot presents the efficiency for DIS events ( $E'_e > 20$  GeV) as a function of the scattered electron impact point on the Spacial plane. The right plots displays a comparison of the efficiency as a function of the Spacial cluster energy. The background estimation for this plot is based on the PHOJET simulation.

## 6.6 Event Validation using the Central Drift Chambers

The 1996 data analysis aimed to measure the double differential DIS cross section at largest possible  $y$ , or correspondingly at lowest energies of the scattered electron below 7 GeV. In this kinematic range the  $\gamma p$  background becomes very large. More strict selection criteria have to be applied in order to reduce it. Also a better estimate for the remaining background contamination was required than obtained by the Monte Carlo simulation which had an uncertainty of 20 – 30%. Both these goals were achieved by linking the Spacial cluster to a track in the CJC. The more strict selection of charged particles together with the possibility to demand the charge of the track to be positive reduces the background much stronger than the simple CIP validation. Employing the charge symmetry (Sec. 3.6.1) of the background its remaining amount was estimated using the events rejected by the charge requirement. This amount was subtracted bin by bin.

The CJC acceptance region is well suitable for the highest  $y$   $F_L$  analysis for four  $Q^2$  bins 12 – 25 GeV<sup>2</sup>. But the link to the CJC had also some drawbacks, requiring to reproduce the track link efficiency and the CJC charge resolution.

### CJC Acceptance and Link Efficiency

The CJC track acceptance was studied as a function of  $R_{CJC} = (Z_{CJC} - Z_{\text{vertex}}) \tan \theta_e$ , see Fig 6.14-left, where  $Z_{CJC} = -112.4$  cm is the backward limit of the sensitive chamber volume. This variable determines the radius at which the scattered electron, defined by the Spacial cluster and the event vertex position, escapes the CJC.

A CJC track was assumed to be linked to a BDC point if the distance between its helix extrapolation to the BDC plane and the BDC point was smaller than 6 cm. The track link efficiency for DIS events with  $E'_e > 20$  GeV as a function of  $R_{CJC}$  is presented in Fig. 6.14-right. A cut of  $R_{CJC} > 30$  cm was applied in the analysis. For  $R_{CJC}$  values bigger than 30 cm the link efficiency was about 90% in the data and 95% in the Monte Carlo simulation. A global 5% correction was applied to the latter.

A distribution of the distances between the extrapolated CJC track and the BDC point for data and Monte Carlo simulation is presented in Fig. 6.15-left. A long tail in the data distribution up to

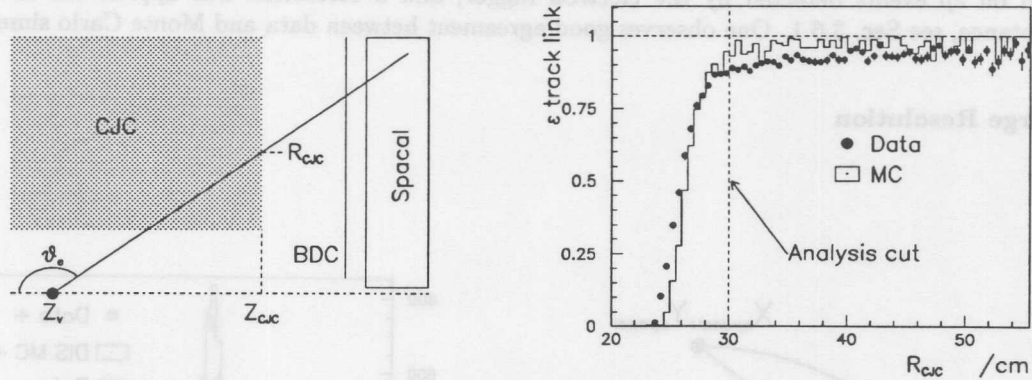


Figure 6.14: Left: schematic view of the  $R - Z$  cross section of the backward H1 detector, used for the CJC link efficiency definition. Right: CJC track link efficiency as a function of  $R_{CJC}$  for data and Monte Carlo simulation.

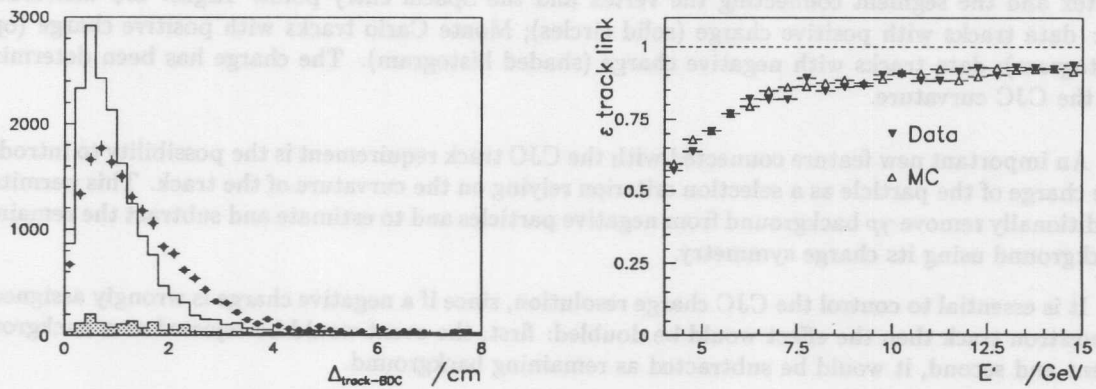


Figure 6.15: Left: Distribution of the spatial difference of a CJC track extrapolated to the BDC plane and the BDC point reconstruction. Solid circles represent data. The shaded histogram is the  $\gamma\gamma$  background estimated with the acceptance corrected tagged events (Sec. 3.6.1). The open histogram corresponds to the sum of simulated DIS and background distributions. The plot is based on the 1996  $F_L$  analysis. All cuts apart from the  $E - p_z$  cut and the CJC-BDC link requirement are applied. Right: efficiency of the CJC track - BDC link as a function of the cluster energy  $E'$ .

$\Delta_{track-BDC} \approx 4$  cm is caused by the CJC  $\theta$  measurement bias for tracks not linked to the Z chambers which was not reproduced in Monte Carlo simulation. For  $\Delta_{track-BDC} = 6$  cm, where the cut was applied, the influence of the discrepancy between data and Monte Carlo distributions vanishes.

The efficiency of the CJC track - BDC point link as a function of the cluster energy is presented in Fig. 6.15-right for data and Monte Carlo simulation. The photoproduction background was estimated based on  $ep$  events detected by the electron tagger, and a correction was applied for the tagger acceptance, see Sec. 3.6.1. One observes good agreement between data and Monte Carlo simulation.

### Charge Resolution

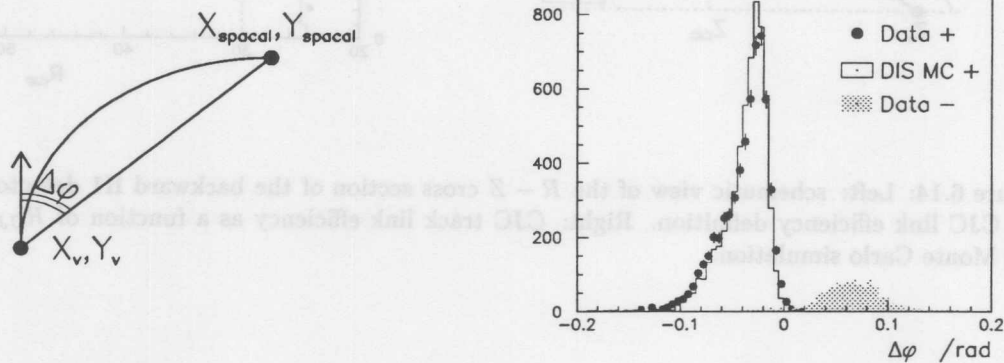


Figure 6.16: Left:  $x, y$  projection of the scattered electron track.  $X_v, Y_v$  define the vertex position,  $X_{spacal}, Y_{spacal}$  the Spacal entry point.  $\Delta\phi$  is the azimuthal angle between the track direction at the vertex and the segment connecting the vertex and the Spacal entry point. Right:  $\Delta\phi$  distribution for: data tracks with positive charge (solid circles); Monte Carlo tracks with positive charge (open histogram); data tracks with negative charge (shaded histogram). The charge has been determined by the CJC curvature.

An important new feature connected with the CJC track requirement is the possibility to introduce the charge of the particle as a selection criterion relying on the curvature of the track. This permits to additionally remove  $\gamma p$  background from negative particles and to estimate and subtract the remaining background using its charge symmetry.

It is essential to control the CJC charge resolution, since if a negative charge is wrongly assigned to a positron track then the effect would be doubled: first, the event would be rejected as a background event and second, it would be subtracted as remaining background.

Two methods were introduced to cross check the CJC charge resolution. One was based on a pure geometry estimation, the other on a study of the  $P_t$  resolution of the track comparing to the Spacal energy measurement. The idea of the first approach is illustrated in Fig. 6.16-left. Let us consider the  $X, Y$  projection of an event with a vertex  $X_v, Y_v$ , a positron track reconstructed in the CJC and the Spacal center of cluster position  $X_{spacal}, Y_{spacal}$ . In this plane the trajectory of the positron can be approximated by an arc of a circle. We denote as  $\Delta\phi$  the azimuthal angle between the track direction at the interaction point, reconstructed in the CJC, and the segment connecting the vertex and the Spacal cluster position. The sign of  $\Delta\phi$  is defined by the direction of the track rotation and therefore can be used for an independent charge determination. Closed circles (shaded histogram) in Fig. 6.16-right show the  $\Delta\phi$  distribution of tracks from  $ep$  interactions with positive (negative) charge



determined in the CJC. The open histogram represents the Monte Carlo simulation of  $\Delta\phi$  for positive tracks. The plot is restricted to events with  $E' < 15$  GeV. For both data and Monte Carlo simulation in 99.5% of the cases the charges assigned by the CJC and by the sign of  $\Delta\phi$  agree. The remaining 0.5% can be explained as being due to the tail of the Spacal  $\phi$  resolution. Note that we prefer the Spacal measurement over the BDC information due to its more accurate  $\phi$  resolution, see Sec. 5.1.

The second cross check of the CJC charge resolution was obtained by studying the CJC  $P_t$  resolution using the Spacal energy measurement. A wrong charge assignment in the tracking chamber can occur for events with too straight reconstructed tracks, i.e.  $P_t \rightarrow \infty$ . This can be studied with the backward calorimeter. Fig. 6.17 shows  $E_t^{Spacal}/p_t^{CJC}$  distributions for two different energy slices,  $13 < E' < 15$  GeV and  $25 < E' < 27$  GeV. A too large  $P_t$  reconstructed in the tracker would lead to a tail in the distribution towards  $E_t^{Spacal}/p_t^{CJC} \rightarrow 0$ . This tail is seen for the high energy region. Yet, for  $E' < 15$  GeV the peak is well separated from zero. With a significance of four standard deviations the charge reconstruction in the CJC for  $E' < 15$  GeV appears to be correct as can be concluded from this plot.

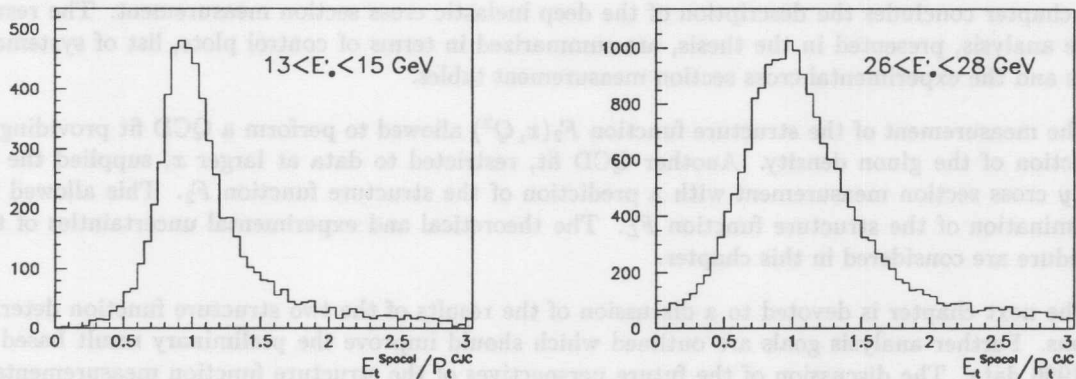


Figure 6.17:  $E_t^{Spacal}/p_t^{CJC}$  distributions for different  $E_e'$  slices, see text. A separation of the  $E_t^{Spacal}/p_t^{CJC}$  distribution from zero corresponds to possibility of a correct charge assignment. This is seen for  $13 < E' < 15$  GeV, while in the high energy interval  $26 < E' < 28$  GeV the tail of the distributions extended towards low  $E_t^{Spacal}/p_t^{CJC}$  values correspond to wrong charge assignments.

It was found in data and Monte Carlo simulation that in more than 98% of the cases only one track was linked to a Spacal cluster within the cut of 6 cm. If more than one track was associated with the cluster and the signs of these tracks were different, a positive sign was chosen.

## Chapter 7

# DIS Cross Section, $F_2$ and $F_L$ Results

This chapter concludes the description of the deep inelastic cross section measurement. The results of the analysis, presented in the thesis, are summarized in terms of control plots, list of systematic errors and the experimental cross section measurement tables.

The measurement of the structure function  $F_2(x, Q^2)$  allowed to perform a QCD fit providing an extraction of the gluon density. Another QCD fit, restricted to data at larger  $x$ , supplied the H1 high  $y$  cross section measurement with a prediction of the structure function  $F_2$ . This allowed the determination of the structure function  $F_L$ . The theoretical and experimental uncertainties of this procedure are considered in this chapter.

The next chapter is devoted to a discussion of the results of the two structure function determinations. Further analysis goals are outlined which should improve the preliminary result based on the 1996 data. The discussion of the future perspectives of the structure function measurements at HERA ends the thesis.

## 7.1 Final Monte Carlo Simulation Adjustment and Control Plots

The previous chapters described many adjustments applied to data or to the Monte Carlo simulation. These are, for example, the  $Z$  vertex reweighting (Sec. 4.4), the energy calibration (Sec. 5.2) and CJC efficiency corrections (Sec 6.6). To study the experimental spectra which depend on the kinematics, a final correction of the Monte Carlo simulation has been important, tuning the assumed DIS cross section to correspond to the experimental measurement.

This correction was done using a reweighting technique. Each Monte Carlo event was weighted by the ratio of the full double differential cross sections calculated from the generated kinematics:

$$W_{kin} = \frac{\sigma_{new}(x, y, Q^2)}{\sigma_{old}(x, y, Q^2)}. \quad (7.1)$$

$\sigma_{old}(x, y, Q^2)$  was evaluated with the GRV-LO 94 parameterization of  $F_2$  and  $F_L = 0$  as used during the Monte Carlo production.  $\sigma_{new}(x, y, Q^2)$  was obtained using the structure functions  $F_2$  calculated from the QCD fit (Sec. 7.4) and  $F_L$  derived from the GRV-503 parameterization of the parton densities. The latter was used as well for the extraction of the structure  $F_2$  from the cross section measurement.

In order to simplify the calculation of the full cross sections, the event kinematics was determined at the hadronic vertex. The Born formula was sufficient in this case.

With such a reweighting technique it is possible to cross check the simulation of the detector response and the applied efficiency corrections which are supposed to result in nearly coinciding experimental and Monte Carlo distributions. For the determination of the DIS cross section, however, the reweighting is less demanding since the cross section assumptions largely cancel in the acceptance calculation (Sec. 3.7).

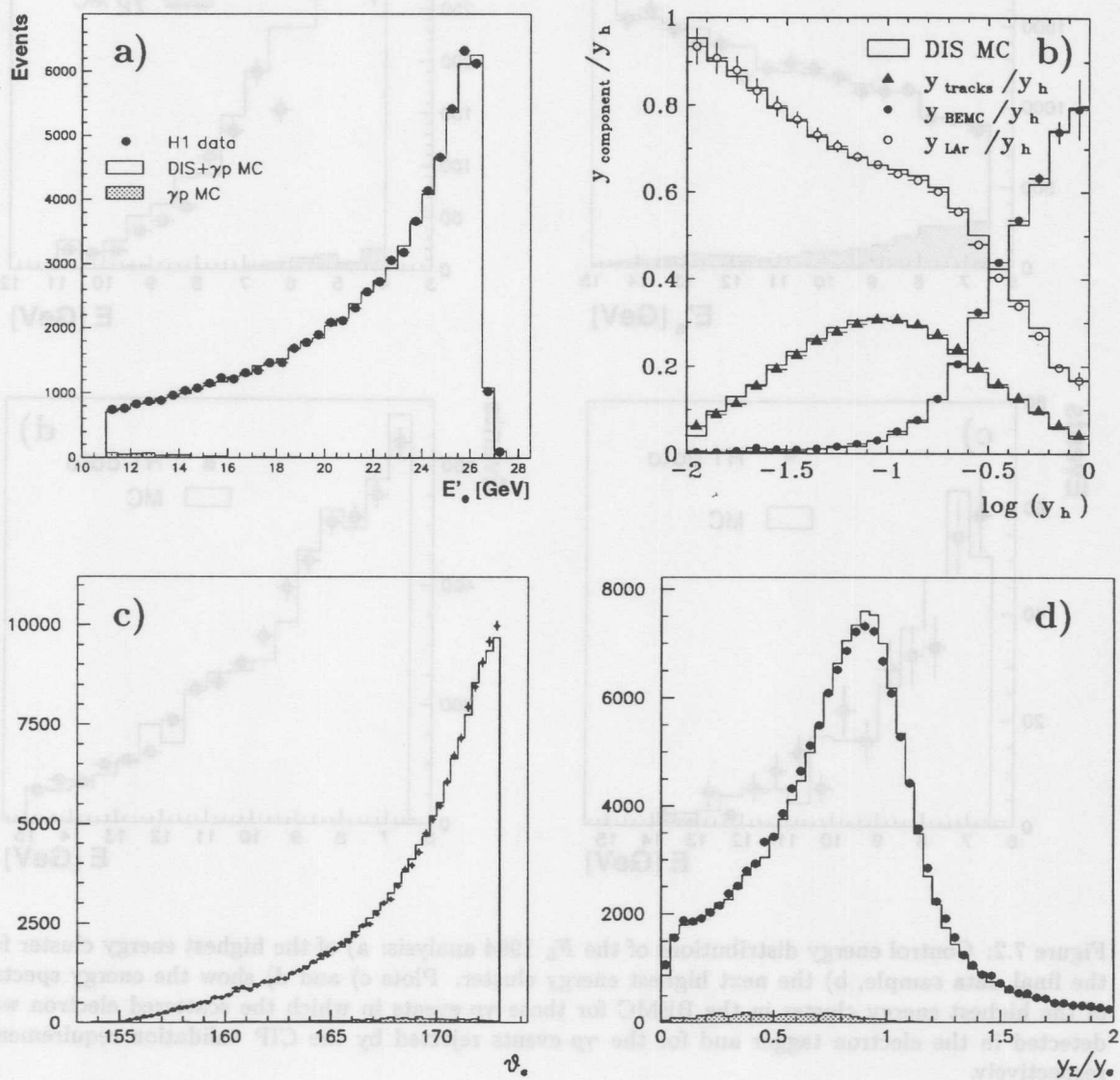


Figure 7.1: Control distributions of the 1994  $F_2$  analysis: a) of the energy of the scattered electron, b) of the fraction of  $y_h$  contributed by tracks, by the LAr calorimeter and by the BEMC (from [33]), c) of the polar angle of the scattered electron and d) of the ratio  $y_z/y_e$ , for  $y_e > 0.05$

Fig. 7.1 presents control plots of the  $F_2$  1994 analysis. Figure a) shows an excellent agreement between experimental and simulated distributions of the scattered electron energy measured in the BEMC. Figure b) compares the different  $y_h$  components. The quality of the Monte Carlo description is slightly better than in the similar figure for the 1996 data (see Fig 5.12). Figure c) shows the

$\theta_e$  distribution which demonstrates a good understanding of the detector acceptance. A control of the hadronic measurement is provided again in figure d), where the  $y_\Sigma/y_e$  distribution is given for  $y_e > 0.05$  (see Fig. 5.14 for the same comparison based on the 1996 data).

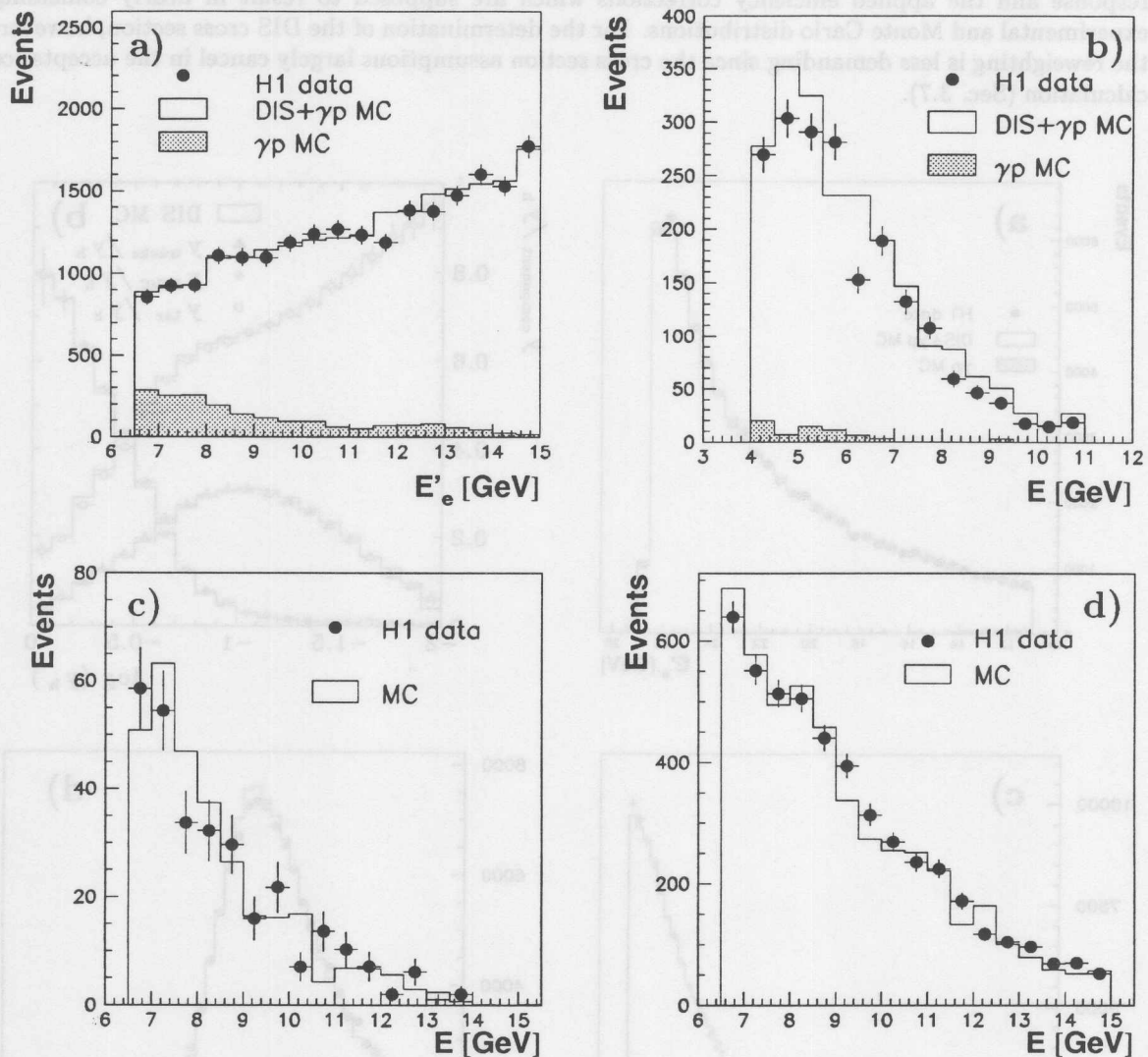


Figure 7.2: Control energy distributions of the  $F_L$  1994 analysis: a) of the highest energy cluster for the final data sample, b) the next highest energy cluster. Plots c) and d) show the energy spectra of the highest energy cluster in the BEMC for those  $\gamma p$  events in which the scattered electron was detected in the electron tagger and for the  $\gamma p$  events rejected by the CIP validation requirement, respectively.

Control distributions of the 1994  $F_L$  analysis are shown in Fig. 7.2. The understanding of the Monte Carlo description of the electron identification is illustrated in plots a) and b), where the energy distributions of the highest and the next highest energy cluster in the BEMC are displayed. Note that only the two highest energy clusters were considered in the  $F_L$  1994 analysis, see Sec. 3.5. The quality of the  $\gamma p$  background control is presented in figures c) and d), which show energy spectra of the highest energy cluster in the BEMC for events in which the scattered electron was detected in electron tagger and for the events rejected by the CIP validation requirement, respectively. The

agreement of the experimental and simulated distributions visible in these plots permitted to reduce the uncertainty of the PHOJET based  $\gamma p$  background estimation from 30% assigned in the 1994  $F_2$  analysis to 20% for the 1994  $F_L$  analysis.

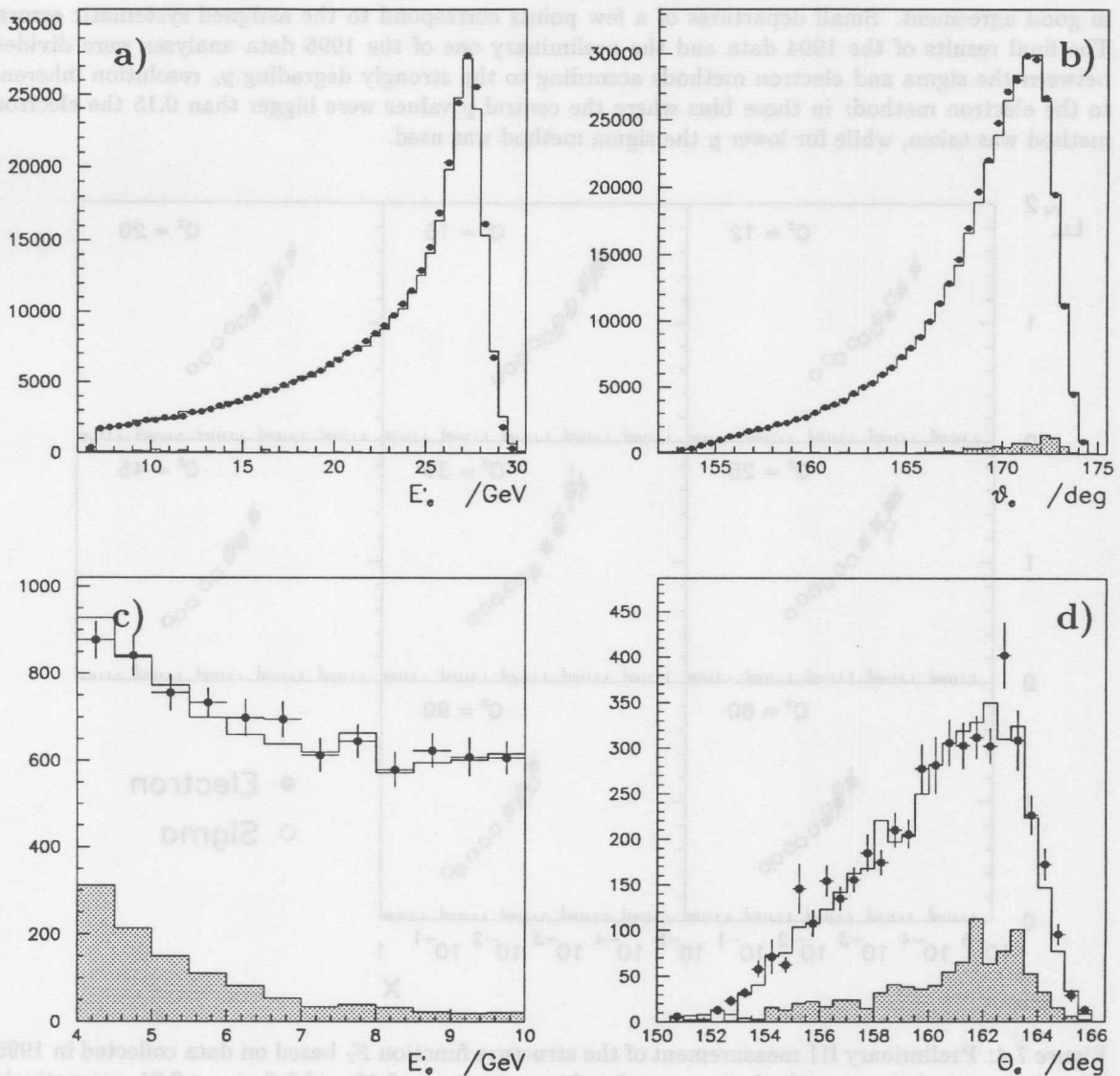


Figure 7.3: Control distributions of the 1996  $F_2$  and  $F_L$  analysis: a) and c), respectively, distributions of the energy of the scattered electron; b) and d), respectively, distributions of the polar angle of the scattered electron. The experimental results are shown as closed circles. The shaded histograms correspond to the  $\gamma p$  background estimation. The open histograms show the sum of the DIS Monte Carlo simulation and the  $\gamma p$  background.

The 1996 analysis has been presented in this thesis in more detail than the studies based on the 1994 data. We refer here to the plots shown in the sections 3.5, 3.6.1, 5.3 for the electron identification, photoproduction background and hadronic  $\gamma$  investigations. A summary of the 1996  $F_2$  and  $F_L$  analyses is displayed in Fig. 7.3. Plots a),c) show the scattered electron energy distributions and b),c) the polar angle distributions for the low  $y$  and the high  $y$  studies, respectively. For the high  $y$  distributions the Monte Carlo reweighting function was modified by adjusting also the longitudinal structure function  $F_L(x, Q^2)$ , derived from the GRV-503 parameterization, to an 1.4 times larger value

as was required by the measurement.

Fig. 7.4 shows the comparison of the determination of the structure function  $F_2$  based on the electron and sigma methods for the 1996 analysis. This test allows to check various systematic errors due to the detector calibration, radiative corrections and different smearing effects. The results are in good agreement. Small departures of a few points correspond to the assigned systematic errors. The final results of the 1994 data and the preliminary one of the 1996 data analyses were divided between the sigma and electron methods according to the strongly degrading  $y_e$  resolution inherent to the electron method: in those bins where the central  $y$  values were bigger than 0.15 the electron method was taken, while for lower  $y$  the sigma method was used.

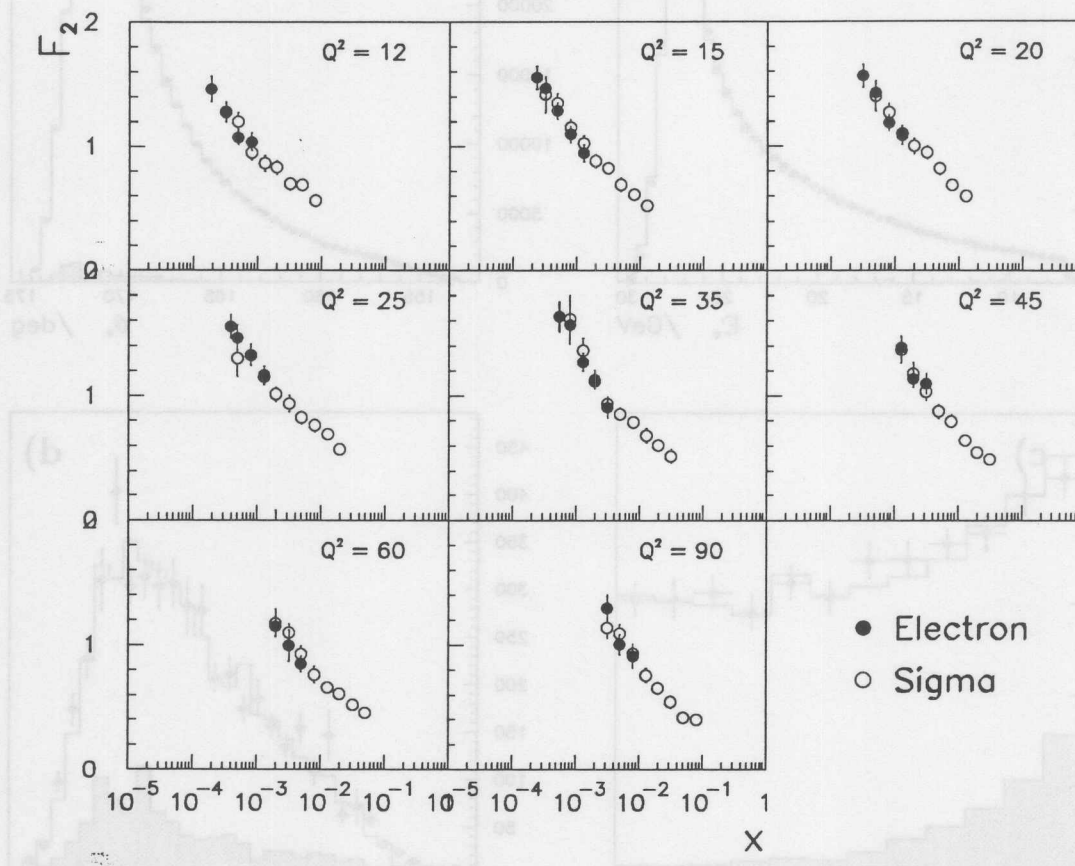


Figure 7.4: Preliminary H1 measurement of the structure function  $F_2$  based on data collected in 1996. The electron and sigma methods were restricted to a range  $y > 0.15$  and  $0.6 < y < 0.01$ , respectively. The errors are quadratical sum of systematic and statistical errors.

## 7.2 Summary of the Systematic Error Sources

Based on the studies presented in the thesis, the sources listed below were considered in the systematic error calculation. To estimate their influence on the cross section measurement they were applied one after another to the Monte Carlo simulation events. The following uncertainties were assigned:

- An uncertainty of the luminosity measurement of 1.5% and 1.4% for the 1994 and 1996 analyses, respectively.

- An uncertainty of 1% (1%) at  $E'_e = 27$  GeV and of 1% (3%) at  $E'_e = 7$  GeV was assigned to the electron energy scale for the BEMC (Spacal) calorimeter (Sec. 5.2). This variation leads to a large uncertainty of the DIS cross section measured with the electron method at low  $y$ , but for  $y > 0.15$  the effect is about 1 – 4%. The resulting uncertainty of the DIS cross section measurement using the sigma method measurement is about 1 – 2%.
- An uncertainty of up to 1 mrad for the electron polar angle measurement which leads to an error on the cross section of 1 – 3%.
- Uncertainties in the hadronic energy scale (Sec. 5.3) of 4% for the LAr calorimeter, of 3% for the  $y_h$  fraction carried by tracks and of 15% for the BEMC and of 7% for the Spacal calorimeters. These errors take into account the intrinsic energy scale uncertainty of each detector and the uncertainty of the sharing of the total hadronic final state energy between the subdetectors. The numbers also include uncertainties due to the treatment of the electronic noise in the calorimeters. The quoted change of the hadronic scale leads to variations of  $F_2$ , calculated by the sigma method, of 1 – 2% in the  $y$  range 0.4 – 0.02. The uncertainty increases at the edge of the  $y$  acceptance to 5 – 7%.
- An uncertainty of the vertex reconstruction efficiency (Sec. 6.1) of overall 2% for the cross section measurement. For the lowest  $Q^2 = 8.5$  GeV<sup>2</sup> bin in the  $F_2$  1994 analysis, where the low luminosity “open triangle” data sample was used, the uncertainty was increased to 4%.
- Uncertainties coming from the imperfect description of various efficiencies, disregarding here the vertex and track link conditions, of 2% for the 1994 and 1996 cross section measurements (Sec. 6).
- Uncertainties in the description of the radiative corrections (Sec. 3.4) of 2% for the DIS cross section measurement for  $y < 0.8$ . The error assigned to the highest  $y$  bin in the 1996  $F_L$  analysis is 3%.
- The following uncertainties are due to the photoproduction background:
  - for the  $F_2$  1994 analysis 30% of the background estimated with the PHOJET program, leading to a maximum cross section error of 3.3% in the lowest  $Q^2, x$  bin;
  - for the 1994  $F_L$  analysis 20% of the PHOJET estimation (Sec 7.1), leading to the maximum 4.3% cross section error in the lowest  $Q^2$  bin;
  - for the 1996  $F_2$  analysis 30% of the PHOJET estimation, which lead to a maximum 3% cross section error;
  - the charge symmetry of the photoproduction background has been experimentally verified up to 3% (Sec. 3.6.1) which for the 1996  $F_L$  analysis lead to a maximum error of 1% due to  $\gamma p$  events.
- The uncertainty in the description of the electron identification gives rise to an additional error for  $y > 0.6$ . It is estimated as 1% and 3% uncertainty for the cross section measurements in the 1994 and 1996 data analyses, respectively (Sec. 3.5).
- The uncertainty of the trigger efficiency leads to an error of the cross section measurement (Sec. 4.6) of 1% for the 1996  $F_2$  and of 3% for the 1996  $F_L$  analyses; a 3% error was assigned for the 1994  $F_L$  analysis which comprised as well uncertainties due to sharpened electron identification cuts.
- The uncertainty of the central track link efficiency leads to an error of the cross section measurement of 3% for the 1996  $F_L$  analysis (Sec. 6.6);
- The uncertainty of the charge resolution for the 1996  $F_L$  analysis leads to a 1% error of the cross section measurement (Sec. 6.6).

- The uncertainty coming from the hadronic vertex requirement in the 1996  $F_L$  analysis leads to an additional error of the cross section measurement of 2% (Sec. 6.1).

The total systematic error of the DIS cross section measurement was about 5% for the range  $0.6 < y < 0.02$ , 7% for  $y < 0.03$  and 6 – 7% for  $0.6 < y < 0.75$  increasing up to 9 – 10% for  $y > 0.75$ .

### 7.3 DIS Cross Section and $F_2(x, Q^2)$ Results

The results of all deep inelastic cross section measurements discussed in this thesis are listed in Tables A.3, A.4, A.5, A.6. Fig. 7.5 shows the structure function  $F_2$  of the 1994, 1995 and the 1996 H1 analyses together with the high  $x$  data of NMC. The analyses presented in this thesis contributed to the 1994 data for  $8.5 \leq Q^2 \leq 120 \text{ GeV}^2$  and to the 1996 data for  $12 \leq Q^2 \leq 90 \text{ GeV}^2$ . The values of  $R(x, Q^2)$  used for the extraction of the structure function  $F_2(x, Q^2)$  were calculated using GRV parton density parameterizations. The corresponding values are given in the tables. Fig. 7.5 shows a remarkable agreement between the 1994 and 1996 data points in spite of the fact that two different backward equipments were used. Small departures between the two datasets are due to local systematic effects, and they are covered by the systematic errors. The curves in the figure show a QCD fit to next-to-leading order which is used for a determination of the gluon density as will be described in the next section.

The structure function  $F_2(x, Q^2)$  in Fig. 7.5 is restricted to bins with central  $y$  values satisfying the condition  $y \leq 0.7$ . The double differential cross section measurements, extending up to  $y = 0.82$  are shown in Fig. 7.6. The 1994 and 1996 H1 datasets are represented here, the analysis described in this thesis contributed to both of them. The curves in the figure are based on the result of the QCD fit to the  $F_2$  measurement at low  $y$  as described in Sec. 7.5. The cross section curves were calculated using three different assumptions on  $F_L$ : the dotted and dashed lines correspond to the limits  $F_L = 0$  and  $F_L = F_2$ , respectively, the solid line represents the cross section with  $F_L$  calculated up to NLO using the gluon and quark distributions obtained by the QCD fit. An indication of a departure of the highest  $y$  experimental points from the NLO QCD calculation is seen. It can be interpreted as a larger structure function  $F_L$  than predicted by this theory.

It is important to stress here that the H1 DIS cross section measurement based on the 1996 data is still preliminary. Although many studies of systematic effects have been performed, especially in the high  $y$  domain (as presented in the thesis), further analysis will take place including the now available data of the 1997 HERA run. This may change the final result. In the following discussion, we will always have in mind this fact but consider to which physics conclusions the current preliminary result hints.

### 7.4 Determination of the Gluon Distribution $xg(x, Q^2)$

Based on the measurement of the structure function  $F_2$  the gluon density function can be extracted within the framework of NLO QCD. In this section a determination of  $xg(x, Q^2)$  from the combined data set, using all H1 data from the years 1994 – 1996, is discussed. More details on this result can be found in [96].

A NLO QCD fit was performed in the  $\overline{MS}$  renormalization scheme using the DGLAP evolution equations [14]. The fit used three light flavours with the charm and bottom contributions added using the NLO calculation of the photon-gluon fusion process [17, 18]. The numeric solution of the evolution equations is described in [43].



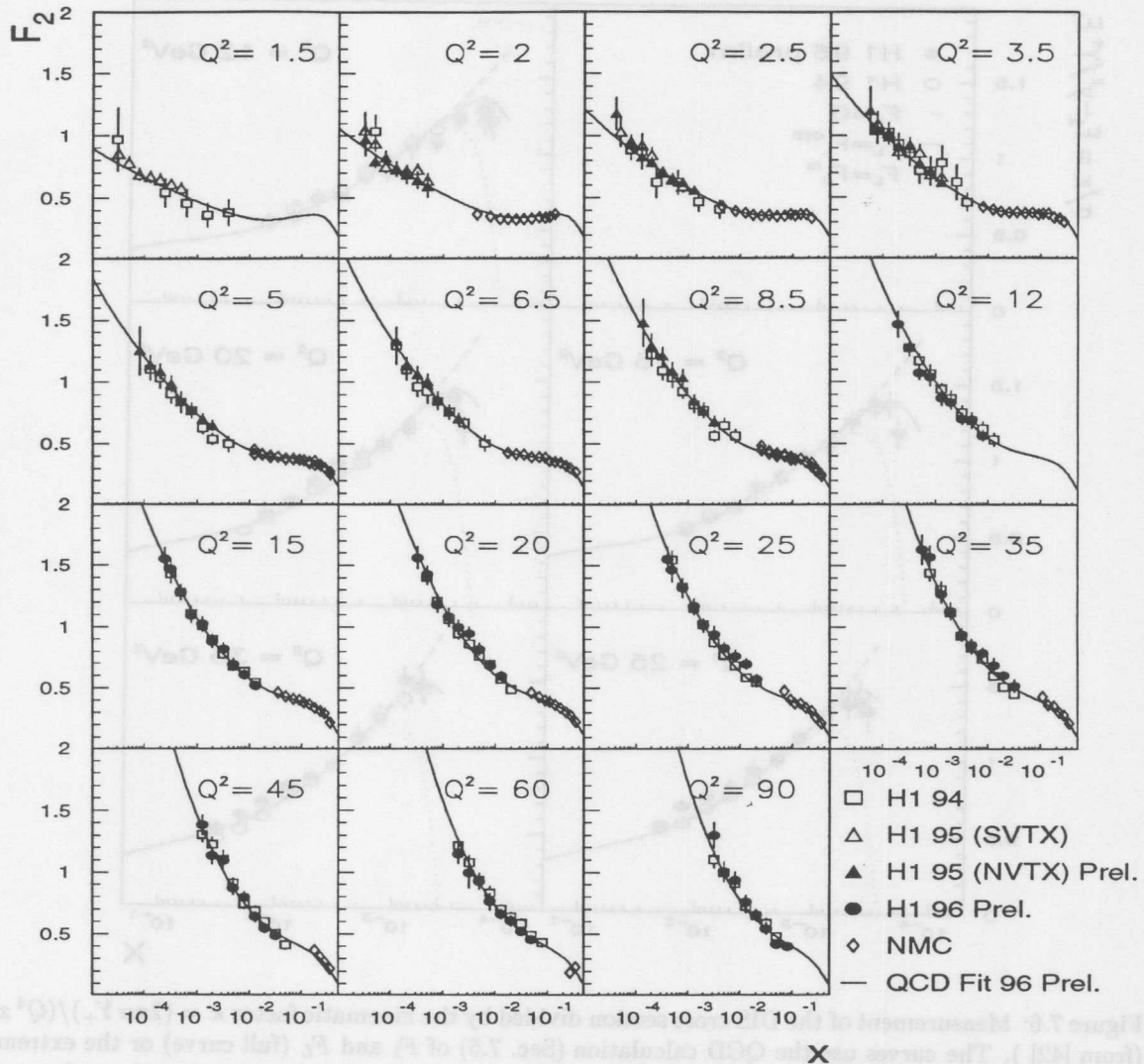


Figure 7.5: Determinations of the structure function  $F_2(x, Q^2)$  by the H1 experiment (from [42]). The curves represent the preliminary result of a NLO QCD fit to the H1, NMC and BCDMS structure function data, described in Sec. 7.4.

The input parton distributions at the starting scale  $Q_0^2$  were parameterized as follows:

$$\begin{aligned}
 xg(x) &= A_g x^{B_g} (1-x)^{C_g}, \\
 xu_v(x) &= A_u x^{B_u} (1-x)^{C_u} (1 + D_u x + E_u \sqrt{x}), \\
 xd_v(x) &= A_d x^{B_d} (1-x)^{C_d} (1 + D_d x + E_d \sqrt{x}), \\
 xS(x) &= A_S x^{B_S} (1-x)^{C_S} (1 + D_S x + E_S \sqrt{x}),
 \end{aligned} \tag{7.2}$$

where  $S = 2\bar{u} = 2\bar{d} = 4\bar{s}$  defines the sea distributions. The momentum sum rule was imposed and the integral over the valence quark distributions was set to 2 for  $u_v$  and to 1 for  $d_v$ .

The starting point of the evolution for the combined fit was chosen to be  $Q_0^2 = 1 \text{ GeV}^2$  contrary to the 1994 fit [33] where  $Q_0^2 = 5 \text{ GeV}^2$  was taken. The reason was that for  $Q_0^2 = 1 \text{ GeV}^2$  the gluon has a valence-like shape and can be better described by the three parameter function (Eq. 7.2) while at higher  $Q^2$  the shape becomes more complicated and the results start to depend on the choice of the initial parameterization.

The fit used 1994 [33] and 1996 [42] H1 data presented in this thesis, H1 data from shifted [39] and nominal vertex runs in 1995 [42] and data from the fixed target experiments NMC [81] and

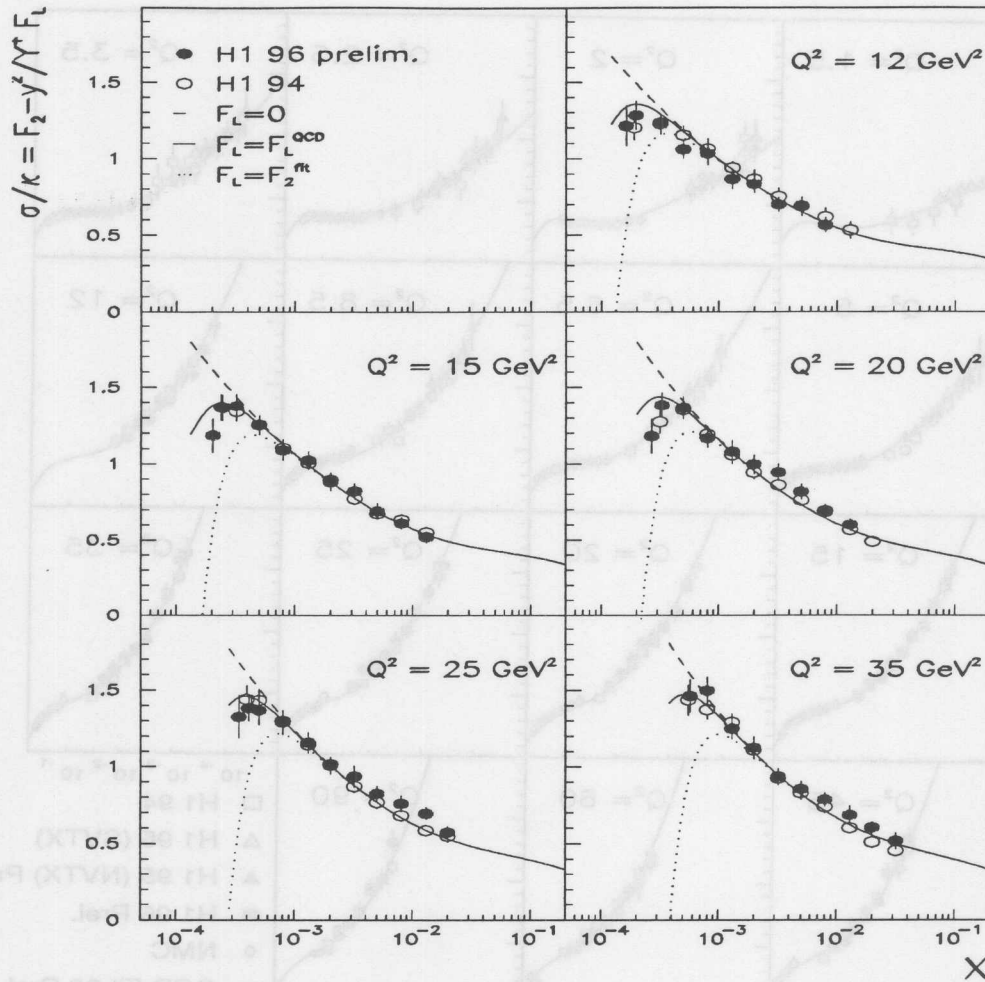


Figure 7.6: Measurement of the DIS cross section divided by the kinematic factor  $\kappa = (2\pi\alpha Y_+)/ (Q^4 x)$  (from [42]). The curves use the QCD calculation (Sec. 7.5) of  $F_2$  and  $F_L$  (full curve) or the extreme assumptions  $F_L = F_2$  (dotted curve) and  $F_L = 0$  (dashed curve). The largest central  $y$  values are 0.82. For  $Q^2 \geq 35 \text{ GeV}^2$  this  $y$  range is outside the Spacal acceptance.

BCDMS [79]. All data with  $Q^2 \geq Q_{min}^2 = 1.5 \text{ GeV}^2$  were included in the fit. To avoid possible higher twist effects, BCDMS data in the range  $x > 0.5$  for  $Q^2 < 15 \text{ GeV}^2$  were excluded from the fit. The normalizations of all datasets were allowed to vary taking into account the quoted normalization errors. For the fit a value of  $\alpha_s(M_Z^2) = 0.118$  was chosen.

To calculate the systematic error band of the gluon density twenty two distinct QCD fits were performed with the input experimental  $F_2$  points changed according to different correlated error sources. Four different groups of systematic errors were distinguished: 1) electron energy scale in the backward calorimeter; 2) electron energy scale in the LAr calorimeter; 3) electron polar angle uncertainty 4) hadronic energy scale uncertainty. The 94 BEMC-BPC based data were changed independently from the Spacal-BDC ones. Nevertheless, due to a similar procedure adopted for the energy calibration and the same CJC based method of the alignment, the systematic uncertainties of the data collected with the 1994 and 1995-1996 detector setups are partially correlated. Conservatively assuming a large correlation, the changes of the gluon density were added linearly inside each group of error sources and then the quadratical sum was calculated over all groups.

The remaining sources of the systematic uncertainties, like uncertainties of various efficiency es-

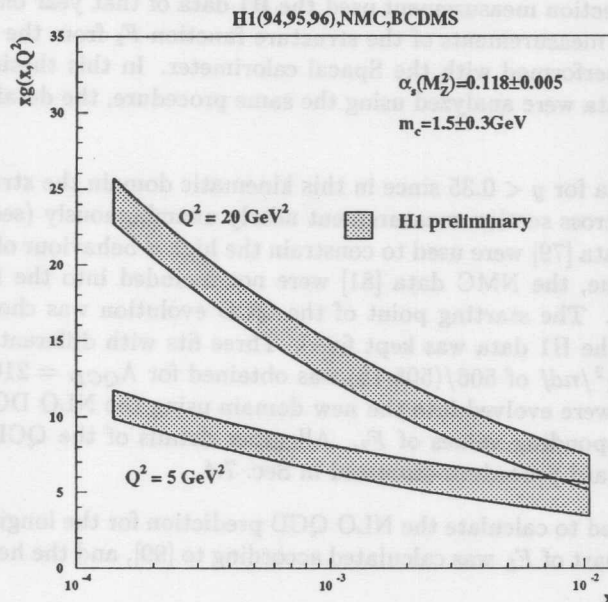


Figure 7.7: Gluon distribution resulting from a NLO QCD fit to the H1 structure function data, to the NMC and BCDMS data. The error band comprises the statistical and systematic errors and also the uncertainties due to  $\alpha_S$ , the charm quark mass  $m_c$  and due to the loosely constrained behaviour of  $xg$  at high  $x > 0.1$  (from [42]).

timations, of  $\gamma p$  background subtraction and of radiative corrections were treated as uncorrelated. They were added quadratically to the statistical errors. These combined errors were included into the fit individually for each measured value.

The resulting distribution  $xg(x, Q^2)$  for  $Q^2$  values of 5 and 20  $\text{GeV}^2$  is displayed in Fig. 7.7. Apart from the systematic uncertainties the error band comprises the effect of the variations of  $\alpha_S(M_Z^2)$  by  $\pm 0.005$  and of  $m_c$  by  $\pm 0.3$   $\text{GeV}$ . The latter effects give rise to large contributions. Taking the  $\alpha_S$  dependence, as an example, the scaling violation of the structure function  $F_2$  is proportional to the product of the gluon density and  $\alpha_s$ , i.e. a change of +4% of  $\alpha_S$  leads to an about -4% change of  $xg$ .

It is known that the determination of the gluon distribution using only the structure functions data obtained with charged leptons leads to a behaviour of  $xg$  at high  $x$  which differs from the result of global analyses which include direct photon data of the WA 70 experiment [98]. Therefore the presentation of the gluon distribution is limited to the range  $x < 0.01$ . A special fit was done with a five parameter gluon distribution fixing the parameters which determine the high  $x$  behaviour of  $xg$  in order to reproduce a rather standard gluon parameterization [97]. This leads to a gluon distribution which was lower by  $\sim 10\%$  at  $x = 0.01$  as compared to the unconstrained, three parameter gluon ansatz. The difference of these two fits was included into the error band. It is almost negligible for  $x \lesssim 10^{-3}$ .

## 7.5 QCD Fit for the Extraction of the Structure Function $F_L(x, Q^2)$

NLO QCD fits were performed using the DGLAP evolution equations in order to extract the longitudinal structure function  $F_L$  by subtracting the  $F_2$  contribution to the cross section, see Sec. 3.8. In order to achieve a partial cancelation of the systematic errors in the subtraction procedure, two

separate fits were done for the 1994 and the 1996 data analyses. The fit for the  $F_L$  extraction based on the 1994 high  $y$  cross section measurement used the H1 data of that year only. The fit for the second  $F_L$  determination used measurements of the structure function  $F_2$  from the data taking periods 1995 and 1996 which were performed with the Spacal calorimeter. In this thesis the 1994  $F_L$  analysis is described. The 1996 data were analyzed using the same procedure, the details of this fit can be found in [96].

The fit used H1 data for  $y < 0.35$  since in this kinematic domain the structure function  $F_2(x, Q^2)$  is defined by the DIS cross section measurement nearly unambiguously (see Sec. 3.8). The BCDMS proton and deuteron data [79] were used to constrain the high  $x$  behaviour of the parton distributions. For the central fit value, the NMC data [81] were not included into the fit to ensure a maximum weight of the H1 data. The starting point of the QCD evolution was chosen to be  $Q_0^2 = 5 \text{ GeV}^2$ . The normalization of the H1 data was kept fixed. Three fits with different, fixed  $\Lambda_{QCD}$  values were performed. The best  $\chi^2/ndf$  of 506/(505-15) was obtained for  $\Lambda_{QCD} = 210 \text{ MeV}$ . The fitted parton distribution functions were evolved into the new domain using the NLO DGLAP equations and used to calculate the corresponding values of  $F_2$ . All other details of the QCD fit program were taken exactly as in the standard procedure discussed in Sec. 7.4.

This fit was also used to calculate the NLO QCD prediction for the longitudinal structure function  $F_L$ . The light flavour part of  $F_L$  was calculated according to [99], and the heavy quark part was added according to [18].

Three kinds of uncertainties arose for the prediction of the structure functions in the high  $y$  region. First of all, these are different assumptions in the QCD fit procedure, like  $\Lambda_{QCD}$  or  $Q_0^2$ . These “theoretical” ambiguities will be discussed in the next section, together with the second source of extrapolation uncertainties related to the residual dependence of the input  $F_2(x, Q^2)$  data points on the assumed  $R(x, Q^2)$  used for their extraction. The section after next is devoted to the last source of uncertainties of the QCD fit caused by the systematic errors of the measured structure function  $F_2$ .

### 7.5.1 Theoretical Uncertainties of the $F_2^{\text{fit}}$ Extrapolation

Tab. 7.1 summarizes the considered changes of the predictions for the structure functions  $F_2$  and  $F_L$  in six  $Q^2$  bins at  $y = 0.7$ . Ten different variations of the standard QCD fit procedure are listed, which affect the predicted  $F_2$  and  $F_L$  functions. The resulting errors were included into the  $F_L$  determination uncertainty and into the  $F_L$  error band, respectively, see Sec. 7.6. The variations include:

- a change of the evolution starting scale to  $Q^2 = 3 \text{ GeV}^2$ ;
- a change of the minimal  $Q^2$  used in the input data points to  $Q_{\text{min}}^2 = 5 \text{ GeV}^2$ ;
- relaxation of the H1 data normalization;
- inclusion of the NMC data into the fit;
- variation of  $\Lambda_{QCD}$  by  $\pm 50 \text{ MeV}$ ;
- inclusion of an additional  $E\sqrt{x}$  term into the parameterization of the gluon density;
- relaxation of the momentum sum rule;
- variation of the charm quark mass by  $+0.4, -0.3 \text{ GeV}$ .

It is interesting to mention here, that while for the gluon density the change of  $\alpha_S$  gave a large contribution to its total uncertainty, this is much reduced for both the  $F_2$  and  $F_L$  predictions. The mechanism of such a compensation is easy to understand: Since the fit is performed to the given  $F_2$  data points, albeit at  $y \leq 0.35$ , the high  $y$   $F_2$  prediction can still not differ much, and a change of

fit assumption	$F_2^{fit}$ change in %						$F_L^{fit}$ change in %						$\chi^2/ndf$
	8.5	12	15	20	25	35	8.5	12	15	20	25	35	
$Q^2$ (GeV <sup>2</sup> )	8.5	12	15	20	25	35	8.5	12	15	20	25	35	
$Q_0^2 = 3$ GeV <sup>2</sup>	-0.8	-0.5	-0.4	-0.3	-0.2	-0.1	-1.4	-0.9	-0.7	-0.5	-0.4	-0.3	506/490
$Q_{min}^2 = 5$ GeV <sup>2</sup>	-0.3	-0.4	-0.6	-0.6	-0.7	-0.8	-2.9	-2.7	-2.6	-2.5	-2.4	-2.3	473/469
H1 norm. free	0.2	0.2	0.2	0.2	0.2	0.2	0.3	0.3	0.3	0.3	0.3	0.3	501/489
NMC data used	1.6	1.5	1.5	1.2	1.1	0.8	6.0	4.7	3.9	3.1	2.5	1.8	783/669
$\Lambda_{QCD} = 160$ MeV	-0.8	-0.8	-0.8	-0.7	-0.8	-0.8	-0.3	-1.0	-1.5	-1.8	-2.1	-2.5	508/490
$\Lambda_{QCD} = 260$ MeV	0.6	0.6	0.6	0.6	0.6	0.7	-0.1	-0.4	-0.6	-0.8	-0.9	-1.1	526/490
$g(x, Q_0^2) \cdot (1 + E\sqrt{x})$	-0.1	-0.1	-0.0	-0.0	-0.0	-0.0	-0.2	-0.1	-0.1	-0.1	-0.1	-0.1	506/489
no mom. sum rule	0.1	0.1	0.1	0.2	0.2	0.2	0.2	0.2	0.1	0.1	0.1	0.1	505/490
$m_{charm} = 1.9$ GeV	-0.1	0.1	0.4	0.5	0.1	-1.3	1.9	0.8	0.2	-0.4	-1.6	-4.5	516/490
$m_{charm} = 1.2$ GeV	0.5	-0.0	-0.0	0.6	1.6	-0.6	-3.0	-2.2	-1.5	+1.2	+1.5	-1.7	507/490
$R = 0$	-1.9	-1.7	-1.6	-1.5	-1.4	-1.2	-3.0	-2.6	-2.4	-2.1	-1.9	-1.7	525/490
$R = \infty$	4.2	4.0	3.9	3.8	3.6	3.4	7.0	6.4	6.1	5.7	5.4	5.0	528/490
Leading order fit	0.1	1.3	2.3	3.3	3.4	2.4							533/490
Massless 4 flavor fit	-1.0	-2.1	-2.2	-2.2	-3.3	-3.5							549/490
Dipole model fit	-1.2	-2.1	-2.4	-2.2	-2.0	-0.1							
"Multiplicity" model fit	1.4	2.5	2.3	2.0	2.0	1.1							
96 $F_L$ fit	2.0	2.0	1.8	1.5	1.2	0.8	-0.3	-0.5	-0.6	-0.8	-0.9	-1.0	

Table 7.1: Uncertainties relatively to the result of the standard calculation of the structure functions  $F_2$  and  $F_L$  at  $y = 0.7$  for various assumptions in the QCD procedure to fit  $F_2$  data for  $y < 0.35$  (see text). The table is based on the  $F_L$  1994 analysis. The last line gives for comparison the difference of  $F_2$  and  $F_L$  between the 1994 and the 1996 data analysis.

$\alpha_S$  is transformed into a compensating change of  $xg(x, Q^2)$ . The structure function  $F_L$  is essentially defined as the product of both, thus its change gets reduced as well. A similar cancellation occurs for the charm quark mass [96], where one could naively expect rather large effects on  $F_L$  since the charm contribution to  $F_L$  is as large as about 20% and its variation due to the quoted change of  $m_c$  for fixed  $xg$  is about 30%. It is thus rather straightforward to calculate, within the DGLAP approach, the structure functions  $F_2$  and  $F_L$  (which is sufficient for this analysis), but it requires more and precise data to separate the rôle of  $xg$ ,  $\alpha_S$  and the heavy flavours.

There is a small dependence left of the structure function  $F_2$  on  $R$  for  $y < 0.35$  (see Fig. 3.11 and Eq. 3.17). The two extreme assumptions  $R = 0$  and  $R = \infty$  were used to estimate this effect. Two corresponding  $F_2$  datasets were derived and these were considered as input to the QCD fits. The resulting variations of the predictions for  $F_2$  and  $F_L$  are listed in the table. This uncertainty of the predicted  $F_2$  can be reduced using instead of the maximum range of  $R$  variations the one that is obtained in the  $F_L$  extraction procedure at high  $y$ . Note that this requires an extrapolation of the  $F_L$  from the high to the low  $y$  domain, i.e. to  $x$  values where no  $F_L$  measurement is available so far. Therefore, the total uncertainty was included into the systematic errors of the determination of the longitudinal structure function  $F_L$ .

Two further possibilities inside the QCD program were studied but not included into the error calculation since the default theoretical approach is believed to be more correct. These are a leading order fit and a fit with the massless quark prescription for the QCD evolution. The resulting variations of the  $F_2$  structure function are small (see Tab. 7.1) if to be compared with the experimental cross section measurement error.

Two phenomenological models were used for the extrapolation of  $F_2$  as an additional cross check. These are the perturbative dipole model with  $k_T$  factorization [28] and an empirical model based on the similarity of the rise of  $F_2$  at low  $x$  and the evolution of the charged particle multiplicity with energy in  $e^+e^-$  collisions [101] ("multiplicity" model). The parameters of the models were determined using the 1994 H1 data for  $y < 0.35$  and obeying the  $Q^2$  boundaries inherent in these approaches. The results of the three-parameter fit of the dipole model and the two-parameter fit of the "multiplicity" model are presented in Tab. 7.1 at the bottom. The high  $y$  predictions of these models agree with the NLO QCD calculation within  $\pm 2.5\%$ .

The table ends with a comparison with the fit which was used for the  $F_L$  determination based on the 1996 data. This fit had different input datasets, different starting scale  $Q_0^2$ ,  $\Lambda_{QCD}$ , and further different assumptions (see Sec. 7.4). Nevertheless, the agreement between the  $F_2$  predictions is better than 2% and the  $F_L$  values almost coincide.

### 7.5.2 Systematic Errors of the $F_2^{\text{fit}}$ Extrapolation

Error source $Q^2$ bin (GeV <sup>2</sup> )	$F_2^{\text{fit}}$ change in %						$\chi^2$	$\sigma$ change in %					
	8.5	12	15	20	25	35		8.5	12	15	20	25	35
$\theta_e + 1$ mrad	-1.3	-1.0	-0.9	-0.7	-0.7	-0.7	528	-2.8	-2.0	-1.3	-0.8	-2.3	-1.6
$\theta_e - 1$ mrad	0.8	0.5	0.4	0.4	0.4	0.6	537	2.2	0.0	2.1	0.4	0.7	2.4
$E'_e + 1\%$	-6.6	-5.8	-5.3	-4.6	-4.1	-3.2	564	-0.8	-1.7	0.0	-0.4	-1.2	-0.0
$E'_e - 1\%$	6.5	5.8	5.2	4.5	3.9	3.0	565	2.4	0.5	1.0	0.0	1.1	0.7
$E_h + 4\%$	-0.7	-0.5	-0.4	-0.3	-0.3	-0.2	521	0.0	0.0	0.0	0.0	0.0	0.0
$E_h - 4\%$	0.3	0.2	0.2	0.1	0.1	0.1	530	0.0	0.0	0.0	0.0	0.0	0.0
Norm. +3%	2.0	2.2	2.3	2.4	2.5	2.6	518	3.0	3.0	3.0	3.0	3.0	3.0
Norm. -3%	-1.9	-2.1	-2.2	-2.3	-2.4	-2.5	531	-3.0	-3.0	-3.0	-3.0	-3.0	-3.0

Table 7.2: Dependence of the extrapolated structure function  $F_2$  on different error sources, calculated with respect to the default QCD fit result (left) and dependence of the measured cross section on the same errors (right), both quoted at  $y = 0.7$ . The  $\chi^2$  values correspond to the QCD fit with the modified  $F_2$  input. The  $\chi^2$  of the default fit is 506.

The QCD fit prediction has also uncertainties due to the systematic errors of the experimental cross section measurement at low  $y$ . These uncertainties are listed in Tab. 7.2. They were estimated by changing the input structure function  $F_2$ , calculated according to a given systematic error source, performing then a new QCD fit with the modified input, and finally comparing at  $y = 0.7$  the new extrapolated  $F_2$  with the default one. In Tab. 7.2 the variations of the  $F_2$  prediction are quoted together with the changes of the experimental cross section measurements at high  $y$ . For a given systematic error source the errors of the extracted structure function  $F_L$  were calculated as:

$$\Delta F_L = \frac{y^2}{Y_+} \left( \Delta F_2 - \frac{1}{\kappa} \Delta \sigma \right). \quad (7.3)$$

The total systematic errors of  $F_L$  were calculated as the quadratic sum of all error sources considered.

One can see, that a partial cancelation of the systematic errors of the  $F_L$  measurement occurred for the  $\theta_e$  and the global normalization changes. The first one was reduced by half of its magnitude, the second one by more than 2/3. The variations of the fit prediction caused by a change of the electromagnetic energy scale of  $\pm 1\%$  are much larger than the corresponding cross section change. They dominate the systematic errors of the  $F_2$  extrapolation. One notices also, that the  $\chi^2$  for these fits is increased by about 60 units.

There are two reasons for this large instability of the fit extrapolation. Firstly, the systematic errors of the 94 shifted vertex and radiative events [33] analyses due to  $E'_e$  variation were relatively large. Secondly, the input  $F_2$  was composed of measurements based on the electron (for  $y \geq 0.15$ ) and sigma (for  $y < 0.15$ ) methods (see Sec 7.3). An increase of  $E'_e$  leads thus to an increase of the measured cross section for  $y \geq 0.15$  but to a decrease of the low  $y$  cross section. This "kink" results in large  $\chi^2$  and  $F_2$  variations. For the  $F_L$  extraction, based on the 1995 and 1996 Spacal data, the variations of the extrapolated  $F_2$  were found to be twice smaller. This is related to a better precision of these data.

The high values of the structure functions  $F_2^{\text{fit}}$  and  $F_L^{\text{fit}}$  obtained from the fits to the 1994 and the combined 1995-1996 data are given in Tab. 7.3. For  $F_2$  the dominating uncertainty in the 1994 data analysis was due to the systematic errors which in the 1996 data analysis are reduced to about 2/3 of the 1994 values being thus only slightly larger than the theoretical fit uncertainty.

$Q^2$	$x$	$y$	$F_2^{fit}$	$\Delta^{sys} F_2^{fit}$	$\Delta^{th} F_2^{fit}$	$F_L^{fit}$	$\Delta^{sys} F_L^{fit}$	$\Delta^{th} F_L^{fit}$
1994 fit								
8.5	0.000135	0.7	1.39	0.09	0.03	0.27	0.04	0.02
12.0	0.000190	0.7	1.47	0.09	0.03	0.30	0.03	0.02
15.0	0.000238	0.7	1.52	0.09	0.04	0.31	0.03	0.02
20.0	0.000317	0.7	1.57	0.08	0.03	0.34	0.03	0.02
25.0	0.000396	0.7	1.59	0.07	0.03	0.35	0.02	0.02
35.0	0.000554	0.7	1.61	0.06	0.03	0.36	0.02	0.01
1996 fit								
12.0	0.000162	0.82	1.56	0.06	0.04	0.35	0.02	0.02
12.0	0.000197	0.68	1.49	0.05	0.04	0.33	0.02	0.02
15.0	0.000202	0.82	1.61	0.05	0.04	0.35	0.02	0.02
15.0	0.000246	0.68	1.54	0.05	0.04	0.33	0.02	0.01
20.0	0.000270	0.82	1.66	0.05	0.04	0.36	0.02	0.02
20.0	0.000328	0.68	1.58	0.04	0.03	0.34	0.01	0.01
25.0	0.000338	0.82	1.69	0.05	0.03	0.36	0.01	0.01
25.0	0.000410	0.68	1.60	0.04	0.03	0.34	0.01	0.01
35.0	0.000574	0.68	1.60	0.04	0.03	0.33	0.01	0.01

Table 7.3: Values of the structure functions  $F_2^{fit}$  and  $F_L^{fit}$  obtained from fits to the 1994 and the combined 1995-1996 data, extrapolated to the high  $y$  region.  $\Delta^{sys}$  and  $\Delta^{th}$  show the systematic and theoretical uncertainties of the corresponding quantity. The systematic error of the  $F_2^{fit}$  extrapolation corresponds to the complete uncertainty, without subtraction of the correlated part of the cross section measurement.

## 7.6 Extraction of the Structure Function $F_L(x, Q^2)$

The values of the longitudinal structure function  $F_L(x, Q^2)$  are listed in Tables A.1 and A.2. The total systematic errors of the measurement were calculated as a quadratic sum of the theoretical uncertainties of the  $F_2^{fit}$ , of the correlated systematic uncertainties common to the fit and the high  $y$  cross section measurement, as was described in the previous section, and of the uncorrelated systematic uncertainties, specific to the high  $y$  measurement. The latter include uncertainties due to the  $\gamma p$  background, electron identification, various detector and trigger efficiencies and radiative corrections (see Sec. 7.2). The two groups of systematic uncertainties (uncorrelated and correlated) contributed equally to the measurement based on the 1994 data, while the errors of the 1996 measurement were dominated by the uncorrelated experimental uncertainty of the high  $y$  cross section measurement. Note that the increased sensitivity to the structure function  $F_L$  lead to smaller total  $F_L$  errors in the highest  $y$  bin of the 1996 analysis in spite of the fact that the cross section measurement errors are larger. It is important to mention here, that the statistical error has a significant contribution to the total uncertainty in the  $y = 0.82$  bin of the 1996 measurement caused by the smaller luminosity and by the subtraction of the  $\gamma p$  background.

The systematic errors of the measurements at the same  $y$  value are strongly correlated. Note that there is no single dominating source among the systematic uncertainties. The uncertainties of the 1994 and 1996 analyses are rather different, not only due to changes in the backward experimental setup, but also due to the unlike treatment of the  $\gamma p$  background and radiative corrections. The systematic errors of the measurement at  $y = 0.68$  and  $y = 0.82$  are different for most of the sources:  $\gamma p$  estimation, trigger efficiency, radiative corrections, track link efficiency. As a cross check the procedure used for the highest  $y$  analysis was applied, wherever it was kinematically possible, for lower  $y$  values. The resulting cross section is in very good agreement with the one used for the official presentation. Thus the track link procedure and charge dependent background treatment appeared to be well understood.

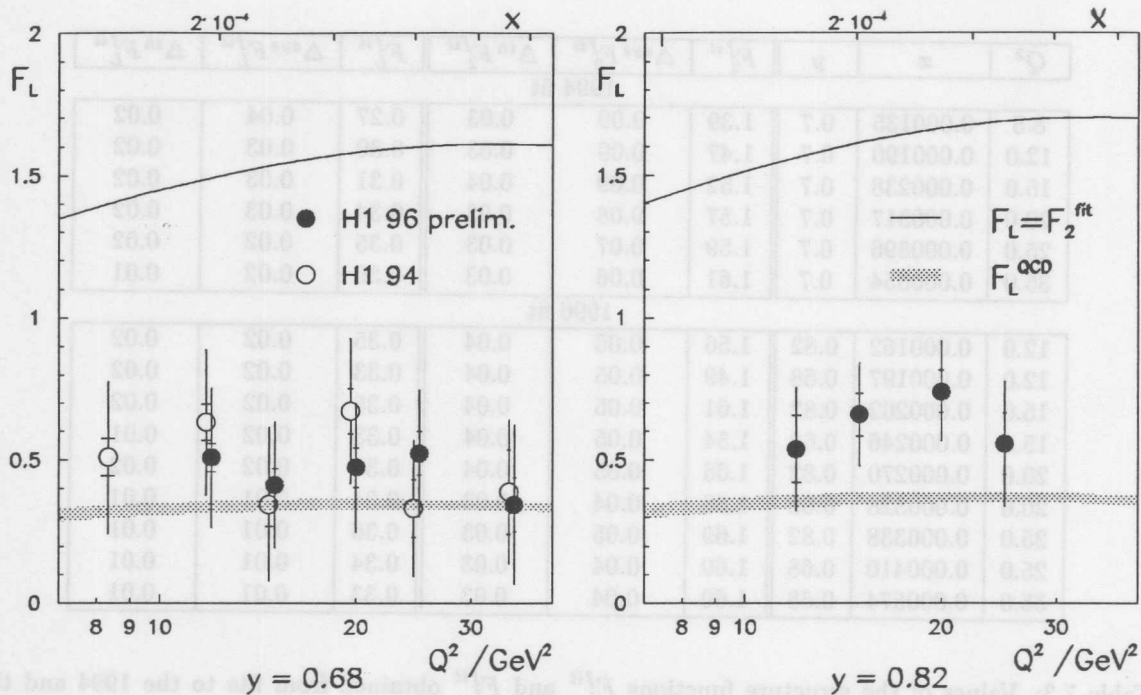


Figure 7.8: Determination of the longitudinal structure function  $F_L(x, Q^2)$  as a function of  $Q^2$  or  $x = Q^2/sy$  for  $y = 0.68$  and  $y = 0.82$  (from [42]). The inner error bars are the statistical errors. The full error bars represent the statistical and systematic errors added in quadrature. The error bands represent the uncertainty of the  $F_L$  calculation (Sec. 7.5). The upper lines define the allowed upper limit of  $F_L = F_2$ , where  $F_2$  is given by the QCD fit.

Fig. 7.8 shows the determined longitudinal structure function  $F_L$ . The 1994 results, calculated at  $y = 0.7$ , are shown together with the 1996 result calculated at  $y = 0.68$ . The shaded bands correspond to the NLO QCD calculation of the structure function  $F_L$ , as explained in Sec. 7.5. The solid lines represent the values of the structure function  $F_2$  obtained from the QCD fit. They represent the upper limit for  $F_L$ . Both the  $F_L$  and  $F_2$  predictions are derived using 1996 data, yet the difference with the 1994 result is small (see Tab. 7.1).

The 1994 and 1996 data points agree very well. Even using the 1994 data alone, it was already possible to state that the extremes  $F_L = 0$  and  $F_L = F_2$  are excluded [41] with 2.3 and 4.0 times the total error, respectively. While for spin 1/2 partons  $F_L = 0$  has been expected [10] at low  $x$  copious gluon radiation is made responsible in QCD for a significant longitudinal structure function. The data points have a tendency to lie even higher than the NLO QCD prediction. This tendency is more pronounced for the highest  $y$  measurement at  $y = 0.82$ , which was obtained with the 1996 data.

## 7.7 $F_2(x, Q^2)$ at High $y$

The studies of systematic and theoretical uncertainties of the structure function  $F_L$  (see Sec. 7.5) showed that its QCD prediction in the high  $y$  region is rather well constrained. This is visible in Tab. 7.3 and from the error bands, presented in Fig. 7.8. Therefore it is also possible to use this prediction to extract the structure function  $F_2$  from the cross section measurement at all  $y$  values.

The result of this determination is presented in Fig. 7.9 together with the NLO QCD fit prediction. One can see that for the lowest  $x$  values in each  $Q^2$  bin the measured  $F_2$  values lie lower than the



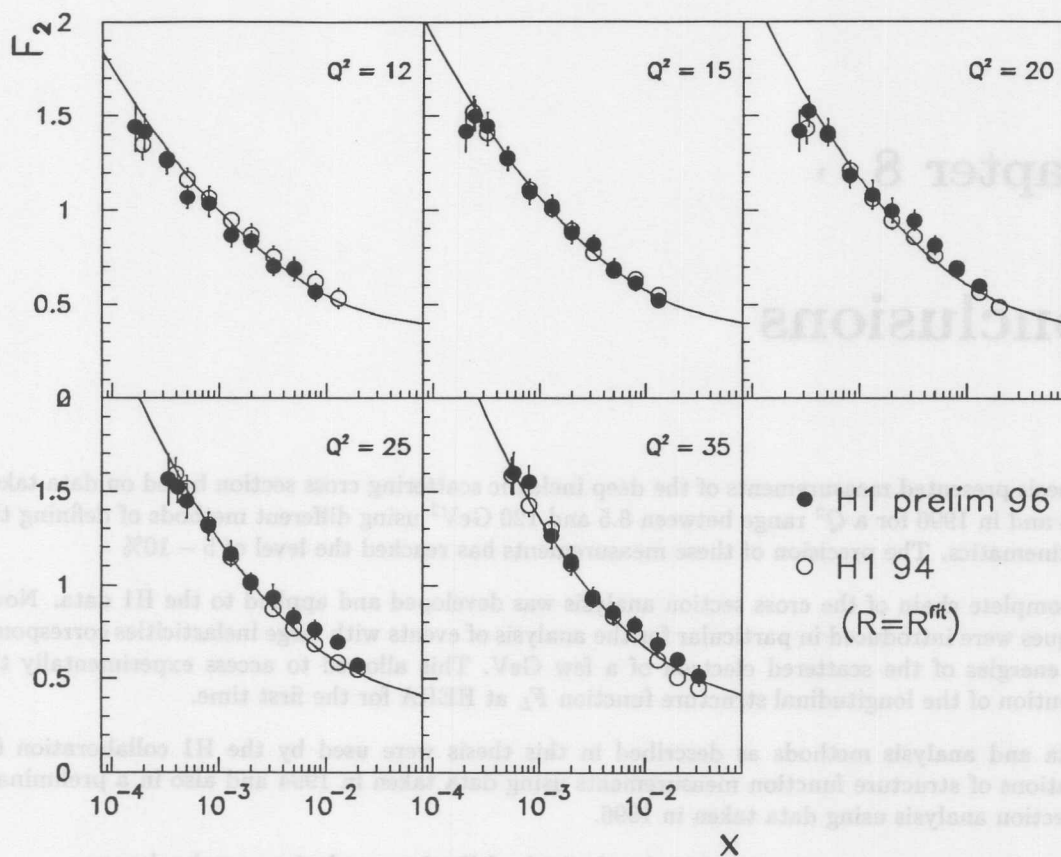


Figure 7.9: Determination of the structure function  $F_2(x, Q^2)$  using  $F_L(x, Q^2)$  obtained from the QCD fit (Sec. 7.5). The curve represents the QCD fit to the structure function  $F_2$  at  $y < 0.35$ . The lowest  $x$  points for  $Q^2 \leq 25 \text{ GeV}^2$  correspond to  $y = 0.82$ .

expectation. This effect is especially pronounced for the bins at 12 – 25  $\text{GeV}^2$ , where the highest  $y = 0.82$  values are reached. It is visible that the rise of  $F_2$  towards low  $x$  values declines, for  $Q^2$  bins at 15 and 25  $\text{GeV}^2$  the structure function starts to decrease. As was discussed in the previous sections, this effect could be explained by an unexpectedly large contribution of the structure function  $F_L$ . If, however, this behaviour is caused by the structure function  $F_2$  itself, some other effects should be introduced, for example, saturation of the gluon density. Clarification of this behaviour requires to run HERA at different proton beam energies, i.e. to measure  $F_L$ , and also to check  $F_2$  at the same  $x$  but lower  $y$  using data at higher  $E_p$  energies which may become available already in 1998.

# Chapter 8

## Conclusions

This thesis presented measurements of the deep inelastic scattering cross section based on data taken in 1994 and in 1996 for a  $Q^2$  range between 8.5 and 120 GeV<sup>2</sup> using different methods of defining the event kinematics. The precision of these measurements has reached the level of 5 – 10%

A complete chain of the cross section analysis was developed and applied to the H1 data. Novel techniques were introduced in particular for the analysis of events with large inelasticities corresponding to energies of the scattered electron of a few GeV. This allowed to access experimentally the contribution of the longitudinal structure function  $F_L$  at HERA for the first time.

Data and analysis methods as described in this thesis were used by the H1 collaboration for publications of structure function measurements using data taken in 1994 and also in a preliminary cross section analysis using data taken in 1996.

From the measurements presented in the thesis the following conclusions can be drawn:

- The H1 measurements of the DIS cross section from 1994 and 1996/5 are in good agreement with each other in spite of the exchanged backward equipment of the H1 detector.
- For  $Q^2 > 1$  GeV<sup>2</sup> the structure function  $F_2(x, Q^2)$  exhibits a strong rise towards low  $x$  values which increases with increasing  $Q^2$ . This is valid for the domain  $y < 0.35$ , where the  $F_2$  measurement is nearly unaffected by contributions from the longitudinal structure function  $F_L$ . The statement is still true if the  $F_2$  extraction is extended to  $y < 0.7$  with  $R$  calculated according to any QCD based parameterization of the parton densities.
- The structure function  $F_2(x, Q^2)$  is well described by NLO QCD for the kinematic domain  $y < 0.7$ .
- A NLO QCD fit applied to all H1 data up to  $y = 0.6$  and high  $x$  data from the fixed target experiments, was used to obtain the gluon distribution. The experimental uncertainty of this determination was found to be small (about 5%). A large contribution to this uncertainty comes from the uncertainty of the  $\alpha_S$  determination.
- Two distinct QCD fits were performed based on the H1  $F_2(x, Q^2)$  measurement at  $y < 0.35$  and fixed target experiments at high  $x$ . The first fit used 1994 data and the second one 1995,1996 data. These fits provide predictions of the structure functions  $F_2(x, Q^2)$  and  $F_L(x, Q^2)$  at high  $y$ . They agreed within 2% precision. The theoretical uncertainties of these extrapolations were found to be effectively small due to mutual compensations. That is true for the structure function  $F_2$  since it is directly constrained by the measurement. More delicate cancellations of the uncertainties were observed for the prediction of  $F_L$ , which was also found to be well constrained within about 10% precision.

- The QCD calculation of the structure function  $F_2$  at high  $y$  was used to extract the contribution of the longitudinal structure function to the measured DIS cross section. The uncertainty of the determination of  $F_L$  is dominated by the experimental errors. The longitudinal structure function  $F_L(x, Q^2)$  was found to be significantly distinguishable from both extremes  $F_L = 0$  and  $F_L = F_2$ .
- Assuming a persistent rise of  $F_2$  as described by QCD towards the low  $x$  limit of the kinematic range the derived  $F_L$  data points tend to overshoot the theoretical expectation. The measured cross section at high  $y$  could be consistently explained by values of the structure function  $F_L$  about 1.5 times higher than the prediction in NLO QCD.
- Alternatively, the high  $y$  DIS cross section measurement was used for an  $F_2$  determination with  $F_L$  values derived from NLO QCD. The resulting structure function was found to be lower than expectation, the rise towards low  $x$  slowing down, in fact, for  $Q^2 = 15, 25 \text{ GeV}^2$   $F_2(x, Q^2)$  decreases. This phenomenon may be in principle explained by some additional effects influencing the QCD evolution, like a saturation of the gluon density. Note, however, that the effect has a pronounced  $y$  dependence. Moreover, the feature of  $F_2$  to rise towards low  $x$  holds for the same  $x$  values at lower  $Q^2$ . Therefore the new phenomenon should setup at relatively large  $Q^2$ . The tendency of the double differential cross section measurement to be lower than the QCD expectation is thus rather related to larger values of  $F_L$  than to a saturation behaviour of  $F_2$ . With the present accuracy it can also still be some combination of systematic and statistical errors which lead to an underestimated measurement.

Obviously, it is important to finalize the DIS cross section measurement. Several improvements of the preliminary 1996 analysis are intended before the next H1 results will be published. These are:

- Increase of the statistics in the high  $y$  kinematic domain. This will permit to reduce the statistical errors for the highest  $y$  bins and to use a finer binning. The latter would allow to study in more detail the  $y$  dependence of the cross section, which has a rich information on  $F_L$ . This then would permit to explore fully the excellent resolution of the electron method at high  $y$ . New data collected with subtrigger S9 in 1997 will help for this purpose with a luminosity of about  $5 \text{ pb}^{-1}$  collected in this year. Yet, more data is necessary to be collected since the complete measurement requires about  $20 - 30 \text{ pb}^{-1}$  of the luminosity.
- A better cross section measurement at low  $Q^2$ . In the current H1 analysis the data of the 1995 running period was used for  $Q^2 \leq 8.5 \text{ GeV}^2$ . The reason was the trigger setup, not tuned for inclusive cross section measurements at large  $\theta_e$  in 1996. More precise low  $Q^2$  data ( $Q^2 \in 2 - 10 \text{ GeV}^2$ ) will permit to constrain better the QCD fit to the structure function  $F_2$ , especially for the extrapolation into the region of the  $F_L$  determination. This might lead to the first  $\alpha_S$  measurement based on the structure function data at HERA. A special "low  $Q^2$ " run has been performed in 1997, with about  $1.5 \text{ pb}^{-1}$  of collected luminosity. A new tracking device, the backward silicon tracker (BST), which was fully operational in 1997, will allow to improve the  $\theta_e$  resolution and to extend the measurement towards low and high  $y$ . Altogether, this will lead to a complete usage of the new features of the H1 experiment after the backward detector upgrade.
- Larger statistics at higher  $Q^2$ . The data collected with inclusive triggers in the 1996-1997 running periods ( $\mathcal{L} \sim 20 \text{ pb}^{-1}$ ) should allow to perform a more precise measurement of the structure function  $F_2$  using the H1 backward detector up to  $Q^2$  values of  $150 \text{ GeV}^2$ .

These are the main steps foreseen before the H1 publication of the new deep inelastic cross section measurement. The future of the inclusive DIS cross section measurements at HERA has been discussed in detail in [102]. Related to H1, the main points are:

- increase of collected statistics for the high  $Q^2$  measurement, based on the LAr calorimeter, leading to a DIS cross section measurement up to  $Q^2 \sim 20000 \text{ GeV}^2$ ;

- measurement of the low  $Q^2$  transition from DIS to the photoproduction regime with a new Very Low  $Q^2$  (VLQ) calorimeter and also using a special run period with reduced electron beam energy;
- expansion of the  $y$  range of the measurement, which should be possible with the new silicon tracking chambers, partially installed in 1997;
- measurement of the  $F_L$  structure function, based on runs with different proton energy from  $E_p = 400$  to 1000 GeV. In view of the observations presented in this thesis the last measurement should yield particularly interesting results.

# Appendix A

## Tables of the Experimental Results

$Q^2 / \text{GeV}^2$	$x$	$F_L$	$\Delta_{stat}$	$+\Delta_{syst}$	$-\Delta_{syst}$	$\Delta_{exp}^{unc}$	$\Delta_{exp}^{cor}$	$\Delta_{fit}$
8.5	0.000135	0.51	0.06	0.29	0.27	0.17	0.19	0.06
12.0	0.000190	0.63	0.06	0.28	0.25	0.15	0.18	0.07
15.0	0.000238	0.35	0.08	0.29	0.27	0.15	0.19	0.08
20.0	0.000317	0.67	0.08	0.28	0.26	0.14	0.18	0.07
25.0	0.000396	0.33	0.10	0.25	0.22	0.15	0.14	0.07
35.0	0.000554	0.39	0.15	0.24	0.21	0.14	0.14	0.07

Table A.1: The longitudinal structure function  $F_L$  from the 1994 analysis with statistical and systematic errors:  $\Delta_{exp}^{unc}$  - the uncorrelated experimental cross section error at high  $y$ ,  $\Delta_{exp}^{cor}$  - the correlated experimental error of the extrapolated  $F_2$  and  $\Delta_{fit}$  - the error introduced by the theoretical QCD fit uncertainty.

$Q^2$	$x$	$y$	$F_L$	$\Delta_{stat}$	$\Delta_{exp}^{unc}$	$\Delta_{exp}^{cor}$	$\Delta_{fit}$	$\Delta_{tot}$
12.0	0.000162	0.82	0.538	0.117	0.152	0.070	0.067	0.215
12.0	0.000197	0.68	0.510	0.050	0.191	0.107	0.092	0.244
15.0	0.000202	0.82	0.659	0.075	0.137	0.064	0.062	0.180
15.0	0.000246	0.68	0.414	0.058	0.177	0.086	0.085	0.222
20.0	0.000270	0.82	0.741	0.075	0.139	0.049	0.056	0.175
20.0	0.000328	0.68	0.474	0.068	0.181	0.085	0.076	0.225
25.0	0.000338	0.82	0.557	0.108	0.173	0.064	0.051	0.220
25.0	0.000410	0.68	0.525	0.075	0.186	0.073	0.070	0.225
35.0	0.000574	0.68	0.346	0.094	0.213	0.126	0.066	0.279

Table A.2: Preliminary values of the structure function  $F_L$  based on the 1996 data with statistical and systematic errors:  $\Delta_{exp}^{unc}$  - the uncorrelated experimental cross section error at high  $y$ ,  $\Delta_{exp}^{cor}$  - the correlated experimental error of the extrapolated  $F_2$  and  $\Delta_{fit}$  - the error introduced by the theoretical QCD fit uncertainty.



$Q^2$	$x$	$y$	$\sigma_{red}$	$\Delta\sigma_{red}^{stat}$	$\Delta\sigma_{red}^{sys}$	$\Delta\sigma_{red}^{tot}$	$R$	$F_2$	$\Delta F_2^{stat}$	$\Delta F_2^{sys}$	$\Delta F_2^{tot}$
35.0	0.000554	0.7	1.435	0.062	0.077	0.099	0.37	1.634	0.071	0.088	0.113
35.0	0.00080	0.4833	1.372	0.036	0.049	0.060	0.36	1.442	0.038	0.051	0.064
35.0	0.00130	0.2974	1.288	0.032	0.051	0.060	0.35	1.308	0.032	0.052	0.061
35.0	0.00200	0.1933	1.110	0.027	0.052	0.058	0.33	1.116	0.027	0.052	0.059
35.0	0.00320	0.1208	0.926	0.024	0.038	0.045	0.32	0.928	0.024	0.038	0.045
35.0	0.00500	0.0773	0.831	0.023	0.040	0.046	0.30	0.832	0.023	0.040	0.046
35.0	0.00800	0.0483	0.739	0.022	0.035	0.041	0.27	0.739	0.022	0.035	0.041
35.0	0.01300	0.0297	0.600	0.019	0.025	0.031	0.24	0.600	0.019	0.025	0.031
35.0	0.02000	0.0193	0.508	0.019	0.019	0.027	0.20	0.508	0.019	0.019	0.027
35.0	0.03200	0.0121	0.452	0.019	0.026	0.032	0.16	0.452	0.019	0.026	0.032
45.0	0.00130	0.3824	1.272	0.037	0.047	0.060	0.32	1.305	0.038	0.048	0.061
45.0	0.00200	0.2485	1.214	0.034	0.049	0.059	0.31	1.225	0.034	0.049	0.060
45.0	0.00320	0.1553	1.101	0.032	0.058	0.066	0.30	1.105	0.032	0.058	0.066
45.0	0.00500	0.0994	0.911	0.028	0.033	0.043	0.28	0.912	0.028	0.033	0.043
45.0	0.00800	0.0621	0.743	0.025	0.029	0.038	0.26	0.743	0.025	0.029	0.038
45.0	0.01300	0.0382	0.686	0.024	0.031	0.039	0.22	0.686	0.024	0.031	0.039
45.0	0.02000	0.0249	0.599	0.022	0.027	0.035	0.19	0.599	0.022	0.027	0.035
45.0	0.03200	0.0155	0.505	0.021	0.023	0.031	0.15	0.505	0.021	0.023	0.031
45.0	0.05000	0.0099	0.411	0.022	0.028	0.036	0.12	0.411	0.022	0.028	0.036
60.0	0.00200	0.3314	1.192	0.041	0.047	0.063	0.29	1.213	0.042	0.048	0.064
60.0	0.00320	0.2071	1.073	0.037	0.045	0.058	0.28	1.079	0.037	0.045	0.058
60.0	0.00500	0.1326	0.935	0.033	0.043	0.054	0.26	0.937	0.033	0.043	0.054
60.0	0.00800	0.0828	0.829	0.031	0.046	0.055	0.24	0.830	0.031	0.046	0.055
60.0	0.01300	0.0510	0.701	0.028	0.029	0.040	0.21	0.701	0.028	0.029	0.040
60.0	0.02000	0.0331	0.639	0.027	0.025	0.037	0.18	0.639	0.027	0.025	0.037
60.0	0.03200	0.0207	0.586	0.026	0.028	0.038	0.14	0.586	0.026	0.028	0.038
60.0	0.05000	0.0133	0.492	0.025	0.023	0.034	0.11	0.492	0.025	0.023	0.034
60.0	0.08000	0.0083	0.432	0.027	0.023	0.035	0.08	0.432	0.027	0.023	0.035
90.0	0.00320	0.3107	1.088	0.051	0.047	0.070	0.26	1.103	0.052	0.048	0.071
90.0	0.00500	0.1988	0.992	0.045	0.047	0.065	0.24	0.997	0.045	0.047	0.065
90.0	0.00800	0.1243	0.907	0.041	0.056	0.069	0.22	0.908	0.041	0.056	0.069
90.0	0.01300	0.0765	0.726	0.035	0.040	0.053	0.19	0.726	0.035	0.040	0.053
90.0	0.02000	0.0497	0.650	0.033	0.031	0.045	0.17	0.650	0.033	0.031	0.045
90.0	0.03200	0.0311	0.587	0.030	0.034	0.045	0.13	0.587	0.030	0.034	0.045
90.0	0.05000	0.0199	0.481	0.027	0.019	0.033	0.10	0.481	0.027	0.019	0.033
120.0	0.00500	0.2651	1.009	0.093	0.075	0.120	0.23	1.018	0.094	0.076	0.121
120.0	0.00800	0.1657	0.911	0.068	0.056	0.088	0.21	0.914	0.068	0.056	0.088
120.0	0.01300	0.1020	0.754	0.063	0.111	0.128	0.18	0.755	0.063	0.111	0.128
120.0	0.02000	0.0663	0.570	0.049	0.057	0.075	0.16	0.570	0.049	0.057	0.075
120.0	0.03200	0.0414	0.582	0.048	0.060	0.077	0.13	0.582	0.048	0.060	0.077
120.0	0.05000	0.0265	0.402	0.035	0.045	0.057	0.10	0.402	0.035	0.045	0.057
120.0	0.08000	0.0166	0.330	0.032	0.034	0.047	0.07	0.330	0.032	0.034	0.047

Table A.4: H1 results of the DIS cross section measurement ( $\sigma_{red} = \sigma/\kappa$ ) and determination of the structure function  $F_2$  based on the 1994 data (continuation) with statistical, systematic and total errors.  $R$  represents values of  $R(x, Q^2)$  used for the extraction of the structure function  $F_2$ .





$Q^2$	$x$	$y$	$\sigma_{red}$	$\Delta\sigma_{red}^{stat}$	$\Delta\sigma_{red}^{sys}$	$\Delta\sigma_{red}^{tot}$	$R$	$F_2$	$\Delta F_2^{stat}$	$\Delta F_2^{sys}$	$\Delta F_2^{tot}$
45.0	0.00130	0.3830	1.346	0.024	0.075	0.079	0.310	1.381	0.025	0.077	0.081
45.0	0.00200	0.2490	1.125	0.020	0.067	0.070	0.290	1.135	0.020	0.067	0.070
45.0	0.00320	0.1560	1.094	0.021	0.078	0.080	0.280	1.097	0.021	0.078	0.081
45.0	0.00500	0.1000	0.872	0.016	0.053	0.056	0.260	0.873	0.016	0.053	0.056
45.0	0.00800	0.0620	0.797	0.015	0.049	0.051	0.240	0.797	0.015	0.049	0.051
45.0	0.01300	0.0380	0.642	0.013	0.041	0.043	0.220	0.642	0.013	0.041	0.043
45.0	0.02000	0.0250	0.549	0.011	0.040	0.042	0.190	0.549	0.011	0.040	0.042
45.0	0.03200	0.0160	0.488	0.011	0.037	0.038	0.170	0.488	0.011	0.037	0.038
60.0	0.00200	0.3320	1.131	0.024	0.073	0.077	0.280	1.150	0.024	0.074	0.078
60.0	0.00320	0.2080	0.990	0.021	0.124	0.126	0.270	0.996	0.021	0.125	0.126
60.0	0.00500	0.1330	0.924	0.020	0.065	0.068	0.250	0.926	0.020	0.065	0.068
60.0	0.00800	0.0830	0.762	0.017	0.065	0.067	0.230	0.763	0.017	0.065	0.067
60.0	0.01300	0.0510	0.664	0.015	0.040	0.043	0.210	0.664	0.015	0.040	0.043
60.0	0.02000	0.0330	0.607	0.015	0.039	0.042	0.180	0.607	0.015	0.039	0.042
60.0	0.03200	0.0210	0.523	0.013	0.034	0.037	0.160	0.523	0.013	0.034	0.037
60.0	0.05000	0.0130	0.456	0.012	0.032	0.034	0.130	0.456	0.012	0.032	0.034
90.0	0.00320	0.3110	1.282	0.034	0.098	0.104	0.250	1.299	0.034	0.099	0.105
90.0	0.00500	0.1990	0.999	0.026	0.076	0.080	0.230	1.004	0.026	0.076	0.080
90.0	0.00800	0.1250	0.933	0.025	0.066	0.070	0.210	0.934	0.025	0.066	0.070
90.0	0.01300	0.0770	0.758	0.021	0.051	0.055	0.190	0.758	0.021	0.051	0.055
90.0	0.02000	0.0500	0.658	0.019	0.043	0.047	0.170	0.658	0.019	0.043	0.047
90.0	0.03200	0.0310	0.546	0.016	0.044	0.047	0.150	0.546	0.016	0.044	0.047
90.0	0.05000	0.0200	0.419	0.013	0.032	0.034	0.120	0.419	0.013	0.032	0.034
90.0	0.08000	0.0120	0.401	0.015	0.031	0.034	0.090	0.401	0.015	0.031	0.034

Table A.6: Preliminary H1 results of the DIS cross section measurement ( $\sigma_{red} = \sigma/\kappa$ ) and determination of the structure function  $F_2$  based on the 1996 data (continuation) with statistical, systematic and total errors.  $R$  represents values of  $R(x, Q^2)$  used for extraction of the structure function  $F_2$ .

## Appendix B

# Z-Vertex Reconstruction

This appendix is devoted to the crucial task of reconstructing the  $Z$ -vertex and polar angles of the tracks in the central tracking chambers. We discuss here the final stage of the problem, namely the link of the tracks recognized in the CJC with the  $Z$ -point information from the  $Z$ -chambers. A technique, known as the "Method of deformable templates" (DTM) [93, 103] was used for this purpose. The algorithm has been implemented as a CTREC module of the standard H1 reconstruction package and it has been used since 1994.

### Problem Formulation

Track finding in the central tracker of the H1 detector starts from the jet chambers CJC1 and CJC2 (see Sec. 2.2.2). It is based almost exclusively on drift times measured in the  $r\phi$ -plane, as the spatial precision in this plane is about two orders of magnitude better than for  $Z$ . Only on a later stage of the track reconstruction the measured  $Z$ -values are used. As a result of the CJC reconstruction, one has the tracks classified as originating from the primary or secondary (two prong neutral particle decays) vertices or as cosmic track candidates. The task of the link procedure, described here, is to update the CJC track information with the data from the two  $Z$ -drift chambers, the inner (CIZ) and the outer (COZ) one.

Before describing the application of the deformable template method to the  $Z$ -link, it is important to explain problems of the standard approaches. First of all, in the presence of noise and inefficiency the relatively small number of sense wires in the  $Z$ -chambers makes a stand alone reconstruction of tracks rather inefficient. A better strategy is to use initially CJC tracks and then to pick up hits from the CIZ and COZ. Yet, if one tries to do that for different jet chamber tracks separately, a wrong identification can reject the track from the primary vertex, since the  $Z$ -measurement using the  $Z$ -chambers is by more than order of magnitude more precise than the one with the CJC. This is evidently worse than not to link the track with the  $Z$ -chambers at all. A better way is to perform a vertex fit using the jet chambers information only and to link the tracks with the  $Z$ -chambers afterwards, combining recognition and track-vertex fitting step into one procedure as it was proposed in [100]. However, this is a very time consuming procedure if a simple combinatorial search is performed. In the case of  $N$  tracks with  $M$   $Z$ -point link opportunities for each of them it leads to  $N^M$  possible combinations that have to be tested.

The main purpose to use the deformable template method is to overcome this combinatorial difficulty. To describe it let us start with the general definitions.

In the uniform magnetic field tracks are helices. Thus in the  $SZ$ -plane, where  $S$  is the path along the track in the  $XY$ -plane, tracks are straight lines. It is natural to use the following parameterization:

$$Z(S) = a \cdot S + Z_0, \quad (\text{B.1})$$

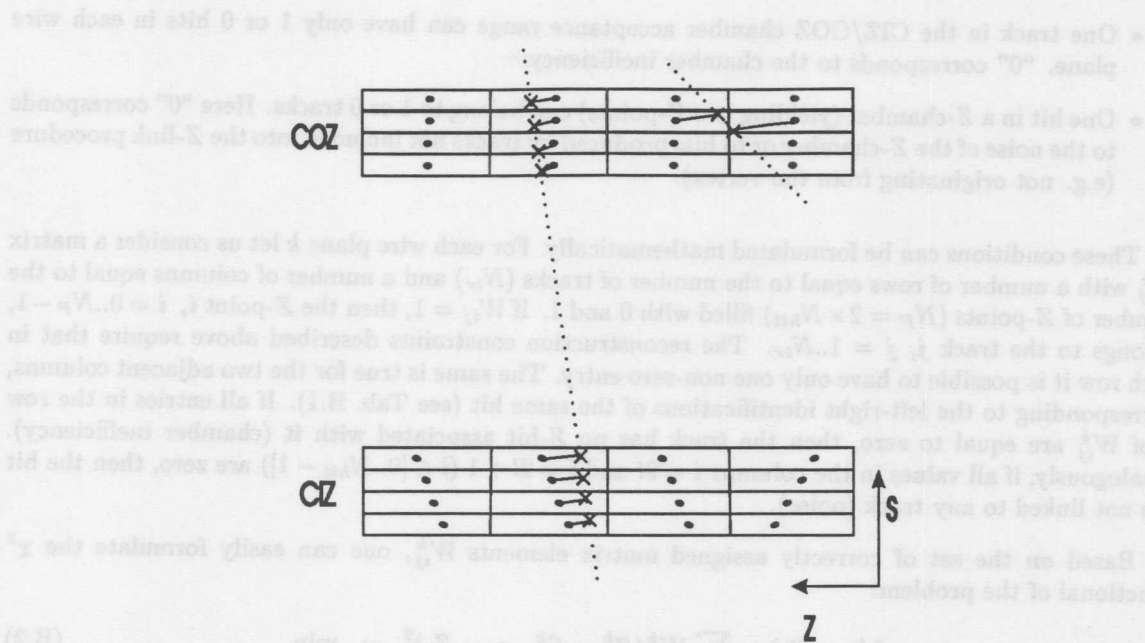


Figure B.1: Illustration of the  $Z$ -link procedure. Transverse views of the CIZ and COZ chambers are schematically represented as boxes with horizontal and vertical lines corresponding to the radial chamber walls and to the cathode planes, respectively. The sense wires are drawn as dots inside each drift cell. Sense wires, combined horizontally, form eight wire planes. Drift cells, grouped vertically, four in CIZ and four in COZ, correspond to chamber rings which are actually are 16 for the CIZ and 24 for the COZ, more than drawn. The dotted lines display tracks crossing the chambers. Crosses indicate the origins of the ionisation clusters closest to the sense wires. The drift paths are sketched as solid lines from the ionisation cluster to the sense wire. The left track is an example of a particle passing through the chambers at small angle (with respect to the normal direction) with one hit produced at each plane of the sense wires. The right track shows the case when a track, crossing the cathode plane of the COZ can produce two hits in the same wire plane.

where  $a$  is the slope of the track and  $Z_0$  is the  $Z$ -coordinate of the track at  $S = 0$ .

Let us consider a track crossing both  $Z$ -chambers at small angle with respect to the normal to their surfaces producing electron-ion pairs which drift to the sense wires and cathode planes, respectively (see Fig. B.1). According to the electric field configuration, each of the  $Z$ -chambers is divided into a number of drift cells with a sense wire in the center. We will assume that in the  $S - Z$  projection these cells are boxes.  $S$ -boundaries of the drift cells are determined by the chamber walls and  $Z$ -boundaries by the cathode planes.

The track can produce a signal detected by the sense wire if and only if it crosses its drift cell. We will call the time measurement converted to the drift distance in the  $Z$  direction a  $Z$ -hit. Tracks passing the drift cells at the same distance from the sense wire, left or right, correspond to the same drift time (so-called left-right ambiguity). Therefore one  $Z$ -hit gives rise to two  $Z$ -points requiring a left-right identification of that hit.

Four cells in the CIZ and four in the COZ form 8 wire planes according to the sense wires  $R$ -positions. For not very inclined tracks one can assume that these cross drift cells only once in each plane<sup>1</sup>. Since the double hit resolution of the CIZ and COZ is about 3 mm and the track density in the H1 detector is usually not too high, it is possible to require that two tracks do not share the same  $Z$ -hit.

To summarize the statements above, one can formulate the following *reconstruction constraints*:

<sup>1</sup>A special case occurs when a track crosses a cathode plane between two adjacent drift cells and can produce hits in both of them, see below and also Fig. B.1.

- One track in the CIZ/COZ chamber acceptance range can have only 1 or 0 hits in each wire plane. "0" corresponds to the chamber inefficiency.
- One hit in a Z-chamber (yielding two Z-points) can belong to 1 or 0 tracks. Here "0" corresponds to the noise of the Z-chamber or to hits produced by tracks not included into the Z-link procedure (e.g. not originating from the vertex).

These conditions can be formulated mathematically. For each wire plane  $k$  let us consider a matrix  $W_{ij}^k$  with a number of rows equal to the number of tracks ( $N_{tr}$ ) and a number of columns equal to the number of Z-points ( $N_P = 2 \times N_{hit}$ ) filled with 0 and 1. If  $W_{ij}^k = 1$ , then the Z-point  $i$ ,  $i = 0..N_P - 1$ , belongs to the track  $j$ ,  $j = 1..N_{tr}$ . The reconstruction constraints described above require that in each row it is possible to have only one non-zero entry. The same is true for the two adjacent columns, corresponding to the left-right identifications of the same hit (see Tab. B.1). If all entries in the row  $j$  of  $W_{ij}^k$  are equal to zero, then the track has no Z-hit associated with it (chamber inefficiency). Analogously, if all values in the columns  $i = 2l$  and  $i = 2l + 1$  ( $l \in [0..N_{hit} - 1]$ ) are zero, then the hit  $l$  is not linked to any track (noise).

Based on the set of correctly assigned matrix elements  $W_{ij}^k$ , one can easily formulate the  $\chi^2$  functional of the problem:

$$\mathcal{L}(a_j, Z_0) = \sum_{k,i,j} W_{ij}^k (Z_{ij}^k - S_{ij}^k \cdot a_j - Z_0)^2 \rightarrow \min, \quad (\text{B.2})$$

the sum extends over all wire planes ( $k$ ), Z-points ( $i$ ) and tracks ( $j$ ). Here  $Z_{ij}^k$  denotes the Z-point measurement and  $S_{ij}^k$  the path to the Z-point in the XY-plane<sup>2</sup>.

The sum in Eq. B.2 is performed over all tracks with the same hypothesis. In the case of primary vertex tracks, one has  $N_{tr}$  track slopes and one common  $Z_0$  value as parameters of the minimization. A procedure to handle a system of linear equations, obtained by minimizing the functional (B.2) in this case, was taken from the CJC reconstruction [100]. For secondary vertex tracks the momentum conservation constraint was added using the Lagrange multipliers technique.

Details of the DTM implementation do not depend on the hypothesis the tracks were fitted to. Thus, in the further discussion the general form of Eq. B.2 corresponding to the primary vertex fitted tracks is used. The method of deformable templates is described in the next section.

### Method of Deformable Templates

A detailed formulation of the deformable template approach can be found in [93, 103]. The key idea of the method is to modify the functional (B.2) by adding to it a new parameter, the so-called *temperature*. The combinatorial search among possible  $W_{ij}^k$  values is replaced by an iterative minimization of this new functional with the temperature going to 0. At zero temperature the modified functional coincides with the initial one, at non-zero temperature the main difference is that the weights  $W_{ij}^k$  are allowed to be real numbers between 0 and 1. These values can be understood as probabilities that the point  $i$  belongs to track  $j$ ; the update rule for them has a special form to ensure the satisfaction of the reconstruction constraints.

A standard way to derive the form of this modified functional and update rule for  $W_{ij}^k$  is to use the Mean Field Theory approximation from statistical physics [103]. Here we will follow a simpler approach, closer to the detector implementation, leading to the same result.

Let us consider once again a track crossing the Z-chambers (see Fig. B.1). After the CJC reconstruction one has an initial approximation of its parameters. The estimated errors of these can be

<sup>2</sup>Both  $S_{ij}^k$  and  $Z_{ij}^k$  in Eq. B.2 depend on the track parameters due to different XY-paths and equal time contour corrections for the Z-chambers [84].

$$N_{track} \left\{ \begin{array}{|c|c|c|c|} \hline & & 0 & 0 \\ \hline & & 0 & 0 \\ \hline & & 0 & 0 \\ \hline 0 & 0 & 0 & 1 \\ \hline \end{array} \right. \quad \underbrace{\hspace{10em}}_{N_p = 2N_{hit}}$$

Table B.1: Matrix of weights for a wire plane (see text). Rows correspond to different tracks, columns to different  $Z$ -points. Vertical double lines separate pairs of left-right identifications of the same hits. A '1' standing in the 4-th row and 4-th column means that the right image of the second  $Z$ -hit is linked to the 4-th track.

transformed into a track  $Z$ -measurement uncertainty in the region of the  $Z$ -chambers. We will denote this uncertainty as  $\sigma_{track}$ . As the CJC measurements are too rough, there are usually several  $Z$ -points lying in the acceptable region around the track (standard  $3.5\sigma_{track}$  band). Thus it is impossible to determine immediately and unambiguously which point belongs to the track. Nevertheless, for each point we can define a *probability* that it is produced by this track. That means that we will replace the combinatorial decisions 0 or 1 for  $W_{ij}^k$  by real numbers between 0 and 1. We will now use not only one point on the  $Z$ -plane as a link candidate for the track but all, with different probabilities or weights. These weights should be greater for points lying closer to the current track position and it is natural to assume that they have a Gaussian distribution with the width defined by the *track* error  $\sigma_{track}$ . One can then use an additional parameter, the temperature  $T$ , and expect:

$$W_{ij}^k \sim \exp\left(-\frac{D_{kij}^2}{T\sigma_{chamber}^2}\right). \quad (\text{B.3})$$

Here  $D_{kij}$  is the distance from the  $Z$ -point  $i$  situated on the wire plane  $k$  to the track  $j$  and  $\sigma_{chamber}$  is the resolution of the  $Z$ -chamber. According to the above reasoning, the initial temperature should satisfy the condition:

$$T_{init} \approx \left(\frac{\sigma_{track}}{\sigma_{chamber}}\right)^2. \quad (\text{B.4})$$

Once a minimum of the functional (B.2) with a new definition of  $W_{ij}^k$  is found, one obtains an updated set of track parameters with smaller errors and the temperature can be decreased. This procedure should be repeated until the temperature is less than some value  $T_{stop}$ .

The next step is to force the weights update rule to satisfy the recognition constraints at  $T = 0$ . For non-zero temperature, the value of the weight  $W_{ij}^k$  should be smaller, if some other point in the same wire plane  $k$  was already assigned to the track  $j$  with a large weight, or if any of the left-right identifications of the  $Z$ -hit  $l = i/2$  is used by another track. That can be obtained by normalizing  $W_{ij}^k$  over all tracks, which share the  $Z$ -hit  $l$  and over all hits, which belong to the track  $j$ . For example, in Tab. B.1, this region for  $W_{34}^k$  and  $W_{44}^k$  is indicated by the numbers. To allow the situation, when all the weights in this region are equal to 0, one has to add some "extra value" to the denominator and

write the following formula for the update rule<sup>3</sup>:

$$W_{ij}^k = \frac{\exp\left(-\frac{D_{kij}^2}{T\sigma_{chamber}^2}\right)}{\sum_{\alpha,\beta} \exp\left(-\frac{D_{k\alpha\beta}^2}{T\sigma_{chamber}^2}\right) + \exp\left(-\frac{\lambda}{T}\right)} \quad (\text{B.5})$$

$\alpha = 0..N_P - 1, \beta = j;$   
 $\beta = 1..N_{track}, \alpha = 2 * (i/2), 2 * (i/2) + 1.$

The meaning of the parameter  $\lambda$  becomes clear if as in [103] one takes the limit of Eq. (B.5) at  $T \rightarrow 0$ . To do that we will divide the formula (B.5) by the numerator:

$$W_{ij}^k = \frac{1}{1 + \sum_{\alpha \neq i, \beta \neq j} \exp\left(-\frac{(D_{r\alpha\beta}^2 - D_{kij}^2)}{T\sigma_{chamber}^2}\right) + \exp\left(-\frac{(\lambda\sigma^2 - D_{kij}^2)}{T\sigma_{chamber}^2}\right)}. \quad (\text{B.6})$$

The summation in the last equation is performed over the same region as in Eq. B.5 excluding the point  $\alpha = i, \beta = j$ .

From the formula (B.6) one can see that  $W_{ij}^k$  goes to 0 if there is another Z-point lying closer to the track  $j$  or if there is another track lying closer to the hit  $i/2$ . If the point  $i, j$  corresponds to the minimal distance, then  $W_{ij}^k$  goes to 1 if this distance is smaller than  $\sqrt{\lambda}\sigma$ . Thus  $\lambda$  has the meaning of a *cut-off parameter*. At zero temperature it is set to be equal to  $\lambda(0) = \lambda_0 = 3.5^2$ . Since the effective resolution is proportional to the square root of the temperature, we will parameterize  $\lambda$  as:

$$\lambda(T) = \gamma T + \lambda_0, \quad (\text{B.7})$$

where  $\gamma$  is constant.

One can mention here that since the weights  $W_{ij}^k$  depend on the distances from the points to the tracks, they also depend on the track parameters. This makes the functional (B.2) highly nonlinear. We will assume that its minimum is not far from the initial approximation. This is true for the first iteration, as the overall weight of the Z-points is small at the high temperature (see the next section). This can be ensured for all other iterations by reducing the temperature change between them. Then a two step minimization procedure for a fixed temperature is used. Firstly, given the distances from the tracks to the Z-points all  $W_{ij}^k$  are calculated according to Eq. B.5. Secondly, assuming the weights are fixed the new track parameters are obtained by solving the system of linear equations. If the changes of  $a_j, Z_0$  and  $W_{ij}^k$  are small enough, the procedure is stopped, otherwise it is repeated again.

### Details of the DTM Implementation

The normalization using all Z-points inside one wire plane simplifies the pattern recognition in various situations. Suppose, for example, one track crossing a Z-chamber produces 4 real hits, one of those may be accompanied with noise (see Fig. B.2-a) which happens in drift chambers when a signal is followed by so-called afterpulses. At high temperature all of them have equal weights before normalization (if  $T\sigma_{chamber}^2 \gg D_{kij}^2$ , see Eq. B.3). After the average over a wire plane is taken (Eq. B.5), the "true" points have four times bigger weight than the "ghost" ones improving thus the track recognition.

One can imagine a situation, when this normalization leads to a reduction of the hit link efficiency. In Fig. B.2-b one can see two tracks lying close to a point 1 and a point 2 which probably belongs to track 2. Both points belong to the same wire plane  $k$ . At zero temperature, point 2 cannot be

<sup>3</sup>To handle the situation when the track crosses the cathode plane between two drift cells and can lead to more than one Z-hit on a wire plane, the Z-points corresponding to the next sense wire and the opposite left-right identification are additionally excluded from the summation in the equation.

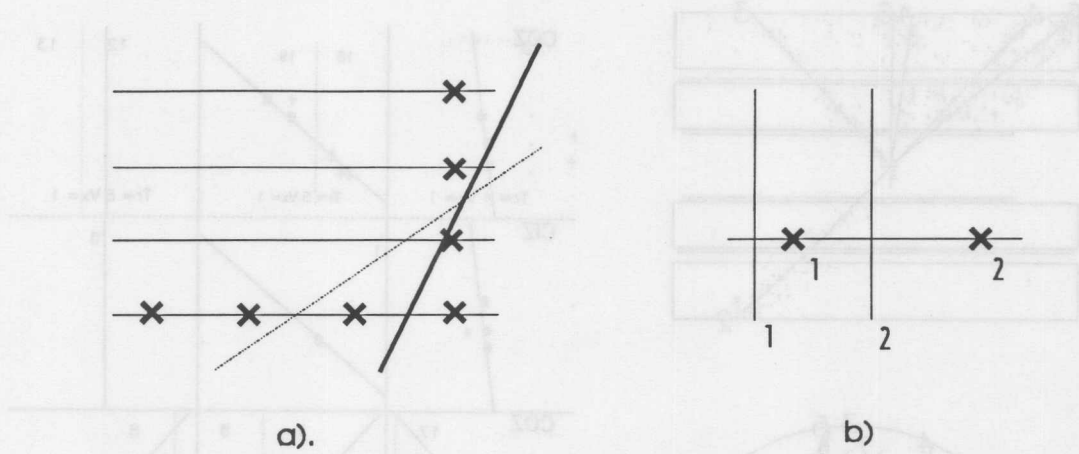


Figure B.2: a) An example of a track crossing a Z-chamber vertically and producing 4 real hits one with 3 afterpulses. The horizontal lines represent the wire planes, crosses display the Z measurements. Four crosses ordered vertically correspond to the “true” measurement while three additional hits on the first wire plane are afterpulses. The solid (dotted) inclined line indicates the result of the straight line fit to the measurements if the normalization over all Z-points in one wire plane is performed (absent). b) A “problematic” situation for the normalization over Z-points in a wire plane. The vertical lines indicate two tracks. The horizontal line corresponds to a wire plane, crosses show the Z-points produced by the tracks. At zero temperature Z-point 2 can not be assigned to track 2 since point 1 lies closer to the latter. The situation is resolved at high temperature (see text).

assigned to track 2 as there is another point lying closer to it. This track can not take point 1 either, as this lies closer to track 1. But to belong to the second track, point 2 should be not further apart than  $3.5 \sigma_{chamber}$  from it. That means that the distance between two hits should be smaller than  $7\sigma \sim 3 \text{ mm}$  — just at the limit of the chambers doublehit resolution. In the case of the H1 detector with not very high track density, this is rather unlikely.

The situation described above does not produce any problem at all at high temperature. As  $D_{k11} \sim D_{k12} \sim D_{k22} = D$  and  $D_{k21} \gg D$ , one can find such a temperature, for which weights before normalization satisfy the relation:  $W_{11}^k \sim W_{12}^k \sim W_{22}^k = W$  and  $W_{21}^k \sim 0$ , such that after normalization one has

$$W_{ij}^k \sim \begin{pmatrix} 1/2 & 1/3 \\ 0 & 1/2 \end{pmatrix}$$

i.e. a bigger probability for the point 2 to belong to the second track.

One of the important quantities characterizing the track quality is the number of points linked in each Z-chamber. As their internal efficiency is usually rather high (80-96%) it is very improbable to have only one linked point for a chamber. On the other hand, if the track crosses it close to the sense wire supporting rods or through the cathode plane a coherent inefficiency of all wire planes of a Z-chamber is possible. Therefore, it is better to avoid linking one hit at all. In order to achieve this, we can extend further our weighting technique and introduce an additional weight over all Z-points in one chamber  $ch$  which is given by the formula:

$$\begin{aligned} \Sigma_j^{ch} &= \sum_{i,k \in ch} W_{ij}^k, \\ V_j^{ch} &= \begin{cases} 0, & \text{if } \Sigma_j^{ch} \leq 1 \\ \Sigma_j^{ch} - 1, & \text{if } 1 < \Sigma_j^{ch} < 2 \\ 1, & \text{if } \Sigma_j^{ch} \geq 2. \end{cases} \end{aligned} \quad (\text{B.8})$$

Then the main minimization problem has the following form:

$$\mathcal{L}_Z = \sum_{ch} V_j^{ch} \sum_{k_{ch,i,j}} W_{ij}^{k_{ch}} (Z_{ij}^{k_{ch}} - S_{ij}^{k_{ch}} \cdot a_j - Z_0)^2 \rightarrow \min. \quad (\text{B.9})$$

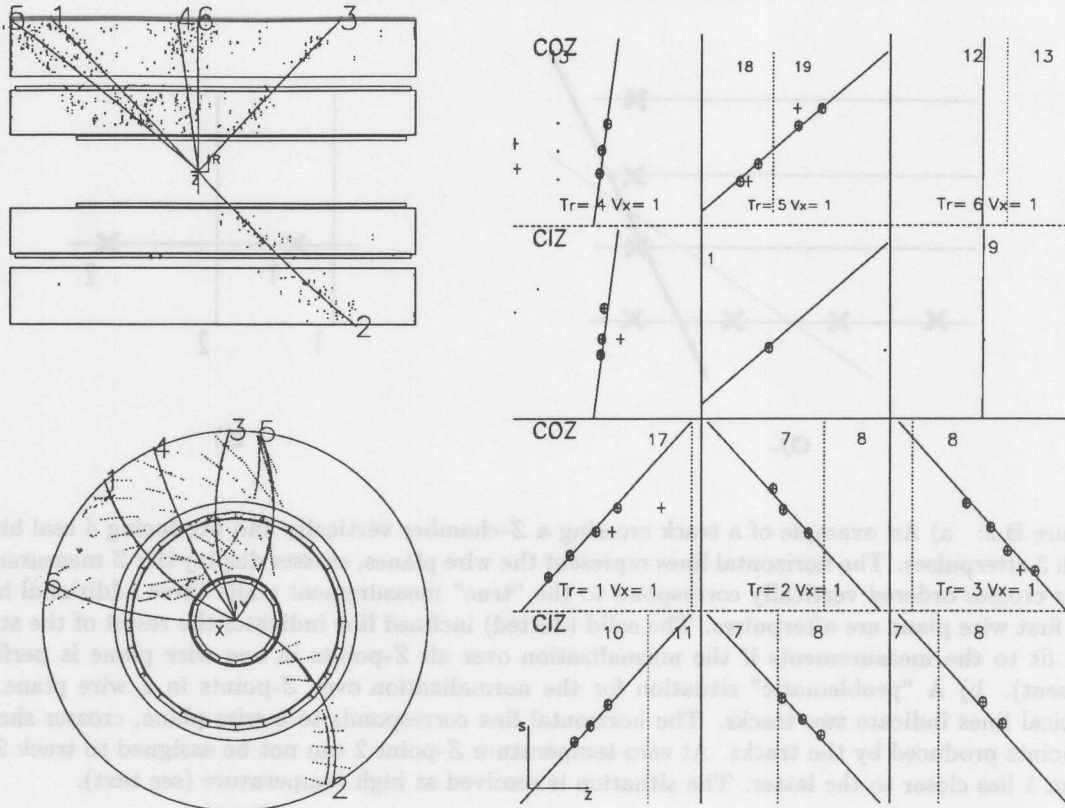


Figure B.3: An event reconstructed in the H1 detector. Only tracks linked to the primary vertex are drawn. The upper left part of the picture shows the  $Z$ - $R$  view of the central tracker, the lower left – the  $X$ - $Y$  cross section. The right picture shows a detailed view of each of the six tracks (6 sub-pictures, from left to right and from bottom to top) inside the  $Z$ -chambers in  $Z$ - $S$  projection. Crosses indicate  $Z$ -points accepted for the linking procedure, circles represent points linked to the track. Numbers at the top of each sub-picture correspond to the chamber rings, dots to the sense wire positions, vertical dotted lines to the cathode planes. One can see some afterpulses in the  $Z$ -chambers. This fact increases the importance of the wire plane normalization. Note that the CIZ point linked to track 5 was not used in the fit due to  $V_1^{ch} = 0$  (see text).

A link procedure with the tracks already reconstructed in one of the detectors has one important specific feature. The minimization problem contains not only the  $Z$ -chamber part (Eq. B.9), but also the part from the CJC:

$$\mathcal{L}_{all} = \frac{1}{\sigma_{CJC}^2} \mathcal{L}_{CJC} + \frac{1}{\sigma_Z^2} \mathcal{L}_Z. \tag{B.10}$$

As the tracks are already recognized in the CJC, it should be kept at zero temperature and then  $\sigma_{CJC}$  is the intrinsic resolution of the chamber. To introduce the smearing of the  $Z$ -chambers resolution at non-zero temperature, one can add quadratically its intrinsic resolution and the width of the weight distribution:

$$\sigma_Z^2(T) = \sigma_{chamber}^2(1 + 0.5T). \tag{B.11}$$

The physical meaning of the formula above is that by decreasing the temperature we introduce a smooth way of including the  $Z$ -chamber measurements avoiding the dramatical spatial precision change discussed in [100].

The “black box” formulation of the DTM algorithm in a FORTRAN-like notation is given below:



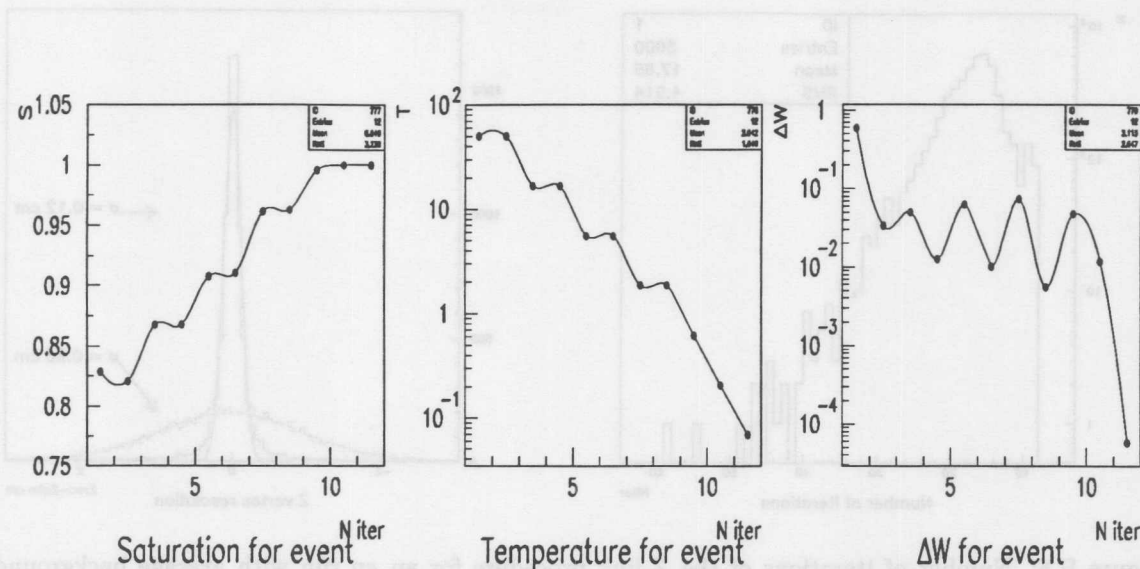


Figure B.4: Saturation (left), temperature (center) and average weight change (right) as a function of the iteration number for the event shown in Fig.B.3.

```

T = Tinit          ! Initial temperature
Ai = Aicjc        ! Initial tracks-vertex
Z = Zcjc          ! parameters from CJC reconstruction
do while (T>Tstop)
! Check average change of the track parameters and the weights:
do while (DA,DZ,DW > DAsstop,DZstop,DWstop)
Find new W
Find new Ai,Z
enddo
T = T/Tstep
enddo
    
```

The results of the algorithm processing are updated tracks and vertex parameters and a list of relations between tracks and Z-points. A Z-point was assumed to be linked to the track if its weight at the final temperature was bigger than a fixed value  $W_{on} > 0.5$ .

**Results**

The Deformable Template Method showed stable behaviour for both the Monte Carlo simulation and real data. In Fig. B.3 one can see a typical electron-proton scattering event in the central tracker of the H1 detector. The internal efficiency of the chambers is high, normally 3 – 4 hits per track are reconstructed in the COZ and 2 – 3 in the CIZ<sup>4</sup>. Track #6 is not linked to either Z-chamber which is an example of a coherent loss: in the CIZ it hits the wire support (see left figure, radial view); it traverses the COZ parallel and close to the cathode plane. Since the CJC Z-resolution is about 1 cm, it is most likely that this track passes the chamber directly through a cathode rod.

Fig. B.4 shows, iteration by iteration, the internal behaviour of the main parameters of the algorithm applied to the same event. The event saturation is the fraction of the Z-hits unambiguously

<sup>4</sup>A complicated electric field structure of the CIZ causes a low probability to produce more than 3 hits by one track.

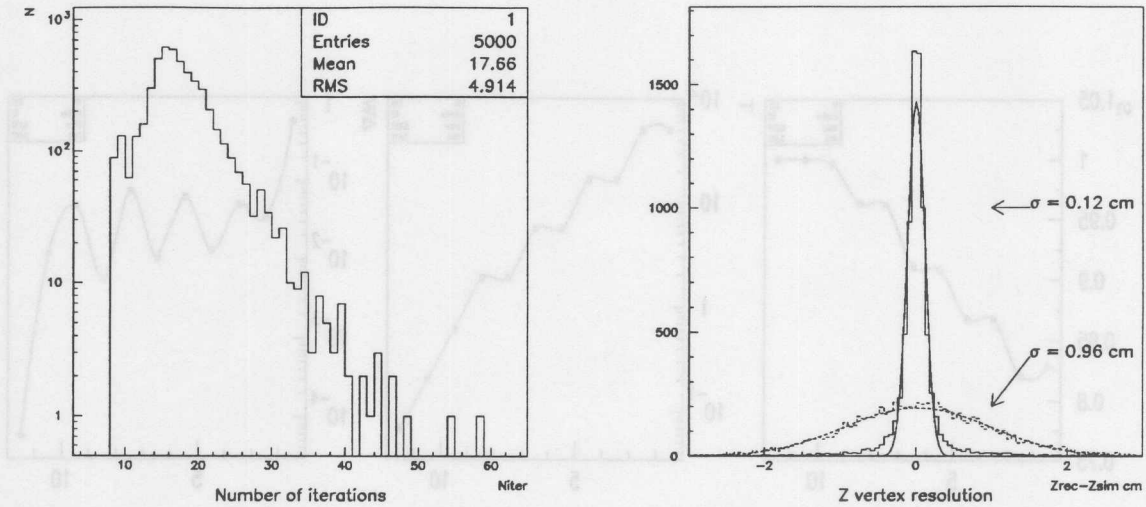


Figure B.5: Number of iterations of the  $Z$ -link procedure for an  $ep$  run with average background conditions (left).  $Z$ -vertex resolution for simulated events (right). The dashed line corresponds to the  $Z$ -vertex before use of the  $Z$ -chambers, the full line is obtained after linking the  $Z$ -chamber hits to the CJC tracks.

associated to the CJC tracks defined as:

$$S = \frac{1}{N_{plane} N_{track}} \sum_{k=1}^{N_{plane}} \sum_{j=1}^{N_{track}} \left[ 1 - \sum_{i=1}^{N_{Zpoint}} W_{ij}^k (1 - W_{ij}^k) \right]. \quad (\text{B.12})$$

If all weights of the  $Z$ -points are close to 1 or to 0, i.e. they are recognized with a high probability as linked to some track or as noise, the saturation is close to 1. On the contrary, if for many tracks several  $Z$ -points have the same small weight, the saturation is small. In the plot B.4-left one can see that the saturation for the selected event is a rising function of the iteration number. It is basically defined by the temperature (central figure). For the last iterations the saturation approaches 1 while the corresponding average change of the  $W_{ij}^k$  (right figure) drops below 0.001. It is interesting to mention here, that two iterations per one temperature value were enough to satisfy the convergence criteria (see central figure).

A distribution of the number of iterations for an  $ep$  run with average background conditions is presented in Fig. B.5-left. The mean CPU time to process one event by the  $Z$ -link procedure was about 50 msec on a MIPS R4400 processor of a Silicon Graphics Computer.

Fig. B.5-right shows the improvement of the vertex  $Z$ -coordinate determination for the simulated events in comparison to the CJC reconstruction before the  $Z$ -link. One can see that the accuracy increased by one order of magnitude.

The efficiency of the  $Z$ -link algorithm was determined with Monte Carlo simulation. Defined as a fraction of events, satisfying the condition  $|Z_{vertex}^{sim} - Z_{vertex}^{Rec}| < 3.5 \sigma_{Z_{vertex}^{rec}}$  the  $Z$  vertex link efficiency was found to be about 98%. Here  $Z_{vertex}^{Rec}$  ( $Z_{vertex}^{sim}$ ) denote the reconstructed (simulated)  $Z$ -vertex positions and  $\sigma_{Z_{vertex}}$  is the estimated error of the reconstructed vertex.

# Bibliography

- [1] L.N. Hand, Phys. Rev. **129** (1963) 1834.
- [2] J.D. Bjorken, Phys. Rev. **148** (1966) 1467.
- [3] J.D. Bjorken, Phys. Rev. **179** (1969) 1547.
- [4] M. Gell-Mann, Phys. Lett. **8** (1964), 214.
- [5] C. Zweig, CERN Report Nos. TH 401,402, 1964.
- [6] S.L. Adler, Phys. Rev. **143** (1966) 1144.
- [7] J.D. Bjorken, Phys. Rev. **163** (1967) 1767.
- [8] D.J. Gross and C.H. Llewellyn Smith, Nucl. Phys. **B14** (1969) 337.
- [9] K. Gottfried, Phys. Rev. Lett. **18** (1967) 1154.
- [10] C.G. Callan, D.J. Gross, Phys. Rev. Lett. **22** (1969) 156.
- [11] R.M. Barnett et al., Phys. Rev. **D54** (1996) 1.
- [12] J.C. Collins, D.E. Soper, G. Sterman, World Scientific, Singapore, 1989
- [13] R.K. Ellis, W.J. Stirling, B.R. Webber, QCD and Collider Physics, Cambridge University Press, 1996.
- [14] Yu.L. Dokshitzer, Sov. Phys. JETP **46** (1977) 641;  
V.N. Gribov and L.N. Lipatov, Sov. J. Nucl. Phys. **15** (1972) 438 and 675;  
G. Altarelli and G. Parisi, Nucl. Phys. **B126** (1977) 298.
- [15] M.A. Shifman, A.I. Vainshtein and V.I. Zakharov, Nucl. Phys. **B147** (1979) 385, 448, 519.
- [16] W.L. van Neerven, Proceedings of the Workshop Future Physics at HERA, vol. 1, eds. G. Ingelman, A. De Roeck, R. Klanner, DESY (1996) 56.
- [17] M. Glück, E. Reya and A. Vogt, Z.Phys. **C67** (1995) 433.
- [18] E. Laenen et al., Nucl. Phys. **B392** (1993) 162.
- [19] E.A. Kuraev, L.N. Lipatov, V.S. Fadin, Sov. Phys. JETP **44** (1976) 443.  
E.A. Kuraev, L.N. Lipatov, V.S. Fadin, Sov. Phys. JETP **45** (1977) 199.  
Y.Y. Balitsky, L.N. Lipatov, Sov. J. Nucl. Phys. **28** (1978) 822.
- [20] V.S. Fadin, L.N. Lipatov and M.I. Kotsky, hep-ph/9704267.
- [21] T. Jaroszewicz, Phys. Lett. **B116**, (1982) 291.
- [22] S. Catani and F. Hautmann, Phys. Lett. **B315** (1993) 157, Nucl. Phys. **B427** (1994) 475.

- [23] R.D. Ball and A. De Roeck, Proceedings of the DIS 96 workshop, eds G.D Agostini and A. Niro, World Scientific, Singapore, (1996) 669.
- [24] S. Catani, Zeit. Phys. **C70** (1996) 263.
- [25] R.D. Ball and S. Forte, Phys. Lett. **B351**, (1995) 313.
- [26] S. Catani, preprint DFF 248/4/96;  
S. Catani, Proceedings of the DIS 96 workshop, eds G.D Agostini and A. Niro, World Scientific, Singapore, (1996) 165.
- [27] R.S. Thorne, Phys. Lett. **B392** (1997) 463.
- [28] A. Mueller, Nucl. Phys. **B392** (1994) 373;  
H. Navelet et al., Phys. Lett. **B385** (1996) 357.
- [29] CTEQ Collaboration, Handbook of Perturbative QCD, 1993.
- [30] I. Abt et al., Nucl. Phys. **B407** (1993) 515.
- [31] T. Ahmed et al., Nucl. Phys. **B439** (1995) 471.
- [32] S. Aid et al., Phys. Lett. **B354** (1995) 494.
- [33] S. Aid et al., Nucl. Phys. **B470** (1996) 3.
- [34] A. Panitch, Ph. D. Thesis Universite Libre de Bruxelles (1996).
- [35] E. Evrard, Ph. D. Thesis, Vrije Universiteit Brussel, IIHE (ULB-VUB) (1996).
- [36] B. Gonzalez-Pineiro, Ph. D. Thesis, Université de Paris (1996).
- [37] H1 collaboration, A Measurement of the Proton Structure Function  $F_2(x, Q^2)$  at High  $Q^2$  at HERA, paper submitted to the International EPS Conference, Jerusalem 1997, August 1997.
- [38] M. Botje, M. Klein, C. Pascaud, Proceedings of the Workshop Future Physics at HERA, vol. 1, eds. G. Ingelman, A. De Roeck, R. Klanner DESY (1996) 33.
- [39] C. Adloff et al., Nucl Phys. **B497** (1997) 3.
- [40] L. Bauerdick, A. Glazov, M. Klein, Proceedings of the Workshop Future Physics at HERA, vol. 1, eds. G. Ingelman, A. De Roeck, R. Klanner DESY (1996) 77.
- [41] S. Aid et al., Phys. Lett. **B393** (1997) 452.
- [42] H1 Collaboration, A Measurement of the Inclusive Deep Inelastic  $ep$  Scattering Cross Section at Low  $Q^2$  at HERA, paper submitted to the International EPS Conference, Jerusalem 1997, August 1997.
- [43] C. Pascaud and F. Zommer, LAL preprint LAL/95-05.
- [44] B. H. Wiik, Proc. of the XXIV Int. Conf. on High Energy Physics, ed. Springer-Verlag, Berlin (1989) 404.
- [45] I. Abt et al., Nucl. Instr. and Meth. **A386** (1997) 310 and **A386** (1997) 348.
- [46] H. Abramowicz et al., Nucl. Instr. and Meth. **A180** (1981) 429.
- [47] H1 BEMC Group, Nucl. Instr. and Meth. **A372** (1996) 399.
- [48] J. Katzy, Ph.D. Thesis (in German), Heidelberg (1997).
- [49] H1 Collab., RPC report 93/02 March 8, (1993).

- [50] H1 Spacal Group, Nucl. Instr. Meth. **A386** (1997) 397.
- [51] H1 Spacal Group, Nucl. Instr. Meth. **A382** (1996) 395.
- [52] H1 Spacal Group, Nucl. Instr. Meth. **A374** (1996) 149.
- [53] W. Eick et al., Nucl. Instr. Meth. **A386** (1997) 81.
- [54] R. Brun et al., PAW long write-up, CERN Program Library, Q 121, Geneva.
- [55] F. Jaquet and A. Blondel, "An ep facility for Europe", Proceedings, ed. by U. Amaldi, Hamburg (1979).
- [56] U. Bassler and G. Bernardi, Nucl. Instr. and Meth. **A361** (1995) 197.
- [57] K.C. Hoeger, Proceedings of the Workshop Physics at HERA, vol. 1, eds. W. Buchmüller, G. Ingelman, DESY (1992) 43;  
S. Bentvelsen, J. Engelen, P. Kooijman, Proceedings of the Workshop Physics at HERA, vol. 1, eds. W. Buchmüller, G. Ingelman, DESY (1992) 23.
- [58] R. Brun et al., GEANT long write-up, CERN Program Library, W5103, 1989.
- [59] Proceedings of the Workshop Physics at HERA, vol. 1, eds. W. Buchmüller, G. Ingelman, DESY (1992).
- [60] G.A. Schuler and H. Spiesberger, Proceedings of the Workshop Physics at HERA, vol. 3, eds. W. Buchmüller, G. Ingelman, DESY (1992) 1419.
- [61] A. Kwiatkowski, H. Spiesberger and H.-J. Möhring, Comp. Phys. Comm. **69** (1992) 155.
- [62] A. Arbuzov et al., DESY preprint 95-185 (1995).
- [63] A. Courau, P. Kessler, Phys. Rev. **D46**, 117 (1992).
- [64] G. Ingelman, Proceedings of the Workshop Physics at HERA, vol. 3, eds. W. Buchmüller, G. Ingelman, DESY (1992) 1366.
- [65] L. Lönnblad, Comp. Phys. Comm. **71** (1992) 15.
- [66] T. Sjöstrand, Comp. Phys. Comm. **82** (1994) 74.
- [67] G. Marchesini et al., Comp. Phys. Comm. **67** (1992) 465.
- [68] H. Jung, Comp. Phys. Comm. **86** (1995) 147.
- [69] A. H. Mueller, Nucl. Phys. **B415** (1994) 373.
- [70] G. Grindhammer, Observation of Low  $x$  Phenomena in Hadronic Final States, hep-ph/9709255.
- [71] B. Andersson et al., Phys. Rep. **97** (1983) 31.
- [72] B.R. Webber, Nucl. Phys. **B238** (19984) 492;
- [73] R. Engel and J. Ranft, Phys. Rev. **D54** (1996) 4244.
- [74] H. Kaufmann, private communication.
- [75] T. Kurča, private communication.
- [76] A. Meyer Ph.D. Thesis, Hamburg University, 1997.
- [77] M. Derrick et al., Z.Phys **C69** (1996) 607.
- [78] M. Derrick et al., Z.Phys **C72** (1996) 399.

- [79] BCDMS Collaboration, A.C. Benvenuti et al., *Phys. Lett.* **B223** (1989) 485; CERN preprint CERN-EP/89-06 (1989).
- [80] E665 Collab., M.R. Adams et al., *Phys. Rev* **D54** (1996) 3006.
- [81] NMC Collaboration, M. Arneodo et al., *Phys. Lett.* **B364** (1995) 107.
- [82] F. Willeke, (in German) HERA Seminar Bad Lauterberg 1995, preprint DESY-HERA 95-03 (1995) 177.
- [83] S. Levonian, A. Panitch, H1 internal report, H1-09/95-454 (1995).
- [84] J. Haack, Ph.D. Thesis (in German) Humboldt University, Berlin (1995).
- [85] T.C. Awes et al., *Nucl. Instr. and Meth.* **A311** (1992) 130.
- [86] A. Panitch, Internal Note H1 H1-08/95-449 (1995).
- [87] C. Pfeiffer, M. Dirkmann, Internal Note H1-01/97-512 (1997).
- [88] J. Janoth, Ph.D Thesis (in German), Heidelberg (1997).
- [89] M. Dirkmann, Internal Note H1-05/96-477 (1996).
- [90] C. Arndt, Diploma Thesis (in German), Hamburg (1995).
- [91] J. Janoth et al., Internal Note H1-11/95-464 (1995)
- [92] P. Verrecchia Internal Note H1-09/95-456 (1995).
- [93] A. Yuille et al., Harvard Robotics Laboratory Technical Report no. 90-7 (1990).
- [94] U. Bassler and G. Bernardi, Internal Software Note 51-06 (1995).
- [95] V. Shekelyan, presentation to the ELAN Group (1996).
- [96] F. Lehner, Ph.D. Thesis (in German), University of Hamburg, (1998), to be submitted
- [97] A.D. Martin, R.G. Roberts, W.J Strling, *Phys. Lett.* **B387** (1996) 419.
- [98] W. Vogelsang and A. Vogt, DESY preprint 95-096 (1995).
- [99] E.B. Zijlstra and W. van Neerven, *Nucl. Phys.* **B383** (1992) 525.
- [100] V. Blobel, private communication.
- [101] A. De Roeck and E.A. De Wolf, DESY preprint 96-143 (1996), hep-ph/9609203.
- [102] Proceedings of the Workshop Future Physics at HERA, vol. 1, eds. G. Ingelman, A. De Roeck, R. Klanner, DESY (1996).
- [103] M. Ohlsson et al., LU TP 91-27 (1991).
- [104] S. Baginyan, A. Glazov, G. Ososkov, JINR E10-94-328 (1994).

## Acknowledgments

First of all I wish to thank sincerely Dr. G. Chelkov who supported my visit to DESY IfH Zeuthen in May 1994, Prof. V. Blobel who first suggested me a possibility of writing Ph.D thesis at this institute and Prof. P. Söding who offered me a possibility to work at DESY IfH Zeuthen starting from January 1995.

During my stay at the institute I felt steady support from the members of the Zeuthen H1 group. Their help, especially at the beginning of my work, was of great value for me. I would like to specially thank J. Haack, H. Kaufmann, P. Kostka, T. Naumann for their introduction to the very details of the H1 operation, their help during the writing of the central tracking software and analysis of the H1 data.

Since January 1995 I enjoyed the common work on one of the most interesting phenomena of nature, the structure of the proton, with the other members of the H1 ELAN group. First of all I would like to thank the members of the 1994 crew: U. Bassler, G. Bernardi, B. Pinero, G. Raedel. Especially, I would like to thank E. Evrard and A. Panitch who introduced me to the deepest secrets of the analysis and with whom I enjoyed the most my stay in Hamburg.

A new method of the determination of the structure function  $F_L$  would not have appeared without many fruitful discussions with colleagues from the H1 collaboration. Here I wish to thank C. Pascaud, P. Marage, F. Zomer and A. De Roeck for advice and help. I would like to address special thanks to W. Krasny, whose criticism helped to understand better the strong and the weak sides of this new approach.

I liked very much the analysis of the 1996 data together with F. Lehner, V. Shekelyan, A. Zhokin, and other members of ELAN. I would like to specially thank T. Kurča, with whom I shared most of the discoveries and difficulties of this work. I would like to thank him also for his comments on the draft of the thesis.

Separately I wish to express my gratefulness to M. Klein. (Actually, If I would make it "inclusive", I would have to add his name to each paragraph.) He helped me during my first steps of the analysis, with him I share the idea of  $F_L$  extraction, his advice was very important for me during writing this thesis.

Finally, I would like to thank my wife Anja for her support during our stay in Germany. Special thanks I have for my son Fedor, who kindly allowed me from time to time to use our home computer for typing in this work.

